Grating Aligned Ferroelectric Liquid Crystal Devices

Peter James McCormack Wyatt

University of Leeds

School of Physics and Astronomy

Submitted in accordance with the requirements for the degree of

Doctor of Philosophy

September 2019

The candidate confirms that the work submitted is his own, except where work which has formed part of jointly authored publications has been included. The contribution of the candidate and the other authors to this work has been explicitly indicated below. The candidate confirms that appropriate credit has been given within the thesis where reference has been made to the work of others.

For those who have stumbled across this thesis, I hope that you find what you were looking for.

Acknowledgements

First and foremost I'd like to thank my supervisor Prof Cliff Jones. Without Cliff's continual motivation, love of "impossible" physics and "quick-look-sees", the ideas and hard work that went into this thesis would almost certainly not exist. A massive thank you to Dr Mamatha Nagaraj too for important discussions and contributions to the work, and importantly keeping the project in check during weekly meetings. A huge thanks to Dr James Bailey for teaching me almost everything about device fabrication, and importantly guiding me towards becoming a more competent scientist. Cheers to Dr Dan Baker for never being too busy to help fix something or help set up a quick experiment (raises pint glass). And thanks to Dr Guy Bryan-Brown at Display-Data for useful discussions and letting me come visit your clean room.

I'd like to thank my SOFI family. We had an excellent time in Durham together for our first six months as "Cohort 2". Its a shame you didn't all come with me to Leeds. A massive thanks to all those involved with the course who made it such an enjoyable and rewarding experience.

Thanks to the Soft Matter Physics Group in Leeds. Mainly for frequenting the pub with me, but also for the support and help you've provided while I've stumbled through the world of liquid crystals. A huge shout out to all the Pint of Science volunteers for providing an excellent opportunity to go to the pub, for science! Also thanks to the central team who have welcomed me as a chapter manager. Pint

of Science truly is an addiction.

And to possibly the most important of all: Mum and Dad, thanks for everything; George and Anna, thanks for being the strangest siblings, Kaaw!; Cleo and Cairo, Meow!; and Matt for being the most wonderful house-mate. And to all my friends and family that ultimately make life pleasant.

Abstract

This thesis is concerned with the vertical grating alignment of ferroelectric liquid crystals (FLCs). FLCs exhibit fast electro-optic response times compared to traditional nematic devices, and so are of particular interest for use in micro-displays and liquid crystal on silicon (LCoS) spatial light modulators. Unfortunately such materials are highly susceptible to shock induced flow. This work introduces the VGA-FLC device geometry: a vertical grating aligned ferroelectric liquid crystal display. The vertical alignment gives preferential alignment to the smectic layers, and the amplitude and pitch of the grating ensure stable alignment of the **c**-director of the FLC. The combined effect is shown to result in a shock-stable FLC geometry. The device is addressed with in-plane electric fields, and is shown to obtain fast optical response times. The theory and physics of the device is explored, and further experiments are suggested that can be performed for device optimisation.

Abbreviations

A_{PP}	Peak to Peak Amplitude
C	Polymer Concentration
d	Cell Gap
d_A	Smectic Layer Spacing
$\mathbf{E}$	Electric Field
h_{film}	Film Thickness
$\mathbf{k}$	Smectic Layer Normal
n	Refractive Index
$\mathbf{n}$	Orientational Director
$\mathbf{P}_S$	Spontaneous Polarisation
R_0	Helical Pitch
S	Orientational Order Parameter
T	Temperature
T_{NI}	Phase Transition Temperature (here between N and I)
γ_ϕ	Rotational Viscosity
Δn	Birefringence
θ_C	Smectic C Cone Angle
λ	Wavelength (of Light)
$\tau_{(ON/OFF)}$	Response Time (On / OFF)
*	Indicates Chiral Molecule
(*)	Indicates Chiral Molecule, Not Exhibiting a Helical Structure

LCD	Liquid Crystal Display
(S)TN	(Super) Twisted Nematic Display
DSM	Dynamic Scattering Mode
TFT	Thin-Film Transistor
VA(N)	Vertically Aligned (Nematic)
IPS	In-Plane Switching
SLM	Spatial Light Modulator
FLCOS	Ferroelectric Liquid Crystal on Silicon
FLC(D)	Ferroelectric Liquid Crystal (Display)
VGA-FLC	Vertical Grating Aligned Ferroelectric Liquid Crystal
AM	Active Matrix
PM	Passive Matrix
LC	Liquid Crystal
N	Nematic Phase
N*	Chiral Nematic Phase
SmA	Smectic A Phase
SmC	Smectic C Phase
SmC*	Chiral Smectic C Phase
SS(FLC)	Surface-stabilised (Ferroelectric Liquid Crystal)
UV	Ultra-violet
SB	Soft Bake
PEB	Post-Exposure Bake
HB	Hard Bake
DWL	Direct Write Lithography
The DWL	The Direct Write Lithography Machine
SEM	Scanning Electron Microscopy
SE	Secondary Electrons
BSE	Backscattered Electrons
ITO	Indium Tin Oxide
IDE	Interdigitated Electrode
PP2	Photopolymer 2
C_8	Trichloro-octyl silane
POM	Polarising Optical Microscopy

Contents

List of Figures xv

1 Motivation and Direction: Liquid Crystals for Future Display and Device Applications 1

1.1 The Rise of the Liquid Crystal Display 1

1.2 Ferroelectric Liquid Crystals for Future Display and Non-Display Applications 5

1.3 Thesis Roadmap 7

2 An Introduction to Liquid Crystals for Electro-Optic Displays and Devices 9

2.1 Nematic Liquid crystals 9

2.1.1 Order Parameter 10

2.1.2 Biaxiality 12

2.1.3 Cholesterics and Chirality 13

2.1.4 Refractive Indices 13

2.1.5 Elastic Constants and Free Energy 15

2.1.6 Permittivities and Electric Fields 17

2.1.7 The Liquid Crystal Cell and Surface Anchoring 18

2.2 Smectic Liquid Crystals 20

2.2.1 Symmetry and Ferroelectricity 23

2.2.2 SmC and SmC* Free Energy 24

2.2.3 SmC and SmC* Electric Energies 29

2.2.4 Ferroelectric Liquid Crystal Alignment 30

2.3 Liquid Crystals in Electro-Optic Devices 32

2.3.1 Polarisation Optics for Liquid Crystal Displays 32
2.3.2 General Birefringent Retarder 32
2.3.3 Gooch-Tarry Equation for a Twisted Nematic 33
2.3.4 Passive Matrix Addressing 37
2.3.5 Active Matrix Addressing 37
2.4 Ferroelectric Liquid Crystals in Electro-Optic Devices 41
2.4.1 The Surface Stabilised Ferroelectric Liquid Crystal Display 41
2.4.2 Deformed Helix Mode 44
2.4.3 Electrically Suppressed Helix Mode 46
2.4.4 Vertically Aligned Deformed Helix Mode 46
2.4.5 Diffractive Applications 48
2.5 Summary - Chapter 2 48

3 Experimental Methods **51**
3.1 Introduction 51
3.2 Photolithography: The Basics 52
3.2.1 An Introduction to Photolithography 52
3.2.2 Photoresists 52
3.2.3 Wafer Cleaning and Clean Rooms 54
3.2.4 Spin Coating 55
3.2.5 Soft Bake 56
3.2.6 Exposure: Pattering Photoresists 56
3.2.7 Post-Exposure Bake 60
3.2.8 Development 60
3.2.9 Hard Baking 60
3.3 Photolithography: Creating Microstructures for Liquid Crystal Containment 61
3.3.1 SU-8: A Negative-Tone Resist 61
3.3.2 OmniCoat: An Adhesion Promoter 62
3.3.3 SU-8 Processing Optimisation 64
3.3.4 SU-8 Processing Optimisation for “Thin” ($< 10\ \mu m$) Films 65
3.4 Characterisation of Microstructures 67
3.4.1 Scanning Electron Microscopy (SEM) 67

3.4.2 Surface Profilometry . . . 68
3.4.3 SU-8 Film Thickness Measurements . . . 70
3.5 Replication of Microstructures . . . 70
3.5.1 Stamp Fabrication . . . 73
3.5.2 Embossing into Photopolymer . . . 73
3.6 Photolithography: Creating Photomasks and Fabricating Patterned Electrodes . . . 75
3.6.1 IDE Design . . . 76
3.6.2 Creating Photomasks with Direct Write Lithography . . . 77
3.6.3 Etching Chrome . . . 77
3.6.4 Replicating IDEs using a Mask Aligner . . . 78
3.6.5 Etching ITO Glass . . . 80
3.6.6 IDE Analysis . . . 80
3.7 Vapour-Phase Silane Deposition . . . 81
3.8 Cell Construction . . . 84
3.8.1 Cell Gaps . . . 85
3.9 Polarising Optical Microscopy (POM) . . . 86
3.10 Characterisation of FLCs . . . 87
3.10.1 Spontaneous Polarisation Measurements . . . 88
3.10.2 Transmission Measurements . . . 92
3.10.3 Shock-Induced Flow . . . 92
3.10.4 Response Time Measurements . . . 93
3.11 Summary - Chapter 3 . . . 93

4 The VGA-FLCD: A Vertical Grating Aligned Ferroelectric Liquid Crystal Device 95
4.1 Introduction . . . 95
4.2 Towards Shock-Stability in FLCs . . . 96
4.3 The VGA-FLC Device Idea . . . 105
4.4 The VGA-FLC Device Theory . . . 109
4.4.1 In-Plane Switching of a Homeotropic FLC . . . 110
4.4.2 Compressions in the SmC Phase . . . 114
4.4.3 Boundary Layer Conditions for a Homeotropic SmC . . . 118

4.5 Summary - Chapter 4 120

5 Fabrication of Surface-Relief Gratings for Liquid Crystal Alignment 121

5.1 Introduction 121

5.1.1 Creating Sinusoidal-Like Surface-Relief Gratings 122

5.1.2 SEM of Surface-Relief Gratings 130

5.1.3 Optics of Surface-Relief Gratings 131

5.1.4 Gratings for VGA-FLC Devices 133

5.2 Summary - Chapter 5 133

6 Textures of Homeotropic Smectic C Alignment 137

6.1 Introduction 137

6.2 Textures on Cooling a Homeotropic FLC 138

6.2.1 Undulations in the SmC(*) 144

6.2.2 Transmission Measurements of Smectic C(*) Layer Undulations 150

6.2.3 Chiral Domains and Layer Undulations 151

6.3 Shock Induced Flow in a Homeotropic FLC 153

6.4 Summary - Chapter 6 157

7 Textures of Homeotropic Smectic C(*) Alignment in the VGA-FLC Geometry 159

7.1 FLC Textures Formed on Homeotropic Surface-Relief Gratings . . 160

7.1.1 The Grating Amplitude and Pitch 160

7.1.2 Thermal Undulations and Smectic Layer Formation 165

7.1.3 Heating VGA-FLC Devices 172

7.2 Shock Induced Flow in a Homeotropic FLC with Surface-Relief Gratings 173

7.3 Oily streaks: A Hypothesis for the Grating Defects 177

7.4 Summary - Chapter 7 178

8 Addressing the VGA-FLC Device with In-Plane Electric Fields 181
8.1 Introduction . . . 181
8.2 In-Plane Fields and the VGA-FLC Device . . . 182
8.2.1 ON Response . . . 182
8.2.2 Determination of Defect Origin . . . 185
8.2.3 OFF Response . . . 185
8.2.4 Electro-Optic Response . . . 188
8.2.5 Ion Flow in FLCs . . . 190
8.2.6 Method for Addressing the VGA-FLC Device . . . 194
8.3 Response Times of the VGA-FLCD . . . 197
8.3.1 τ_{ON} Measurements . . . 197
8.3.2 τ_{OFF} Measurements . . . 199
8.3.3 Achieving Sub-millisecond Response Times . . . 200
8.4 Summary - Chapter 8 . . . 201

9 Conclusions and Future Work 203
9.1 Conclusions . . . 203
9.2 Future Work . . . 208
9.2.1 Removal of Grating-Induced Defects . . . 208
9.2.2 Pitch, Amplitude, Surface Treatment and Ferroelectric Material . . . 210
9.3 Publications . . . 211

10 References 213

List of Figures

1.1 The chemical structure of 5CB, a member of the family of first stable nematic room temperature liquid crystals. 3

2.1 A schematic of a solid crystal, liquid crystal and isotropic liquid phase of a material that displays a nematic phase on heating. The director, a unit vector **n**, defines the average orientation of the anisotropic axis, or the long molecular axis. 11

2.2 A schematic diagram of a): the uniaxial nematic and b): the biaxial nematic phases, where **n** is the director, and the coordinate geometry is defined by the polar angles ξ, η and ζ. 12

2.3 The indicatrix for a): uniaxial, and b): biaxial liquid crystals. . . 14

2.4 A 2D schematic of the splay (K_1), twist (K_2) and bend (K_3) Frank elastic constants in the x, z-plane. 16

2.5 Schematic of a): the liquid crystal cell, b): planar surface treatments, and c): homeotropic surface treatment. 19

2.6 Schematic diagrams depicting the layered structure of the Smectic A (SmA) and Smectic C (SmC) phases. The molecules are confined to layers, where each layer can be modelled as a 2D liquid. In the SmA the director **n** is parallel to **k**, while in the SmC, **n** makes an angle θ_c to **k**. The layer spacings are shown by d_A and d_C, where the schematic eludes to the smaller layer spacing of the SmC. . . . 21

2.7 A schematic diagram of the smectic C coordinate geometry, re-defined from the polar angles ξ, η and ζ as the azimuthal angle $\eta \equiv \varphi$, $\xi \equiv \theta_c$ (the cone angle, the tilt of **n** relative to **k**), and $\zeta \equiv \psi$ is the rotation about **n** which represents the simple biaxial order parameter. **C2** is defined to be perpendicular to the plane of molecular tilt, **k** is the smectic layer normal and **c** the **c**-director (the in-layer projection of **n**). 22

2.8 A schematic diagram of the possible smectic layer elastic distortions. The black arrow indicates the **c**-director. 28

2.9 The characteristic layer geometries of the SmA and SmC(*) found with three planar pre-tilt surface conditions: no pre-tilt, parallel pre-tilt and anti-parallel pre-tilt. 31

2.10 A schematic of the twisted nematic (TN) geometry operating in the normally white (NW) mode where, a): OFF, and b): ON. . . 34

2.11 An example of passive matrix (PM) multiplexing, where D and S represent the applied potential difference to the row and column electrodes respectively. 38

2.12 A schematic diagram of active matrix (AM) addressing thin-film transistors (TFTs). a): The main componesnts of the TFT consist of gate, source and drain electrodes, an insulating layer and an a-Si semiconductor. b): Applying $-V_{GD}$ depletes the semiconductor of electrons and so depletes current flow, so $V_{SD} = 0$. c): Applying $+V_{GD}$ allows electrons to accumulate and allowing current flow from the source to the drain (I_{SD}). 39

2.13 A schematic diagram of the SSFLC device geometry. a),b): 3D sketches of the two bistable states, which are switched between by supplying a sufficiently large electric field (**E**) across the ITO substrates, where the spontaneous polarization ($\mathbf{P}_s$) aligns with the direction of the field, and so rotating the **c**-director (**c**), 180° around the cone angle (θ_c). Crossed polarisers are aligned such that the two states are either bright or dark. c),d): 2D sketches of the same geometry, emphasising the orientation of **c** and $\mathbf{P}_s$ w.r.t. **E**. e): A sketch of the FLC mesogen contained to the smectic C* cone, where **a** is the layer normal and **n** the director, and θ_c can exist at any point on the boundary of the cone. 42

2.14 A schematic of the deformed helix FLC (DHFLC) geometry, in a): the OFF, and b): ON states, which are dark and bright respectively. 45

2.15 A schematic of the vertically aligned deformed helix FLC (VADHFLC) geometry, in a): OFF, and b): ON states, which are dark and bright respectively. 47

3.2 The Direct Write Lithography machine (referred to as the DWL). The lasers are contained within the box. The DWL is currently open, as to expose the vacuum chuck. When the lid is closed, the chuck repositions into the protective casing. 57

3.3 A labelled photograph of the mask aligner. The mask and wafer are loaded, aligned with the mounted microscope, and then positioned under the UV lamp. 59

3.4 The chemical structures of the components of SU-8 2025. a): The SU-8 monomer, bisephenol-A novolak glycidyl ether. b): The photo-acid generator, triarylsulfonium hexafluoroantimonate salts. c): The organic solvent, cyclopentanone. 63

3.5 The SU-8 monomer polymerisation reaction which occurs at the epoxy groups. 64

3.6 Scanning electron microscopy (SEM) images of SU-8 cubes, with varying sized holes, made with the DWL. Design: $60 \times 60\ \mu m^2$ square with holes. A $40 \times 40\ \mu m^2$ hole is shown in b) and c). Measured feature height: $25.1 \pm 0.5\ \mu m$. a),b): SEM images taken with the wafer angled in the detector, $\sim 1.5°$, emphasising the vertical side walls. c): SEM image taken normal to the substrate, showing the rounded edges and flat top. d): Schematic diagram of the expected structures. 69

3.7 The measured film thickness of SU-8 2025 spun at 3000 rpm on ITO glass substrates. Thickness is plotted versus the density of SU-8 monomer solids. Pure SU-8 2025 has 68.55 % SU-8 monomer solids, or a density of 1.219 $gmol^{-1}$. Purple squares: expected film thickness based on the MicroChem data sheet [156]. Teal triangles: measurements made from scanning electron microscopy (SEM). Orange circles: measurements made from surface profilometry (Dektak). Fit: a fit of Equation 3.1 of the form $h_{film} = AC^{\beta}$, where here $A \propto \frac{\eta(T)^{\gamma}}{\omega^{\alpha}} = 0.018 \pm 0.002$, and $\beta = 37.3 \pm 0.9$ showing that h_{film} follows the expected trend at high concentrations of SU-8. The films at lower concentrations are thicker than expected induced by modifications to the SB and PEB to prevent cracking and delamination (see Section 3.3.4). The experimental errors are the size of or smaller than the data points. 71

3.9 The chemical structures of the acrylate monomers used to create the photopolymer named PP2. a): Sartomer 502, and b): Sartomer 349. 74

3.10 A schematic diagram of the IDE design for in-plane electric field. a): A to scale diagram of the electrode, where the "+" and "−" indicate where the wires are to be soldered, and the grey square indicates where the active area with electrode fingers is located. The final electrode area is $1.5 \times 1.5\ cm^2$. b): The individual electrode fingers are 10 μm wide and spaced 20 μm apart. Each electrode is 5.25 mm long, resulting in an overlap between the positive and negative terminals of $5 \times 5\ mm^2$. 76

3.11 The etching process for ITO glass and a chrome mask blank. a): A patterned wafer is prepared on an ITO wafer. It is essential to post bake this before submerging in the acid bath. b): The wafer is submerged in an acid bath, made of 1 : 1 : 1 solution of water, glycerol and dilute HCl (37 % in water). A low heat is applied to maintain constant etching rates. An aluminium catalyst is used for etching chrome. c): The wafer is removed from the acid bath, and rinsed in water. The resistance of the etched regions is confirmed to be zero before continuing, otherwise continue etching. d): The photoresist is removed with acetone. e): A schematic of under-etch, resulting in smaller than expected features. 79

3.12 The etching rate of ITO glass in a 1 : 1 : 1 ratio mix of water, glycerol and hydrochloric acid (37 % HCl in water). The resistance is measured by taking the wafer out of the etching solution and drying. The etching uniformity is low close to the end of the etch, as can be seen by the large error bars above 4000 s. The uniformity can be increased by continuously agitating the solution during the etch and controlling the temperature of the etchant. 81

3.13 a): The chemical structure of trichloro-octyl silane (C_8). The silane forms covalent bonds with the substrate due to its reactive chlorine (Cl^-) groups. These react with surface hydroxyl groups (OH^-) of impurities in the substrates photopolymers, forming hydrochloric acid (HCl). The C_8 molecules then form Si-O-Si bonds between one another to form a uniform monolayer, which gives good homeotropic alignment to LCs. b): A schematic diagram of the vapour phase silane deposition chamber. Compressed air is passed through the rig from left to right at 0.01 m^3s^{-1}. A drop of silane is added to the evaporation chamber, and heated at 80 $°C$ to vaporise it. This then passes though a heated copper pipe (to prevent it condensing) and into the desiccator, where it can react with the wafer. Unreacted silane and HCl exit the desiccator and dissolve in the water bath, and any remaining by products react with the steel wool. The initial volume of C_8, temperature vaporised at and the length of time the reaction is allowed to run determine the quality of the monolayer on the wafer. 82

3.14 A typical dataset for the current-reversal technique for measuring the spontaneous polarisation ($\mathbf{P}_s$) of a FLC. Measurement taken at 30 $°C$ with a 113 Hz triangular waveform with $V_{PP} = 30\ V$ for SCE13* in a $d = 1.7\ \mu m$ AP cell. a): Black line: the applied waveform, Purple squares: The output voltage response. b): Data replotted to allow the area under the curve due to the $\mathbf{P}_s$ to be calculated using the trapezium rule. 90

3.15 Spontaeous polarisation measurements for three mixtures of SCE13*. a),b): $\mathbf{P}_s$ plotted against temperature. Data fit using Equation 2.26, of which the fitting parameters are given in Table 3.1. c),d): $\mathbf{P}_s$ versus mole fraction of enantiomer for three mixtures as a function of temperature, showing a linear dependence with regards to the ratio of enantiomers in the mixture. 0.0 indicates that there is an equal ratio of left and right handed enantiomers (the racemic mixture, showing no $\mathbf{P}_s$), and 1.0 indicates that there is just one of the enantiomers present (the chiral mixture, showing the maximum $\mathbf{P}_s$). The gradient is equal to the $\mathbf{P}_s$ of the 100 % mixture at that temperature. The experimental errors are calculated to be 5 % for the 100 % and 8 % mixtures, and 10 % for the 5 % mixture of the maximum measured $\mathbf{P}_s$, calculated from the precision of the area measurement in Figure 3.14b and errors associated with mass measurements of the materials. 91

4.4 A schematic diagram of the VGA-FLC Device. a): Surface-relief gratings are embossed on to the two surfaces of the cell, one of which is an IDE, the other has no electrode. b): In the OFF state, the **c**-director is surface stabilised through the cell, and controllably oriented by the gratings, such that **g** is perpendicular to **c**. This creates a dark state for the device when viewed with POM. c): To switch to the ON state, in-plane electric fields are applied to induce a 90° twist of the **c**-director through the device. This creates a bright state, if the correct cell gap is chosen to satisfy the Gooch-Tarry equation (Equation 2.64). d): The grating vector, **g**, is aligned such to be perpendicular to the applied electric field , **E**. This ensures that the spontaneous polarisation vector, $\mathbf{P}_s$ will respond to the electric field, as allows a 90° twist though the device. e): A sketch of the SmC* mesogen for reference, where **a** is the layer normal and **n** the director. 107

4.5 A schematic diagram showing the sinusoidal undulation of smectic A layers at a boundary. The wavelength of the undulation is $\frac{2\pi}{k}$. The effect of the undulation is seen far into the sample, where the penetration length is given by ($l = \frac{1}{\Lambda k^2}$), which is greater than λ. Diagram adapted from [92]. 116

4.6 A schematic of the SmA layer compressions induced by a sinusoidal surface-relief grating, where $\Delta d_A \simeq \theta^2/2$. 118

5.2 The variation in peak-to-peak amplitude (A_{PP}) versus the exposure dose using direct write lithography (DWL) for four different surface-relief grating experiments using dilutions of 29.97 ± 0.05 % SU-8 2025 in cyclopentanone. The films vary in thickness by 1.3 ± 0.3 μm due to variations in temperatures during processing. The trends in A_{PP} are comparable to those of a 1.6 μm thick sample shown in Figure 5.1. A_{PP} increases up to a maximum, at which point it decreases towards the limit and a flat SU-8 film is obtained. This is due to high levels of photo-acid and SU-8 monomer diffusion occurring caused by the relatively high exposure doses. The curves appear have shifted with increasing film thickness for a particular exposure dose. 128

5.3 Variations in the peak-to-peak amplitudes (A_{PP}) versus exposure dose for different thicknesses of SU-8 2025 films. Purple squares: 65.5 % SU-8 in cyclopentanone, for a 5.6 ± 0.2 μm thick film. Teal triangles: 46.1 % SU-8 for a 3.0 ± 0.2 μm thick film. Orange circles: 29.9 % SU-8 for a 1.4 ± 0.1 μm thick film. The 1.4 ± 0.1 μm thick film shows the same trends as observed in Figure 5.2, whereby A_{PP} first increases with increasing dose, and then begins to decrease. The thicker films don't show this initial increasing A_{PP}, and instead start from a maximum and decease on increasing dose. 129

5.4 SEM images of SU-8 surface relief gratings. a,b): $h_{film} = 2.32 \pm 0.05\ \mu m$, dose of 500 $mJcm^{-2}$, resulting in a $A_{PP} = 0.77 \pm 0.02 \mu m$ with 1.6 μm offset. c): $h_{film} = 0.66 \pm 0.09\ \mu m$, dose of 1000 $mJcm^{-2}$, resulting in $A_{PP} = 0.59 \pm 0.05\ \mu m$ with no offset. 130

5.5 The white light transmissions of SU-8 surface-relief gratings, normalised against ITO glass. Figure 5.1 shows the profile of these gratings. a): The transmission versus wavelength of light measured for 9 different grating profiles. b): The transmission versus peak-to-peak amplitude (A_{PP}) for these gratings. A linear trend is obtained showing that the transmission decreases on increasing A_{PP}. 132

5.6 The surface profiles of the two master gratings used in Section 8 for fabricating prototype VGA-FLC devices. These masters were created using a 30 % dilution of SU-8 2025, and exposed using a 2 μm, 375 nm laser in the DWL. Final SU-8 layer thickness: $0.84 \pm 0.05\ \mu m$. Grating amplitudes: Purple line: $A_{PP} = 0.23 \pm 0.08 \mu m$, using a dose of 550 $mJcm^{-2}$, and teal line: $A_{PP} = 0.26 \pm 0.07 \mu m$, using a dose of 1200 $mJcm^{-2}$. a): A 20 μm cross-section of the grating profiles measures in the y-direction, showing the differences obtained by varying the dose. b): One peak of the gratings, with the axes adjusted to be at the same scale. 134

6.1 Analysis of the schlieren texture of the homeotropic, surface stabilised FLC SCE13* at 50 $^{\circ}C$ (Part 1). a): The schlieren texture found when cooling into the non-chiral Smectic C* phase, characterised by a texture of 4-brush defects. b): A full-wave plate is added at 45° to the crossed polarisers, and c): rotated 90° to its initial orientation. Areas that are blue are of a higher retardation and indicate the the **c**-director is parallel to the wave plate, and those that are orange are perpendicular. 141

6.2 Analysis of the schlieren texture of the homeotropic, surface stabilised FLC SCE13* at 50 $°C$ (Part 2). a): A -1 strength defect is magnified and characterised by rotation of the polarisers clockwise, and the anticlockwise brush rotation determines the defect as a saddle bend. b): Similarly a $+1$ strength defect is magnified and determined to move clockwise, with the rotation of the polarisers, indicating bend deformations in the director field. Purple and red dots indicate where the defect is located in Figure 6.1a. c,d): Sketches of the director field for ± 1 defects found in this Figure, both of which are associated with bend elastic deformations, which are expected for the SmC(*) phase. 142

6.3 The alignment of homeotropic smectic layers. a): At a particular temperature, layers have a spacing equal to d_C. b): On cooling, new layers are formed to accommodate this layer shrinking characterised by a local tilt about a disclination formed within the smectic layers. 143

6.4 Layer undulations in the surface stabilised SmC*. Here a $d = 25 \pm 1\ \mu m$, homeotropic cell is filled with 8.3% SCE13* resulting in a schlieren texture. a): The temperature was reduced at $1\ °C/min$ through the SmC* phase to induce thermal undulations. Here, $\lambda_{\parallel,\,Optical}$ undulations are clearly observed, and some areas show double undulations where there are additional $\lambda_{\perp,\,Optical}$ undulations. b): After only a few seconds a dislocation line of layer formation sweeps across the sample, behind which the undulating textures dissapear. "Flow" indicates the direction of the thermal gradient. c): A magnification of the double undulating texture, clearly showing the two undulations of different wavelengths. The images have been enhanced to emphasise the textures. 145

6.5 A schematic demonstrating the relative intensity and pitch obtained from undulations arising from the A_{21} and A_{12} elastic deformations in a homeotropic SmC(*). 147

6.6 The optical transmission (I) at 550 nm through a homeotropic device versus the reduced temperature ($\Delta T = T_{CA} - T$) of a 8.3 % SCE13* mixture, $d = 9.8 \pm 0.1$ μm. Good homeotropic nematic and SmA phases were observed. There was no preferred **c**-director orientation resulting in a schlieren texture. Purple diamonds: cooling at 0.1 $°Cmin^{-1}$ from 65 $°C$. Teal triangles: cooling at 0.5 $°Cmin^{-1}$ from 65 $°C$. Black lines are added as a guide to the eye. 150

6.7 Undulations in the SmC*. A thick homeotropic cell (40 μm) filled with 100% SCE13*, close to the transition temperature (57 $°C$), showing both chiral and surface stabilised domains. The chiral domains (dark regions) show no undulating layer textures, whereas the surface stabilised domains do (brighter region). 152

7.4 Graphs of the optical 550 nm transmission of a double grating homeotropic device versus the reduced temperature ($\Delta T = T_{CA} - T$) of Device 1: 5 % SCE13* mixture, $d = 30$ μm, $A_{PP} = 0.24 \pm 0.07$ μm. The black lines are a guide for the eye. a): Repeated measurements for the device cooled at 0.1 $°Cmin^{-1}$. b): Comparison of cooling the device at different rates. Purple squares: 0.1 $°Cmin^{-1}$, teal triangles: 1 $°Cmin^{-1}$, orange diamonds: 5 $°Cmin^{-1}$. 168

7.5 A schematic representation of the frustration in z_{bl} due to the introduction of a surface-relief grating. Black arrows are perpendicular to the grating surface normal. The grating has $A_{PP} = 0.2$ μm and $P = 4$ μm. a): $z_{bl} = 1.8$ μm, b): $z_{bl} = 1$ μm, c): $z_{bl} = 0.2$ μm . . 170

7.6 A graph comparing the three different devices examined in this Section cooled at 0.1 $°Cmin^{-1}$. Purple squares: no gratings, $d = 10$ μm. Orange diamonds: VGA-FLC Device 1: $d = 30$ μm. Teal triangles: VGA-FLC Device 2, $d = 12$ μm. 172

7.9 A sketch showing how the boundary layer over the surface-relief grating must lead to regions of defect formation in the VGA-FLC device. There are no observations of these defects in the textures of SmC* alignment, and so their effect must be small and ordered near to or on the grating surface. 178

8.1 A schematic diagram showing how the total twist of the **c**-director is expected to vary through the cell (z-direction) as a function of applied voltage. The IDEs are located on the bottom axis of the diagram. The purple dotted and dashed lines show a twist less than 90°, or $\frac{\pi}{2}^c$. The teal solid line shows the an optimum 90° twist through the device. The orange dotted line shows an over-twist of the **c**-director, which results in a reduced I. 183

8.2 A schematic diagram showing how the **c**-director twists either ±90° depending on its orientation between IDEs. 184

8.4 The transmission versus frequency response of the two VGA-FLC devices (see Table 5.1). a): VGA-FLC Device 1: $V_{rms} = 20\ V$. Teal triangles: $T = 45\ ^\circ C$. Orange circles: $T = 35\ ^\circ C$. b): VGA-FLC Device 2: Purple squares: $T = 55\ ^\circ C$, $V_{rma} = 30\ V$. Teal triangles: $T = 45\ ^\circ C$ $V_{rms} = 35\ V$. Transmissions (I) were measured with a photodiode and averaging the transmission over a cycle of square waves. The measured I is lower than that the theoretical maximum for these geometries due to **c** oscillating between dark and bright states. The experimental errors are approximately the size of or smaller than the data points. The lines are guides for the eye. 187

8.5 The transmission versus applied voltage of two VGA-FLC devices (see Table 5.1). a): VGA-FLC Device 1: $V_{rms} = 20\ V$, $F = 22\ Hz$. b): VGA-FLC Device 2: Purple squares: $T = 55\ ^{\circ}C$, $F = 100\ Hz$. Teal triangles: $T = 45\ ^{\circ}C$, $F = 50\ Hz$. Orange circles: $T = 35\ ^{\circ}C$, $F = 22\ Hz$. The frequency was varied for each measurement to obtain the maximum transmission (I). The transmission was measured with a photodiode and averaging the transmission over a cycle of square waves. The measured I is lower than that of the theoretical maximum for these geometries as **c** oscillates between dark and bright states. The experimental errors are approximately the size of or smaller than the data points. The lines are guides for the eye. 189

8.6 The transmission versus rotation of the device between crossed polarisers of the two VGA-FLC devices at $T = 45\ ^{\circ}C$ (see Table 5.1). a): VGA-FLC Device 1. b): VGA-FLC Device 2. The frequency was constant at 20 Hz and 50 Hz for the two devices respectively, to obtain the maximum average transmission. Purple squares: 0 V. Teal triangles: 10 V. Orange circles: 20 V. Blue diamonds: 40 V. The transmission (I) was measured with a photodiode and averaging the transmission over a cycle of square waves. Therefore the measured I is lower than that of the theoretical maximum for these geometries due to the **c**-director (**c**) oscillating between dark and bright states. The experimental errors are approximately the size of or smaller than the data points. The lines are guides for the eye. 191

8.10 The length of electrical pulse required to obtain maximum I shown versus temperature, as a function of applied voltage. a): Device 1. b): Device 2. The lines of best fit are guides for they eye, and are not necessarily expected to be linear. 199

Chapter 1

Motivation and Direction: Liquid Crystals for Future Display and Device Applications

"There is nothing like looking, if you want to find something. You certainly usually find something, if you look, but it is not always quite the something you were after."

— J.R.R. Tolkien, The Hobbit: or There and Back Again

1.1 The Rise of the Liquid Crystal Display

If there is one story that I'll remember long after writing this PhD, its the one told by my supervisor as the introduction to most of his talks. It concerns the dawn of the flat screen television.

Stanley Kubrick's 2001: A Space Odyssey (1968) is considered one of the greatest and most influential films ever made. The beginning of the film takes place on board a permanently inhabited international space station, highlighting technologies such as videophone communication and supercomputers with artificial intelligence. A particular scene shows two astronauts eating their breakfast while watching a video on a tablet-like device with a flat-panel display screen.

1. MOTIVATION AND DIRECTION: LIQUID CRYSTALS FOR FUTURE DISPLAY AND DEVICE APPLICATIONS

The audience watching the film at its premier at the Loews Capitol Movie Theatre on Broadway, New York, on Tuesday 28^{th} May 1968 would have been astonished by this. A modern audience in 2020 (52 years later) would not have the same response, being all too familiar with what now seems a mundane, everyday technology. On the same day, just down the street from the films premier, at the Rockefeller Centre on 5^{th} Avenue, this future was unveiled. Here, James Hillier, George Heilmeier and Bernard Lechner demonstrated the world's first liquid crystal display (LCD) [1]. This display utilised the dynamic scattering mode (DSM), and inspired technologists around the world to begin research into the LCD [2–5]. This is considered the start of the information revolution: the dawn of the LCD [6].

Today, LCDs are everywhere. At the time of writing I can see four on my desk: a laptop screen, a monitor, a mobile phone, and a calculator. It is hard to imagine a modern world without them.

The origin of liquid crystals (LCs) begins with their discovery in 1888 by the botanist Friedrich Reinitzer who discovered the liquid crystalline nature of cholesterol benzoate extracted from carrots [7]. He observed two distinct melting points, where the solid material reversibly melted into a cloudy and then a clear liquid, although the discovery of this new phase of matter was not immediately accepted. The work was continued by Otto Lehmann who proved that this was a new phase of matter, and named it "Liquid Crystal" [8]. In 1911, Charles Mauguin confined nematic LCs between rubbed plates, performing experiments on the optics of structures twisted by 90° [9]. Georges Friedel in 1922 was the first to classify three types of LCs, the nematic, smectic and cholesteric phases, by describing their structure and physical properties [10]. Soon after in 1927, Vsevolod Fréedericksz demonstrated the Fréedericksz transition, which later became an essential effect for enabling electro-optic switching for almost all LCD technologies [11]. The first device based on this electro-optic effect in LCs was patented in 1936 by the Marconi Wireless Telegraph Company: a light valve [12].

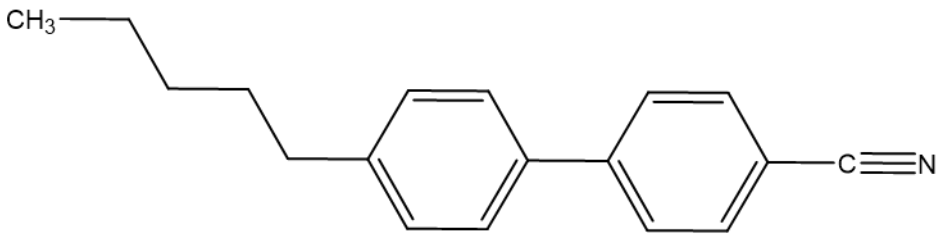

Figure 1.1: The chemical structure of 5CB, a member of the family of first stable nematic room temperature liquid crystals.

The start of LCs for display applications began in the mid 1960s driven by the idea of a "hang on the wall" television, inspired by the works of George Grey, Glenn Brown and Richard Williams [2, 13, 14]. Following the presentation of the DSM display in 1968, research began around the world, resulting in the invention of the twisted nematic (TN) LCD in 1970 by Wolfgang Helfrich [4, 5, 15–18]. This device formed the basic design for the next 30 years of flat-panel LCDs. George Gray and Ken Harrison synthesised the first stable room temperature LC mesogens, of which the most commonly used is 5CB: 4-cyano-4'-pentylbiphenyl, of which the chemical structure is given in Figure 1.1 [19]. This enabled Peter Raynes to formulate the first LC mixture that could operate below 0 $^{\circ}C$ [20]. The worlds first commercial LCD was incorporated into Sharp's electronic calculator in 1973 [21]. The basics were established.

Low power and high information content flat-screen TVs were imminent, seeing success in watches and calculators. However, they could not yet compete with cathode-ray tube displays [22]. The next challenge was to increase the complexity of the LC displays to enable video frame rate, grey-scale and colour. There was one component missing: the recently invented thin-film transistors (TFTs) available in 1973 deteriorated too quickly to pass lifetime tests [23, 24]. TFTs were considered too expensive and low yielding, with no indications that they could ever be made for a mass market. This led to research looking towards alternative modes relying on the discovery of the Alt-Pleshko multiplexing limit for passive matrix (PM) addressing [25]. One approach led to low-cost, black and white super-twisted nematic (STN) displays, but this was limited by its slow

frame rate and maximum of 480 multiplexed lines [26]. Bistable LCDs were also invented towards the end of the 1970s [27], with the surface-stabilised ferroelectric LC (SSFLC) display in 1980 by Clark and Lagerwall proving promising [28]. Ferroelectrics based on PM addressing were a key contender for the next fifteen years for LCD research against active matrix (AM) TFT approaches.

In 1975, Walter Spear and Peter Le Comber discovered a-silicon as a suitable material for TFTs, by 1978 had fabricated a functioning transistor, and built the worlds first α-silicon TFT driven LCD a year later [29–32]. The 1980s saw the first commercial full colour TFT based TN display TVs from Sharp, along with the STN mode [6, 33]. TFTs were finally beginning to meet the complexity requirements to compete with cathode-ray tube (CRT) displays, and saw their first market appearance as a flat panel display for laptop computers. The SSFLC could not compete in this market due to its sensitivity to shock, making it unsuited for portable displays. The SSFLC also lost out on the monitor market due to the superior CRTs. SSFLC development for mainstream displays was minimal by the end of the 1990s, while TFT driven TNs were booming.

Due to the success of laptop computers, TFT TNs attracted large amounts of investment for their flexibility to develop new operating modes to target the CRT monitor market. Eventually, focus also shifted towards the television market. The late 1990s saw vertically aligned (VA) and in-plane switching (IPS) modes for the improvement of viewing angles of nematic displays [34–37]. This was sufficient to displace the CRT as the dominant technology, and the 2000s saw the LCDs in displays ranging from watches to large area monitors [21]. 2007 saw LCD TVs surpass the sales of CRTs. As of 2010, LCDs predominate the display market [38]. At this stage it's hard to imagine a present without them. In essence it was the range of modes that could be enabled by AM addressing with TFTs that led to the success of the LCD, and the adaptability of this technology to provide solutions to competitors. For example, organic light emitting diodes (OLEDs) have a much higher contrast, viewing angle and colour gamut than LCDs, but the LCD technology was able to respond and compete by introducing quantum

dot (QD) colour filter films with a blue-LED back light [39].

1.2 Ferroelectric Liquid Crystals for Future Display and Non-Display Applications

The exploration into LCs did not stop with solving television. There are a plethora of technologies that have been and could still be realised based on LCs. The current "hot topics" in 2019 presented at Display Week, Silicon Valley, CA, hosted by the Society for Information Displays (SID) were:

- bendable, rollable and foldable displays,
- virtual, augmented and mixed reality displays, and
- displays for automotive applications.

There is still an active industry in the discovery and invention of the next generation of display technologies, especially with new contenders entering the market such as OLEDs and micro-LEDs, which are not LC based technologies.

The history of the LCD was ultimately a race for the first to obtain a display capable of full-colour, video rate television. This resulted in some technologies that could not compete at the time, or did not have a suitable market. One of these was the ferroelectric liquid crystal display (FLCD), which proved promising by demonstrating microsecond optical switching times [28]. Following intense research into the design and synthesis of ferroelectric materials for display applications, some commercial displays based on FLC technology came to fruition, although only in small numbers. In the early 1990's Canon launched a passively-addressed, desk-top monitor colour display [40]. It was never shipped to the USA or Europe despite fast switching speeds and high resolution as it was too difficult and expensive to ship and produce, and couldn't compete with CRTs [41]. Other promising technologies for FLCDs were introduced, such as the τV_{min} mode enabling a 17 " video rate, full colour, FLCD [42, 43]. However TFT driven active

matrix addressing NLCs rapidly improved, and so this was the end of the line for large-area FLCDs.

This was not the end of research into FLC technologies, and emphasises the power of the adaptability of TFT driven LCDs. FLCs have an advantage of sub-millisecond response times, and as such are found to be suitable for small area devices such as SLMs for beam steering, optical tweezers, holographic devices and image processing and analysis [44, 45]. Today there is still a high demand for the miniaturisation of electronic technologies requiring small display devices, such as near-to-eye equipment for camera view-finders, virtual, augmented and mixed reality systems, medical imaging and pico-projectors [46–52]. Forth Dimension Displays (ForthDD) in the UK make high resolution micro-displays and SLMs based on FLCs for near-to-eye applications, optical metrology and 3D resolution microscopy by operating at high enough speeds to use frame-sequential colour technologies [53]. As of 2019, research continues into FLCs for non-display applications, for example FLCs have been shown in Pancharatnam-Berry lenses, or even photonic crystal fibres for optical modulators in telecommunications [54–56]. As such, FLC on Silicon (FLCoS) has found a market by filling a gap for fast switching and high resolution applications, enabled because of TFTs and active-matrix addressing.

This thesis is concerned with FLCDs. One of their major problems is the layered structure of the FLC which yields them susceptible to shock-induced flow. Once a well aligned device is disrupted, the layers can become permanently displaced, resulting in an inoperable device. This is not a major problem for the lower-order nematic phases. This thesis aims to explore the shock stability of FLCs by introducing the vertical grating-aligned ferroelectric liquid crystal (VGA-FLC) mode. This geometry is analysed for its resistance to mechanical shocks, and its potential for sub-millisecond response times. If successful, such a geometry will have potential for improving FLCs in LCoS SLMs for use in high-speed adaptive optics, head mounted displays for virtual/augmented reality and telecommunications. Might the FLC finally take the crown?

1.3 Thesis Roadmap

This work is split into three main sections. The first contains the Introduction (Chapter 2) and Experimental Methods (Chapter 3). Here, liquid crystals and their role in electro-optic displays and devices is discussed, as well as exploring the more complex task of containing FLCs. The experimental section introduces photolithography as a means to create variable and reproducible containments for aligning LCs, and explains the analytical techniques used throughout the work.

Part two concerns the device idea: the VGA-FLC geometry. This includes Chapter 4 and explains the theory behind the VGA-FLC geometry as a means to control the FLC **c**-director, while imparting an increased level of shock-resistance, or self-healing. Chapter 5 then explores how to fabricate surface-relief gratings for the device using photolithography techniques developed for this work.

The final section begins by exploring the alignment induced to FLCs with and without surface-relief gratings (Chapter 7), and discusses the observations derived from cooling and mechanical shocks. Chapter 8 analyses prototype electro-optic devices based on the VGA-FLC geometry to explore its potential for high-speed applications. The thesis concludes (Chapter 9) with potential future work and optimisation that may improve the VGA-FLC geometry.

1. MOTIVATION AND DIRECTION: LIQUID CRYSTALS FOR FUTURE DISPLAY AND DEVICE APPLICATIONS

Chapter 2

An Introduction to Liquid Crystals for Electro-Optic Displays and Devices

Chapter 1 introduced the history of liquid crystals (LCs) and their use in electro-optic displays. This Chapter explores these unique properties and how they can be used to enable these technologies, enabled by the anisotropic and fluid properties of LCs. This, coupled with their engineered optical birefringence and dielectric properties allows them to reversibly and controllably respond to electric fields and interact with polarised light. These are the fundamental properties of electro-optic devices. There is an emphasis placed on ferroelectric liquid crystals (FLCs) and their important physical properties for use in displays and devices.

2.1 Nematic Liquid crystals

LCs are a "mesomorphic phase" of matter, an ordered intermediate liquid phase between a crystalline solid and an isotropic liquid. They are usually organic materials, and can be induced to exhibit LC phases by either changes in their concentration in a solvent, or changes in temperature. Those that are obtained through concentration changes are called lyotropic LCs, which are commonly experienced in everyday life, from soaps, to lipid bilayers found throughout the

biological cells in your body. These are not the topic for this project. Here we concentrate on LC phases obtained through temperature changes, called thermotropic LCs. Of the thermotropic LCs, there a number of different shapes that a LC molecule can take: here we only consider those consisting of elongated rod-like molecules, such as 5CB introduced in Figure 1.1. These are called calamitic LCs.

Figure 2.1 presents the differences between the crystalline solid, liquid crystalline and isotropic liquid phases. The LC phase can be seen to show its characteristic average direction of the molecules, defined as the director by the unit vector $\mathbf{n}$. This is the nematic phase (N), where the LC molecules tend to align parallel to one another along some direction. There is no long-range correlation between the position of these molecules relative to one another, and so they may freely translate parallel with one another while maintaining an aligned state. This phase is uniaxial as a result of the rotational symmetry about the anisotropic axis, although the existence of the biaxial thermotropic nematic phase is still in debate [57]. A typical rigid-rod LC molecule has a $4:1$ length to width ratio, for example of the order of $\sim 20\ \mathring{A}\ :\ 5\ \mathring{A}$ [58]. The first NLC was synthesised in 1890 by Gattermann and Ritschke, *p*-azoxyanisole (PAA) [59]. It wasn't until 1969 where the first room temperature NLC was synthesised by Kelker and Scheurle called MBBA (4-methoxybenzylidene-4'-butylaniline), although this was not considered suitably stable for commercial device applications [60].

2.1.1 Order Parameter

For simplicity a NLC molecule is considered to be a cylindrical rigid-rod. In the absence of polarity, $\mathbf{n} = -\mathbf{n}$ and so the two are indistinguishable. Let the axis of one rod be the unit vector $\mathbf{a}$, and exist in the coordinate geometry defined in Figure 2.2a. The direction of $\mathbf{n}$ can be written in terms of polar angles (ξ, η) of $\mathbf{a}$, such that [58, 61]:

$$a_x = \sin\xi\cos\eta\ ,\ a_y = \sin\xi\sin\eta\ ,\ a_z = \cos\xi\ , \tag{2.1}$$

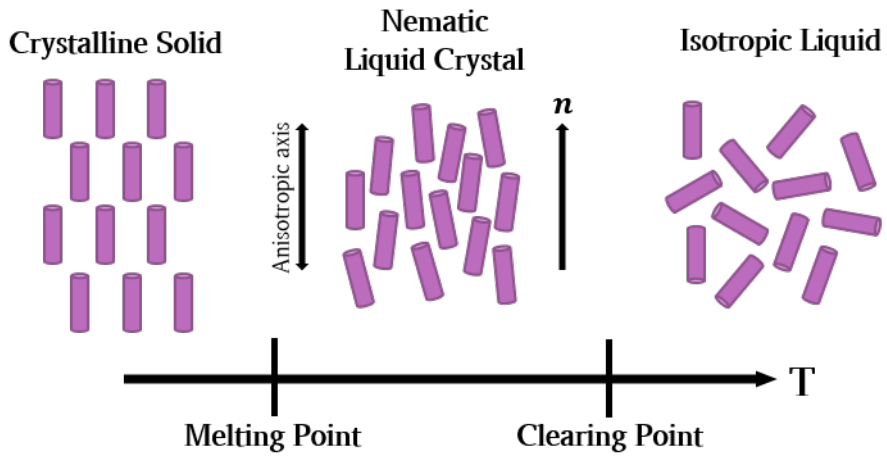

Figure 2.1: A schematic of a solid crystal, liquid crystal and isotropic liquid phase of a material that displays a nematic phase on heating. The director, a unit vector **n**, defines the average orientation of the anisotropic axis, or the long molecular axis.

where **n** is taken to be in the z-direction. The alignment of the rods is described by the distribution function $f(\xi, \eta)d\Omega$, which is independent of η due to cylindrical symmetry, and $f(\xi) \equiv f(\pi - \xi)$. A quadrupole is used to define the order parameter [58]:

$$S = \frac{1}{2}\langle(3\cos^2\xi - 1)\rangle = \int f(\xi)\frac{1}{2}(3\cos^2\xi - 1)d\Omega\,, \tag{2.2}$$

where $\langle\ \rangle$ represent a statistical average. An isotropic liquid (I) satisfies $S = 0$, whilst perfect order would be $S = 1$. NLCs typically have $S = 0.6 \rightarrow 0.8$ [21]. The order parameter is temperature dependent, and varies approximately with [62, 63]:

$$S = \left(1 - \frac{T}{T^*}\right)^{\nu}\,, \tag{2.3}$$

where T is the temperature, T^* is a temperature slightly below T_{NI} (the N to I

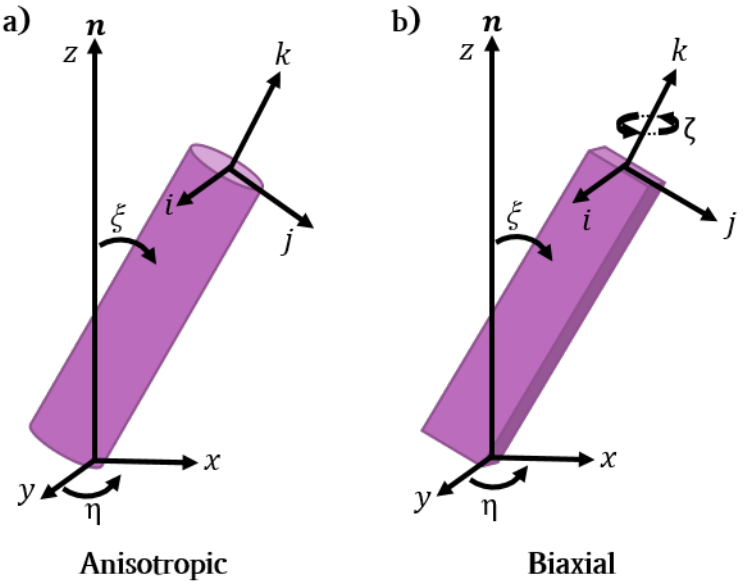

Figure 2.2: A schematic diagram of a): the uniaxial nematic and b): the biaxial nematic phases, where **n** is the director, and the coordinate geometry is defined by the polar angles ξ, η and ζ.

transition temperature), and ν is a material constant which is typically between $0.15 \leq \nu \leq 0.2$. S jumps from $0 \rightarrow 0.43$ at this first order phase transition [62].

2.1.2 Biaxiality

If an NLC is not uniaxial, such that the short-axes are not the same magnitude, the molecule is said to be biaxial. A schematic of such is shown in Figure 2.2b. The biaxial order parameter, D, is introduced to describe orientations of this short axis relative to **n** [64]:

$$D = \frac{3}{2}\langle \sin^2 \xi \cos(2\zeta) \rangle \ . \tag{2.4}$$

In the isotropic phase and for systems with perfect order, $D = 0$. D is usually

small and so has small effects on the material's anisotropic properties, and so is often ignored [64–66].

2.1.3 Cholesterics and Chirality

Chiral molecules dissolved in NLCs can induce a twist distortion, leading to a helical structure and the cholesteric phase (N*). This name arose due to being first observed in cholesterol esters [58]. **n** varies in space, such that:

$$n_x = \cos(pz + \phi) \ , \ n_y = \sin(pz + \phi) \ , \ n_z = 0 \ , \tag{2.5}$$

where the z-direction is that of the helical axis, p is the helical pitch and the chiral wavelength is defined as:

$$q = \frac{2\pi}{p} \ , \tag{2.6}$$

where ϕ is an arbitrary angle. Importantly p is temperature dependent, and commonly increases with decreasing temperature.

2.1.4 Refractive Indices

The refractive index for anisotropic materials such as LCs is related to its orientation. Light propagating though a medium has speed given by:

$$v = \frac{c}{n} \tag{2.7}$$

where c is the speed of light, and n is the refractive index of the medium. LCs are anisotropic and so the observed refractive index is relative to the orientation of the principal axis of the material. In the homeotropic geometry where **n** is aligned parallel to the surface normal (z), the speed of incident light (propagating in z) is unaffected and so is said to behave isotropically. This is called the

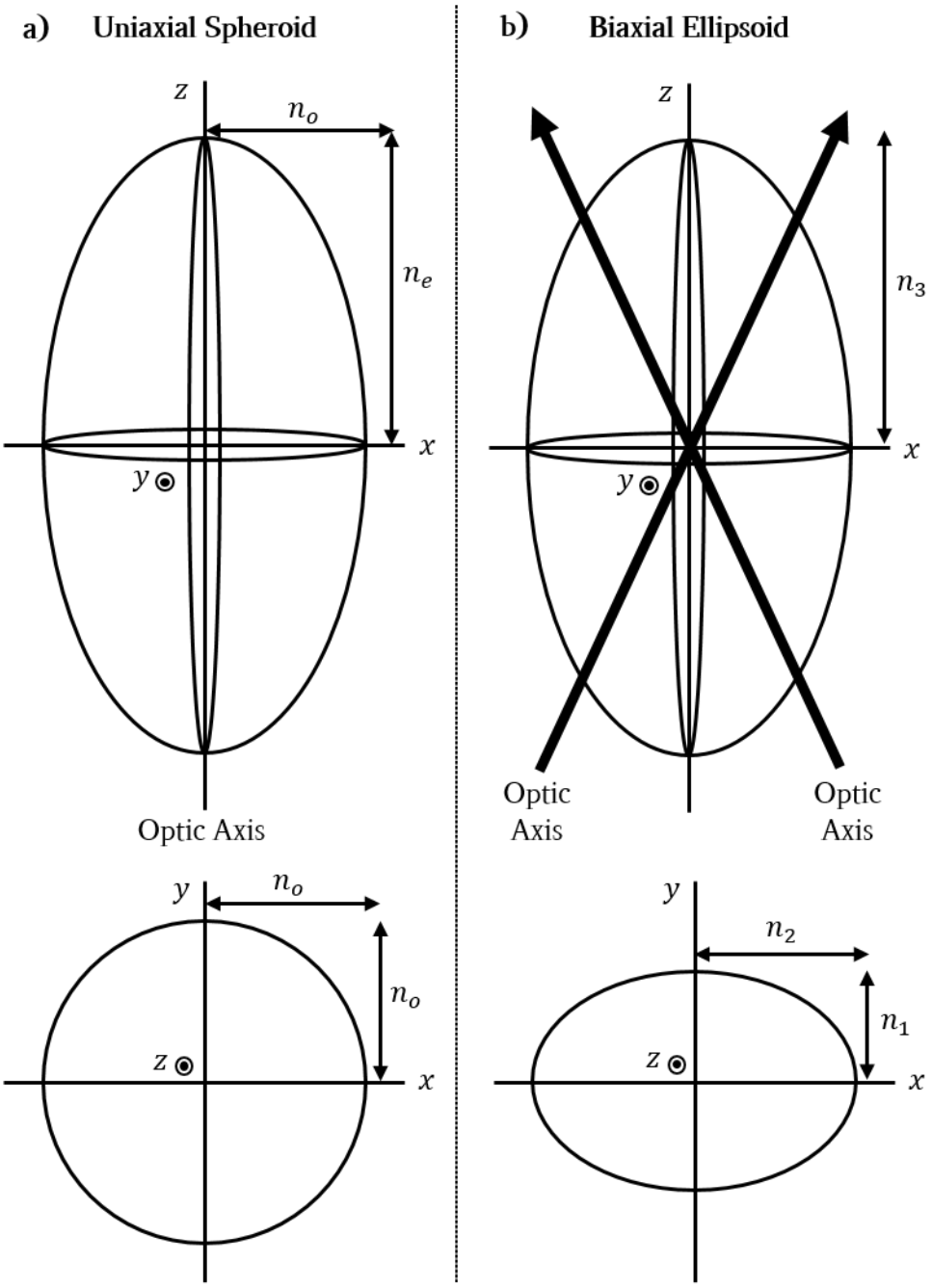

Figure 2.3: The indicatrix for a): uniaxial, and b): biaxial liquid crystals.

ordinary refractive index, n_o or $n_\perp$. Light propagating perpendicular to this experiences the extraordinary refractive index, n_e or $n_\parallel$. A uniaxial material has just one optic axis, while biaxial materials such as the SmC have two optic axes. This can be represented with an indicatrix, shown in Figure 2.3 for a material with $n_o < n_e$ [67]. This allows the calculation of the effective n to be calculated if n_e and n_o are known. The indicatrix is an ellipsoidal surface that maps n to the principal axes and allows the measurement of n_e and n_o.

A geometrical equation for light propagating in the arbitrary **S** direction is given by:

$$Uniaxial: \quad \frac{{S_x}^2 + {S_y}^2}{{n_o}^2} + \frac{{S_z}^2}{{n_e}^2} = 1 \ , \tag{2.8}$$

$$Biaxial: \quad \frac{{S_x}^2}{{n_1}^2} + \frac{{S_y}^2}{{n_2}^2} + \frac{{S_z}^2}{{n_3}^2} = 1 \ , \tag{2.9}$$

where $n_1 < n_2 < n_3$. If the LC molecule is tilted at an angle from the direction of light propagation, for example in the case of a homeotropic SmC(*), the observed refractive indices are given by:

$$\frac{1}{{n'_e}^2} = \frac{\sin^2\gamma}{{n_o}^2} + \frac{\cos^2\gamma}{{n_e}^2} \ ; \ n'_o = n_o \ , \tag{2.10}$$

where γ is the tilt angle of the molecule relative to the incident light, and for a SmC, $\gamma \equiv \theta_c$ [68, 69].

2.1.5 Elastic Constants and Free Energy

Deformations in the director field of a LC in a containment are defined by the boundary conditions and electric fields, and are best described using a continuum theorem rather than considering individual mesogens. Only slow and smooth rotations in **n** are considered such that the optical properties remain the same as those for a uniaxial system. There are three possible types of changes to the orientation of **n**, which is assumed to be in the z-direction such that $\mathbf{n}_0 = (0,\ 0,\ 1)$.

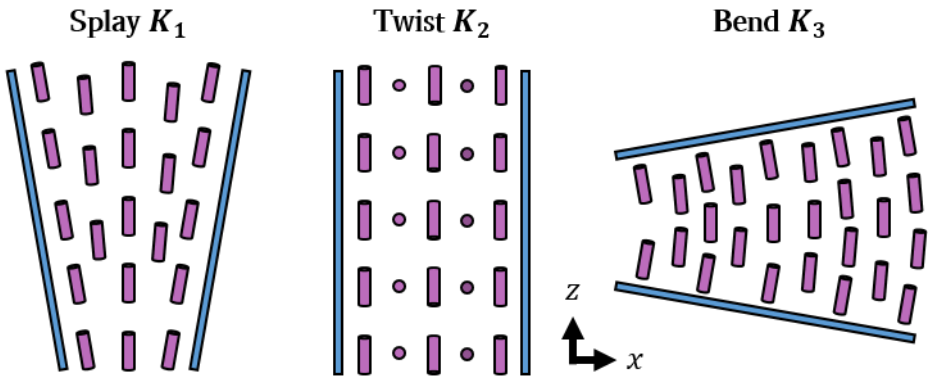

Figure 2.4: A 2D schematic of the splay (K_1), twist (K_2) and bend (K_3) Frank elastic constants in the x, z-plane.

These small changes are Δx, Δy and Δz, which lead to six curvature components that can be written in Frank notation as [70]:

$$splay: \ s_1 = \frac{\partial n_x}{\partial x} \ , \ s_2 = \frac{\partial n_y}{\partial y} \ , \tag{2.11}$$

$$twist: \ t_1 = \frac{\partial n_y}{\partial x} \ , \ t_2 = \frac{\partial n_x}{\partial y} \ , \tag{2.12}$$

$$bend: \ b_1 = \frac{\partial n_x}{\partial z} \ , \ b_2 = \frac{\partial n_y}{\partial z} \ . \tag{2.13}$$

These can be depicted as shown in Figure 2.4. The free energy of a LC is expressed in terms of a volume integral of the free energy density (w) as a quadratic function of the above six curvature strains [70, 71]:

$$w = k_i a_i + \frac{1}{2} k_{ij} a_i a_j \ , \ i, j = 1, 2, \ldots 6, \ , \tag{2.14}$$

where k_i and k_{ij} are the curvature elastic constants, and $a_1 = s_1$, $a_2 = t_2$, $a_3 = b_1$, $a_4 = -t_1$, $a_5 = s_2$ and $a_6 = b_2$.

Considering symmetry and uniaxiality, the nematic free energy density is given by [70]:

$$w_F = \frac{1}{2}K_1(\nabla \cdot \mathbf{n})^2 + \frac{1}{2}K_2(\mathbf{n} \cdot \nabla \times \mathbf{n})^2 + \frac{1}{2}K_3(\mathbf{n} \times \nabla \times \mathbf{n})^2 \,, \tag{2.15}$$

where the Frank elastic constants are given by [70]:

$$K_1 = k_{11},\ K_2 = k_{22},\ and\ K_3 = k_{33} \,, \tag{2.16}$$

and are shown schematically in Figure 2.4.

2.1.6 Permittivities and Electric Fields

LCs are dielectric due to their anisotropic nature, where the dielectric permittivities are given by $\varepsilon_\parallel = \varepsilon_3$ and $\varepsilon_\perp = \varepsilon_1 = \varepsilon_2$ relative to a parallel or perpendicular $\mathbf{n}$ and $\mathbf{E}$, respectively. The electric displacement for a uniaxial material is given by:

$$\mathbf{D} = \varepsilon_0 \boldsymbol{\varepsilon} \mathbf{E} \,, \tag{2.17}$$

where:

$$\boldsymbol{\varepsilon} = \begin{pmatrix} \varepsilon_1 & 0 & 0 \\ 0 & \varepsilon_2 & 0 \\ 0 & 0 & \varepsilon_3 \end{pmatrix} \,, \tag{2.18}$$

ε_0 is the permittivity of free space ($\varepsilon_0 = 8.85 \times 10^{-12}\ m^{-3}kg^{-1}s^4A^2$), and $\mathbf{E}$ is the electric field (where $\mathbf{E} \parallel \mathbf{n}$). The general solution is:

$$\mathbf{D} = \varepsilon_0 \varepsilon_\parallel \mathbf{E} + \varepsilon_0 \Delta\varepsilon (\mathbf{n} \cdot \mathbf{E})\mathbf{n} \,, \tag{2.19}$$

where $\Delta\varepsilon$ is the dielectric anisotropy, defined to be $\Delta\varepsilon = \varepsilon_\parallel - \varepsilon_\perp$.

The free energy in Equation 2.15 can be updated to include the dielectric energy density, given by:

$$w_{elec} = -\frac{1}{2}\varepsilon_0 \Delta\varepsilon (\mathbf{n} \cdot \mathbf{E})^2 \ . \tag{2.20}$$

2.1.7 The Liquid Crystal Cell and Surface Anchoring

The containment for LCs is of great importance. A simple device requires that **n** is controllably aligned. There are many ways to control **n**, but the most common, and that which will be considered throughout this project, is the LC contained between two parallel glass plates with transparent patterned electrodes, shown in Figure 2.5. This is called a cell. These plates are separated using spacer beads or film and secured with a sealant. This ensures a uniform cell gap (d) over the active electrode area. The desired **n**-field is achieved by adding alignment layers, or surface treating, the glass slides before constructing the cell. The application of a field that overcomes the elastic forces will reorient **n**, and controllably change the polarisation of incident light. Importantly this should return to its initial alignment when the field is removed.

Planar and homeotropic alignment are considered here and shown in Figure 2.5, although hybrid alignments also exist. Planar alignment is obtained by rubbing a polymer layer. This introduces microgrooves with a pitch and peak to peak amplitude of around 200 $\mathring{A}$ and 10 $\mathring{A}$ respectively [72–74]. The nematic order induced at this surface by local melting uniformly aligns the director perpendicular to the surface normal, and (usually) parallel to the direction of rubbing. A small pre-tilt of **n** is also usual. Homeotropic alignment aligns **n** parallel to substrate normal, and can be obtained using surfactants with variable hydrocarbon tail lengths [73, 75]. Different alignment methods result in different anchoring energies. This is the energy required to move **n** at the surface from its preferred orientation, and should be strong enough to overcome the bulk elastic forces in the LC to obtain uniform alignment. A good example of this is the TN mode,

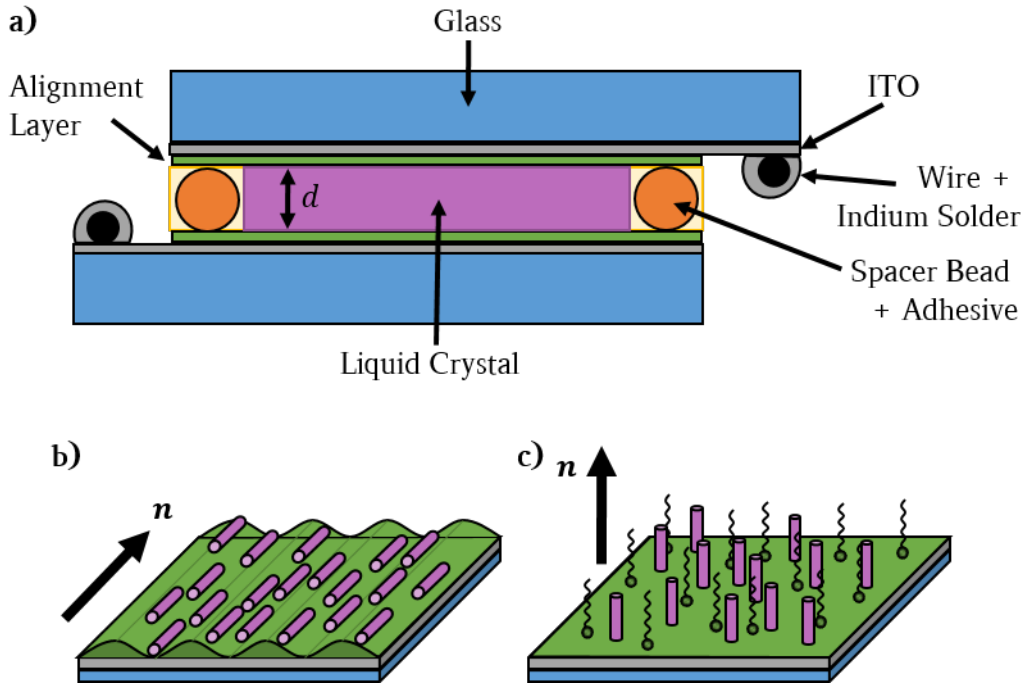

Figure 2.5: Schematic of a): the liquid crystal cell, b): planar surface treatments, and c): homeotropic surface treatment.

which uses rubbed planar alignment on each surface oriented perpendicular to one another to induce a 90° twist through the cell [15]. Chapter 3 introduces the surface treatment methods used in this project.

2.2 Smectic Liquid Crystals

Smectic LCs are layered structures with a well defined interlayer spacing, named after their soap-like mechanical properties (smectic = soap in Greek). The smectic phases exist at lower temperatures than the nematic phase. Two smectic phases are of interest to this work: smectic A (SmA) and smectic C (SmC), shown schematically in Figure 2.6 [76, 77]. The SmC exists at lower temperatures than the SmA.

2.2.0.1 Smectic A

The molecular structure of the smectic A phase is given in Figure 2.6. They are simply characterised here by a layered structure with a layer spacing or thickness, d_A, close to but lower than that of the LC molecule [78]. Within these layers, there is no long range order such that each layer can be considered as a two-dimensional (2D) layer of liquid. This phase is therefore optically uniaxial and rotationally symmetric about the optic axis, where the optic axis is normal to the plane of the layers, here labelled as $\mathbf{k}$. And as with NLCs, $\mathbf{k} = -\mathbf{k}$. The order parameter for the SmA phase is typically $S =\sim 0.8$.

2.2.0.2 Smectic C

A schematic diagram of the SmC coordinate geometry is given in Figure 2.7. The molecular structure of the SmC phase is also characterised by 2D liquid layers, however the long molecular axis is tilted away from $\mathbf{k}$, and is optically biaxial [79, 80]. This is defined by the smectic tilt or smectic layer angle, θ_C. This typically results in a shrinking of the layer thickness proportional to the tilt angle,

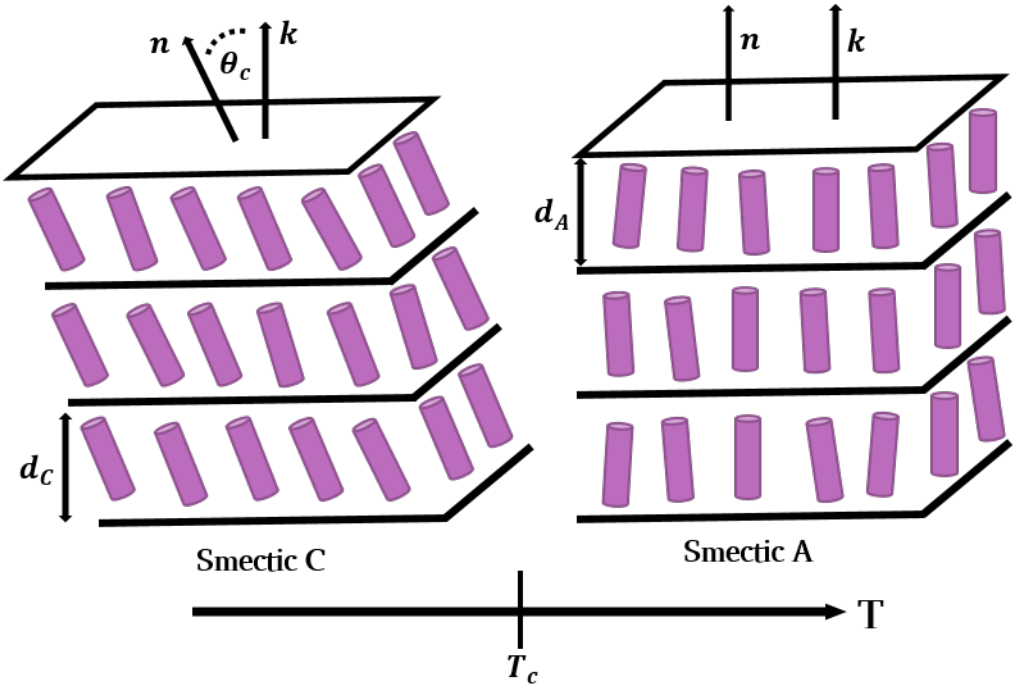

Figure 2.6: Schematic diagrams depicting the layered structure of the Smectic A (SmA) and Smectic C (SmC) phases. The molecules are confined to layers, where each layer can be modelled as a 2D liquid. In the SmA the director **n** is parallel to **k**, while in the SmC, **n** makes an angle θ_c to **k**. The layer spacings are shown by d_A and d_C, where the schematic eludes to the smaller layer spacing of the SmC.

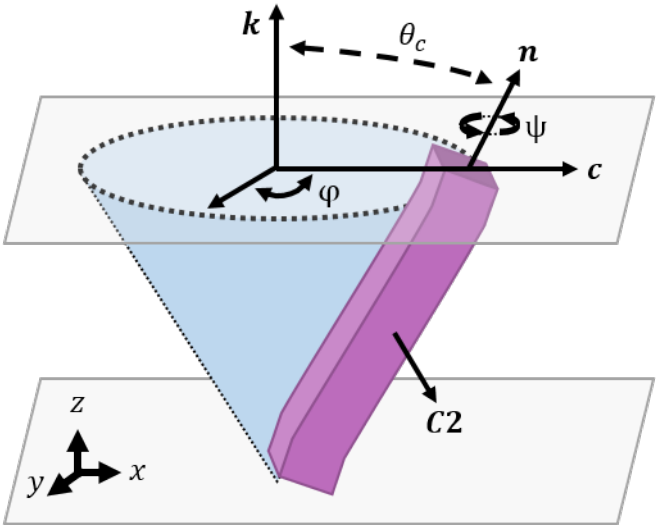

Figure 2.7: A schematic diagram of the smectic C coordinate geometry, redefined from the polar angles ξ, η and ζ as the azimuthal angle $\eta \equiv \varphi$, $\xi \equiv \theta_c$ (the cone angle, the tilt of **n** relative to **k**), and $\zeta \equiv \psi$ is the rotation about **n** which represents the simple biaxial order parameter. **C2** is defined to be perpendicular to the plane of molecular tilt, **k** is the smectic layer normal and **c** the **c**-director (the in-layer projection of **n**).

following: [58]:

$$d_C = d_A \cos\theta_C \ , \tag{2.21}$$

although de Vries materials have a layer spacing that remains almost constant over a wide temperature range through the SmA and SmC* phases [81–83]. In fact d_C tends to increase on cooling [84].

A unit vector parallel to the projection of **n** onto the smectic layer is defined as the **c**-director. This is oriented in the layer plane by an azimuthal angle φ. There are two additional order parameters describing the ordering of the long and short axes relative to the plane of the tilt (the **C2** axis is perpendicular to the plane of tilt). These are [85]:

$$P = \frac{3}{2}\langle \sin^2 \xi \cos(2\eta) \rangle \ , \tag{2.22}$$

$$C = \langle \frac{1}{2}(1 + \cos^2 \xi)\cos(2\zeta)\cos(2\eta) - \cos\xi \sin(2\zeta)\sin\eta \rangle \ , \tag{2.23}$$

where P and C describe the fluctuation of the long and short axes respectively. Usually a simpler biaxial order parameter is used:

$$\Omega = \langle \cos(2\psi) \rangle \ , \tag{2.24}$$

where ψ is the rotation about the **n**-director.

The SmA to SmC transition can be first or second order depending on the material, although henceforth only the second order transitions are considered. Additionally, θ_C increases with decreasing temperature following:

$$\theta_c = \theta_0 (T_c - T)^{\alpha_0} \ , \tag{2.25}$$

where θ_0 is a constant, T_c is the smectic A to C temperature transition, T is the temperature, and α_0 is an exponent theoretically predicted to be 0.5 [86]. Experimentally, results usually vary around $0.35 \leq \alpha_0 \leq 0.5$ [68]. This implies that the SmC layer spacing must also decrease with decreasing T.

2.2.1 Symmetry and Ferroelectricity

The chiral SmC phase (SmC*) has a sufficiently low symmetry such that it exhibits ferroelectricity, and was first predicted and demonstrated by R. Meyer [87]. These phases can naturally occur by incorporating a chiral element into the mesogenic molecule, and can also be achieved by introducing a chiral dopant to

a host material that exhibits a SmC phase [58, 68, 88]. SmC* phases may possess a spontaneous polarisation ($\mathbf{P}_s$). Ferroelectricity arises from a component of the polarisation not averaging to zero and remaining invariant over all symmetry operations.

All LC molecules possess a dipole moment, with components parallel to the axes of the molecule (μ_1, μ_2 and μ_3). In the N and SmA phases there is a uniaxial symmetry as a result of the rotational freedom around $\mathbf{n}$, as $\mathbf{n} \equiv -\mathbf{n}$. All rotations are equally likely, and so there is no net dipole and so no $\mathbf{P}_s$. The SmC phase has a hindrance of rotation about $\mathbf{n}$, and so has biaxial symmetry. This has two possible symmetry operations: two-fold rotation axis, and mirror plane. Therefore there is an inversion symmetry for each dipole (μ_1, μ_2 and μ_3), and so no $\mathbf{P}_s$. Chirality in LCs removes the mirror plane symmetry, resulting in a $\mathbf{P}_s$ in the SmC* phase, with a direction in the layer plane and perpendicular to the plane of tilt (parallel to **C2**). Interestingly, the chirality of the phase results in no net polarisation of a bulk sample, as $\mathbf{c}$ precesses about $\mathbf{k}$ in a helix, of pitch R_0. Therefore the helix must be suppressed to take advantage of the $\mathbf{P}_s$, which can be achieved in numerous ways: surface-stabilisation, mixing oppositely twisting compounds with the same sign of $\mathbf{P}_s$, or coupling with an electric field ($\mathbf{E}$) [68, 89].

The $\mathbf{P}_S$ is temperature dependent:

$$\mathbf{P}_S = P_0(T_c - T)^{\beta} \,, \tag{2.26}$$

where P_0 is a material or mixture constant, and β is an exponent derived from Landau theory, predicted to be 0.5, and found to be smaller experimentally [58].

2.2.2 SmC and SmC* Free Energy

The static theory for SmC and SmC* materials is based on the nonlinear continuum theory proposed by Leslie, Stewart and Nakagawa [90, 91]. First, the theories assume that the viscous stresses are identical for both the SmC and SmC* LCs,

with the main difference being different elastic, dielectric and ferroelectric energies. Other assumptions include incompressible layers and equally spaced layers. The layer normal is defined as **k**, and the **c**-director **c**, and giving the **n**-director as:

$$\mathbf{n} = \mathbf{a}\cos\theta_c + \mathbf{c}\sin\theta_c \ , \tag{2.27}$$

with the unit vector **b** introduced, defined to be orthogonal to **a** and **c**:

$$\mathbf{b} = \mathbf{a} \times \mathbf{c} \ , \tag{2.28}$$

and is parallel to the spontaneous polarisation vector $\mathbf{P}_s$. The energy density, w, is associated with distortions to the **n**-director, which is in the form given by [92]:

$$w = w(\mathbf{a}, \mathbf{c}, \nabla\mathbf{a}, \nabla\mathbf{c}) \ , \tag{2.29}$$

with the total free energy given by:

$$W = \int_V w(\mathbf{a}, \mathbf{c}, \nabla\mathbf{a}, \nabla\mathbf{c}) dV \ , \tag{2.30}$$

where V is the volume of the sample. The energy density must be invariant to rigid body rotations, and $\mathbf{a} \to -\mathbf{a}$ and $\mathbf{c} \to -\mathbf{c}$ due to the requirement of $\mathbf{n} \to -\mathbf{n}$. Therefore the energy density for the non-chiral SmC takes the form of [90]:

$$\begin{aligned} w = \frac{1}{2}K_1(\nabla\cdot\mathbf{a})^2 + \frac{1}{2}K_2(\nabla\cdot\mathbf{c})^2 + \frac{1}{2}K_3(\mathbf{a}\cdot\nabla\times\mathbf{c})^2 \\ + \frac{1}{2}K_4(\mathbf{c}\cdot\nabla\times\mathbf{c})^2 + \frac{1}{2}K_5(\mathbf{b}\cdot\nabla\times\mathbf{c})^2 + K_6(\nabla\cdot\mathbf{a})(\mathbf{b}\cdot\nabla\times\mathbf{c}) \\ + K_7(\mathbf{a}\cdot\nabla\times\mathbf{c})(\mathbf{c}\cdot\nabla\times\mathbf{c}) + K_8(\nabla\cdot\mathbf{c})(\mathbf{b}\cdot\nabla\times\mathbf{c}) \\ + \frac{1}{2}K_9(\nabla\cdot\mathbf{a})(\nabla\cdot\mathbf{c}) \ , \end{aligned} \tag{2.31}$$

where K_i , $i = 1, 2, 3 \ldots 9$ are elastic constants with the surface terms omitted.

Next, the nonlinear energy for small perturbations is considered [93]. Such elastic deformations are described by setting:

$$\mathbf{a} = \hat{\mathbf{a}} + \mathbf{\Omega} \times \hat{\mathbf{a}} \ , \ \mathbf{b} = \hat{\mathbf{b}} + \mathbf{\Omega} \times \hat{\mathbf{b}} \ , \ \mathbf{c} = \hat{\mathbf{c}} + \mathbf{\Omega} \times \hat{\mathbf{c}} \ , \tag{2.32}$$

where:

$$\hat{\mathbf{a}} = (0, 0, 1) \ , \ \hat{\mathbf{b}} = (0, 1, 0) \ , \ \hat{\mathbf{c}} = (1, 0, 0) \ , \ \hat{\mathbf{\Omega}} = (\Omega_x, \Omega_y, \Omega_z) \ , \tag{2.33}$$

and Ω is a small rotation in the smectic layers, where the result in combination with Equation 2.31 gives [93]:

$$\begin{aligned} w = \frac{1}{2}A_{12}(\Omega_{y,x})^2 + \frac{1}{2}A_{21}(\Omega_{x,y})^2 - \frac{1}{2}A_{11}(\Omega_{x,x})^2 \\ B_1(\Omega_{z,x})^2 + \frac{1}{2}B_2(\Omega_{z,y})^2 + \frac{1}{2}B_3(\Omega_{z,z})^2 + B_{13}\Omega_{z,x}\Omega_{z,z} \\ - C_1\Omega_{x,x}\Omega_{z,x} + C_2\Omega_{x,y}\Omega_{z,y} \ , \end{aligned} \tag{2.34}$$

where:

$$\begin{aligned} K_1 = A_{21} \ , \ K_2 = B_2 \ , \ K_3 = B_1 \ , \\ K_4 = B_3 \ , \ K_5 = 2A_{11} + A_{12} + A_{21} + B_3 \ , \ K_6 = -(A_{11} + A_{21} + \frac{1}{2}B_3) \ , \\ K_7 = -B_{13} \ , \ K_8 = C_1 + C_2 - B_{13} \ , \ K_9 = -C_2 \ . \end{aligned} \tag{2.35}$$

This can be written in terms of just the vectors $\mathbf{b}$ and $\mathbf{c}$ to write the SmC energy density in a particularly convenient form [90, 94]:

$$w = \frac{1}{2}A_{12}(\mathbf{b} \cdot \nabla \times \mathbf{c})^2 + \frac{1}{2}A_{21}(\mathbf{c} \cdot \nabla \times \mathbf{b})^2$$

$$+A_{11}(\mathbf{b}\cdot\nabla\times\mathbf{c})(\mathbf{c}\cdot\nabla\times\mathbf{b})+\frac{1}{2}B_1(\nabla\cdot\mathbf{b})^2+\frac{1}{2}B_2(\nabla\cdot\mathbf{c})^2$$
$$+\frac{1}{2}B_3\left[\frac{1}{2}(\mathbf{b}\cdot\nabla\times\mathbf{b}+\mathbf{c}\cdot\nabla\times\mathbf{c})\right]^2$$
$$+B_{13}(\nabla\cdot\mathbf{b})\left[\frac{1}{2}(\mathbf{b}\cdot\nabla\times\mathbf{b}+\mathbf{c}\cdot\nabla\times\mathbf{c})\right]^2$$
$$+C_1(\nabla\cdot\mathbf{c})(\mathbf{b}\cdot\nabla\times\mathbf{c})+C_2(\nabla\cdot\mathbf{c})(\mathbf{c}\cdot\nabla\times\mathbf{b})\ . \tag{2.36}$$

The constants A_{12}, A_{21} and A_{11} are related to bending of the smectic layers, B_1, B_2, B_3 and B_{13} to the reorientation of the **c**-director, and C_1 and C_2 relate the coupling of these deformations. Using Equation 2.36 it is possible to easily visualise these five basic deformations of non-chiral smectic layers. A schematic diagram of this is given in Figure 2.8.

Adjusting for the SmC* is not too complex. The vector $\mathbf{b}=\mathbf{a}\times\mathbf{c}$ is parallel to the spontaneous polarisation vector, and can be written as $\mathbf{P}_s=P_0\mathbf{b}=-P_0\mathbf{b}$, where $P_0=|\mathbf{P}_s|$ [95]. An adjustment to the elastic energy density, w, is made which adds two additional terms [96]:

$${w_1}^*=A_{11}\delta(\mathbf{c}\cdot\nabla\times\mathbf{c}-\mathbf{b}\cdot\nabla\times\mathbf{b}) \tag{2.37}$$
$${w_2}^*=\frac{1}{2}B_3q(\mathbf{c}\cdot\nabla\times\mathbf{c}+\mathbf{b}\cdot\nabla\times\mathbf{b})\ , \tag{2.38}$$

where δ is a chiral elastic constant, and q is the wave vector defined in Equation 4.18. Thus the chiral elastic energy density takes the form:

$$w_f=w+{w_1}^*+{w_2}^*\ , \tag{2.39}$$

and so by ignoring surface contributions, the bulk elastic energy is [96]:

$$w_f=\frac{1}{2}A_{12}(\mathbf{b}\cdot\nabla\times\mathbf{c})^2+\frac{1}{2}A_{21}(\mathbf{c}\cdot\nabla\times\mathbf{b})^2$$
$$-A_{11}\left[\frac{1}{2}(\mathbf{c}\cdot\nabla\times\mathbf{c}-\mathbf{b}\cdot\nabla\times\mathbf{b})-\delta\right]+\frac{1}{2}B_1(\nabla\cdot\mathbf{b})^2+\frac{1}{2}B_2(\nabla\cdot\mathbf{c})^2$$

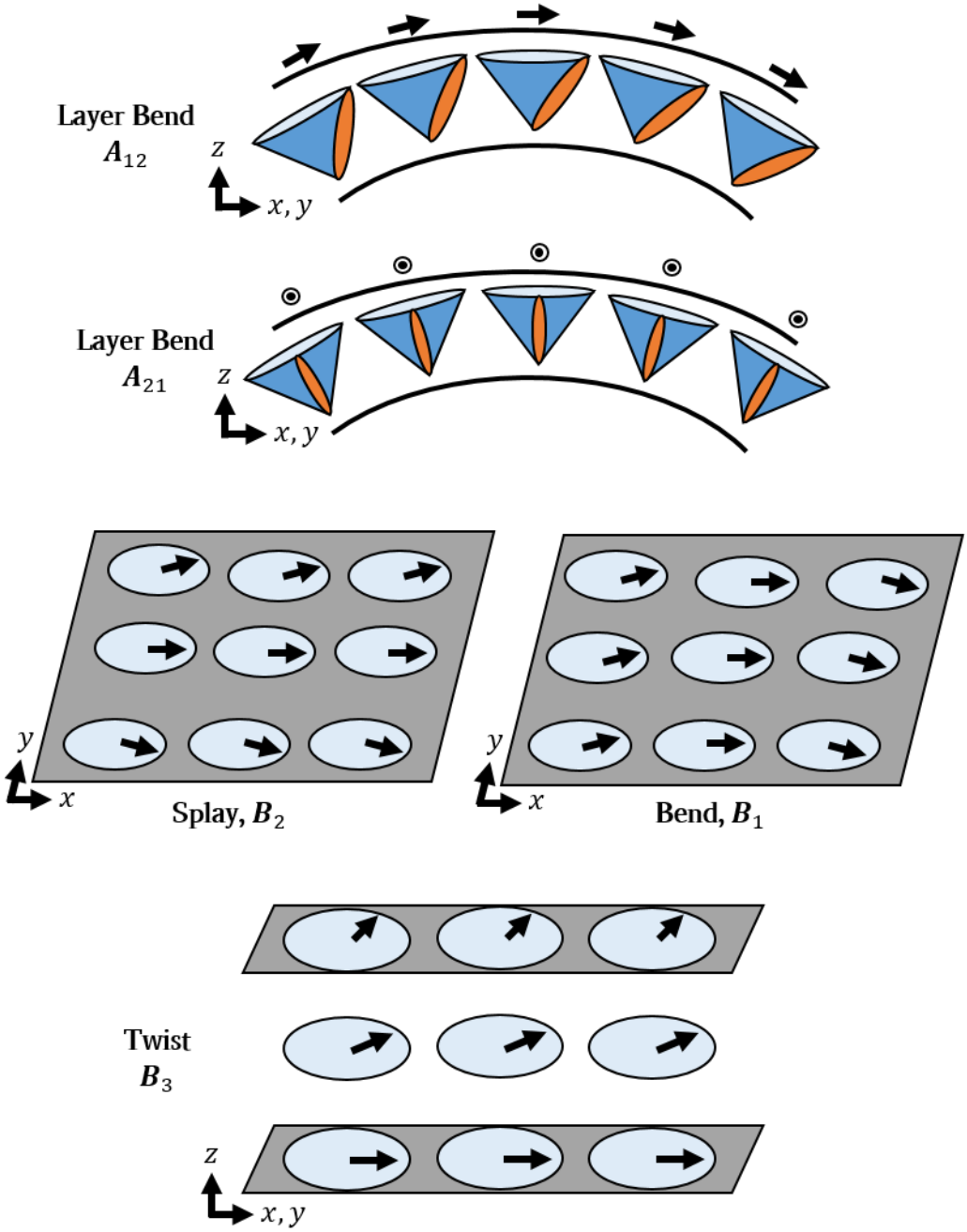

Figure 2.8: A schematic diagram of the possible smectic layer elastic distortions. The black arrow indicates the **c**-director.

$$+\frac{1}{2}B_3\left[\frac{1}{2}(\mathbf{b}\cdot\nabla\times\mathbf{b}+\mathbf{c}\cdot\nabla\times\mathbf{c})+q\right]^2$$
$$+B_{13}(\nabla\cdot\mathbf{b})\left[\frac{1}{2}(\mathbf{b}\cdot\nabla\times\mathbf{b}+\mathbf{c}\cdot\nabla\times\mathbf{c})\right]^2$$
$$+C_1(\nabla\cdot\mathbf{c})(\mathbf{b}\cdot\nabla\times\mathbf{c})+C_2(\nabla\cdot\mathbf{c})(\mathbf{c}\cdot\nabla\times\mathbf{b})\ . \tag{2.40}$$

2.2.3 SmC and SmC* Electric Energies

To find the total energy of the SmC system in the presence of an electric field, the dielectric energy density for the nematic in Equation 2.20 can be combined with Equation 2.27 to give [92]:

$$w_{elec}=-\frac{1}{2}\varepsilon_0\varepsilon_a(\mathbf{a}\cdot\mathbf{E}\cos\theta+\mathbf{c}\cdot\mathbf{E}\sin\theta)^2\ . \tag{2.41}$$

This is strictly true if the dielectric biaxiality is considered small and so neglected [97]. This is a satisfactory assumption for this work, but not always correct to assume [98–100].

The contribution of $\mathbf{P}_s$ in the SmC* is given by [95]:

$$\mathbf{P}_s=P_0\mathbf{b}\ ,as\ \ , \tag{2.42}$$

as $\mathbf{P}_s\perp\mathbf{c}$, as introduced in Section 2.2.1. This creates the additional term that must be added to Equation 2.41:

$$w_{pol}=-\mathbf{P}_s\cdot\mathbf{E}\ , \tag{2.43}$$

which is minimised when $\mathbf{P}_s$ and $\mathbf{E}$ are parallel. This leads to the electric energy

density due to an electric field for a SmC* to be [92]:

$$w_{elec} + w_{pol} = -\frac{1}{2}\varepsilon_0\varepsilon_a(\mathbf{a}\cdot\mathbf{E}\cos\theta + \mathbf{c}\cdot\mathbf{E}\sin\theta)^2 - \mathbf{P}_s\cdot\mathbf{E}\ , \tag{2.44}$$

resulting in the total energy density to be $w^* = w_f + w_{elec} + w_{pol}$, which is just the combination of Equation 2.36 and 2.44 [92]. It should be noted that w_{pol} couples linearly with $\mathbf{E}$, while w_{elec} couples quadratically, as so it is usual to consider that $w_{pol} >> w_{elec}$ and so neglect the w_{elec} term altogether [92].

2.2.4 Ferroelectric Liquid Crystal Alignment

Smectic alignment is achieved in much the same way as for NLCs, however extra care must be taken to ensure the layers are desirably aligned. For planar homogeneous alignment, this can be obtained by slowly cooling the nematic phase into the SmA phase to obtain the "bookshelf" geometry, shown in Figure 2.9 [28]. This alignment can be slowly cooled into the SmC(*) phase to ensure uniform layers, again shown in Figure 2.9 [28]. There are two possible alignments for the SmC(*) phase in a parallel rubbed planar geometry, determined by the cell gap, d [58]. Large d results in a chiral structure forming dechiralisation lines (unwinding lines) as the director is free to twist in the bulk [69]. If d is sufficiently small, such that:

$$4d < R_0 \tag{2.45}$$

then the helix is suppressed, producing the surface-stabilised FLC (SSFLC) state. This was first demonstrated by Clark and Lagerwall in 1980, and marks the first time that the potential for FLCs in displays was realised [28]. The director must lie on the smectic cone resulting in two possible orientations, which results in the bistability observed in the SSFLC [28]. This is discussed further in Section 2.4.1.

Cooling into the surface-stabilised state from the SmA results in a chevron layer structure [101]. The state forms to conserve the number of smectic layers

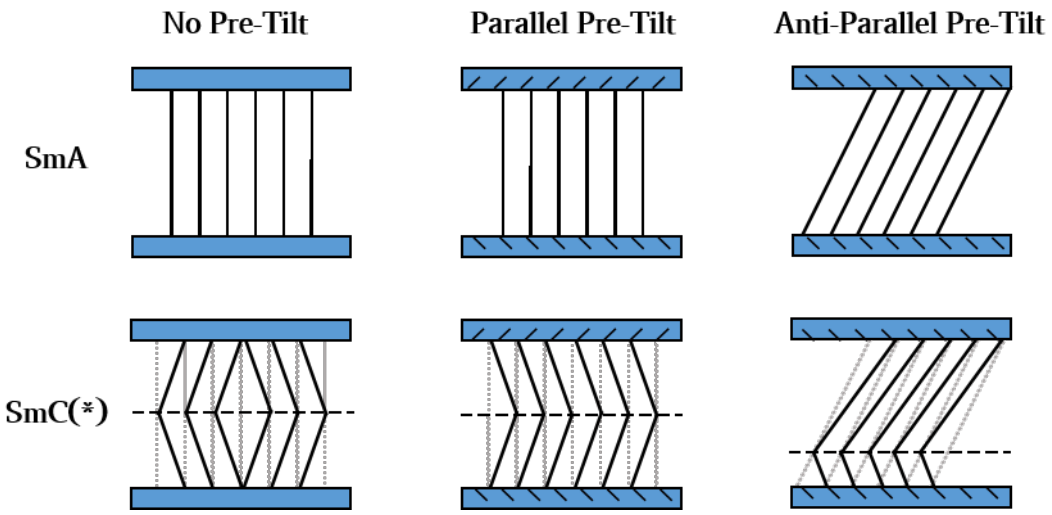

Figure 2.9: The characteristic layer geometries of the SmA and SmC(*) found with three planar pre-tilt surface conditions: no pre-tilt, parallel pre-tilt and anti-parallel pre-tilt.

due to Equation 2.21, rather than breaking and reforming layers. The layer periodicity therefore remains constant at the surfaces, resulting in a lower energy state as there is no energy barrier associated with breaking this alignment [69]. The layer tilt as a function of temperature is given by:

$$\delta_c = \pm\cos^{-1}\left(\frac{d_C(T)}{d_A}\right) = \delta_0\left(1 - \frac{T}{T_{CA}}\right)^{\alpha_c}, \tag{2.46}$$

where T_{CA} is the SmA to SmC temperature transition and α_c is a exponent derived from Landau theory. The magnitude of $\frac{\delta_c}{\theta_c}$ is constant and temperature independent [102]. The chevron structure can be controlled by the pre-tilt. Parallel pre-tilt prefers a C1 chevron orientation orientation, that is, the layers form in the direction of the pre-tilt. A low or zero pre-tilt gives no preference for the direction of chevron formation, and so there is an even distribution of C1 and C2 chevron structures, where a C2 chevron structure is one that forms against the direction of pre-tilt [101, 103, 104]. It is usual for the C1 state to be preferred just below T_c, and for C2 to become energetically favourable on cooling, resulting

in hairpin (face-to-face chevrons) and lightening (back-to-back chevrons) zig-zag defects [105]. This is shown in Figure 2.9. In the case of an anti-parallel rubbed device, the SmA bookcase layer alignment is tilted, where the tilt angle is approximately equal to the pre-tilt angle. The chevron interface shifts towards one surface in the SmC(*) resulting in asymmetric chevrons, again shown in Figure 2.9 [68, 106].

2.3 Liquid Crystals in Electro-Optic Devices

2.3.1 Polarisation Optics for Liquid Crystal Displays

Chapter 4 introduces the VGA-FLC, for which the optics of a TN are used. Consider the case where **c** (and hence $\mathbf{P}_s$) is in the plane of the cell and **E** is applied parallel to one of the surfaces. At that surface, the **c**-director reorients to 90° from the opposing surface and forms the equivalent of a twisted nematic geometry (albeit one where the director is constantly at the cone angle to the plane of the cell). For such geometries, it becomes important to consider the optics, and this is done simply by considering the **c**-director to be a TN.

2.3.2 General Birefringent Retarder

For a general birefringent retarder, ignoring reflections and refractions and just considering the polarisation state, made with a uniform director alignment and cell gap, the polarisation state can be calculated using the Jones Matrix [107]:

$$\begin{aligned}\begin{pmatrix} E'_x \\ E'_y \end{pmatrix} &= \begin{pmatrix} 1 & 0 \\ 0 & 0 \end{pmatrix} \begin{pmatrix} \cos\phi & -\sin\phi \\ \sin\phi & \cos\phi \end{pmatrix} \begin{pmatrix} e^{-i\frac{\Gamma}{2}} & 0 \\ 0 & e^{i\frac{\Gamma}{2}} \end{pmatrix} \begin{pmatrix} \cos\phi & \sin\phi \\ -\sin\phi & \cos\phi \end{pmatrix} \begin{pmatrix} 0 & 0 \\ 0 & 1 \end{pmatrix} \begin{pmatrix} 0 \\ 1 \end{pmatrix} \\ &= \begin{pmatrix} -2i\sin\phi\cos\phi\sin\frac{\Gamma}{2} \\ 1 \end{pmatrix}, \end{aligned} \tag{2.47}$$

where the retardation due to the LC birefringence (Δn) is [108, 109]:

$$\Gamma = \frac{2\pi\Delta nd}{\lambda} \,, \tag{2.48}$$

and $E'_{x/y}$ is the electric field vector of the transmitted light travelling in the z-direction, ϕ the angle of the slow-axis of the material between crossed polarisers, λ the wavelength of incident light, and d the thickness of the birefringent layer, referred to as the cell gap. We use $\lambda = 550\,nm$ for white light as the human eye is most sensitive to this wavelength [110]. The transmission (T) for this simple retarder is then given by:

$$T = \frac{E'^{*}E'}{E^{*}E} = \frac{{E'_x}^2 + {E'_y}^2}{{E_x}^2 + {E_y}^2} = \sin^2(2\phi)\sin^2\frac{\Gamma}{2} \,, \tag{2.49}$$

$$T = \sin^2(2\phi)\sin^2(\frac{\pi\Delta nd}{\lambda}) \,, \tag{2.50}$$

where E^* is the conjugate of E. Taking Equation 2.50, the maximum transmission is found at the quarter wave plate condition, where $\Delta nd = \frac{\lambda}{4}$, and orientated with the director at $\pm 45°$ between crossed polarisers. Conversely, the dark state is obtained with the director at multiples of 90° between crossed polarisers, and is independent of the cell gap, d.

2.3.3 Gooch-Tarry Equation for a Twisted Nematic

The twisted nematic (TN) mode creates a 90° twist of $\mathbf{n}$ through the device by utilising rubbed planar alignment on opposing substrates oriented perpendicular to one another. A schematic of the TN mode is shown in Figure 2.10, where the LC has a positive $\Delta\varepsilon$. Such a device can operate between either parallel or crossed polarisers, resulting in the normally black (NB) or normally white (NW) modes respectively. A voltage significantly larger than the threshold (V_{th}) is applied to reorient $\mathbf{n}$ in the bulk to appear optically isotropic, and so the NW mode become dark, and NB becomes bright. The threshold voltage for a positive $\Delta\varepsilon$

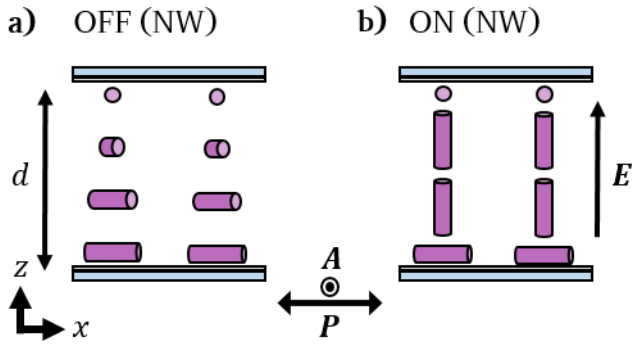

Figure 2.10: A schematic of the twisted nematic (TN) geometry operating in the normally white (NW) mode where, a): OFF, and b): ON.

NLC is given by [111]:

$$V_c = \pi \sqrt{\frac{K_{11}}{\varepsilon_0 \Delta\varepsilon}} \, . \tag{2.51}$$

Jones matrices can be used to calculate the final polarisation state of a TN device. A retarder can be defined as a series of N birefringent retarders, each at a slightly different angle to the next [107, 112–115]:

$$\frac{\Gamma}{N} = \frac{2\pi \Delta n d}{\lambda N} \, ; \tag{2.52}$$

$$\phi_{j+1} = \phi_j + \frac{\Phi}{N} \, , \; j = 0, 1, 2 \ldots, N-2 \, , \tag{2.53}$$

where Φ is the total twist angle, which in this case is $\Phi = 90°$. The matrix, M, is given by the multiplicative sum of these elements, M_j, by [21]:

$$M = \prod_{j=1}^{N} \left(R(\phi_j) \cdot M_j \cdot \overline{R(\phi_j)} \right) \, , \tag{2.54}$$

$$\equiv \prod_{j=1}^{N} \left(R(-\phi_j) \cdot M_j \cdot R(\phi_j) \right) \ , \tag{2.55}$$

$$= R(-\Phi) \left[\begin{pmatrix} e^{-i\frac{\Gamma}{2N}} & 0 \\ 0 & e^{i\frac{\Gamma}{2N}} \end{pmatrix} R\left(\frac{\Phi}{N}\right) \right]^N \ , \tag{2.56}$$

$$= R(-\Phi) \left[\begin{pmatrix} \cos\frac{\Phi}{N} e^{-i\frac{\Gamma}{2N}} & \sin\frac{\Phi}{N} e^{-i\frac{\Gamma}{2N}} \\ -\sin\frac{\Phi}{N} e^{i\frac{\Gamma}{2N}} & \cos\frac{\Phi}{N} e^{i\frac{\Gamma}{2N}} \end{pmatrix} \right]^N \ , \tag{2.57}$$

where R is the rotation matrix. With an infinite number of N's, the limit as $N \to \infty$ [21, 115]:

$$M_\infty = \begin{pmatrix} \cos\Phi & -\sin\Phi \\ \sin\Phi & \cos\Phi \end{pmatrix} \begin{pmatrix} \cos\chi - i\frac{\Gamma}{2}\frac{\sin\chi}{\chi} & \Phi\frac{\sin\chi}{\chi} \\ -\Phi\frac{\sin\chi}{\chi} & \cos\chi + i\frac{\Gamma}{2}\frac{\sin\chi}{\chi} \end{pmatrix} \ , \tag{2.58}$$

where:

$$\chi = \sqrt{\Phi^2 + \left(\frac{\Gamma}{2}\right)^2} \ . \tag{2.59}$$

The transmission is solved as in Equation 2.49, and gives:

$$\begin{aligned} T = &\left\{ \cos\chi \cos(\Phi + \phi_1 - \phi_2) + \frac{\Phi}{\chi} \sin\chi \sin(\Phi + \phi_1 - \phi_2) \right\}^2 \\ &+ \left\{ \left[1 - \left(\frac{\Phi}{\chi}\right)^2 \right] \sin^2\chi \cos^2(\Phi + \phi_1 - \phi_2) \right\} \ , \end{aligned} \tag{2.60}$$

where ϕ_1 and ϕ_2 are the input and output polariser directions relative to the input director of the liquid crystalline material. For example, between crossed polarisers for the bright state, $\phi_1 = 0°$ and $\phi_2 = 90°$. As a sanity check, this equation

for a twisted device (Equation 2.60) becomes equal to the transmission of a retardation plate with no twist (Equation 2.50) as $\Phi = 0$ between crossed polarisers.

The Gooch-Tarry equation for the transmission of the NW mode between crossed polarisers with a 90° twist is obtained by setting $\Phi = 90°$, $\phi_1 = 0°$ and $\phi_2 = 90°$ [112, 113]:

$$T = 1 - \frac{\sin^2\left(\frac{\pi}{2}\sqrt{1 + \left(\frac{2\Delta nd}{\lambda}\right)^2}\right)}{1 + \left(\frac{2\Delta nd}{\lambda}\right)^2} , \tag{2.61}$$

where to make $T = 1$, the R.H.S. of the equation is chosen to be equal zero. For parallel polarisers to obtain the NB mode, Equation 2.60 simply becomes:

$$T = \frac{\sin^2\left(\frac{\pi}{2}\sqrt{1 + \left(\frac{2\Delta nd}{\lambda}\right)^2}\right)}{1 + \left(\frac{2\Delta nd}{\lambda}\right)^2} . \tag{2.62}$$

There are a series of maximum and minimum values for the transmissions of Equations 2.61 and 2.62 at a series of specific conditions, given by:

$$\frac{\Delta nd}{\lambda} = \sqrt{m^2 - \frac{1}{4}} , \; m = 1, 2, 3 \ldots , \tag{2.63}$$

where the first minimum is found at:

$$\Delta nd = \frac{\sqrt{3}}{2}\lambda , \; m = 1 . \tag{2.64}$$

At higher order minima, the transmission becomes less sensitive to changes in retardation until the Mauguin limit is reached whereby polarised light will be rotated by 90° and transmitted independent of the cell gap and input wavelength of light [21]. This seems like the ideal limit, however, this requires large values of either Δn or d, both of which are not realistic or practical for creating a functioning device. Further device optimisation shows that the TN display can be operated by only inducing a 75° twist angle [21, 116]. This reduces the maximum

transmission to only 98.4 % compared to a twist of 90°, while decreasing the cell gap to 80 % the initial size, potentially yielding up to 50 % faster response times [21, 116].

2.3.4 Passive Matrix Addressing

In passive matrix (PM) addressing, the electrodes are shaped into a desired pattern (such as the seven-segment image used for numbers on a calculator) and the opposing electrode is the common electrode. All electrodes are addressed from the bonding ledge, and simple designs can be directly driven, but more complex designs require matrix addressing or multiplexing. Here, the electrodes are split into N rows and M columns for a M × N display, requiring M + N connections. An example of a 2 × 2 matrix is given in Figure 2.11. Pixels are addressed by sequentially scanning the rows ($V = +S$), and simultaneously the columns are provided with data signals to determine the ON and OFF states ($V = \pm D$), where the potential difference per pixel is defined to be the row minus column voltage. The high voltages $|(S + D)|$ must be distinguishable from the low voltages $|(S - D)|$, and each row is addressed for $\frac{1}{N}$ of a time frame. Once the signal is removed, each pixel will relax back to its OFF state.

The maximum number of lines that can be driven for a particular S and D is determined by the Alt-Pleshko limit [25]. This describes that as the amount of multiplexing increases, the larger the voltage that must be delivered by the driver. A typical STN display has 240 rows and applies an electrical potential difference of $S + D = 20\ V$. Importantly the addressing scheme must include a DC balance in the waveform to avoid the electrical breakdown of the LC resulting in image sticking [21].

2.3.5 Active Matrix Addressing

Thin-film transistors (TFTs) enable LCDs to be active matrix (AM) addressed, which enables much higher levels of multiplexing than PM addressing. For ex-

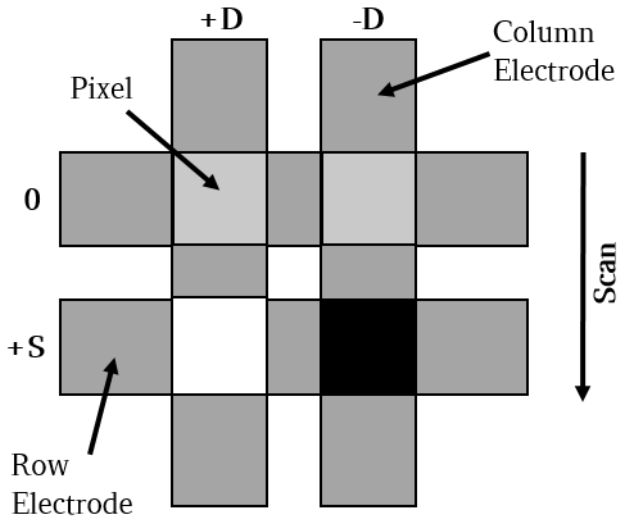

Figure 2.11: An example of passive matrix (PM) multiplexing, where D and S represent the applied potential difference to the row and column electrodes respectively.

ample, PM addressing was limited to $N = 240$, while a 4k UHD TV (ultra high definition television) with AM addressing has $N = 2160$. A TFT is placed behind each (sub)-pixel of a display, and applies a charge to switch the LC to any of 256 grey levels. The TFT is a field effect transistor (FET) formed from metal-insulator-semiconductor layers. They are deposited on pre-patterned gate electrodes, doped with hydrogen, and then source and drain electrodes are patterned on top of the TFT.

A negative voltage applied between the gate and the drain ($-V_{GD}$) results in the semiconductor becoming depleted of electrodes. This prevents a current flow between the source and drain electrodes. If a positive voltage is applied to the gate (V_{GD}), electrons are allowed to accumulate and so enabling current flow between the source and the drain (I_{SD}). If the drain is positive, current flows from the source to the drain, while if the drain is negative, current flows from the drain to the source.

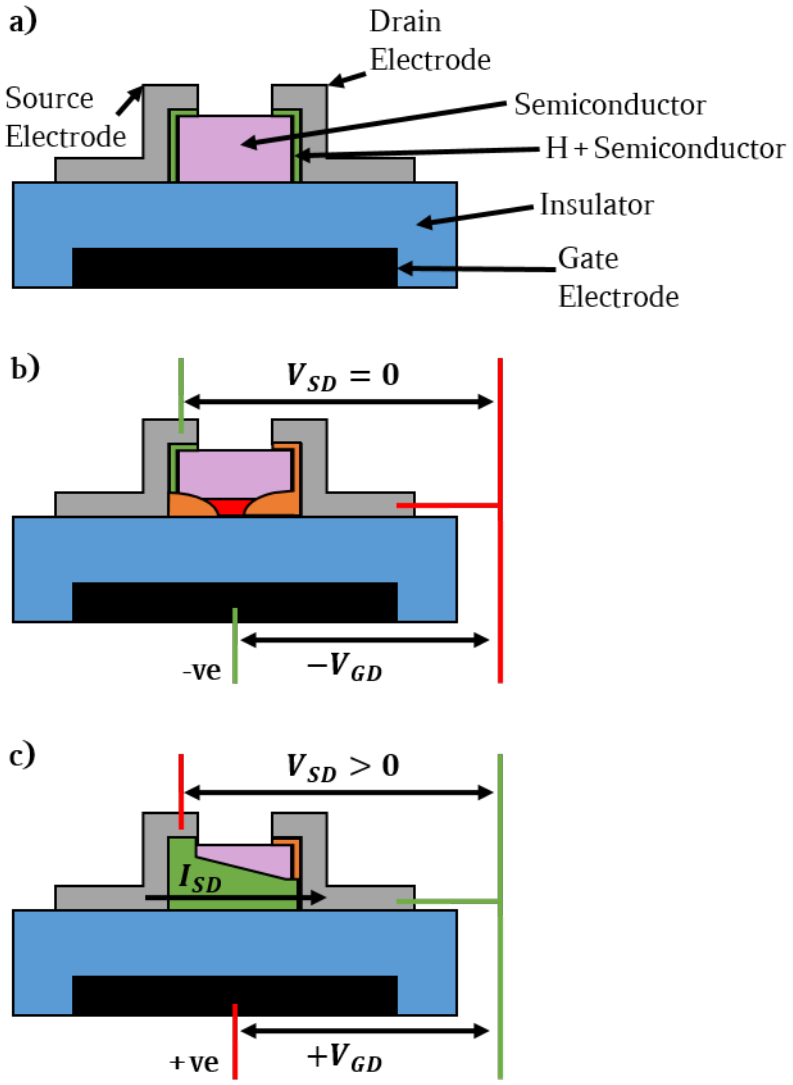

Figure 2.12: A schematic diagram of active matrix (AM) addressing thin-film transistors (TFTs). a): The main componesnts of the TFT consist of gate, source and drain electrodes, an insulating layer and an a-Si semiconductor. b): Applying $-V_{GD}$ depletes the semiconductor of electrons and so depletes current flow, so $V_{SD} = 0$. c): Applying $+V_{GD}$ allows electrons to accumulate and allowing current flow from the source to the drain (I_{SD}).

The TFT plate has row and column bus lines that allow the TFT to be addressed. The rows are connected to the gate, and the columns to the source. The ITO pixel electrodes are connected to the drain. A TFT matrix is addressed line by line much like for PM. The gate electrodes are opened with $+15\ V_{GD}$ to to switch them on, or OFF with a $-5\ V_{GD}$. Simultaneously, data voltages are applied to the source and so charging any ON rows to an appropriate voltage. Once charged, the gate is closed with $-5\ V_{GD}$ before scanning the next row. The total time to address the display is τN, where τ is the response time. The polarity of the data signal is reversed between frames to minimise the amount of direct current the LC is exposed to.

Typical panels operate at 60 Hz, and so considering the 4k display with 2160 rows, each pixel must not fully discharge before the next 16.7 ms frame time, resulting in [117]:

$$\tau_{OFF} > 200\tau N\ , \tag{2.65}$$

assuming an exponential decay of the charge. Similarly, the pixel must be charged to a sufficiently high level in the addressing time [117]:

$$\tau_{ON} > 0.1\tau\ . \tag{2.66}$$

The decay time of the voltage across a pixel is related to the leakage current of the transistor and also the conductivity of the the LC. If the conductivity of the LC is too high, the pixel will discharge too quickly, and is quantified by the voltage holding ratio (VHR) which represents the time it takes for the voltage across the pixel to decay by 50 % [118]:

$$VHR = \sqrt{\frac{R_{ON}C_p}{2\tau N}\left[1 - \exp\left(-\frac{2\tau N}{R_{ON}C_p}\right)\right]}\ , \tag{2.67}$$

where R_{ON} is the resistance, C_p is the pixel capacitance, N is the number of rows to be addressed, and τN is the frame rate. Ionic impurities are minimised in LCs designed for use in AM addressing to maximise VHR and so ensuring a high

contrast display.

2.4 Ferroelectric Liquid Crystals in Electro-Optic Devices

2.4.1 The Surface Stabilised Ferroelectric Liquid Crystal Display

The surface-stabilised FLC (SSFLC) geometry for FLC containment was first invented by Clark and Lagerwall in 1980 [28], using planar alignment and shearing the substrates to control the **n**-director (**n**) and smectic layer normal (**k**) to lie perpendicular to the substrate normal. A schematic diagram of the SSFLC device geometry if given in Figure 2.13. The helical twist through the device was suppressed through ensuring that the total natural twist with no boundaries does not exceed 90°, resulting in Equation 2.45.

This bistable device switches between dark and bright states, known as the Clark-Lagerwall effect where both configurations are equal in energy [28]. The $\mathbf{P}_S$ lies perpendicular to **n** and latches to **E** provided by plate electrodes. The director will switch to lie in one of two bistable states depending on the sign of the field polarity, which are separated by twice the cone angle of the SmC* material. θ_C is typically designed to be 22.5° so that the device switches between bright and dark states when oriented between crossed polarisers. To ensure a state of maximum transmission of white light is obtained, d must satisfy a multiple of the half-wave plate condition [102]:

$$\Delta nd = (m + \frac{1}{2})\lambda \; ; \; m = 1, 2, 3 \ldots \; , \tag{2.68}$$

where Δn is the birefringence of the SmC* and λ the wavelength of incident light (green is commonly used at 550 nm). The intensity of the transmitted light is

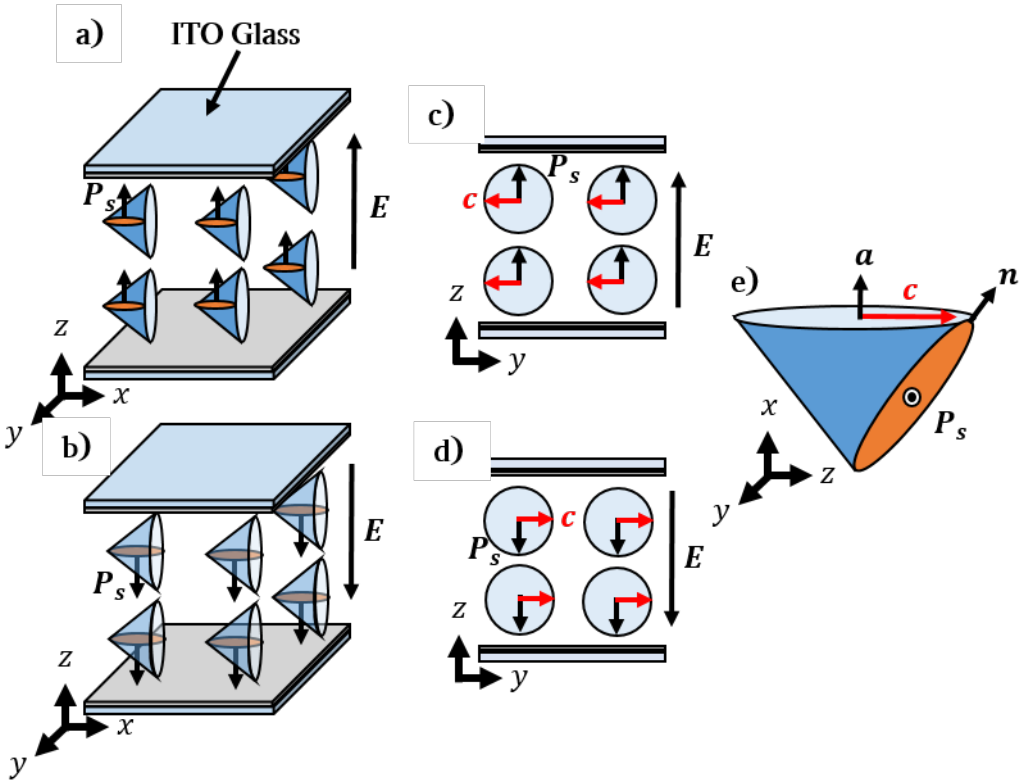

Figure 2.13: A schematic diagram of the SSFLC device geometry. a),b): 3D sketches of the two bistable states, which are switched between by supplying a sufficiently large electric field (**E**) across the ITO substrates, where the spontaneous polarization ($\mathbf{P}_s$) aligns with the direction of the field, and so rotating the **c**-director (**c**), 180° around the cone angle (θ_c). Crossed polarisers are aligned such that the two states are either bright or dark. c),d): 2D sketches of the same geometry, emphasising the orientation of **c** and $\mathbf{P}_s$ w.r.t. **E**. e): A sketch of the FLC mesogen contained to the smectic C* cone, where **a** is the layer normal and **n** the director, and θ_c can exist at any point on the boundary of the cone.

given by:

$$I = I_0 \sin^2(2\alpha) \left(\frac{\pi \Delta n d}{\lambda} \right) \tag{2.69}$$

where α is the angle between the optic axis and input polarisation and I_0 is the intensity of the incident light. Optical response times for the Clark-Lagerwall effect in the SSFLC are given by:

$$\tau_{ON}{}^{(FLC)} \simeq \tau_{OFF}{}^{(FLC)} \propto \frac{\gamma_\phi(T)}{\mathbf{P}_S \mathbf{E}} \, , \tag{2.70}$$

where τ_{ON} and τ_{OFF} are the ON and OFF times for the FLC respectively, and $\gamma_\phi(T)$ is the rotational viscosity which is temperature dependent. This is much faster than for a NLC, which generally has a response time of:

$$\tau_{ON}{}^{(N)} \propto \frac{\gamma_1}{\epsilon_0 \Delta\varepsilon \mathbf{E}^2 - \left(\frac{\pi}{d}\right)^2 \mathbf{K}} \quad , \quad \tau_{OFF}{}^{(N)} \propto \frac{d^2 \gamma_1}{\pi^2 \mathbf{K}} \, , \tag{2.71}$$

where γ_1 is the rotational viscosity for a NLC and $\mathbf{K}$ is a one-constant approximation of the splay, twist and bend elastic constants. Note that the NLC response time depends on $\frac{1}{\mathbf{E}^2}$ and the decay time does not depend on $\mathbf{E}$ at all, whereas for the FLC both ON and OFF times are related to $\propto \frac{1}{\mathbf{E}}$. These factors result in response times of FLCs that are hundreds of times faster than those found in NLCs, and so kick-started research into FLCs as "the technology of the future" throughout the 1980's and 1990's [45].

Two driving voltages are used to switch between the bistable states of the SSFLC. A D.C. voltage is applied for purely a fast electro-optic response, such as is required for shutters, where the material has a large $\mathbf{P}_s$. This is used for FLCs on silicon (FLCoS) in spatial light modulators (SLMs) with active matrix addressing for a variety of technologies including head-mounted displays and micro-projectors [46, 48, 50, 51]. The second method is the application of pulses to cause $\mathbf{n}$ to remain above the "mid-point" until the pulse is removed and so

allowing **n** to relax back to the opposite state [69].

For a high $\mathbf{P}_s$ material, there is a linear decrease in τ_{ON} with increasing V. For low $\mathbf{P}_s$ materials, the dielectric anisotropy will begin to play a role. The behaviour is similar until at high voltages where the quadratic coupling begins to effect the response time, whereby there is an increase in τ_{ON} [119]. This is the premise for the τV_{min} mode utilising passive matrix addressing and short duration pulses [120, 121].

2.4.1.1 Operating Modes Beyond the Surface Stabilised Ferroelectric Liquid Crystal Display

The SSFLC introduced surface stabilisation as a means to remove the helix from the FLC whilst maintaining the $\mathbf{P}_s$ [28]. Such an effect can also be obtained by creating a large helical twist, $R_0 >> d$. There are also modes that are designed to keep the helix intact during electro-optic addressing. Overall, multiple electro-optic modes have been presented for creating devices based on FLCs to create both fast-switching displays and devices [122]. These modes are not limited to utilise PM addressing and bistability as for the SSFLC. These modes have been designed to take advantage of AM addressing, allowing them to be monostable.

2.4.2 Deformed Helix Mode

In the planar geometry of the deformed helix FLC (DHFLC), d is is much larger than R_0 ($d >> R_0$) and so the SmC* remains helical within the device [123]. A schematic is shown in Figure 2.14. The incident light must also have $\lambda > R_0$ to avoid diffractive effects, and so the pitch is controlled to be $R_0 \sim 0.1 - 0.3\ \mu m$. The birefringence is controlled by electrically deforming the helix, and so controllably varying the effective birefringence up to the point where the helix is unwound. This is governed by:

$$E_u = \frac{\pi^2}{16}\frac{q^2 K_{22}}{P_s}\ , \tag{2.72}$$

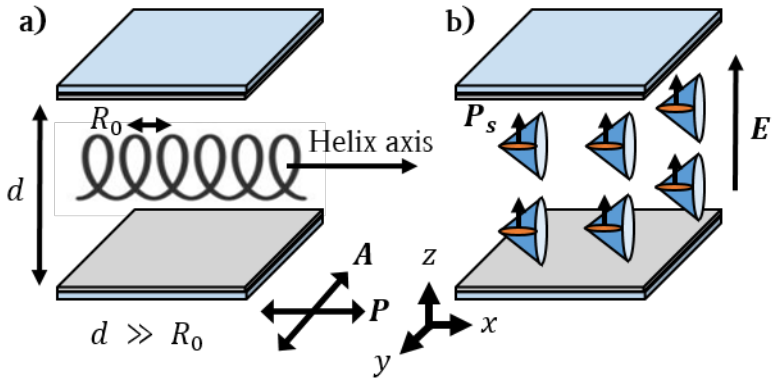

Figure 2.14: A schematic of the deformed helix FLC (DHFLC) geometry, in a): the OFF, and b): ON states, which are dark and bright respectively.

where E_u is the electric field required to unwind the helix and $q = \frac{2\pi}{R_0}$ (the helix wave vector) [52, 124]. The response times in low fields (E/E_u) are independent of P_s and R_0:

$$\tau = \frac{\gamma_\phi}{\mathbf{K}{q_0}^2} \, , \tag{2.73}$$

and shows fast ($\sim 10\ \mu s$) and reversible switching for small electric fields, while ensuring $\mathbf{E} < \mathbf{E}_u$ to avoid hysteresis [125, 126]. The optical transmission is given by:

$$I = \sin^2 \left[2(\varphi_P - \varphi_R(x)) \sin^2 \left(\frac{\pi \Delta n_{eff} d}{\lambda} \right) \right] \, , \tag{2.74}$$

where φ_P is the angle of the polariser relative to the helix axis, and φ_R is the angle of projection of the helix axis in the x, y-plane. Maximum transmission is obtained for $\varphi_P = 0$, $\varphi_R = \pi/4$, and $\Delta nd = \lambda/2$. Benefits over the SSFLC include high operational speeds at low driving voltages, less sensitive to surface treatment and cell gap variations, and natural grey-scale through control of Δn by varying $\mathbf{E}$ [126]. It should be noted that the OFF state is not completely dark due to the chirality of the FLC, and must be addressed to switch between dark

and bright states [126].

2.4.3 Electrically Suppressed Helix Mode

The electrically suppressed helix FLC (ESHFLC) mode shows similar characteristics as the DHFLC shown in Figure 2.14 below a threshold voltage $V \leq V_c$ [127, 128]. Above this voltage, the helix becomes completely suppressed [128]. The ESHFLC mode then has the same response time behaviour observed for the SSFLC. It differs in its initial conditions without an applied field where it has a helix rather than surface stabilisation. The lack of surface stabilised state is thought to be a key factor in the ESHFLC mode displaying good alignment for a FLC, with high contrast ratios and fast switching speeds at low voltages [129]. To achieve this alignment, the helical elastic energy must be equal to, and not less than, the normalised anchoring energy of the alignment [129]:

$$K_{22}q^2 \geq \frac{2{W^0}_Q}{d} \ , \tag{2.75}$$

where ${W^0}_Q$ is an anchoring energy coefficient. Good shock stability is observed for the ESHFLC mode. The optical contrast is restored completely within $10s$ following a shock, and no defects are seen in the optical texture following this and electrical addressing [129, 130]. It should be noted that the electric field must be continuously applied, as the OFF state has two domains separated by twice the FLC cone angle [130].

2.4.4 Vertically Aligned Deformed Helix Mode

The DHFLC geometry can't be used for phase-only modulation in SLMs. This is because it is the orientation of the optic axes moving which creates polarisation state changes of the incident light [131]. Electro-optic switching using the orientational Kerr effect can be used to overcome this, which was used in polymer-stabilised blue phase LCs (PSBPLCs) [132]. The Kerr effect is an electro-optic

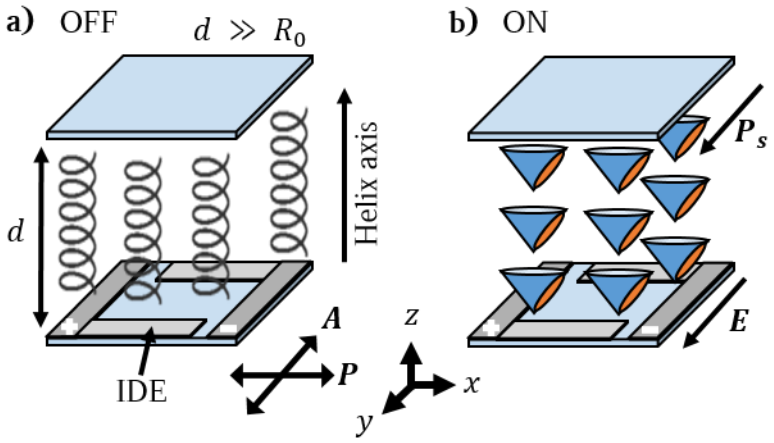

Figure 2.15: A schematic of the vertically aligned deformed helix FLC (VADHFLC) geometry, in a): OFF, and b): ON states, which are dark and bright respectively.

effect generated in liquids:

$$\Delta n = \lambda K_{Kerr} E^2 \tag{2.76}$$

where K_{Kerr} is the Kerr constant [132]. This effect can be utilised in vertical aligned (VA) FLCs with a low R_0, such as used for the DHFLC [133–135]. A schematic diagram of the vertically aligned DHFLCs (VADHFLCs) mode is shown in Figure 2.15. Here R_0 is parallel to the substrate normal. Fields can be applied to a VADHFLC mode using interdigitated electrodes (IDEs) to provide in-plane switching (IPS) fields to achieve a rotatable wave plate [131, 134, 136]. The in-plane component of the optic axis is approximately linear, unlike the refractive indices which are proportional to $\mathbf{E}^2$ caused by electrically induced distortions to the helical twist of the FLC [131, 136, 137]. The orientational Kerr effect only arises at low applied electric fields ($E < E_u$). At fields near to and above those unwinding the helix (E_u) there are deviations to the $\mathbf{E}^2$ dependence, which begins to elliptically polarise the transmitted light [122].

This geometry shows fast electro-optic switching and is hysteresis-free. It is hindered by limitations set by the maximum driving voltage and the non-uniform fields from IDEs causing defects to form above the electrodes following operation. This limits the electrode spacing that can be used for the IDEs as uniform fields are a requirement for this mode, which can result in the formation of focal conic defects [138]. The use of double IDEs (one on each substrate) has been suggested as a way to improve the field uniformity, although has not been demonstrated [122].

2.4.5 Diffractive Applications

With regards to non-display applications, the helical pitch of FLCs can be utilised to provide diffractive profiles [139]. Their natural diffraction efficiency is poor, but can be modified by adding, for example, carbon nano-tubes [140]. In addition the FLC director can be guided in a periodic distribution of polymer networks, controlling the diffraction profile with in-plane electric fields [141]. The ESHFLC mode has also been utilised with photoalignment techniques to create periodic alignment domains which are switched between dark and diffracting states [142]. There have been more complex geometries shown such as Fresnel lenses and a Pancharatnam-Berry lens which show fast switching speeds and high optical contrast [56, 143, 144].

2.5 Summary - Chapter 2

This Chapter has introduced the main properties of liquid crystals for use in electro-optic displays and devices. Nematic and smectic phases have been discussed in terms of their molecular order, as well as the origin of ferroelectricity resulting in a spontaneous polarisation in chiral smectic C materials. The important physical properties of both N and SmC are described, including their alignment, refractive indices, elastic constants, free energy and permittivities. The main differences between active and passive matrix addressing has also been

described, the former being responsible for the success of the LCD by enabling highly adaptable operating modes. The important polarisation optics are discussed that will be used for building prototype VGA-FLC devices in Chapter 4. Finally the PM addressed SSFLC is described, and the new FLC modes that have been explored enabled by PM addressing, including vertical alignment of the smectic layers and non-display applications. The aforementioned methods for utilising FLCs in electro-optic devices show a variety of advantages and disadvantages, while highlighting the wide range of techniques that can be used to satisfy particular requirements for certain applications. Importantly, there are two significant decisions made when designing the containment for a FLC: alignment and desired director field. These are further discussed in Chapter 4.

2. AN INTRODUCTION TO LIQUID CRYSTALS FOR ELECTRO-OPTIC DISPLAYS AND DEVICES

Chapter 3

Experimental Methods

3.1 Introduction

The experimental methods used and developed throughout this work are described in this Chapter. The standard processes and techniques used to create microstructures and temporary stencils for creating photomasks using photolithography will be introduced. The equipment and techniques to do so were new to the group and so were first set up and parameterise for fabricating tailored LC devices. The suggested standard operating procedures based on this preliminary work are presented to provide general working processes for creating standard devices. Following this, specific modifications to these processes were implemented for creating (sub)-micron sized liquid crystal containments and for fabricating complex patterned electrodes. The analytical techniques used to determine the profiles of these structures are detailed, including surface profilometry and scanning electron microscopy (SEM). Techniques are described for replicating these microstructures, and how to surface treatment is used to give controlled alignment to LCs when incorporated into LC cells. Finally the analytical techniques used to analyse liquid crystals in prototype geometries is introduced, including polarising optical microscopy (POM), electrical addressing and measurements of transmission, response times and FLC spontaneous polarisation of SCE13*.

3.2 Photolithography: The Basics

3.2.1 An Introduction to Photolithography

Lithography, derived from the Greek words for "stone" and "write", was a process invented in 1796 in which a carved stone was inked and treated with chemicals to transfer an image onto paper [145]. Photomasking and the chemical processing of printed circuit boards in 1943 was the first example of "photolithography". This eventually lead to the first commercial integrated circuit in 1961 processed using photoetching. These devices are found almost everywhere today, and importantly in many electro-optic displays and electric devices. The performance of photolithography is importantly determined by its resolution and minimum feature size that can be fabricated, and production throughput or efficiency (the number of wafers that can be made per hour). The photolithography process requires a set of steps, which vary depending on the method of exposure and type of photoresist being used. A summary of these steps is provided in Figure 3.1.

3.2.2 Photoresists

Photoresists are composed of three main components: a polymer, a sensitiser, and a solvent. The solvent allows the polymer to be deposited on the wafer through spin coating, the polymer changes structure when exposed to UV radiation, and the sensitiser controls the rate of the chemical reaction or polymerisation [145]. There are two types of photoresist: positive and negative tone. In positive tone, UV radiation causes the polymer to rupture, weakening it, resulting in the exposed resist to increase in solubility to its developing solution. Oppositely, negative tone resists strengthen by the polymer chains chemically cross-linking when exposed to UV radiation. This significantly reduces the exposed areas of the negative-tone resist solubility to its developer. The sensitizer is designed to "bleach" to the incoming UV, rendering it transparent to that wavelength which allows the use of thick films as the incident radiation will permeate through the resist to the substrate. The choice of resist is determined by the requirements of the desired application, and depends on factors including desired resolution,

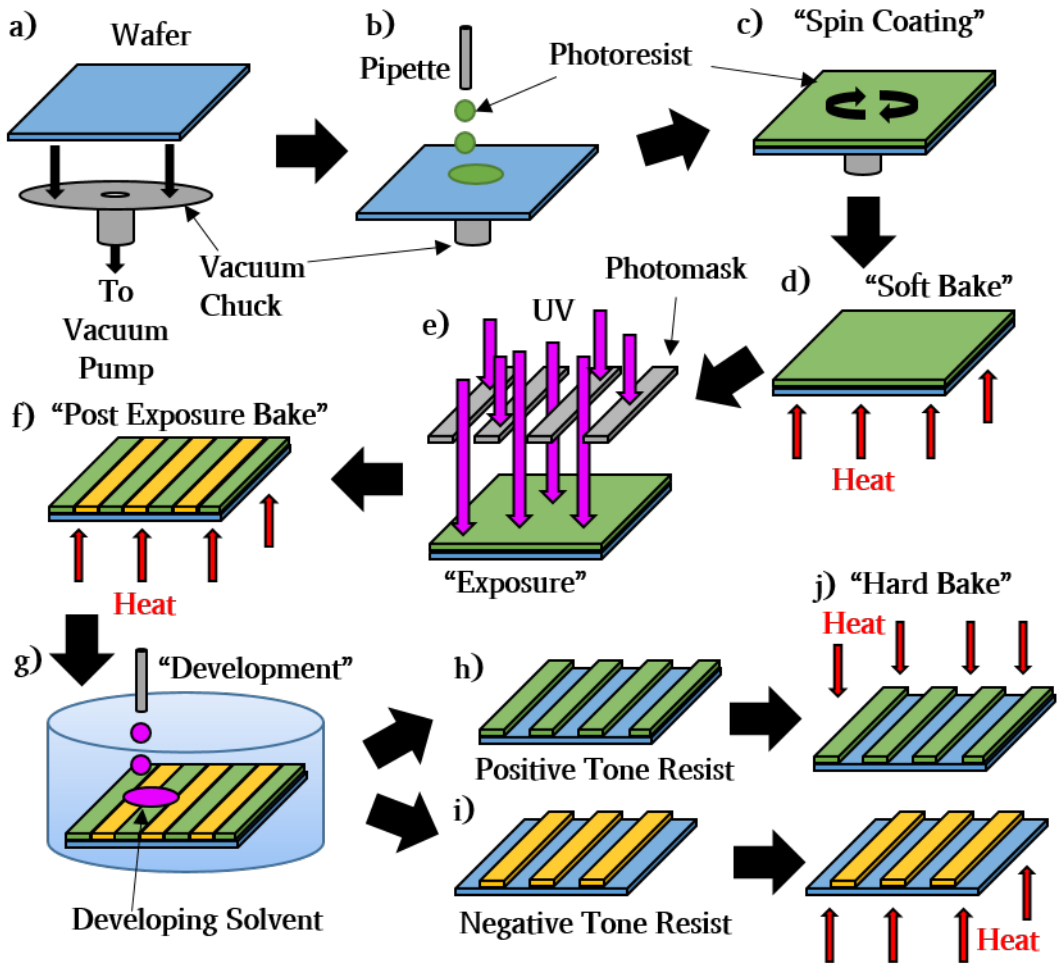

Figure 3.1: A schematic diagram of the photolithography process. a): A cleaned wafer is placed on the spin coater vacuum chuck, and a vacuum is applied to hold it firmly in place. b): A photoresist is added to the wafer. c): The vacuum chuck spins at a chosen speed to create a uniform film thickness of photoresist. d): The wafer is soft baked to remove residual solvent from the photoresist. e): The wafer is exposed to patterned UV light, here shown with a photomask using a mask aligner. Alternatively, direct write lithography can be used. f): The wafer is post exposure baked to complete or halt the chemical reaction initiated by the UV exposure. g): The wafer is developed using a solvent, which removes the unpolymerised photoresist. h): If a positive tone photoresist is used, the exposed regions are removed. i): If a negative tone photoresist is used, the unexposed regions are removed. j): The wafer is hard baked to solidify the remaining patterned photoresist so that it can be used in further processing.

ease of processing, speed, and cost. In general, negative resists are best suited for permanent features such as high resolution shapes and patterns, while positive tone resists are softer and prove more appropriate as a temporary stencil such as is required for electrode etching. In addition, positive tone resists are better suited for use in hard contact mode with a mask aligner as it is more solid before exposure than negative tone resists. Both are used throughout the fabrication stages of this work.

3.2.3 Wafer Cleaning and Clean Rooms

Wafers must be devoid of both chemical and particulate contaminants before processing by removing solvent stains and dust. Stains lead to adverse effects during evaporation processes, while particulates can cause undesirable masking effects and damage. First, wafers are cleaned thoroughly by placing them in the following solvents one after the other in an ultrasonic water bath each for 30 $mins$: soapy water (a $1:10$ ratio of Decon-90 surfactant to deionized (DI) water), DI water, acetone, methanol and isopropanol. Wafers are dried above 100 $^{\circ}C$ to evaporate excess water before processing, and residual organic residues are removed from the substrate surface using an UV-Ozone cleaner. This is all performed in a clean room to prevent further contamination during processing. There is a clean room classification system for determining its cleanliness. For example a Class 1 clean room does not exceed one 0.5 μm particle per cubic foot of air, while a Class 100 clean room allows 100x 0.5 μm particles per cubic foot. The clean rooms used throughout this project are approximately a Class 10,000-100,000, where there are $> 10,000$x 0.5 μm and > 70 5 μm particles per cubic foot. Ultimately the class of the clean room determines the smallest feature size that can be fabricated reliably . In addition, the room was lit with amber light to avoid degradation of the photoresist while preparing the wafers. Where possible, the clean room environment should be controlled for:

- airborne particulates,
- temperature,

- air pressure,
- humidity,
- vibration,
- lighting.

Of these environmental controls, only the lighting and the temperature during photopatterning have been controlled, whilst particulates and vibrations have been minimised where possible.

3.2.4 Spin Coating

Photoresists can be deposited on a clean wafer in a variety of ways, including, but not limited to spin coating, spray coating and dip coating [145]. Spin coating was chosen due to working for a variety of wafer sizes and materials, while easily allowing variations to the photoresist thickness by varying the spin speed. The wafer is placed onto the vacuum chuck of the spin coater, which holds it in place. The photoresist is then dispensed directly onto the wafer. The wafer is then spun at a low speed (around 500 rpm) for a few seconds to help dispense the photopolymer, and then controllably ramped up to the desired spin speed (typically $3000 - 4000$ rpm) for up to 60 s to obtain the correct film thickness. The thickness of the photoresist film (h_{film}) following spin coating is determined by [146, 147]:

$$h_{film} \propto \frac{C^{\beta}\eta^{\gamma}(T)}{\omega^{\alpha}} \, , \tag{3.1}$$

where C is the polymer concentration (measured in $g/100 - mL$ of solution), η the viscosity, and ω the rotation speed (measured in rotations per minute), with α, β and γ exponential factors specific to the photoresist. Therefore h_{film} can be controlled by changing the concentration of solvent or the spin speed, but can also be influenced by the room temperature, as η is temperature dependent. A

build up of photoresist may occur at the edges of the wafer, and should be removed to maintain a uniform film thickness over the sample. This is of particular importance if using a photomask to ensure good contact with the wafer and so maximising the resolution and aspect ratio of features. The photoresist is removed from the fridge and allowed to reach room temperature before processing to allow it to degas to limit air bubble formation on deposition onto the wafer, and avoiding temperature gradients and so variations to Equation 3.1. Figures 3.1a-c show a schematic diagram of the spin coating process. The spin coater used was a model WS-650-MZ from Laurell Tech. Corp..

3.2.5 Soft Bake

Following spin coating the photoresist still contains some residual solvent (up to 15 %) and built-up stresses [145]. These are removed by baking the wafers on a hot plate or in an oven, and the optimum process varies depending on the type of resist and its thickness. The SB is always performed before the exposure.

3.2.6 Exposure: Pattering Photoresists

The wafers are exposed to UV light to pattern the photoresist. Two techniques are utilised: maskless, and with a photomask.

3.2.6.1 Direct Write Lithography (DWL)

One aim of this project is to create variable and tunable containments for liquid crystals. This is not always practical using a photomask as they are time consuming and expensive to create, can only be used to replicate features already in the design, and negative resists tend to be liquid during exposure and unsuitable for hard contact photolithography. Therefore direct write lithography, a form of maskless lithography, was used for prototyping [148, 149]. For this, a MicroWriter ML2 DWL machine (Durham Magneto Optics Ltd.) is used (referred to as the

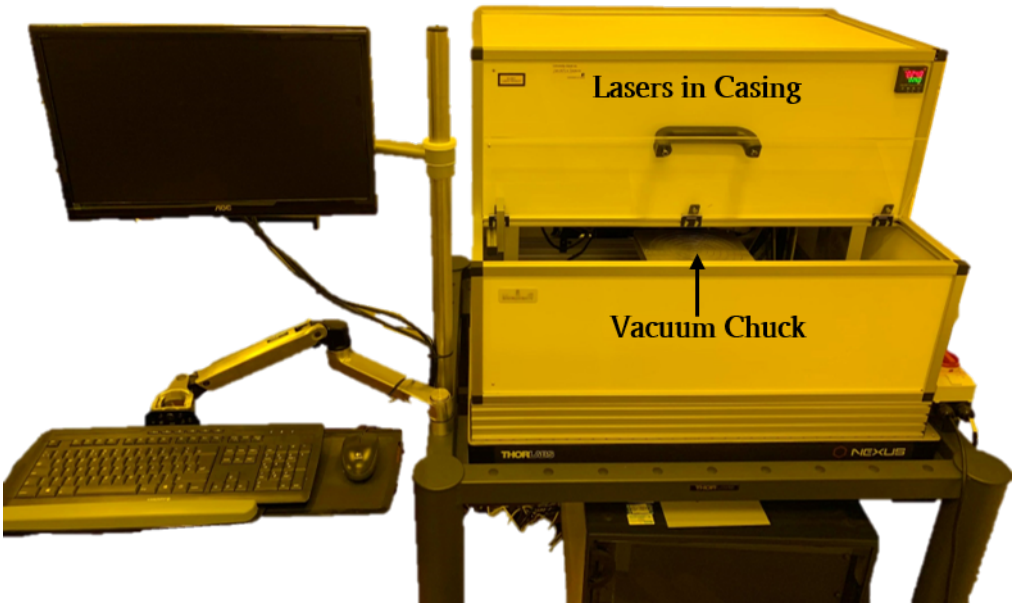

Figure 3.2: The Direct Write Lithography machine (referred to as the DWL). The lasers are contained within the box. The DWL is currently open, as to expose the vacuum chuck. When the lid is closed, the chuck repositions into the protective casing.

DWL) [150]. This is shown in Figure 3.2. This has the choice of two exposure wavelengths of different resolutions:

- i-line radiation ($\lambda = 365\ nm$), 2 μm diameter laser,
- h-line radiation ($\lambda = 405\ nm$), 0.6, 1 and 5 μm diameter lasers.

The DWL uses an x, y-raster of the substrate chuck to selectively expose the wafer with a desired pattern, in replacement of the photomask. The wafer is held firmly in place with a vacuum. These methods allow sub-micron printing accuracy (100 nm minimum addressable grid), although the actual resolution is limited by the diameter of the laser and the sensitivity of the photoresist. There is no variation of the chuck in the z-direction (up and down), and so this is a 2D printing process and it is not trivial to make complex 3D structures. For example, the height of the structure is determined by the thickness of the photoresist, while the shape at the top and bottom surfaces can be anything, from a circle creating a cylinder, to a complex series of channels for microfluidics where the channel depth remains constant. Chapter 5 looks towards pushing the DWL to its limits to create simple 3D surface-relief gratings.

3.2.6.2 Mask Aligner

A limitation of the DWL is that a design must be written line-by-line, and so the larger the design, the longer the duration of exposure takes. For example, writing a 4×4 array of interdigitated electrodes (an area of $8 \times 8\ cm^{-2}$) takes upwards of 20 hrs. Using a mask aligner and a photomask with the desired design would take seconds. The lamp is designed to provide a controlled UV intensity, directionality and uniformity over the wafer area, creating a transfer of the photomask image in a photoresist. Photomasks can be made using the DWL. A diagram of the mask aligner (Model 200, OAI) is given in Figure 3.3. The mercury lamp produces i-line radiation ($\lambda = 365\ nm$). The mask is mounted to the mask holder, and the wafer to the wafer chuck, and both are secured using a vacuum. The wafer is aligned with the photomask using the mounted microscope (if required), and then brought into hard contact with the mask where an additional vacuum holds

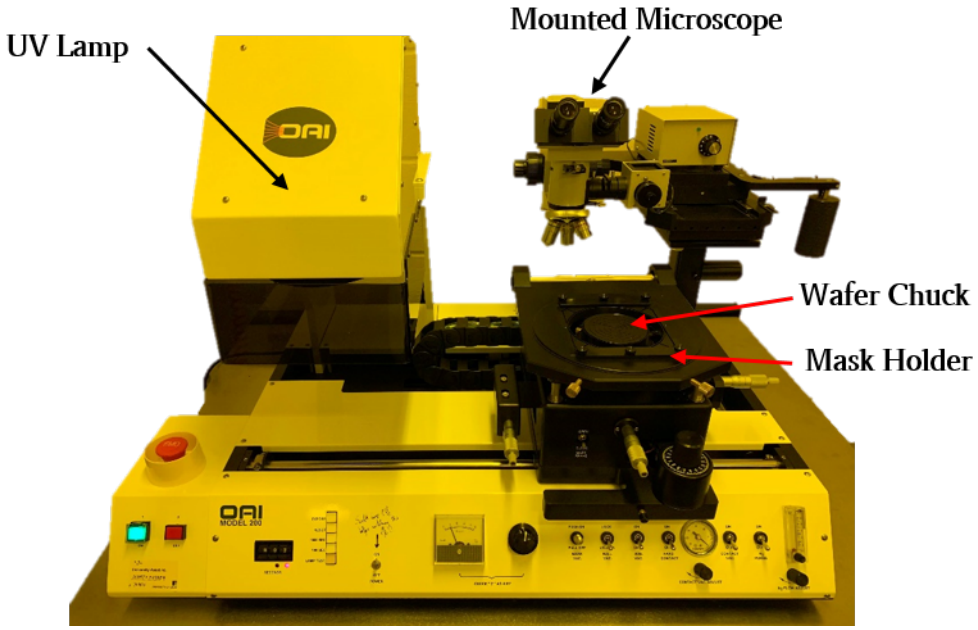

Figure 3.3: A labelled photograph of the mask aligner. The mask and wafer are loaded, aligned with the mounted microscope, and then positioned under the UV lamp.

the two together. The wafer is then exposed to UV radiation. The power of the mercury lamp is 200 W, resulting in an intensity of 40 Wcm^{-2} over a 5 in wafer.

3.2.7 Post-Exposure Bake

A post-exposure bake (PEB), completes or halts the reaction initiated by exposure to UV radiation, and is usually only required for negative-tone resists. This process acts to increase the rate of the chemical reactions initiated during exposure by baking at an increased temperature. The chemical process of this procedure is described in Section 3.3.1 for the negative tone photoresist SU-8.

3.2.8 Development

Following exposure and the PEB, there are now regions of exposed and unexposed photoresist on the wafer. The wafer is developed by immersion or spraying with a solvent that dissolves the unpolymerised photoresist, leaving behind the pattern transferred by the UV light. This is an example of wet development. The chosen solvent develops based on variations of molecular weight (due to cross-linking and polymerisation), reactivity changes, and changes is polarity [151]. The time period that the wafer is submerged in the solvent and the temperature of the solvent are important to control. Too short, and residual photoresist will remain on the wafer where not wanted, and too long may result in the polymerised regions swelling and delaminate, or even itself dissolve.

3.2.9 Hard Baking

Following development, the process is almost complete, and the desired structure should remain on the wafer. Before further processing, the wafer must be hard baked to anneal the remaining photoresist film to adhere it to the substrate, due to weakening through the solvent swelling or penetrating the resist. It also hardens the film so that it becomes more resistant to solvents in future processing.

The hard bake may induce some flow or melt which can change the wall angles of the structures, and makes the resist more difficult to remove from the substrate, which might not be beneficial. There may also be some shrinkage in the feature sizes.

3.3 Photolithography: Creating Microstructures for Liquid Crystal Containment

In this Section, the use of SU-8 as a permanent, negative-tone photoresist is explored for fabricating microstructure to use for liquid crystal alignment and containment. The procedures described here have been set up, developed and optimised as part of this project. The permanent SU-8 structures can be used directly in a LC cell, or can be replicated and embossed into alternative photopolymers.

3.3.1 SU-8: A Negative-Tone Resist

SU-8 is a high contrast, epoxy based negative-tone photoresist, designed for use in microelectronic applications which require permanent, thick, chemically and thermally stable features [152]. It was patented in 1992 by IBM, and commercially available by 1996 [153]. Films of SU-8 have a high optical transmission above 360 nm of > 95 %, and structures with near-vertical sidewalls can be made in film thicknesses of 0.5 to 200 μm [154–156]. This makes it ideal for creating permanent microstructures to be used in electro-optic devices, and for creating masters for replication purposes.

The SU-8 monomer is bisephenol-A novolak glycidyl ether, of which the chemical structure is shown in Figure 3.4. Each molecule contains 8 epoxy groups, thus the name. This is dissolved in the organic solvent cyclopentanone. The amount of solvent can be varied to change the polymer concentration (C), and so the film thickness (h_{film}) on spin coating (see Equation 3.1). This is combined with

the photo-acid generator triarylsulfonium hexafluoroantimonate salt (the sensitiser), which is an onium salt [152]. Onium salts generate strong Lewis acids when exposed to UV radiation. Lewis acids contain empty orbitals capable of accepting electron pairs which catalyse the polymerisation of the SU-8 monomers during the PEB [154]. Here, the photo-acid breaks the epoxy group rings and enables significant cross-linking, resulting in an insoluble polymer network [157]. The chemical reaction is shown in Figure 3.5 [158]. The PEB controls the rate of photo-acid diffusion and ensures it does not diffuse into unexposed regions, enabling high resolution structures with vertical side-walls in the photoresist.

SU-8 2025 (MicroChem) is used throughout this project, which contains 68.55 % solids, or a density of 1.219 $gmol^{-1}$, and creates a 28.1 ± 0.5 μm thick film when spin coated at 3000 rpm [156]. It can be diluted using cyclopentanone, which decreases the concentration of SU-8 monomer solids. Section 3.4.3 presents the experimental results for SU-8 processing.

3.3.2 OmniCoat: An Adhesion Promoter

Before spin coating SU-8, it is usually beneficial to apply an adhesion promoter, especially for thinner films (< 10 μm) or small structures ($< 10 \times 10$ μm^2). This is because of photoresists not adhering strongly to silicon or glass wafers due to preferentially forming hydrogen bonds with water molecules absorbed from the air to the wafer surface [145]. To prevent this, the wafer surface is primed with an adhesion promoter, which changes the surface chemistry to repel water and form better resist adhesion. OmniCoat (MicroChem LTD.) is specifically designed to strongly adhere to SU-8 [159]. Omnicoat is composed of a proprietary polymer and surfactant ($< 2\%$) in the solvents cyclopentanone and propylene glycol methyl ether. It is applied immediately after the wafer has been cleaned in the UV-Ozone machine via the following process:

- Add 1 mL OmniCoat per inch of wafer,
- Spin coat at 500 rpm for 5 s with an acceleration of 100 rpm/s, and ramp to 3000 rpm for 40 s with an acceleration of 255 rpm/s,

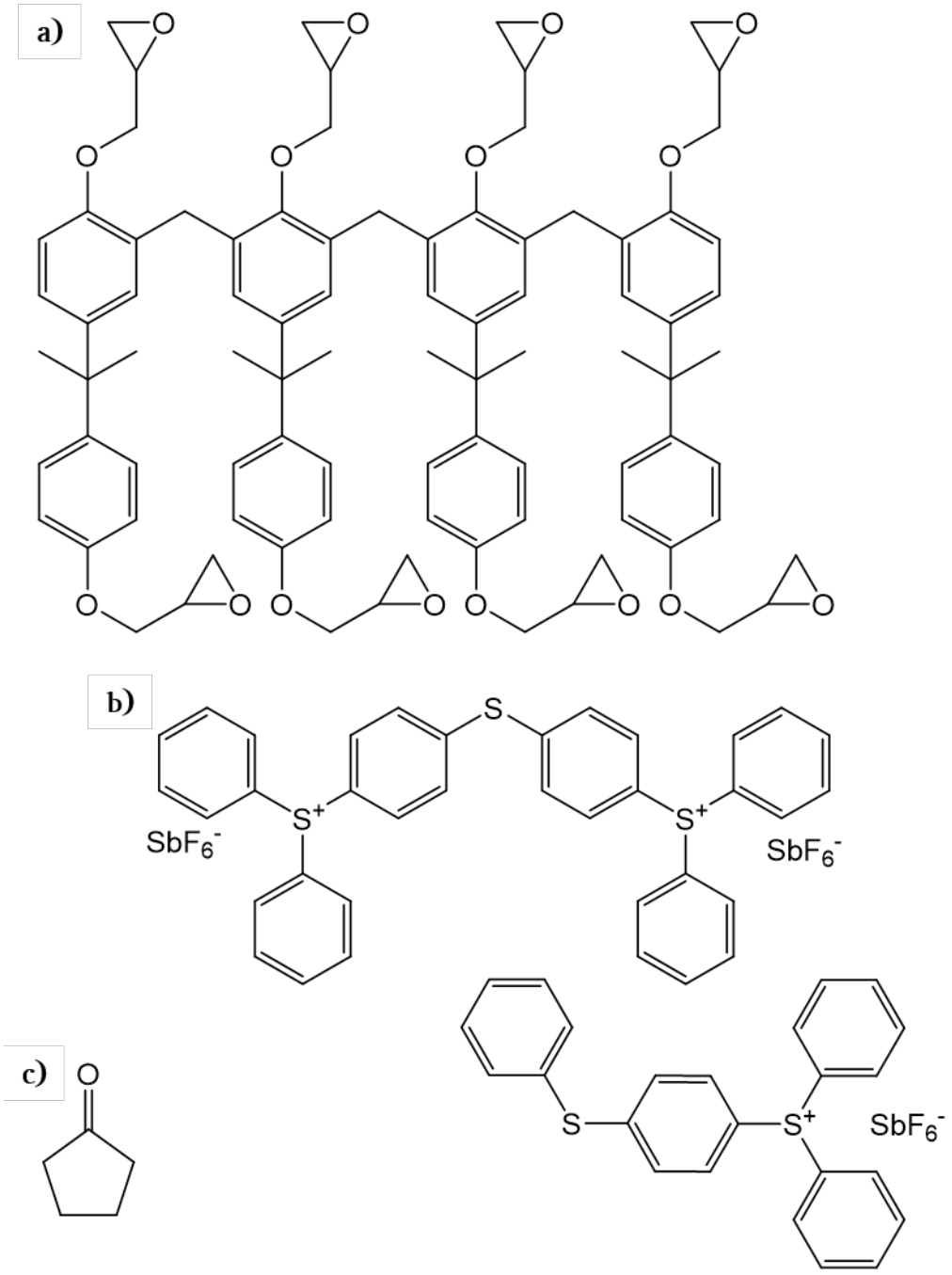

Figure 3.4: The chemical structures of the components of SU-8 2025. a): The SU-8 monomer, bisephenol-A novolak glycidyl ether. b): The photo-acid generator, triarylsulfonium hexafluoroantimonate salts. c): The organic solvent, cyclopentanone.

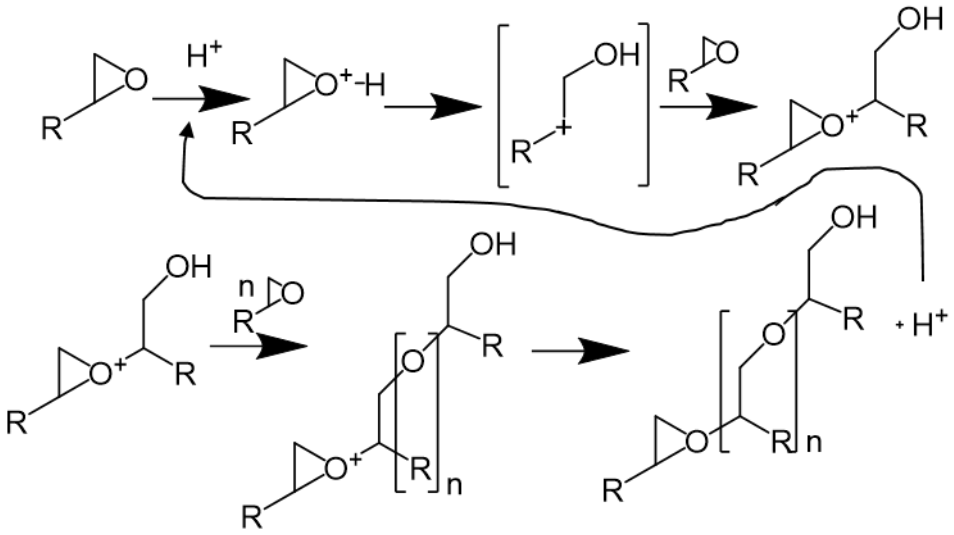

Figure 3.5: The SU-8 monomer polymerisation reaction which occurs at the epoxy groups.

- Bake at 150 $°C$ for 2 $mins$,
- Allow to cool to room temperature before applying SU-8.

This results in an ~ 17 nm thick film, which was sufficient for the fabrication of structures in this study [159, 160]. Additional layers can be added by repeating the process to further increase the adhesion if required.

3.3.3 SU-8 Processing Optimisation

SU-8 is processed using the following programme, modified from the recommended processes through experimental results. These parameters work well for films ≥ 10 μm.

- **Spin Coat**:
  - Dilute SU-8 2025 to the desired concentration using cyclopentanone (by mass, using Figure 3.7), shake well, and leave overnight to de-gas,
  - Dispense ~ 1 mL per inch of wafer,

  - 10 s at 500 rpm with an acceleration of 100 rpm/s,
  - 40 s at 3000 rpm with an acceleration of 255 rpm/s.

- **SB**: $1-4$ $mins$ at 95 $^{\circ}C$.
- **Exposure**: $500-1400$ $mJcm^{-2}$,
  - Note: This is highly dependent on both film thickness, feature size and feature complexity. In general, the thicker the film, the larger the required dose. A dose of 1200 $mJcm^{-2}$ will usually produce acceptable features over the thickness range of SU-8 2025. A dose test should always be performed when creating a new design at a particular thickness.
- **PEB**: $1-5$ $mins$ at 95 $^{\circ}C$.
- **Development**:
  - Solvent: propylene glycol monomethyl ether acetate;
  - Pipette ~ 1 mL of solvent per $cm^(-2)$ of wafer while spinning on spin coater at 500 rpm over a period of ~ 1 min, or until clearly developed;
  - Remove from spinner, and rinse again in developing solvent for ~ 10 s, and then IPA for ~ 10 s.
- **Hard Bake**: 180 $^{\circ}C$ for $1-2$ hrs.

3.3.4 SU-8 Processing Optimisation for "Thin" (< 10 μm) Films

The SU-8 photoresist and its recommended processing guidelines are designed to create features with vertical side-walls, and works well for structures with heights and feature sizes of > 10 μm. However, as the film thickness of SU-8 is reduced by diluting with the cyclopentanone solvent, the structures begin to crack and delaminate due to residual stresses induced during the post-exposure bake (PEB) [157, 161–163]. This was not observed for films with heights > 10 μm. This is due to the generation of both intrinsic and extrinsic stresses. Intrinsic

stresses arise during crosslinking in the PEB, and also during solvent evaporation and structure shrinking due to polymerisation, while extrinsic stresses arise from temperature changes and differences in the coefficients of thermal expansion between the photoresist and substrate [157]. These stresses are exacerbated in "thin" films, but can be reduced with adjustment to the processing procedures.

To reduce the intrinsic stresses, a higher volume of solvent should be retained during UV exposure, allowing a higher mobility of SU-8 monomers and generated photo-acid diffusion. This allows polymerisation to occur at lower temperatures, and so enabling a reduction in the PEB temperature [164]. This reduces the extrinsic stresses, resulting in crack-free structures. The following changes in processing are therefore implemented for "thin" films of SU-8 ($< 4\ \mu m$), and modifications made for films ($> 4\ \mu m$) based on experimental results:

- **Soft Bake (SB)**
  - Films $> 10\ \mu m$: $T = 95\ ^{\circ}C$ for $1\ mins$,
  - Films $> 4\ \mu m$: $T = 65\ ^{\circ}C$ for $5\ mins$,
  - "Thin" Films ($< 4\ \mu m$): $T = 30\ ^{\circ}C$ for $30\ mins$ (acting as an "ambient" temperature evaporation),
- **Post Exposure Bake (PEB)**
  - Films $> 10\ \mu m$: $T = 95\ ^{\circ}C$ for $1 - 2\ mins$,
  - Films $> 4\ \mu m$: $T = 65\ ^{\circ}C$ for $30\ mins$,
  - "Thin" Films ($< 4\ \mu m$): $T = 50\ ^{\circ}C$ for $30\ mins$.

Features as thin as $0.5\ \mu m$ can be achieved using the aforementioned methods. The methods for films $> 4\ \mu m$ are used over those for films $> 10\ \mu m$ for these dilutions of SU-8 to avoid variations occurring due to the differing techniques. There are no changes required for the spin coating and development steps, which remain as described in Section 3.3.3. The exposure dose does change however, and this varies depending on the film thickness and quality of structures required. Good structure quality can still usually be obtained for doses at $\sim 1200\ mJcm^{-2}$.

The optimum dose varies depending on the desired feature size and edge quality. Chapter 5 shows how variations in the exposure dose and higher solvent levels during processing are key for fabricating a variety of varying amplitude, sinusoidal-like surface-relief gratings.

3.4 Characterisation of Microstructures

The microstructures were characterised for their height, side-wall verticality and overall profile using scanning electron microscopy (SEM) and surface profilometry. These techniques are outlined here.

3.4.1 Scanning Electron Microscopy (SEM)

SEM was performed using a tabletop microscope, TM3030Plus Series (Hitachi High-Technologies Corp.). SEM has an advantage over surface profilometry as it can image vertical side-walls. It also has an advantage over optical microscopy for imaging SU-8 structures as they can be magnified to a larger size due to greater focal depth, and provides a stereoscopic image (enhances the perceived depth). Importantly the SU-8 photoresist becomes easier to distinguish from the ITO glass substrate, as both appear optically transparent in the visible wavelengths.

SEM scans a sample with an electron beam in a vacuum which interacts with the surface chemistry. Secondary electrons (SE) and backscattered electrons (BSE) are generated through these interactions, which are detected to produce an image. SEs are reflected near the surface of the sample, and reflect the topographical structure. BSEs are reflected by the atoms within the sample, and so their image represents the compositional distribution of the sample surface. SEs were used for imaging the SU-8 microstructures.

Sample preparation for using in SEM was the main limitation for imaging microstructures fabricated in SU-8. First only x, y-rotation using the SEM stage was

available, with no z-rotation. Therefore samples were mounted at a known angle to measure the structure height. Additionally, structures are generally positioned at the centre of the wafer as this is the most uniform region of the photoresist. The wafers must therefore be cut or snapped to a smaller size to fit into the SEM sample holder. This can damage and delaminate the structures. This results in the specific structures being unusable once they have been imaged using SEM. Good images could be taken of the SU-8 structures without spluttering a conducting layer of gold.

Figure 3.6 highlights the benefits and limitations of using SEM to analyse SU-8 microstructures. A design of 60×60 μm^2 squares with various sized holes (Figure 3.6c has a 40×40 μm^2 hole, for example) were written into a undiluted SU-8 2025 (a 100 % mixture), processed as described in Section 3.3.4 on an ITO glass substrate. SEM images were taken using the SE technique. Figures 3.6 a) and b) were taken with an angled wafer, while Figure 3.6 c) was taken normal to the wafer. The images show structures with vertical side walls, and slightly rounded edges and corners. These qualities stay true for thinner film thickness, although resolving the side walls becomes difficult for films < 4 μm. Figure 3.7 includes film thicknesses measured using this technique. Using a reduced SB and PEB temperature produced thicker structures than expected through standard processing [157].

3.4.2 Surface Profilometry

SEM provides good images for visualising the microstructures made with photolithography, although is limited in its ability to quickly and non-destructively measure their feature sizes. A good alternative is surface profilometry. This technique uses a cantilever-like stylus in contact with the wafer to build up an image. It is capable of measuring step heights of < 10 nm (maximum of 1 mm) [165]. The equipment is located in a clean room, and so structures that have been analysed can be reused in cell fabrication.

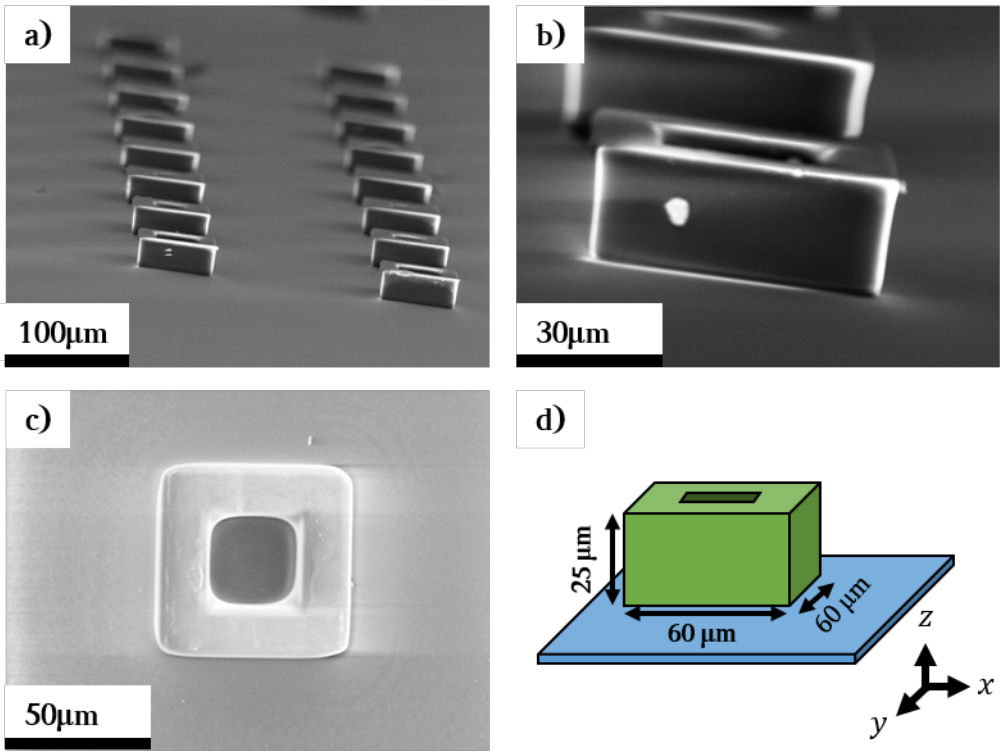

Figure 3.6: Scanning electron microscopy (SEM) images of SU-8 cubes, with varying sized holes, made with the DWL. Design: 60×60 μm^2 square with holes. A 40×40 μm^2 hole is shown in b) and c). Measured feature height: 25.1 ± 0.5 μm. a),b): SEM images taken with the wafer angled in the detector, $\sim 1.5°$, emphasising the vertical side walls. c): SEM image taken normal to the substrate, showing the rounded edges and flat top. d): Schematic diagram of the expected structures.

The machine used was a DektakXT Stylus Profiler (Bruker Corp.). It applies a force with the stylus of $0.1 \rightarrow 15\ mg$ and maps the surface of the wafer in one direction to build up a 3D image of the topography. The stylus can be changed to have a radius of either 0.2 or 2 μm, which affects the x, y-resolution. This provides accurate measurements of the heights of the microstructures, but can't resolve the vertical sidewalls. Film thicknesses measured with this technique are presented in Figure 3.7.

3.4.3 SU-8 Film Thickness Measurements

Figure 3.7 shows how the film thickness of SU-8 2025 varies with the dilution of cyclopentanone, keeping the spin speed constant at 3000 rpm. ITO glass was used as the substrate. A fit of Equation 3.1 to the expected film thickness is shown in Figure 3.7b. This can be used to predict the optimum dilution to obtain a specific film thickness. The experimental data fits closely at thicknesses $> 4\ \mu m$, but begins to deviate at lower thicknesses (outside of the experimental error). This is due to the temperature during spin coating is not controlled, leading to variations in the viscosity of the photoresist (a temperature dependent variable in Equation 3.1). The temperatures of the SB and PEB are also lowered for fabricating "thin" films to increase adhesion and reduce cracking, which results in thicker films [157].

3.5 Replication of Microstructures

Master microstructures made in SU-8 using the DWL (Section 3.3) were replicated by creating a stamp. These were used to emboss a photopolymer to quickly replicate the microstructures with a high accuracy and minimal offset. Embossing can be used to recreate components with nanometer precision, an example being isotropic optical components such as sub-micrometer surface-relief gratings [166–168]. A schematic of the embossing process is given in Figure 3.8.

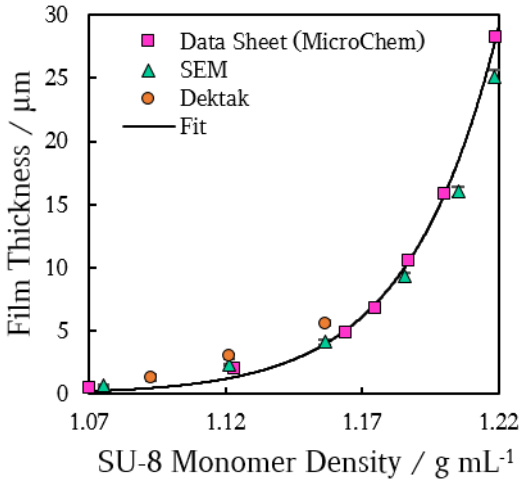

Figure 3.7: The measured film thickness of SU-8 2025 spun at 3000 *rpm* on ITO glass substrates. Thickness is plotted versus the density of SU-8 monomer solids. Pure SU-8 2025 has 68.55 % SU-8 monomer solids, or a density of 1.219 $gmol^{-1}$. Purple squares: expected film thickness based on the MicroChem data sheet [156]. Teal triangles: measurements made from scanning electron microscopy (SEM). Orange circles: measurements made from surface profilometry (Dektak). Fit: a fit of Equation 3.1 of the form $h_{film} = AC^{\beta}$, where here $A \propto \frac{\eta(T)^{\gamma}}{\omega^{\alpha}} = 0.018 \pm 0.002$, and $\beta = 37.3 \pm 0.9$ showing that h_{film} follows the expected trend at high concentrations of SU-8. The films at lower concentrations are thicker than expected induced by modifications to the SB and PEB to prevent cracking and delamination (see Section 3.3.4). The experimental errors are the size of or smaller than the data points.

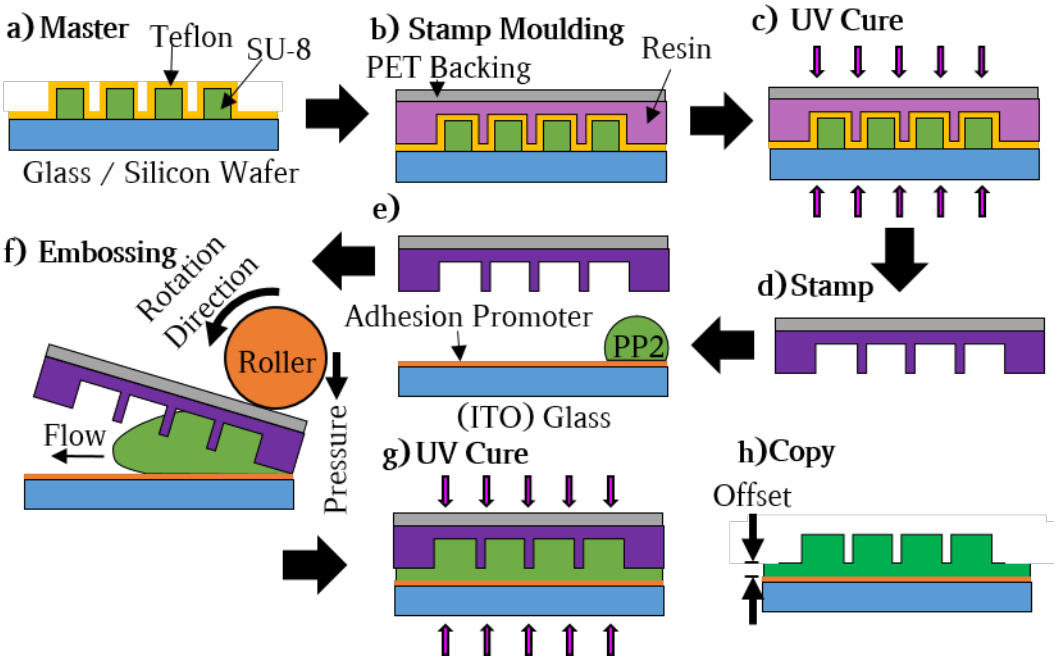

Figure 3.8: A schematic diagram of the embossing process. a): A master is created in SU-8 using the DWL and coated in Teflon to create a non-stick surface. b): Creating the stamp. A photocurable resin is added on top of the master, and a PET sheet placed over that. c): The master/resin/PET sample is cured in UV to solidify the resin. d): The stamp is peeled from the master, resulting in an inverse of the structures. e): The photopolymer mixture PP2 is placed on top of the desired substrate (usually patterned ITO) which has been treated with an adhesion promoter. The stamp is placed on top of this. f): The stamp is embossed using a pressurised roller that is rotating. This pushes the stamp into close contact with the substrate, filling the holes in the stamp with PP2. g): The substrate/PP2/stamp sample is cured in UV to solidify the PP2. h): The stamp is peeled from the copy and discarded. This process with the flexible stamp should produce a low or zero offset.

3.5.1 Stamp Fabrication

The master is first cleaned in UV-Ozone for 5 *mins*. It is then coated with a release layer of Teflon AF1601S (DuPont) dissolved in Fluorinert FC-40 (1 : 2 ratio) via spin coating (a ramp to 3000 *rpm* for 30 *s*) and baked at 180 °*C* for 1 *hr* [169]. This prevents the photopolymer mould from sticking, and so increases the number of times the master can be reused. A resin for creating the mould is made from 45 % 1,6-Hexanediol diacrylate (HDDA, an acrylic monomer), 15 % trimethylolpropane triacrylate (TMPTA, also an acrylic monomer), and 40 % Actilane 420 by mass. 4 % of the photoinitiator Genocure LTM is then added to this mixture. This resin is deposited onto the SU-8 master ($\sim$ 2 μL per cm^{-2}) and topped with a 125 μm thick piece of PET film (Melinex 506). This has been previously cut to the size of the substrate that will be embossed, rinsed in IPA and blown dry with compressed air to remove particulates, and finally cleaned in UV-Ozone for 5 *mins*. The PET/resin/master is cured in a UV light-box for 2 *mins* to partially set the resin. The PET film is them peeled off and the cure is finished in the UV-Ozone cleaner for 5 *mins*. The PET film should be coated in a layer of patterned resin, which is the inverse of the master. This is the stamp. The master is rinsed in IPA and Acetone to remove any residual resin, which is usually found at the edges of the stamp where the resin is too thick to cure.

3.5.2 Embossing into Photopolymer

A substrate (usually ITO glass or a patterned electrode) is cleaned as described in Section 3.2.3, and exposed to UV-Ozone for 5 *mins* immediately before use. An adhesion promoter is added, made from a 5 : 3 mixture of diluted acetic acid (10 % acid in water) and a mixture of 3-(Trimethoxysilyl)propyl methacrylate in methanol (1 : 200). A droplet ($\sim$ 2 μL per cm^{-2}) of this adhesion promoter is pipetted onto the ITO glass substrate and spin coated at 3000 *rpm* for 60 *s*. This is followed by a bake at 130 °*C* for 60 *s*.

A droplet ($\sim$ 2 μL per cm^{-2}) of the photopolymer PP2 is pipetted onto the adhesion promoter coated substrate. PP2 is a three-component mixture pho-

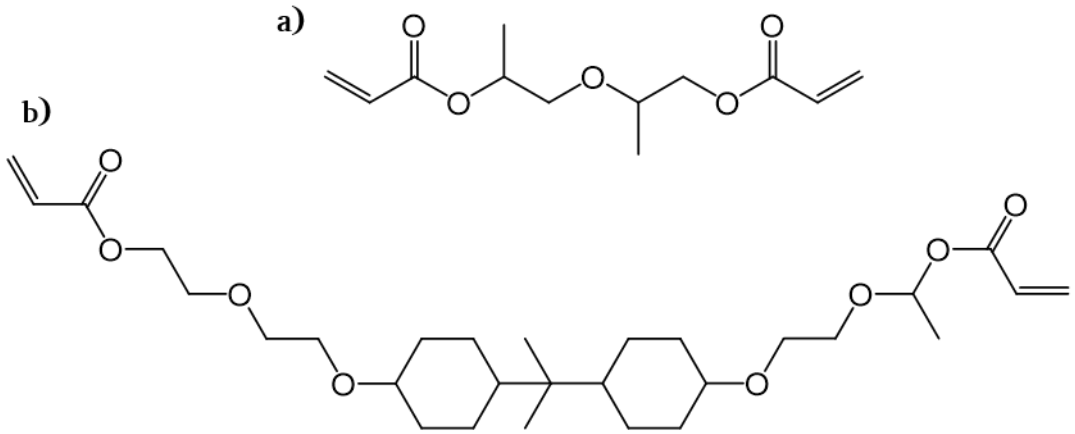

Figure 3.9: The chemical structures of the acrylate monomers used to create the photopolymer named PP2. a): Sartomer 502, and b): Sartomer 349.

topolymer, created by combining the acrylate monomers Sartomer 508 (57 % by weight) and Sartomer 349 (38 % by weight) with a the photoinitiator Genocure LTM (5 % by weight) [170]. The chemical structures of these monomers are shown in Figure 3.9. The composition of PP2 was designed for embossing applications for electro-optic applications, such that the shrinkage once cured is controlled to be enough to release it from the mould but not damage the structures, has a suitable viscosity (70 cP) for ambient embossing, and is optically transparent [167, 170]. The refractive indices of PP2 have not been matched to the LC material, which would avoid diffractive effects occurring [167]. PP2 is suitable for vapour-phase silane deposition, which is further explained in Section 3.7. SU-8 was not used as it is not designed for use in embossing: it is too viscous, and the residual solvent levels required would lead to large amounts of shrinking once cured.

Next the stamp is carefully placed on top of the PP2 coated ITO substrate (feature side down). Care should be taken if the embossed structure needs to be aligned with an ITO electrode. This ITO/PP2/stamp sample is then embossed on an embossing machine. This consists of a metal plate and a pressurised roller. The plate moves under the roller at a set speed, and the pressurised roller pushes

the stamp into the PP2 photopolymer, squeezing any excess out from under the stamp. The roller is formed from a 5 cm diameter steel cylinder with a 5 mm thick rubber coating of shore hardness 70. The shore hardness defines the resistance of the roller to indentation. The flexible stamp is key to obtaining low offset. The roller pressure was set at 4 bar, and the plate moved under the roller at a speed of 6.5 $mm\ s^{-1}$. The sample is then partially cured in a UV light-box for 2 $mins$ (power of 2.5 $mW cm^{-2}$). The stamp is peeled off to remove it from the substrate and discarded. The photopolymer is only initially partially cured so that the stamp can be easily removed, otherwise it may stick and crack. Finally the cure is finished in UV-Ozone for 5 $mins$. The embossed microstructures are then ready for surface treatment if required (see Section 3.7).

Embossing PP2 under these conditions onto IDEs results in an average offset of 0.22 ± 0.04 μm and a film roughness of 7 ± 1 nm, measured using surface profilometry (Section 3.4.2). The ITO features are 0.105 ± 0.005 μm tall (Section 3.6.6), resulting in an offset of just 0.11 ± 0.04 μm. The optimised embossing process should theoretically result in zero offset. This could be obtained by adjustment of the roller speed and pressure, the hardness of the roller, and reducing the viscosity of the photopolymer by heating the roller and plate [171]. Zero offset is not obtained due to the small size of the ITO substrates ($\sim 2 \times 2\ cm^{-2}$), which often result in poor adhesion to the stamp. This can be alleviated by increasing the substrate and stamp size.

3.6 Photolithography: Creating Photomasks and Fabricating Patterned Electrodes

The design and fabrication of patterned interdigitated electrodes (IDEs) was required for creating in-plane fields across LC cells. There are four main processes required to fabricate these in-house. These are: electrode design, mask fabrication, electrode patterning and acid etching.

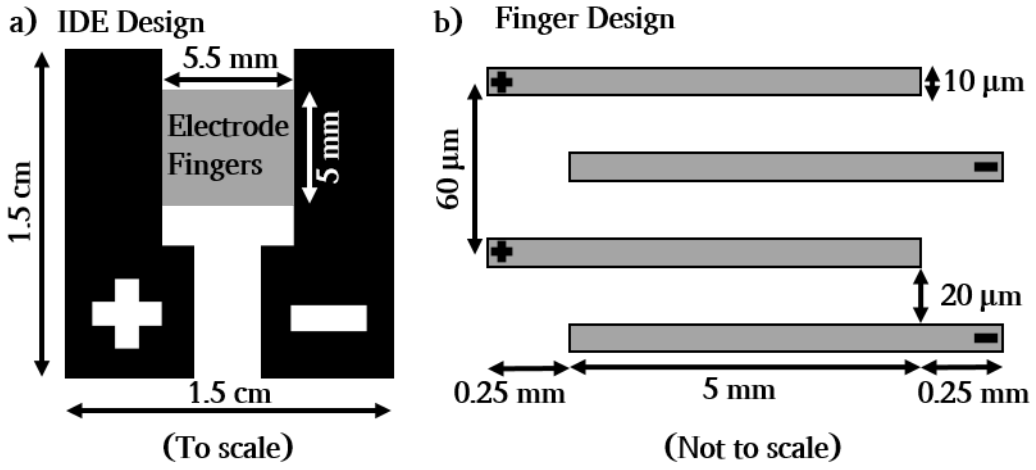

Figure 3.10: A schematic diagram of the IDE design for in-plane electric field. a): A to scale diagram of the electrode, where the "+" and "−" indicate where the wires are to be soldered, and the grey square indicates where the active area with electrode fingers is located. The final electrode area is $1.5 \times 1.5\ cm^2$. b): The individual electrode fingers are 10 μm wide and spaced 20 μm apart. Each electrode is 5.25 mm long, resulting in an overlap between the positive and negative terminals of $5 \times 5\ mm^2$.

3.6.1 IDE Design

A simple IDE design was made for applying in-plane fields across LC cells. Figure 3.10 shows a schematic of the design. The most important features are the electrode fingers, which ultimately determine the magnitude of the electric field over the LC. In order to maximise yield, the electrode fingers were designed to be 10 μm wide and spaced 20 μm apart, for a pitch of 60 μm, over an active area of $5 \times 5\ mm^2$. The relatively large electrode gap minimises the chance of the electrodes shorting due to fabrication variables, such as dust particles depositing on the wafers during spin coating through to the exposure stages. The electrodes were made into a 4×4 array, which was designed to be written with a 5 in photomask, and replicated onto $8 \times 8\ cm^2$ ITO glass plates. The sizes were determined by the mask holder on the mask aligner.

3.6.2 Creating Photomasks with Direct Write Lithography

There are two options for obtaining a photomask: purchase from an external company, or make in-house starting with a mask blank. The IDE design was chosen to be fabricated in-house by fabricating a photomask with the DWL. It is recommended to buy a mask if smaller features are required as the clean rooms are not a high enough grade to reliably create smaller features.

Mask blanks are made from thick soda lime glass ($5 \times 5 \times 0.09\ in^3$), with one surface coated in reflective chrome and pre-coated with a positive tone photoresist (AZ1518). This resist is similar to Shipley S1813 used in Section 3.6.4, and has the same processing procedures. Washing off the AZ1518 and replacing with Shipley S1813 is a cheap alternative to buying additional mask blanks if the electrode patterning is unsuccessful. Mask blanks come ready to pattern with UV out the box, and so no SB is required. The DWL was used to write the electrode design on the mask blanks. The main electrodes were written with the 5 μm, 405 nm laser, and the electrode fingers with the 1 μm, 405 nm laser, with a global dose of 400 $mJcm^{-2}$. There is no PEB required for this positive resist. The exposed mask blank is developed by submerging in Microposit MF-319 Developer (a solution of $\sim$ 2.5 % tetramethylammonium hydroxide (TMAH) in water) for $\sim$ 40 s, or until the exposed regions have fully developed. The mask is rinsed in water to stop the reaction [172]. The mask blank should now have Shipley S1813 patterned electrodes covering the chrome.

3.6.3 Etching Chrome

A solution of deionised water, glycerol and hydrochloric acid (37 % HCl in water) is prepared at a 1 : 1 : 1 ratio in a fume hood, and placed on a hot plate at 30 $^{\circ}C$ to ensure repeatable etching rates. The patterned mask blank is placed in the etching solution and allowed to wet, and aluminium foil is brought into contact with the chrome to catalyse and begin the reaction. Once the reaction starts ($\sim$ 2 $mins$), the chrome will etch in a matter of seconds. The mask is

placed in water to stop the reaction. The mask is then rinsed in acetone to remove the remaining photoresist, and cleaned thoroughly as per Section 3.2.3. The photomask is now ready for use with the mask aligner, and can be used to quickly replicate IDEs. A schematic of the etching process is given in Figure 3.11.

3.6.4 Replicating IDEs using a Mask Aligner

Replicating the IDEs using a photomask follows a similar procedure to creating the mask. The positive-tone photoresist Shipley S1813 is used to create a temporary stencil for the acid etch of the ITO layer (see Section 3.2.2) [173].

- ITO glass is cut to $8 \times 8\ cm^{-2}$ square wafers, and cleaned following Section 3.2.3. The wafer should be cleaned in the UV-Ozone machine immediately before continuing processing.
- Shipley S1813 is allowed to equilibrate to room temperature overnight before spin coating . Dispense $\sim$ 15 mL on the clean ITO wafer (ITO side up), loaded into the spin coater. The photoresist is spun with the following parameters to produce a $\sim$ 1.2 μm thick film:
  - 400 rpm for 10 s at an acceleration of 100 rpm/s,
  - 1000 rpm for 10 s at an acceleration of 100 rpm/s,
  - 4000 rpm for 60 s at an acceleration of 255 rpm/s.
- SB the wafer at 115 $^{\circ}C$ for 60 s.
- The wafer is loaded into the mask aligner, and brought into hard contact with the photomask. The wafer is exposed to UV for 9.3 s. The mask is cleaned immediately after exposure with acetone to remove Shipley, and IPA to remove drying marks.
- The wafer is developed in Microposit MF-319 Developer (a solution of $\sim$ 2.5 % tetramethylammonium hydroxide (TMAH) in water) for $\sim$ 40 s, or until the exposed regions have fully developed, and then rinsed in water to stop the reaction [172]. The wafer is dried with compressed air to avoid

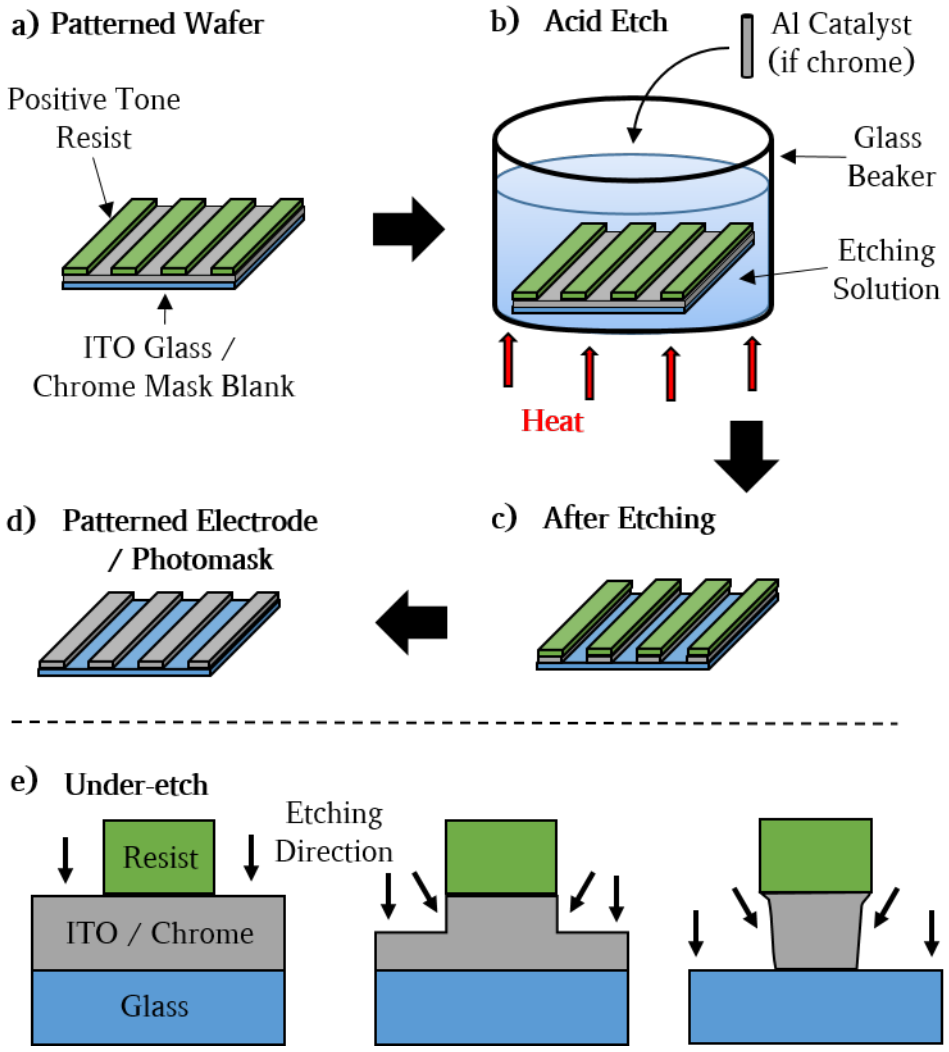

Figure 3.11: The etching process for ITO glass and a chrome mask blank. a): A patterned wafer is prepared on an ITO wafer. It is essential to post bake this before submerging in the acid bath. b): The wafer is submerged in an acid bath, made of 1 : 1 : 1 solution of water, glycerol and dilute HCl (37 % in water). A low heat is applied to maintain constant etching rates. An aluminium catalyst is used for etching chrome. c): The wafer is removed from the acid bath, and rinsed in water. The resistance of the etched regions is confirmed to be zero before continuing, otherwise continue etching. d): The photoresist is removed with acetone. e): A schematic of under-etch, resulting in smaller than expected features.

drying marks, which may interfere with the acid etch. Note that a PEB is not required prior to this development step.

- The wafer is hard baked at 150 $^{\circ}C$ for 15 $mins$. This prevents delamination of the electrode fingers whilst etching.

3.6.5 Etching ITO Glass

A schematic of the ITO etching process if given in Figure 3.11. An acid bath is prepared as per Section 3.6.3. An iron (Fe) catalyst can be used to speed up the reaction, however this is found to etch the IDEs too quickly producing uneven width electrodes. Therefore the wafer is submerged in the etching solution for ~ 75 $mins$, or until etched sufficiently. Care should be taken not to etch the ITO too little as this leads to short circuiting. The etch is complete when no resistance can be measured with an ohmmeter over the etched regions (the wafer must be removed and dried first). If the ITO is etched for too long, the electrodes become "under-etched", whereby the etch begins to strip under the photoresist leading to thinner than predicted electrodes. There will always be a small amount of under-etch using wet etching, as shown in Figure 3.11e. Once the etch is complete, the reaction should be terminated by rinsing with water. Shipley S1813 should be removed with acetone, the IDEs singulated, and cleaned as per Section 3.2.3.

Figure 3.12 shows the etching rate of the ITO glass in the acid bath. There is a large amount of error in the etch times over 4000 s as the etch can be quite uneven over the wafer, which is why the resistance should be checked before terminating the etch.

3.6.6 IDE Analysis

The IDEs were measured for their uniformity and ITO thickness using surface profilometry. The average width of IDEs fabricated using this method are $7.9 \pm 0.7 \mu m$. The high error in this result is due to variations in the rate of the etch between samples, and variations of the etch on individual samples. The

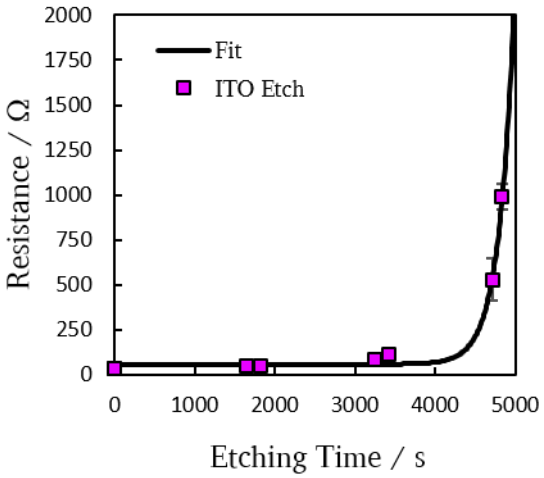

Figure 3.12: The etching rate of ITO glass in a 1 : 1 : 1 ratio mix of water, glycerol and hydrochloric acid (37 % HCl in water). The resistance is measured by taking the wafer out of the etching solution and drying. The etching uniformity is low close to the end of the etch, as can be seen by the large error bars above 4000 s. The uniformity can be increased by continuously agitating the solution during the etch and controlling the temperature of the etchant.

mask also has variations in the electrode finger width from the etch, which exacerbate the variations in the replicated IDEs. The ITO thickness after etching was measured to be $0.105 \pm 0.005\ \mu m$.

3.7 Vapour-Phase Silane Deposition

Of particular interest to this study is the homeotropic alignment of FLCs on a surface-relief grating embossed onto IDE substrates. For this reason spin coating is not considered a viable option, as the process is designed to coat flat surfaces uniformly and so resulting in uneven alignment over structures. Therefore the vapour-phase deposition of trichloro-octyl silane (C_8) was used. The chemical structure for C_8 is shown in Figure 3.13a. The silane uniformly covalently bonds

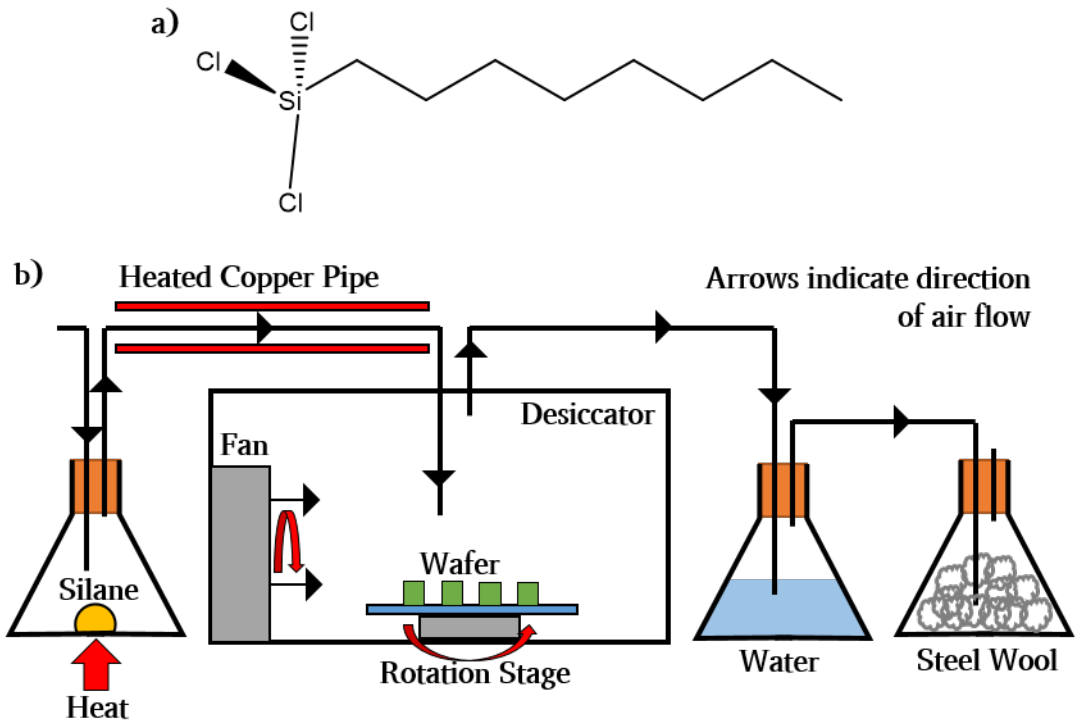

Figure 3.13: a): The chemical structure of trichloro-octyl silane (C_8). The silane forms covalent bonds with the substrate due to its reactive chlorine (Cl^-) groups. These react with surface hydroxyl groups (OH^-) of impurities in the substrates photopolymers, forming hydrochloric acid (HCl). The C_8 molecules then form Si-O-Si bonds between one another to form a uniform monolayer, which gives good homeotropic alignment to LCs. b): A schematic diagram of the vapour phase silane deposition chamber. Compressed air is passed through the rig from left to right at 0.01 $m^3 s^{-1}$. A drop of silane is added to the evaporation chamber, and heated at 80 $°C$ to vaporise it. This then passes though a heated copper pipe (to prevent it condensing) and into the desiccator, where it can react with the wafer. Unreacted silane and HCl exit the desiccator and dissolve in the water bath, and any remaining by products react with the steel wool. The initial volume of C_8, temperature vaporised at and the length of time the reaction is allowed to run determine the quality of the monolayer on the wafer.

with the substrates, either SU-8, PP2, glass or ITO. The substrates have impurities with OH^- binding sites with which the silane will bond, forming hydrochloric acid (HCl) [170, 174]. The rate of the reaction is controlled so that the silane forms a monolayer. Once a covalent bond is formed, Si-O-Si bonds start to form between silanes, eventually building up to form a monolayer over the substrate. Following this, condensation reactions forming a polymer above the surface begin [174]. Therefore it is important to control the rate of silane reaction so that a monolayer is formed, and clumps of polymer don't. The deposition chamber works as follows, and is shown schematically in Figure 3.13b.

Substrates are first exposed to the UV-Ozone cleaner for 5 $mins$ immediately before exposure (see Section 3.2.3). They are then placed in the deposition chamber on the rotating sample holder, which rotates at 10 rpm. This chamber is sealed with PTFE tape to ensure no silane can escape. If there are no leaks in the rig, bubbles should flow through the water in the HCl capture flasks when the air flow is turned on. The C_8 silane is then added (20 μL) to a heated beaker at 80 $°C$ where it is evaporates and passes through the rig via air flow provided at approximately 0.01 $m^3 s^{-1}$. This was the minimum airflow that produced visible air bubbles flowing through the water trap shown in Figure 3.13b. The silane passes into the deposition chamber where it can react at a controlled rate with the substrates. The remaining vapour exits the chamber through the chlorine capture system, where the vaporised silane either dissolves in water or reacts with the steel wool, to prevent it entering the lab. The amount of silane that deposits on the substrate is controlled by varying the time of the exposure. The substrate is then removed from the rig and baked at 180 $°C$ for 1 hr to complete the reaction, strongly bonding the silane to the substrates. Meanwhile the rig is thoroughly cleaned with IPA to remove the build-up of silane, and so ensure repeatable reaction rates.

An exposure time of 5 $mins$ creates a monolayer of silane that gives homeotropic alignment to SCE13*, with a surface roughness of < 1 nm [170]. This process was not varied throughout this study, although can be considered to change the surface anchoring energy. The anchoring strength of C_8 is expected to be

$1.5 \times 10^{-4}\ Jm^2$ [170].

3.8 Cell Construction

Cells are constructed as follows:

- Pattered ITO glass is cut to size (IDEs are $\sim 2 \times 2\ cm^2$) and cleaned following Section 3.2.3.
- If required substrates have microstructures embossed onto them using PP2 (Section 3.5), or permanent features are made in SU-8 using the DWL following Section 3.3.3.
- Substrates are surface treated:
  - Homeotropic alignment induced by silane was applied following Section 3.7.
  - Planar alignment was obtained by spin coating the polyimide SE3510 (Nissan Chemical Corp.) dissolved in n,n-dimethylformamide (66 %/34 %) at 3000 rpm for 60 s, and baked at 180 $°C$ for 1 hr. The surface was rubbed to induce microgrooves to give a directionality to the **n**-director.
- Cell gaps are determined by applying a mixture of glass micro-spheres of known diameter dispersed in UV-curable glue to two edges of one substrate. The opposing substrate is aligned by eye on top, where the treated surfaces face one another. The cells are either sealed in a vacuum bag, or placed between crocodile clips to ensure that an even cell gap is maintained over the active area, of gap determined by the diameter of the spacer beads. The cells are cured in a UV light-box for 10 to 20 $mins$ ($2.5\ mW cm^{-2}$), or until the glue is cured. The active area of the cells was covered with aluminium foil to prevent damage to the alignment layers during the UV exposure.

- Once the cell is constructed, the edges for electrode bonding are cleaned with acetone to remove residual alignment layers, or a scalpel can be used to remove photopolymer if necessary. Wires are connected to the electrodes using an indium solder.

- Finally, the device is capillary filled with the chosen LC. It is usual to fill in the nematic or isotropic phase, as smectic phases are particularly viscous.

Once the cell is constructed, it can be used for analysis. A schematic diagram of a standard test cell was shown in Figure 2.5 in Section 2.1.7.

Devices are capillary filled with the LC materials in the N or I phase to lower their viscosity, particularly important for smectic materials. This can provide poor alignment as the filling direction and therefore flow of the material may influence its alignment within the device. Therefore devices are heated into the I phase and controllably cooled before observations are made. Vacuum filling is not used due to the small amount of the smectic material available.

3.8.1 Cell Gaps

The cell gaps are determined by the size of the spacer beads, but tend to vary from the expected values due to processing limitations (dust, and human error associated with clamping two pieces of glass with glue). The cell gap is determined using reflection spectroscopy on a reflection microscope, and should be determined before the device is filled with LC. First, dark and bright states are determined through the reflection spectra of black tape (low reflection intensity) and a mirrored surface (high reflection intensity), which are set as 0 % and 100 % intensity respectively. The reflection spectra of the empty cell is then measured by placing the cell on the dark surface and observing the interference spectra due to reflections within the air filled gap. The gap is determined using:

$$d = \frac{m\lambda_1\lambda_2}{2(\lambda_2 - \lambda_1)} , \tag{3.2}$$

where m is the number of measured peaks (or troughs), and $\lambda_{1,\,2}$ are the wavelength position of the first and last peak (separated by m peaks). The measurement is taken at least five times over the active area and near to the glue seals of the cells to establish a mean and standard deviation for the cell gap.

3.9 Polarising Optical Microscopy (POM)

The optical textures produced by the alignment of complex LC phases are of particular interest in this work, and are best observed using transmission mode polarising optical microscopy (POM) due to their birefringent nature. The set-up is the same as for a standard optical microscope, with the important addition of linear polarisers positioned before and after the sample stage, the first (furthest from the light source) named the analyser, and the second the polariser. These polarisers can be rotated relative to one another, but in most cases (and unless otherwise stated) are aligned perpendicular, such that they allow no transmitted light through to the eye pieces or other analytical equipment (photodiode / spectrometer / camera). The order of components are:

- Light source (white light),
- Polariser,
- Sample Stage,
- Sample and Hot Stage,
- Objective (5×, 10×. 20× or 50× magnifications),
- Analyser,
- Eye Pieces, Camera, Spectrometer or Photodiode.

Reflection mode can also used, although here only to measure cell gaps (Section 3.8.1) and to quickly analyse patterned electrodes as ITO reflects in a different colour compared to glass (Section 3.6.6).

3.10 Characterisation of FLCs

First, a note and disclaimer on the SmC* material parameters. Device performance is directly related to the LC material properties, and so a material must be optimised according to the requirements of the application. The requirements for nematic materials include phase transition temperature range, refractive indices, elastic constants and elastic properties. For SmC* materials, this escalates to also include the cone angle, pitch and spontaneous polarisation, biaxiality and more elastic constants. This project does not concern developing the optimum SmC* material for use in the VGA-FLC device. It is concerned with fabricating the VGA-FLC geometry to explore whether it provides suitable alignment to a SmC* material. The FLC material used throughout this work is the commercial mixture SCE13*. It has not been optimised for the VGA-FLC geometry, and has been chosen as a well understood and characterised material. It is expected that the performance of this material in the VGA-FLC geometry can be proportionally improved using an optimised material.

SCE13* is a FLC mixture of a chiral dopant in a SmC host material, available from Merck, with the following phase transitions confirmed on cooling [175]:

$$I \xrightarrow[100.8\,^{\circ}C]{} N^{*} \xrightarrow[86.3\,^{\circ}C]{} SmA \xrightarrow[60.8\,^{\circ}C]{} SmC^{*} \xrightarrow[<\,20\,^{\circ}C]{} K\ . \tag{3.3}$$

The transition temperatures, refractive indices, elastic permittivities, elastic coefficients and cone angle are determined by the host, while the dopant determines $\mathbf{P}_s$ and R_0. It has been pitch compensated resulting in an infinite pitch immediately above the N* to SmA transition, allowing the control of uniform smectic layers to form [88, 176]. Two variants of SCE13* were available: the chiral mixture SCE13* made with only one enantiomer, and the racemic form (SCE13-R) made by mixing equal quantities of SCE13* made with an enantiomer pair. Enantiomers are a pair of molecules that are mirror images of one another and so non-superimposable, which arises from a carbon with four different moieties. In this case they are used as the chiral dopant to turn the SmC host material into a chiral SmC*, of which the handedness of the chirality depends on which

enantiomer is used (usually called left and right handed). The racemic form is neither chiral nor ferroelectric.

Importantly the two materials and their mixtures show similar phase transition temperatures ($< 0.5°C$ difference) and alignments arising from their containment and surface effects [177]. This is due to their chemical properties being identical, with the exception of their chirality and therefore inherent $\mathbf{P}_s$ [89, 177]. This is true because of the relatively small amount of chiral dopant in such mixtures, and strictly holds true for materials with a relatively low $\mathbf{P}_s$ such as SCE13* [68]. Furthermore, the smectic cone angle (θ_c) and smectic layer spacing remains constant between mixtures at the same temperatures. Therefore mixtures of SCE13* and SCE13-R only differ in their helical pitch (R_0) and magnitude of their $\mathbf{P}_s$. This will vary with both the ratio of enantiomers in the mixture, and the temperature of the liquid crystal (Equation 2.26). There is a linear dependence of both $\mathbf{P}_s$ and R_0 with the mole and weight fraction of the two enantiomers [177].

The spontaneous polarisation ($\mathbf{P}_s$) of three mixtures were measured, as well as the response times (τ_{ON} and τ_{OFF}). The refractive indices (n_e and n_o) and cone angle (θ_c) remain constant, and values are taken from the extensive literature where necessary.

3.10.1 Spontaneous Polarisation Measurements

The method determines the current flow through a planar aligned layer of FLC by applying a potential difference across a resistor positioned is series with the cell. A resistance of 10 $k\Omega$ was used in these experiments. The voltages were supplied from a waveform generator, and voltage/time measurements taken with an oscilloscope, and the temperature of the cell controlled with a Linkam hot-stage. There are three components that contribute to the current response of the FLC cell: the capacitance (I_c), resistance (I_r) and polarisation realignment (I_p). This

results in a total current flow of:

$$I = I_c + I_p + I_r = C\frac{dV}{dt} + \frac{dP_s}{dt} + \frac{V}{R}\,, \tag{3.4}$$

where V is the applied voltage, t is time, R is the resistance, and C is the capacitance. A triangular waveform was applied as described by Miyasato et al., with a voltage large enough to fully rotate $\mathbf{c}$ ($\sim 5\ V/\mu m$), and a frequency of $F = 113\ Hz$ chosen as a time period long enough to measure the current response and away from the mains electricity frequency [178]. This frequency also avoids the effect of current flow from the movement of ions in the LC material. The cells are treated with rubbed planar alignment and square etched plate electrodes with an active area of $5 \times 5\ mm^2$. The $\mathbf{P}_s$ is obtained by measuring the area (A) under the peak using the trapezium rule obtained from the current reversal technique, which is equal to twice the $\mathbf{P}_s$ of the material:

$$\mathbf{P}_s = \frac{1}{2RA} \cdot \sum_{m=1}^{m-1} \frac{(V_m + V_{m+1})}{2} \cdot (t_m + t_{m+1})\ . \tag{3.5}$$

An example of a current-reversal peak measurement is given in Figure 3.14 for 100 % SCE13* in an AP $d = 1.7 \pm 0.1\ \mu m$ cell. In addition, the application of a square waveform gives an indication of the $\mathbf{n}$ reorientation time which can then be used to calculate a rotational viscosity, although this is not reported in this Thesis [179].

Two mixtures of SCE13* and SCE13-R were prepared to obtain a large helical pitch while maintaining a small $\mathbf{P}_s$. Measurements of the $\mathbf{P}_s$ of these materials, along with the chiral SCE13* are presented in Figure 3.15, and the mixtures and fitting parameters are given in Table 3.1. A racemic mixture is 50% of each enantiomer, and the pure mixture is 100% of just one. The $\mathbf{P}_s$ has been taken to be 0 $nCcm^{-2}$ for the SCE13-R by definition. The results for the 100% SCE13* mixture compare well to the literature [175, 180, 181]. As expected, the $\mathbf{P}_s$ is

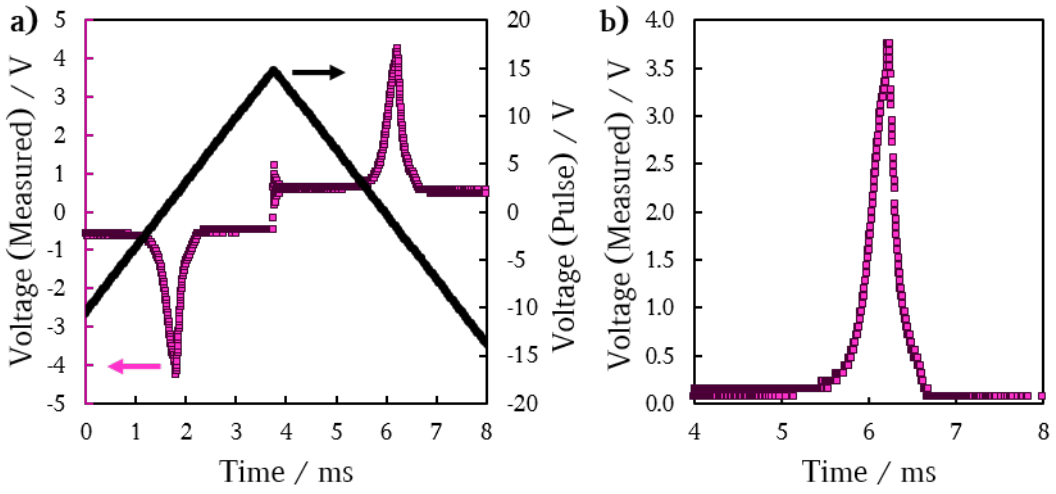

Figure 3.14: A typical dataset for the current-reversal technique for measuring the spontaneous polarisation ($\mathbf{P}_s$) of a FLC. Measurement taken at 30 $°C$ with a 113 Hz triangular waveform with $V_{PP} = 30\ V$ for SCE13* in a $d = 1.7\ \mu m$ AP cell. a): Black line: the applied waveform, Purple squares: The output voltage response. b): Data replotted to allow the area under the curve due to the $\mathbf{P}_s$ to be calculated using the trapezium rule.

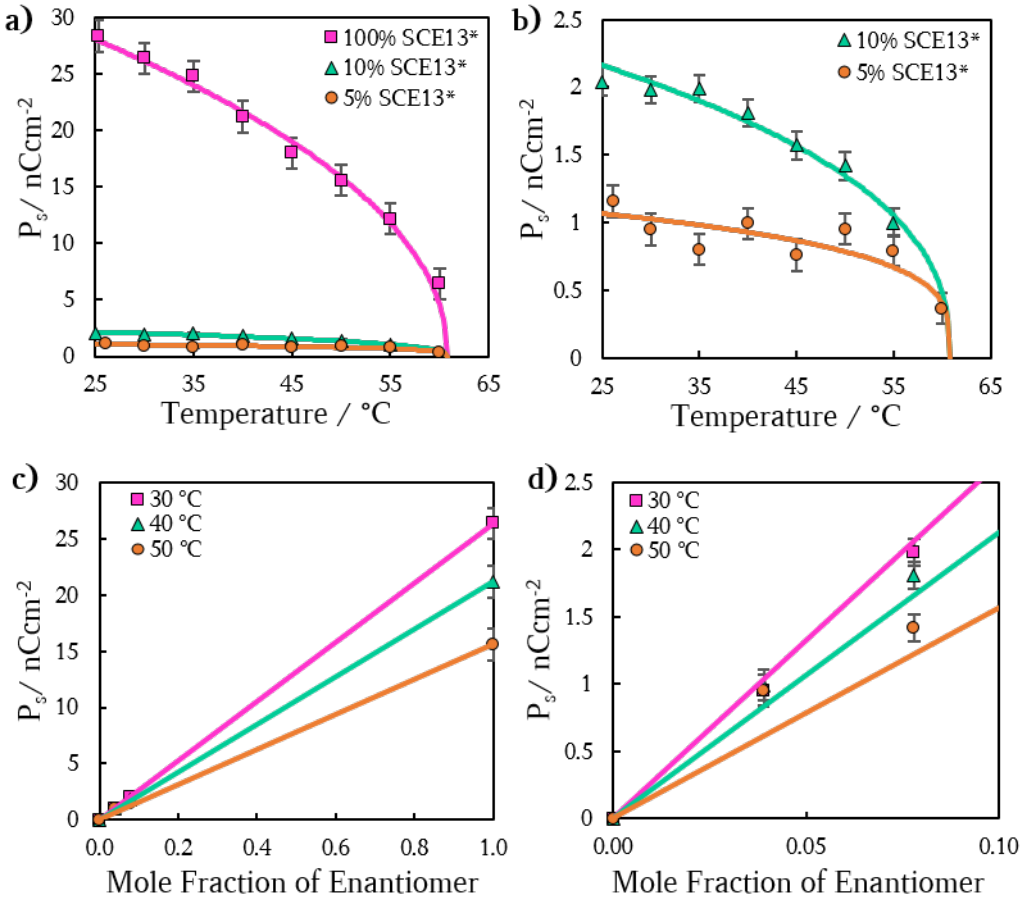

Figure 3.15: Spontaeous polarisation measurements for three mixtures of SCE13*. a),b): $\mathbf{P}_s$ plotted against temperature. Data fit using Equation 2.26, of which the fitting parameters are given in Table 3.1. c),d): $\mathbf{P}_s$ versus mole fraction of enantiomer for three mixtures as a function of temperature, showing a linear dependence with regards to the ratio of enantiomers in the mixture. 0.0 indicates that there is an equal ratio of left and right handed enantiomers (the racemic mixture, showing no $\mathbf{P}_s$), and 1.0 indicates that there is just one of the enantiomers present (the chiral mixture, showing the maximum $\mathbf{P}_s$). The gradient is equal to the $\mathbf{P}_s$ of the 100 % mixture at that temperature. The experimental errors are calculated to be 5 % for the 100 % and 8 % mixtures, and 10 % for the 5 % mixture of the maximum measured $\mathbf{P}_s$, calculated from the precision of the area measurement in Figure 3.14b and errors associated with mass measurements of the materials.

reduced by increasing R_0.

Table 3.1: The mixtures of SCE13* and SCE13-R prepared in this study, along with the fitting parameters P_0 and β used to fit Equation 2.26 to the measured data.

d	SCE13* / %	SCE13-R / %	Ratio	$P_0/nCcm^{-2}$	β
1.7 ± 0.1	100	0	1	6.6 ± 0.4	0.39 ± 0.02
1.6 ± 0.1	8.3 ± 0.7	91.7 ± 0.7	0.083	0.53 ± 0.05	0.39 ± 0.03
10 ± 1	5 ± 1	95 ± 1	0.05	0.43 ± 0.06	0.25 ± 0.05

3.10.2 Transmission Measurements

Experiments were performed to characterise the textures and transmission on cooling homeotropic SmC(*) geometries. Samples were cooled at a controlled rate from the SmA phase into the SmC(*) phase, and the 550 nm optical transmission measured with a spectrometer, and plotted as a function of reduced temperature ($\Delta T = T_{CA} - T$). Bright and dark states were measured as the transmission between parallel (100 %) and crossed (0 %) polarisers in the isotropic phase of the LC devices.

3.10.3 Shock-Induced Flow

A shock was induced over LC devices by applying a downward force parallel to the substrate normal with a blunt instrument (surface area $\sim$ 0.2 mm^2) for a period of one second. The effects are observed using POM. The magnitude of the pressure was determined using an Instron 5564 tensile testing rig, performed with a static load cell with a ± 2 kN limit [182]. This could not be performed simultaneously while performing POM, and so the actual pressures applied over the devices during measurements are based on a calibrated "feel". Values for the applied forces are given in Table 3.2. The applied forces were not large enough to

cause any permanent damage to the alignment layers or substrates of NLC test cells.

Table 3.2: The measured force applied to induce a mechanical shock over LC devices.

	Measured Force / N
Low	4.0 ± 0.7
Medium	7.8 ± 0.7
High	18 ± 1

3.10.4 Response Time Measurements

A waveform generator was used to apply pulses of a given duration and voltage over a LC cell. The optical response of the FLC was measured using a photodiode and recorded with an oscilloscope. The response times were calculated from 10 % to 90 % of the maximum transmission for τ_{ON}, and 90 % to 10 % for τ_{OFF}. The waveforms and results are discussed in Chapter 8 due to the complexity of the geometry.

3.11 Summary - Chapter 3

This Chapter has introduced the experimental methods used throughout this thesis. Photolithography is discussed in detail, using techniques including direct write lithography and mask aligning. The processing procedures for both positive-tone and negative-tone photoresists are summarised, along with modifications to the recommended SU-8 processing to successfully create $< 4\ \mu m$ microstructures to alleviate cracking and delamination. Stamping and embossing methods are described to quickly and accurately replicate masters, as well as etching chrome and ITO for fabricating photomasks and IDEs respectively. The vapour-phase deposition of C_8 silane is implemented to add homeotropic anchoring conditions

to SU-8 and PP2 microstructures. The general methods for constructing cells for LC analysis are also described, in addition to the basics of polarising optical microscopy. Results are presented for the $\mathbf{P}_s$ of three mixture of SCE13* that are used throughout this work.

Chapter 4

The VGA-FLCD: A Vertical Grating Aligned Ferroelectric Liquid Crystal Device

4.1 Introduction

Thus far the ferroelectric liquid crystal (FLC) has been introduced and the role it has played in the display and electro-optic device industries has been discussed. Because of the inherent layered structure resulting in low levels of shock stability compared to NLCs, it has proven a challenge to find mainstream commercial success. Faster switching modes are in demand for modern displays and devices, which are not reachable by current NLC technologies.

FLCs have found success in enabling frame sequential colour optics in projector display applications due to their sub-millisecond response times. Such demands also exist in electro-optic devices, where FLCs can be found as diffractive optics for digital holograms, adaptive beam steering systems and polarisation gratings. High speed communication systems also demand high-speed response times, as well as stable, low-loss, and high temperature range materials, where small operating voltages and low power consumption are important, for optical components such as switches, attenuators and polarisation rotators. It is therefore of high importance to continue exploring FLCs for fast switching and

shock-resistant applications.

The concept for an electro-optic device based on FLCs is proposed in this Chapter. It aims to create a shock-resistant geometry via a homeotropic grating alignment using surface-relief gratings. These are fabricated in Chapter 5. In particular, justifications will be presented for specific design choices and how they are important for a functional device. The alignment of FLCs in the VGA-FLC geometry are characterised in Chapter 7, as well as a looking into the potential for shock-stability in such device. Prototype devices are tested for their electro-optic responses in Chapter 8.

4.2 Towards Shock-Stability in FLCs

The induced alignment and the shock-stability of planar FLCs has been explored extensively and has always been a problem regarding their usefulness in display and device applications. This was introduced in Chapter 2. If the LC material has poor alignment, or does not return to its initial alignment after electrical addressing or a mechanical shock, then the device can not find commercial success. Therefore there is an important decision to be made when choosing the alignment and device geometry when utilising FLCs. Important considerations and justifications for the proposed FLC device will be discussed in detail.

Creating shock-stable geometries for FLCs is still of utmost importance for commercially successful devices. This is particularly true for LCoS devices, where the requirements are not as stringent due to their low areas. The planar aligned SSFLC emerged in the 1980's, but was hugely sensitive to shock induced flow [183]. Figure 4.1 shows the LC texture before and after an applied mechanical pressure of a $1.7 \pm 0.1\ \mu m$ planar rubbed cell at $30\ ^{\circ}C$ filled with the commercial FLC SCE13*. SCE13 was introduced in Chapter 3, and recreates the SSFLC geometry introduced in Section 2.4.1.

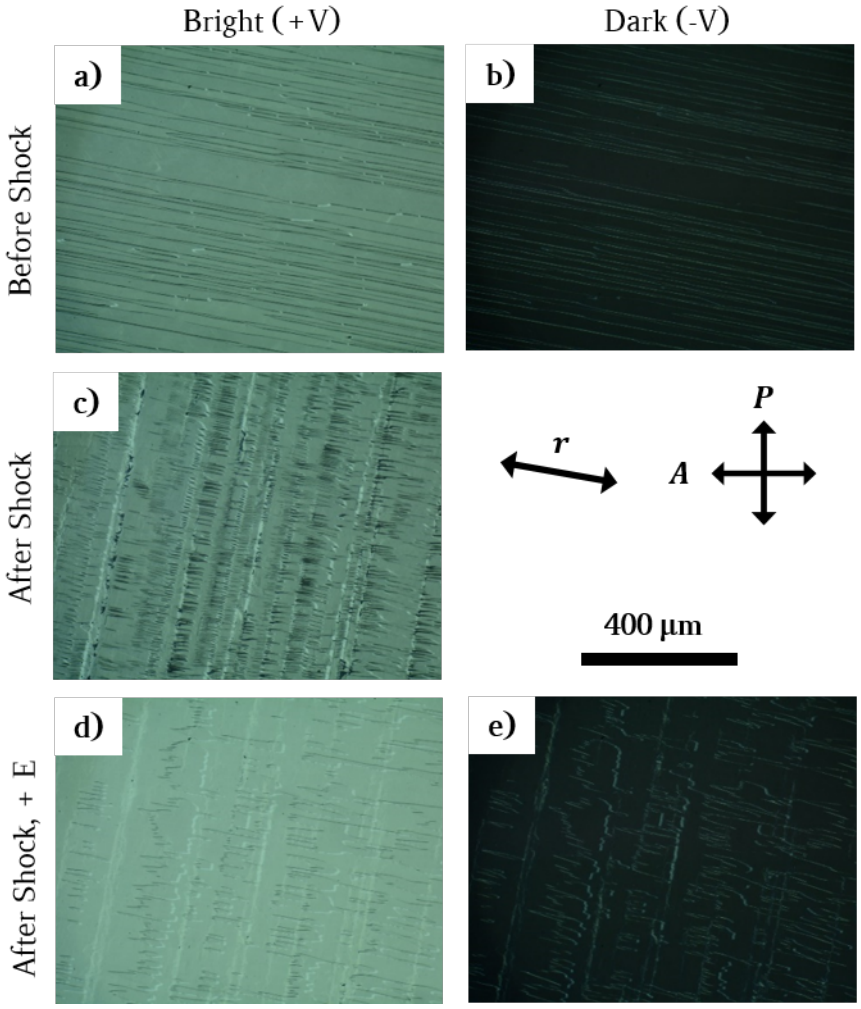
Bright (+V)
Dark (-V)
a)
b)
Before Shock
c)
After Shock
r
P
A
400 µm
d)
e)
After Shock, + E

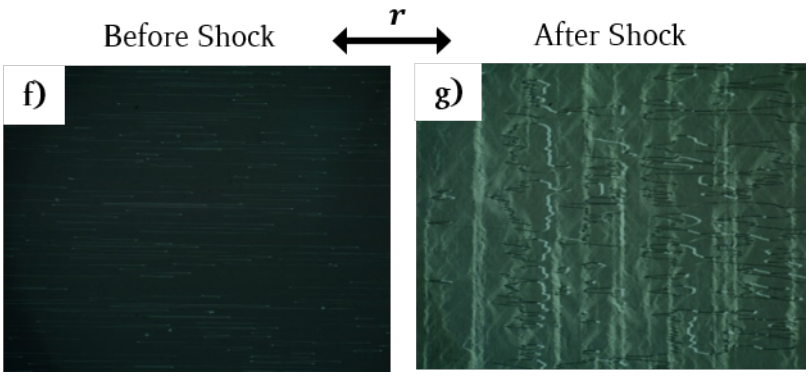

Figure 4.1: Shock induced flow to the FLC SCE13(*) in a $d = 1.7 \pm 0.1\ \mu m$ anti-parallel rubbed planar cell, at $T = 30\ ^{\circ}C$, observed using POM. a-e): The rubbing direction (r) is 10° to the analyser (A). a),b): The texture of the surface-stabilised SmC* following switching between its two bistable states with an electric field ($V_{PP} = \pm\ 5\ V$). The texture is characterised by zigzag defects separating areas of $C1$ and $C2$ chevron layer alignment. c): The bright texture following a mechanical shock. The number of zigzag defects has increased significantly, and **c**-director reorientation has occurred. This texture is stable, and does not return to the texture seen in a). d),e): The application of an electric field does not remove the zigzag defects or smectic layer disruptions, but does remove the unwanted dark textures from the bright state, by reorienting the **c**-director. f),g): r is parallel to the analyser, A. The difference in optical texture before and after shock are clear. The initial dark, high contrast alignment has been left damaged, whereby bright defects and layer distortions cause poor optical contrast. This texture can't be removed, and so this SSFLC alignment is highly susceptible to shock induced flow.

The POM image initially shows good alignment in the SS SmC* phase. The smectic layer normal (**k**) is arranged perpendicular to the substrates, and the director (**n**) lies in the x, y-plane normal to the layers. A needled texture is observed due to the anti-parallel rubbed surface alignment [184]. A mechanical pressure is applied to the cell in Figure 4.1c which results in a reorientation of the **c**-director and smectic layers. Not shown is the induced flow or shear to the FLC whereby the temporary reduction in cell gap causes the volume of liquid in the observed area to decrease, which then 'springs' back on the removal of the force. Noticeably, many more zigzag defects appear in the liquid crystal texture as the layers have not returned to their initial alignment. Following the mechanical shock, these regions remain in the texture, which is to say, this new orientation of disrupted smectic layers is stable and so won't return to their initial ordered alignment. The increase of dark and bright regions in Figure 4.1c indicate that the **c**-director has also been reoriented and not returned to its initial alignment. The zigzag defects remain on the application of an electric field over plate electrodes (appearing dark or bright). On removal of the field, the bright and dark regions return to a state of poor alignment whereby some combination of layer and **c**-director disruption has occurred. Figure 4.1 f) and g) clearly show that the initial dark and high contrast alignment has been permanently disrupted. The planar aligned SSFLC is therefore susceptible to shock induced flow.

Attempts have been made to stabilise this planar SSFLC geometry, such as introducing photocurable monoacrylates to polymer stabilise the SmC* phase to remove the formation of zigzag defects, which also removes the bistability of the device [185]. Other methods to increase the materials resistance to shock induced flow include introducing polymer walls or arrays of columnar spacers to the device, which aim to add structural support to the device to resist shock induced flow to the liquid crystal [186, 187]. Unfortunately such structures lead to a significant increase in operating voltages to achieve the same response times as expected in a FLC, and tend to induce non-uniform fields over the liquid crystal layer [188]. Another option is to synthesise materials that won't tend to form chevrons from the bookshelf structures buckling from the SmA phase, for example de Vries materials that have a constant layer spacing over a wide temperature

range through the SmA and SmC* phases [81–83]. Such materials come with other non-conventional properties such as a lack of nematic phase causing difficulties in alignment so causing difficulties obtaining defect-free devices [81–83].

The homeotropic alignment of FLCs has proven to be successful as an alternative to the planar aligned examples with regard to shock resistance [189, 190]. Homeotropic alignment has however received much less interest than planar alignment, likely due to the requirement of interdigitated electrodes (IDEs) to switch the **c**-director in the plane of the cell [189, 190]. The inactive areas above the IDEs don't respond to applied electric fields and so have been used to position columnar spacers to add mechanical stability to the devices [188, 191]. This geometry was used with the FLC in the deformed helix mode (VADHFLC) and was shown to be stable against external bending of this flexible device [188]. Figure 4.2 shows the surface-stabilised homeotropic alignment of the FLC SCE13* in a non-rubbed $d = 9.8 \pm 0.1\ \mu m$ cell, and rubbed $d = 20 \pm 1\ \mu m$ cell. To ensure a surface stabilised alignment with no chiral domains, a mixture of 8% SCE13* and 92% SCE13-R (see Table 3.1) was used to ensure $4d < R_0$.

The **c**-director has no preferred direction to tilt without rubbing the homeotropic alignment when slowly cooling from the SmA due to a 90° pre-tilt. This results in a schlieren texture under POM of Figure 4.2a. Rubbing the homeotropic alignment induces a directionality to the **c**-director as the pre-tilt is reduced by around 0.5° to avoid poor smectic layer alignment [192]. Compressions and shear induced flow are applied to the smectic layers on the application of a mechanical pressure that are characterised by the appearance of a darker texture of layer undulations (Figure 4.2d). Given time the layers will flow back to their original homeotropic alignment, albeit with some **c**-director reorientation. In-plane electric fields will rotate the **c**-director to align perpendicular to the applied field direction, but will return to the previous schlieren texture state once the field has been removed. However, after prolonged electrical addressing, the **c**-director will tend to align permanently in the direction induced by the field due to a lack of strong initial **c**-director anchoring, and so will not relax back. Therefore homeotropic smectic alignment shows good resistance to compressions and shock-induced flow as the

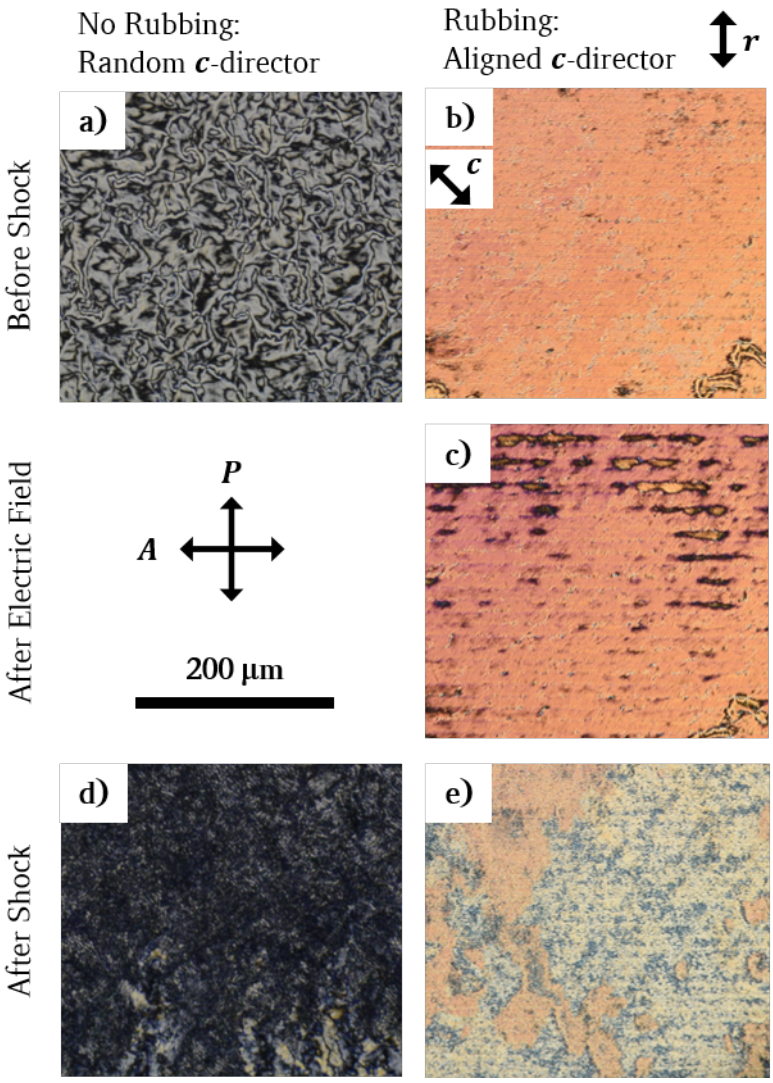
No Rubbing:
Random c-director
Rubbing:
Aligned c-director
r
a)
b)
c
Before Shock
After Electric Field
P
A
200 µm
c)
d)
e)
After Shock

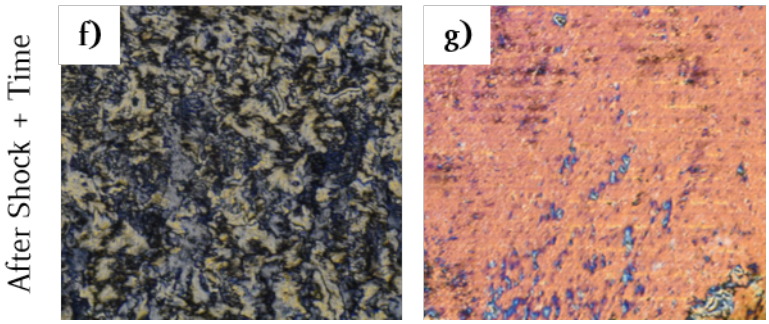

Figure 4.2: The homeotropic alignment of SCE13(*). Both devices are made using octyltrichlorosilane (C_8) to induce homeotropic alignment, as described in Chapter 3. The devices are filled with a 1 : 4 ratio of SCE13* and SCE13-R to reduce the helical pitch to obtain a surface-stabilised state. a): $d = 9.8 \pm 0.1\ \mu m$, non-rubbed alignment, where **c** has no preferred alignment direction, and so forms a schlieren texture. b): $d = 20 \pm 1\ \mu m$, rubbed alignment, where **r** indicates the rubbing direction, and **c** the **c**-director alignment direction. Interestingly, **c** has aligned at 45° to the rubbing direction. c): The application of an electric field reorients **c** to align perpendicular to the field, however eventually **c** will begin to favour this direction of alignment and not return to the position defined by the rubbing direction. d),e) A mechanical shock induces undulations to the smectic layers due to compressions and flow, resulting in a state of poor alignment. f),g) A few seconds after the shock, the undulations dissipate as the layers return to their previous orientation, however the **c**-director orientation has been disrupted.

layers are not permanently disrupted. However there must be a strong, favourable alignment for the **c**-director to relax back to otherwise the contrast of the device will be lost on continual shocks or electrical addressing.

It is important to understand why the homeotropic geometry is more shock stable than the planar geometry. This is related to how the pressure is applied to the device and the resulting induced LC flow. If a pressure is applied to just one surface of the LC cell, a bend to the upper substrate is induced, reducing the volume below it relative to the opposite substrate. If this space is filled with a LC, it must flow away from the compression to allow for this volume change. When the pressure is released the LC will then flow in the opposite direction to refill the initial volume. For a planar aligned NLC, it is reasonable to assume that the **c**-director will align with the direction, or streamlines, of the flow. It is expected that the NLC will return to its initial alignment assuming there has been no damage to the alignment layers which is determined by the anchoring conditions. This is due to the ease at which the NLC can reorient back to its minimum elastic energy state. This holds true for vertical alignment. To confirm this, press a calculator or watch display (must be a TN) with your finger, and the same effects can be observed. It will return back to it's initial alignment restoring the contrast ratio of the device.

For the smectic phases, this shock process has an additional component: the smectic layers. Once disturbed, the smectic layers require a much higher energy to return to their previous alignment. They will remain in a disturbed state rather than flow back to align with the induced alignment determined by the anchoring conditions. In a planar alignment with an applied pressure, the volume filled by the smectic layers will be compressed, and so to accommodate this, will be subject to flow and shear. On removal of the pressure, the layers will remain disrupted as the flow restores to fill the initial volume. Such effects are clearly demonstrated in Figure 4.1 f) and g), whereby the initial dark texture becomes bright due to poorly aligned smectic layers. The effect of shock induced flow on planar SmC* has been widely investigated. It is observed that the layers are tilted to align perpendicular to the direction of an induced shear [183, 193–196].

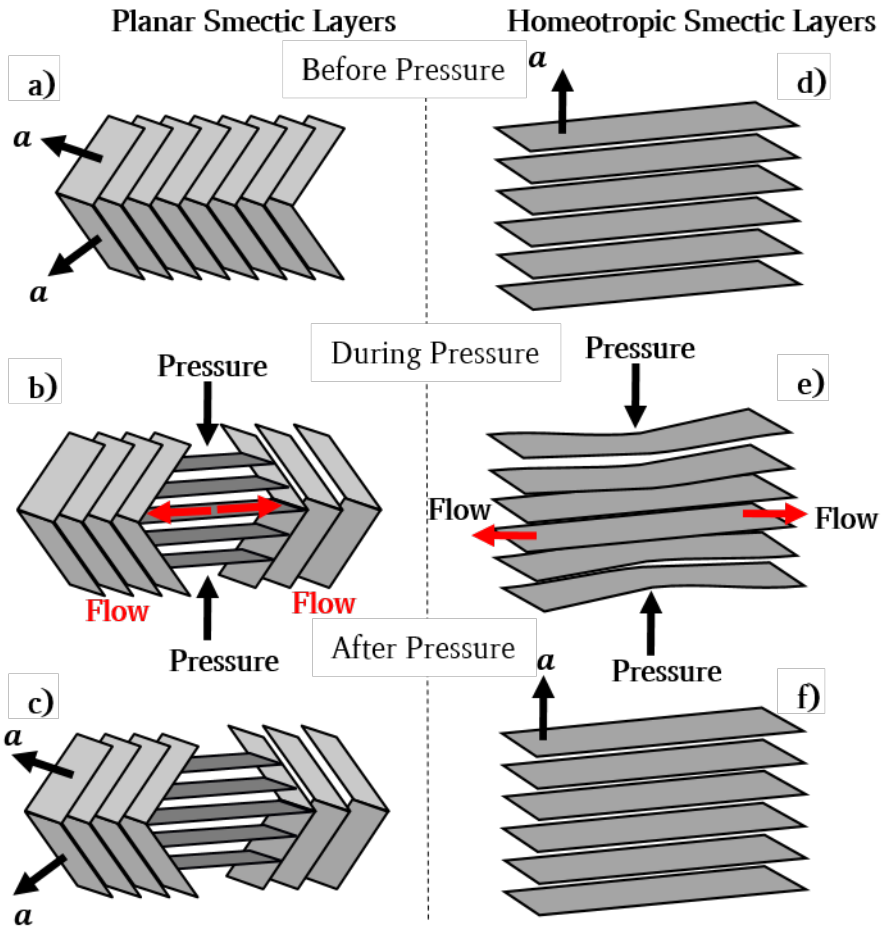

Figure 4.3: A schematic diagram of how the planar and homeotropic alignment of smectic layers responds to a pressure, or shock-induced flow. a-c): The planar alignment tends to form a bookshelf or chevron geometry, and with a sufficient shock will flow towards the homeotropic geometry. The layers become permanently displaced, and will not return to their initial alignment unless heated and cooled back to the SmC* phase. d-f): The homeotropic layers respond to shock induced flow by compressing and flowing over one another, rather than flowing into a planar geometry. Once the pressure is removed, the layers return to their initial alignment. Therefore the homeotropic geometry is less susceptible to shock induced flow than the planar geometry.

In the homeotropic smectic geometry, the layers will compress with a pressure, but the flow will not reorient the layers significantly as the layers are already aligned perpendicular to the induced direction of shear flow [197, 198]. The layers will then return to their initial homeotropic alignment following the force removal, shown in Figure 4.2. These two mechanisms are shown schematically in Figure 4.3. Interestingly, above a threshold shear rate, the smectic layers will begin to buckle, or undulate, in the centre of the cell (the point furthest from the surface anchoring) [197, 199]. The wave vector for these undulations is perpendicular to the direction of shear in the homeotropic geometry. This means that in the planar geometry, as well as layers shearing towards a homeotropic geometry, induced undulations will cause further unrecoverable reorientations to the layers. For the homeotropic case, the layers will realign back to their initial alignment once undulating, as demonstrated experimentally in Figure 4.2. Such undulations are also naturally induced while cooling a homeotropic smectic, as the layers will tend to buckle under stress before forming new layers to accommodate the layer thickness (d_C) decreasing on reducing cone angle (θ_C) [200]. This is not observed in planar alignment as chevrons form to accommodate for the layer shrinkage. To prevent permanent smectic layer deformations arising from shock induced flow these mechanisms suggest that the homeotropic geometry is naturally the most resilient.

4.3 The VGA-FLC Device Idea

A device geometry is proposed for creating a shock-stable and fast-switching FLCD as shown schematically in Figure 4.4. The vertical or homeotropic alignment geometry for smectic layers is the most promising in terms of natural resistance to shock, whereby the layers will compress and slide to return to their initial alignment, rather than rotate and stick in an unfavourable, tilted alignment. It is essential that the FLC **c**-director remains aligned after continuous electrical addressing and following shock-induced flow. To achieve this, low amplitude, low pitch surface-relief gratings are positioned on opposing surfaces of the device, aligned such that the grating vectors, **g**, are parallel. The gratings are treated

by vapour-phase deposition of silane to induce uniform homeotropic anchoring to the nematic, SmA and SmC* phases, described in Chapter 3. The gratings aim to serve two purposes;

- Providing controllable alignment of the **c**-director when cooling from the SmA phase and defining the dark/OFF state,
- Anchoring the **c**-director to a predefined orientation to which it returns when disturbed by an applied electric field or mechanical shock.

The gratings should have an optimum amplitude and pitch to avoid disruptive undulations in the bulk of the smectic layers. If the pitch is too large, or amplitude too small, the gratings will have no obvious effect to the SmC* alignment, leading to schlieren textures observed in Figure 4.2. On the other hand, if the amplitude is too high, or pitch too small, the surface will induce large disruptions to the smectic layers in the bulk. This will lead to a frustrated texture with low contrast, and possibly unable to be effectively electrically addressed. It was found that the optimum peak-to-peak amplitude was approximately $0.2\ \mu m \lesssim A_{PP} \lesssim 0.4\ \mu m$. This is discussed further in Chapter 7. The minimum pitch that could be fabricated was 4 μm, which was kept constant throughout this work (see Chapter 3).

A schematic of the device is shown in Figure 4.4. The orientation of parallel surface-relief gratings creates a uniform **c**-director through the device, and importantly satisfies the surface stabilisation requirement of $4d < R_0$ to ensure a suppressed helical twist (see Figure 4.4a). No light is transmitted when **g** is positioned with the director parallel to either the polariser or analyser when crossed and so appears dark. This is the OFF state of the device. The direction of **c**-director alignment relative to **g** in essence doesn't matter, as the gratings can be positioned either parallel or perpendicular to the induced electric field (**E**) direction produced by IDEs. However, the **c**-director should have a strong preference for the direction in which it aligns with **g** to avoid multiple domains forming when cooling into the SmC* phase, and following a mechanical shock. In this case, **g** is positioned perpendicular to **E**, seen in Figure 4.4b.

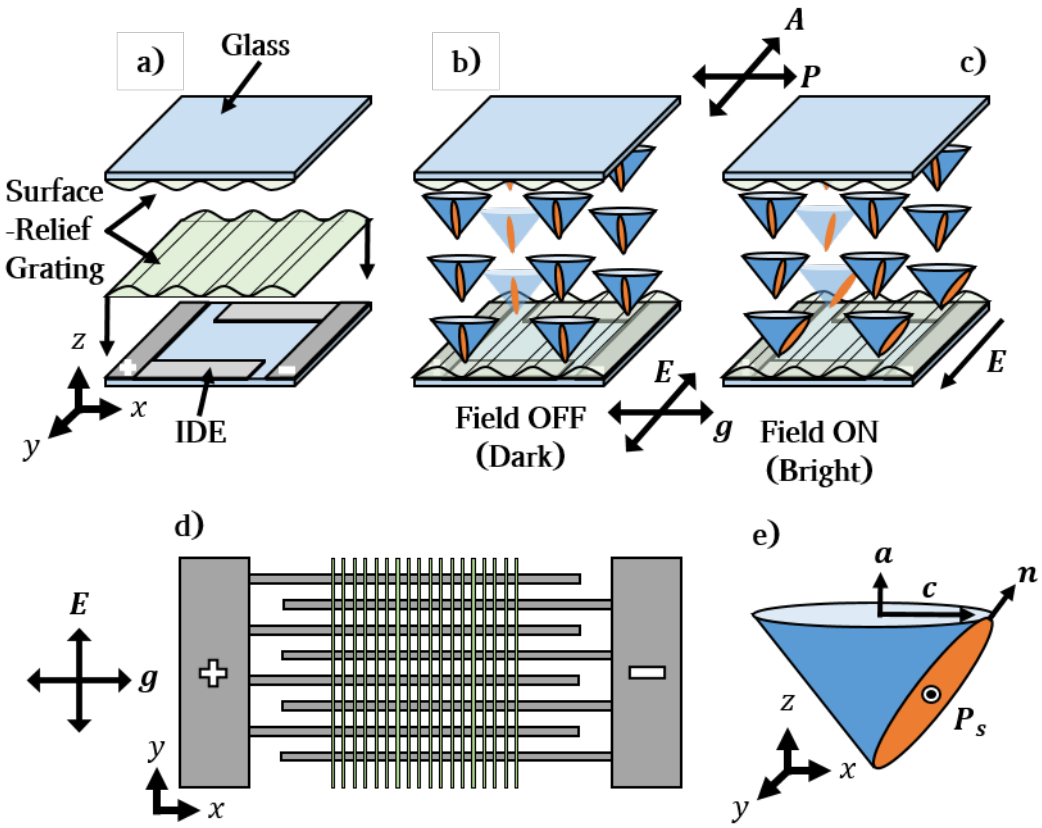

Figure 4.4: A schematic diagram of the VGA-FLC Device. a): Surface-relief gratings are embossed on to the two surfaces of the cell, one of which is an IDE, the other has no electrode. b): In the OFF state, the **c**-director is surface stabilised through the cell, and controllably oriented by the gratings, such that **g** is perpendicular to **c**. This creates a dark state for the device when viewed with POM. c): To switch to the ON state, in-plane electric fields are applied to induce a 90° twist of the **c**-director through the device. This creates a bright state, if the correct cell gap is chosen to satisfy the Gooch-Tarry equation (Equation 2.64). d): The grating vector, **g**, is aligned such to be perpendicular to the applied electric field , **E**. This ensures that the spontaneous polarisation vector, $\mathbf{P}_s$ will respond to the electric field, as allows a 90° twist though the device. e): A sketch of the SmC* mesogen for reference, where **a** is the layer normal and **n** the director.

The device is addressed with in-plane electric fields from IDEs positioned on one substrate. The grating is embossed on top to remove any potential induced alignment from the electrode pattern. This is shown in Figure 4.4d. The IDE's are designed and fabricated as described in Chapter 3, Section 3.6. They should have a width of $w = 10\ \mu m$, gap of $l = 20\ \mu m$, with an overall pitch of $p = 60\ \mu m$, with an overall electrode active area of $A = 5 \times 5\ mm^2$.

The electric field rotates the **c**-director 90° through the depth (z-direction) of cell (Figure 4.4c) to satisfy the Gooch-Tarry Equation for a TN (Equation 2.64). This switches the device from a dark OFF state to a bright ON state. This ON state is analogous to the OFF state of a TN display, except here it is the **c**-director twisting through 90° rather than the **n**-director, with homeotropic and not planar alignment [15]. The biaxiality of the SmC* is considered negligible. Grayscale can be achieved by varying the applied voltage to a value below that which creates a 90° **c**-director twist. Removal of **E** results in the **c**-director naturally relaxing to realign with **g**. This should be proportional to the rotational viscosity (γ_ϕ) of the **c**-director within the smectic layer. If the negative voltage is applied, that is, the positive and negative electrodes are reversed, the **c**-director should rotate 90° in the opposite direction and so creating an optically identical ON state with opposite twist. The device can be addressed with a pulse of the opposite voltage to return the **c**-director to a state of zero total twist. If too long a pulse or high a voltage is applied, the **c**-director will twist in the opposite direction back towards a bright state. It is important to ensure that the device switches at low electric fields to ensure that the layers are not distorted, and also such that the device may find commercial success as high driving voltages are not ideal. This device is not bistable, as with no applied electric field the **c**-director will naturally return to its OFF state.

This is the first time surface-relief gratings have been considered for the alignment and shock-stability of FLCs. The surface-stabilised state has been chosen as it will aid the understanding of the induced alignment on the smectic layers and the effect on the FLC **c**-director. It is also beneficial as mixtures of SCE13* and SCE13-R can be easily made to change the FLCs helical pitch without changing

its material properties, which are well characterised and understood in the literature. SCE13 is introduced in Section 3.10. Understanding and characterising this device is the main focus for this thesis.

4.4 The VGA-FLC Device Theory

The optimum d for the device must first be calculated to enable the device to switch between states of maximum and minimum transmission. It is important to recall from Chapter 2 that the tilt angle, or cone angle (θ_C) of the smectic director is temperature dependent (Equation 2.25). So as temperature decreases, the cone angle increases, which decreases the helical pitch (R_0) [201]. Therefore it is important to ensure that over the operating range of the device that R_0 satisfies $4d < R_0$ to avoid chiral domains forming.

The optimum d requires calculation of the effective birefringence (Δn_{eff}). The refractive indices for SCE13* are taken from the literature [202]. The effective birefringence (Δn_{eff}) of a tilted liquid crystalline material is calculated using Equation 2.10:

$$\frac{1}{{n_{eff}}^2} = \frac{\sin^2\theta_c}{{n_o}^2} + \frac{\cos^2\theta_c}{{n_e}^2} \; ; \; n'_o = n_o \; , \tag{4.1}$$

which leads to an effective birefringence of:

$$\Delta n_{eff} = n'_e - n_o = \frac{n_e n_o}{\sqrt{{n_e}^2 \sin^2\theta_c + {n_o}^2 \cos^2\theta_c}} - n_o \; , \tag{4.2}$$

where n_e and n_o are the extraordinary and ordinary refractive indices respectively. For SCE13*, $n_e = 1.67$, $n_o = 1.49$ and $\Delta\theta_c = 22.3°$ at $30°C$ [202, 203]. Therefore at $30°C$, $\Delta n_{eff} = 0.022$. As the temperature is varied, the cone angle will vary. For example, between $20°C$ to $50°C$ there is a $10°$ angle change, which results in a birefringence variation of 0.008 to 0.025. Following from the equation for a birefringent retarder (Equation 2.48), the surface-stabilised, homeotropic

SmC* phase appears dark when the **c**-director is aligned at 0° between crossed polarisers. For SCE13* at 30 $°C$ to appear white at a rotation of ±45°, a cell gap of $d = 6.3\ \mu m$ is required, which is $> 3\times$ that required for the planar SSFLC geometry [28].

For practical operation, the first minimum ($m = 1$) should be chosen of the Gooch-Tarry minimum (Equation 2.64). Values of $m > 1$ require larger values of d, which is undesirable as the thicker the LC layer, higher operating voltages are required and homogeneous alignment becomes more difficult. The VGA-FLC device operating with surface-stabilised SCE13* at 30 $°C$ requires a cell gap of 22 μm to satisfy the first order minimum for maximum transmission between crossed polarisers.

4.4.1 In-Plane Switching of a Homeotropic FLC

Now that the optimum transmissions of the OFF and ON states of the VGA-FLC device have been calculated, the mechanism by which the ON state will be obtained must be discussed. Figure 4.4 shows that one set of IDEs positioned below the surface-relief grating will be used to induce a 90° twist through the device to create the ON state, with maximum transmission between crossed polarisers at a cell gap of 22 μm at 30°. For ease of both device fabrication and understanding the effect of the electric fields on the homeotropic SmC*, simple comb-like electrodes will be considered over more complex arrangements such as zigzags configurations. These complex electrodes can be considered for increasing the viewing angle of VGA-FLC devices, which is beyond the scope of this project [204]. It is important to note that this VGA-FLC geometry is naturally multi-domain due to the **c**-director twisting in opposite directions over the electrodes (see Figure 8.3), which is a technique used to further increase viewing angles in VAN displays [36]. This device geometry coupled with complex electrodes should satisfy high viewing angle requirements.

The electric field produced by IDEs is much more complex than those produced by simple plate-electrodes. For device functionality, the in-plane component of the field is important at the point furthest from electrodes, but the fields are strongly inhomogeneous close to the electrodes which also vary in the z-direction (parallel to the substrate normal) [205]. The x, y, z-geometry is shown in Figure 4.4, whereby z is normal to the substrate. Only variations in two directions (y & z) are considered, and so this is strictly a 2D model. This is acceptable for the simple comb-like IDE geometry, as effects near the ends of the electrode fingers are not important for device operation. Ignoring liquid crystal permittivity, setting $E = -\nabla\Phi$ and $z \geq 0$, the field in 2D is given by [205]:

$$E_y(u, v, \delta) = \frac{\Phi_0}{l} \sum_n A(n, \delta) \frac{n\pi}{1+\delta} \sin\left(\frac{n\pi y}{1+\delta}\right) \exp\left(-\frac{n\pi v}{1+\delta}\right) ; \tag{4.3}$$

$$E_z(u, v, \delta) = \frac{\Phi_0}{l} \sum_n A(n, \delta) \frac{n\pi}{1+\delta} \sin\left(\frac{n\pi y}{1+\delta}\right) \exp\left(-\frac{n\pi v}{1+\delta}\right) ; \tag{4.4}$$

$$A(n, \delta) = \frac{4}{n\pi} \sin\left(\frac{n\pi}{2}\right) \left[2\left(\frac{1+\delta}{n\pi}\right) \sin\left(\frac{n\pi}{2(1+\delta)}\right) - \cos\left(\frac{n\pi}{2(1+\delta)}\right)\right] , \tag{4.5}$$

where Φ_0 is the electric potential, $u = \frac{y}{l}$, $v = \frac{z}{l}$ and $\delta = \frac{w}{l}$, where l is the electrode gap and w the electrode width, and $A(m, \delta)$ is an expression for the Fourier factor resulting from assuming a linear dependence on y between the electrode space and the solution for the boundary value problems (essentially a constant that scales relating to the ratio of w and l) [205]. Considering just the first Fourier component of the expansion ($n = 1$) leads to:

$$E_y \sim \frac{V}{l} \sin\left(\frac{\pi y}{l+w}\right) \exp\left(-\frac{\pi z}{l+w}\right) ; \tag{4.6}$$

$$E_z \sim \frac{V}{l} \cos\left(\frac{\pi y}{l+w}\right) \exp\left(-\frac{\pi z}{l+w}\right) . \tag{4.7}$$

Averaging over the cell volume for the electric field and again taking only the first Fourier component gives:

$$\langle E_y \rangle \sim \frac{lV}{d} \sin^2 \left\{ \frac{\pi}{2} \left[1 - \exp\left(-\frac{\pi d}{(l+w)} \right) \right] \right\} \; ; \tag{4.8}$$

$$\langle E_z \rangle \sim \frac{lV}{d} \sin \left\{ \frac{\pi}{2} \left[1 - \exp\left(-\frac{\pi d}{(l+w)} \right) \right] \right\} \; . \tag{4.9}$$

Equations 4.6 and 4.7 show that the electric field over the device is periodic (y-direction), and decays exponentially across the bulk (z-direction). However, most treatments assume that if d and w are sufficiently low, the field acts uniformly across the cell plane. The result for the threshold voltage (V_c) assuming inhomogeneous fields for a NLC is therefore [205]:

$$\langle E_{y,c} \rangle = \frac{V_c . g}{l} = \sqrt{\left(\frac{4\pi K}{\varepsilon_a} \right) \left(\frac{\pi^2}{d^2} + \frac{\pi^2}{(l+w)^2} \right)} \; , \tag{4.10}$$

where:

$$g = \frac{l}{d} \sum_m A(m, \delta) \frac{2}{m\pi} \sin^2 \left\{ \frac{m\pi}{2} \left[1 - \exp\left(-\frac{m\pi d}{(l+w)} \right) \right] \right\} \; ; \tag{4.11}$$

and assuming homogeneous fields is [35, 206, 207]:

$$E^{IPS} = \frac{V_c}{d} = \frac{\pi}{d} \sqrt{\frac{4\pi K}{\varepsilon_a}} \; , \tag{4.12}$$

where ε_a is a tensor describing the LC dielectric anisotropy, and K the elastic constant. This results in the ratio:

$$\frac{E_{y,c}}{E^{IPS}} = \frac{1}{g} \sqrt{1 + \frac{d^2}{l^2 (1 + \frac{w}{l})^2}} \; . \tag{4.13}$$

Therefore a basic system for how to compare how in-plane fields vary across the device has been established, and the homogeneous solution (Equation 4.12) and the inhomogeneous solution (Equation 4.10) are compared in Equation 4.13. However, this is true for a switching a dielectric system, and so switching the device using the spontaneous polarisation must too be considered. The ratio between the two threshold's should still hold true despite the different response mechanisms.

4.4.1.1 IPS and the VGA-FLC Geometry

The VGA-FLC device can be modelled simply in 2D by considering just the **c**-director of the surface stabilised SmC*. We can assume that the smectic layers and cone angle are fixed, and the **c**-director rotates in just the x, y-plane. The OFF state of the device is also surface stabilised, so there is no helical twist through the cell, or at least the helical pitch, R_0, should be considered substantially larger than the cell gap, d. The threshold field for unwinding the helical structure with in-plane fields is given by [208, 209]:

$$E_c{}^{IPS} = \frac{\pi^4 K \sin^2\theta_c}{4 P_s {R_o}^2} \,, \tag{4.14}$$

which should be of a similar magnitude to those required to wind up the sample. In the SSFLC geometry, the threshold voltage is given as [210]:

$$E_c{}^{SSFLC} = \frac{\pi^2 K \sin^2\theta_c}{P_s d^2} \,, \tag{4.15}$$

which is of the same form, with the difference being the dependence on d over R_0, as the helix is unwound.

If viscous flow and the dielectric anisotropy contribution are neglected, and elastic isotropy assumed, a torque balance equitation for the homeotropic FLC is

given by [190, 209]:

$$K\nabla^2\varphi - P_sE\sin\varphi = \gamma_\phi\frac{\partial\varphi}{\partial t}\ , \tag{4.16}$$

where φ is the azimuthal angle of the P_s. Resolving this gives the response time, τ_{ON}, as [188, 190, 209]:

$${\tau_{ON}}^{IPS} \sim \frac{\gamma_\phi}{Kq^2 + P_sE} \tag{4.17}$$

where q is the helix wave vector, given by:

$$q = \frac{2\pi}{R_0}\ . \tag{4.18}$$

For the surface stabilised state, $P_s \to \infty$, and so $q \to 0$, resulting in the equation for the response time of the SSFLC given in Equation 2.70 [211]. The OFF time should then be related to:

$${\tau_{OFF}}^{IPS} \sim \frac{\gamma_\phi}{Kq^2} \tag{4.19}$$

which will naturally be slower, and related to the elasticity and viscosity unwinding the **c**-director to realign with the grating. The OFF times should be similar to the ON times if addressing the display to return to it's OFF state. There will be additional restorative forces to consider due to the gratings and elasticity restoring the unwound state.

4.4.2 Compressions in the SmC Phase

Smectic layers can compress and dilate, which has not yet been considered as they can neglected in simple, layered geometries. An additional free energy approximation term can be introduced [58]:

$$w_{comp} = \frac{1}{2}\bar{B}\left(\frac{\partial u}{\partial z}\right)^2 , \tag{4.20}$$

where $u(x, y, z)$ is the vertical displacement (z-direction) of the layers relative to their initial position, and $\bar{B}$ is the layer compression constant. This holds true for the onset of compressions, but can be written to account for post-transitional effects as [200, 212]:

$$w_{comp} = \frac{1}{2}\bar{B}\left\{\frac{\partial u}{\partial z} - \frac{1}{2}\left[\left(\frac{\partial u}{\partial x}\right)^2\left(\frac{\partial u}{\partial y}\right)^2\right]\right\}^2 , \tag{4.21}$$

An energy density for the SmC which has no undulations at its boundaries ($z(0), z(d) = 0$) is given by [200, 213, 214]:

$$w_C = \frac{1}{2}A_{12}\left(\frac{\partial^2 u}{\partial x^2}\right)^2 + \frac{1}{2}(B_2 + A_{21} + 2C_2)\left(\frac{\partial^2 u}{\partial y^2}\right)^2 + \frac{1}{2}[B_1 - 2(A_{11} + C_1)]\frac{\partial^2 u}{\partial x^2}\frac{\partial^2 u}{\partial y^2} + \frac{1}{2}\bar{B}\left\{\frac{\partial u}{\partial z} - \frac{1}{2}\left[\left(\frac{\partial u}{\partial x}\right)^2\left(\frac{\partial u}{\partial y}\right)^2\right]\right\}^2 . \tag{4.22}$$

This theory is of particular importance when applying a pressure normal to the smectic layers (parallel to **k**), as is experienced when a homeotropic SmC cell is exposed to a mechanical shock.

4.4.2.1 Penetration Length

In the VGA-FLC device, gratings will be used to align the **c**-director with the smectic layers in a homeotropic orientation (**k** parallel to the substrate normal). This indicates that there should be some inherent layer undulation induced into the static equilibrium state. This is important, as unlike the NLC, undulations of the smectic layers will penetrate through the layers over a wavelength much larger than the induced distortion [92]. A schematic diagram is given in Figure

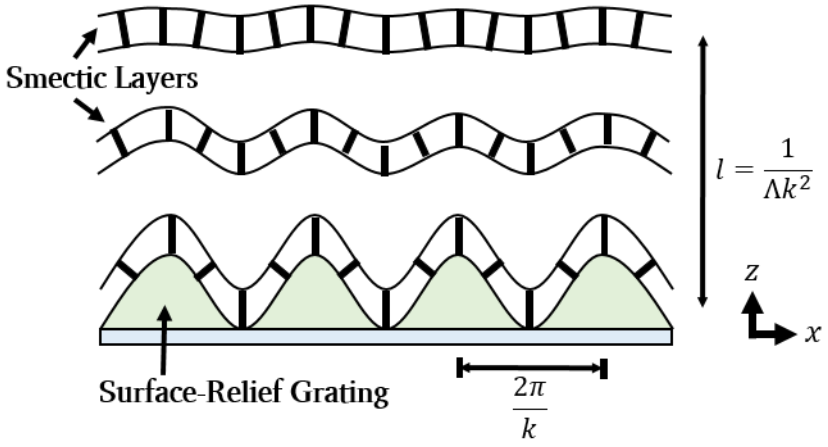

Figure 4.5: A schematic diagram showing the sinusoidal undulation of smectic A layers at a boundary. The wavelength of the undulation is $\frac{2\pi}{k}$. The effect of the undulation is seen far into the sample, where the penetration length is given by ($l = \frac{1}{\Lambda k^2}$), which is greater than λ. Diagram adapted from [92].

4.5. Considering the SmA phase for simplicity, with an induced sinusoidal undulation, the energy density is given by [58]:

$$w_A = \frac{1}{2}K_1\left(\frac{\partial^2 u}{\partial x^2}\right)^2 + \frac{1}{2}\bar{B}\left(\frac{\partial u}{\partial z}\right)^2 \ . \tag{4.23}$$

Solving for the equilibrium solution gives the result of:

$$\frac{\partial^2 u}{\partial z^2} - \Lambda^2\frac{\partial^4 u}{\partial x^4} = 0 \ ; \ \Lambda = \sqrt{\frac{K_1}{\bar{B}}} \ . \tag{4.24}$$

Introducing the boundary condition $u(x,0) = u_0\sin(kx)$, and introducing that the solution must decay as z tends to infinity, the solution becomes [92]:

$$u(x,z) = u_0\sin(kx)\exp\left(-\frac{z}{l}\right) \ , \tag{4.25}$$

where the penetration length is defined as:

$$l = \frac{1}{\Lambda k^2} \ , \tag{4.26}$$

where $k = \frac{2\pi}{\lambda_c}$ is the wave number of the undulations of period λ_c, and u_0 is a constant of the undulation amplitude. For these equations to hold, $|u_0| << 1$, and smaller than the smectic interlayer thickness (which is $20 \sim 80$ $\mathring{A}$), otherwise nonlinear effects would need to be considered [58]. For the case of the SmC*, the only modification that must be made is that $K_1 \rightarrow A_{21}$ or A_{12}.

The surface-relief gratings fabricated in Chapter 5 have a pitch $p = 4$ μm, or in the case of solving Equation 4.26, $\frac{2\pi}{k} = 4$ μm, and setting the characteristic length scale, λ, to be equal to the amplitude of the gratings, $\lambda \sim 0.2$ μm, Equation 4.26 gives $l \sim 2$ μm. However, this length scale is much larger than the smectic interlayer thickness, and so likely does not give a good indication to the actual distortions induced to the smectic layers induced by the grating. A schematic diagram of the compressions is given in Figure 4.6, indicating that undulations in the smectic layers must result in layer compressions. The layers compress generally by a factor $\Delta z \simeq \theta^2/2$, which here results in a reduction in d_A by $\sim \frac{1}{4} d_A$ for this grating profile [212]. The molecules confined to the SmA layers must remain normal to $\mathbf{k}$ for such an undulation to be stable and so physical.

This undulation theory can also be extended to incorporate a second-order term for the penetration length, which gives a relation between the A_{12} and A_{21} elastic coefficients [215]:

$$\Lambda_2 = \left(A_{21} - \frac{{C_2}^2}{B_2} \right)^{\frac{1}{2}} \left(\bar{B} \right)^{-\frac{1}{2}} \ . \tag{4.27}$$

Experimental results give conflicting answers for the magnitude of A_{12} and A_{21}, which is important to determine as it should determine the $\mathbf{c}$-director alignment of the SmC* material on surface-relief gratings. Hinov and Petrov [215] observe $A_{12} > A_{21}$ in NOBA, while theory with results from Findon and Gleeson [216] suggest $A_{12} > -A_{11} > A_{21} > 0$ for "M3", both of which are N $\rightarrow$ SmC materials

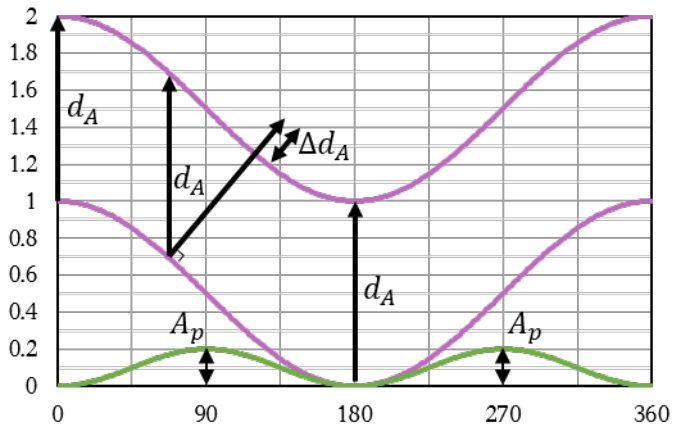

Figure 4.6: A schematic of the SmA layer compressions induced by a sinusoidal surface-relief grating, where $\Delta d_A \simeq \theta^2/2$.

[92]. This indicates that when an undulation is induced into the SmC*, it is expected to preferentially form either an A_{12} or A_{21} undulation relative to $\mathbf{g}$ to give the lowest energy state. The results for SCE13 are discusses in Chapter 7, and it is found that $A_{12} > A_{21}$.

4.4.3 Boundary Layer Conditions for a Homeotropic SmC

One final consideration regarding the governing equations for the VGA-FLC geometry is the effect of the boundary layers (z_{bl}) on the formation of the smectic layers [217]. To help simply describe this effect, two separate cone angles are defined for the SmC: $\theta_c = \theta_{bulk}$ is the equilibrium cone angle found within the cell, and θ_e is the induced cone angle enforced by the boundary conditions at the centre of the cell, where in general $\theta_e \leq \theta_{bulk}$. However close to the SmA $\rightarrow$ SmC transition $\theta_e \cong \theta_{bulk}$. A derivation will not be included here, but the solution with boundary conditions set at $\theta = 0$ at the surfaces ($z = \pm\frac{d}{2}$) for strong homeotropic anchoring, and $\theta = \theta_{bulk}$ in the bulk is given by [217]:

$$\theta = \theta_e \tanh \left[\sqrt{\left(\frac{{\theta_e}^2 d^2 b}{2K} \right)} \cdot \left(\frac{1}{2} + \frac{z}{d} \right) \right] , \tag{4.28}$$

where b is a temperature independent constant, of the order $d = 4 \times 10^4\ Nm^{-2}$ [218]. For this to be reasonable, $\theta_e \leq \theta_{bulk}$ and the solution must be:

$$\sqrt{\left(\frac{{\theta_e}^2 d^2 b}{2K} \right)} >> 1 . \tag{4.29}$$

The director structure through the cell is given by:

$$K \frac{\partial^2 \theta}{\partial z^2} + b\theta(\theta^2 - {\theta_{bulk}}^2) = 0 , \tag{4.30}$$

and it arises that over the bulk of the cell thickness θ_c is approximately its equilibrium value, but rapidly decreases as it approaches the surfaces until it meets the enforced homeotropic boundary condition. Interestingly, if Equation 4.28 is rearranged to be:

$$\theta = \theta_e \tanh \left[\sqrt{\left(\frac{{\theta_e}^2 b}{2K} \right)} \cdot \left(\frac{d}{2} + z \right) \right] , \tag{4.31}$$

it arises that the layer boundary solution is independent of the d, and that z_{bl} is inversely proportional to the cone angle of the equilibrium tilt. This indicates that the larger the cone angle, the smaller the effective boundary layer thickness.

What does this mean for the VGA-FLC device? At low values of θ_c immediately below the SmA $\rightarrow$ SmC* transition, z_{bl} is relatively large. From experimental data by Islam and Elston for SCE13 [217], at just 0.2 $^\circ C$ below the transition temperature, $\theta_c = 1.2^\circ$ and $z_{bl} = 1.9\ \mu m$. At 0.6 $^\circ C$ below the transition temperature, $\theta_c = 3.4^\circ$ and $z_{bl} = 0.4\ \mu m$, which is a significant reduction at such a small temperature decrease. The results follow the same trend on cooling, where the boundary layer thickness becomes smaller. This means that for the grating

aligned device, low cone angles at higher temperatures will have a far larger effect on the alignment in the bulk. This has the potential to cause issues when cooling into the SmC*, as good homeotropic SmA layer alignment is usually key to obtaining good SmC* layer alignment. At lower temperatures where θ_c is high, the boundary layer thickness will become smaller than that of the amplitude of the gratings, and so it is reasonable to assume that there should be no major disruptions induced to the bulk alignment, resulting in good homeotropic alignment. Assuming a constant pitch, it is predicted that a low-amplitude grating will be the least disruptive to the bulk director alignment, assuming it is of an amplitude large enough to align the **c**-director.

4.5 Summary - Chapter 4

This Chapter has introduced the VGA-FLC geometry as a method to controllably align the smectic **c**-director using homeotropic alignment on surface-relief gratings. The device is surface stabilised by suppressing the helical pitch of the FLC creating a uniform **c**-director field that is determined by the gratings on both cell surfaces. This defines the dark or OFF state of the device. It is addressed with in-plane electric fields to induce a 90° twist through the device (z) to satisfy the Gooch-Tarry minimum for maximum transmission of a TN display. This is the ON state. Vertical alignment is chosen to align the smectic layers which promises greater shock stability when compared to the chevron structure found in planar FLCs such as the SSFLC. Relevant theories are also presented that determine the effect of gratings on the alignment of smectic layers, as well as the predicted effect and response times on switching with IDEs. No such device has been constructed before that combines vertical grating alignment and FLCs.

Chapter 5

Fabrication of Surface-Relief Gratings for Liquid Crystal Alignment

5.1 Introduction

This Chapter explores the fabrication processes required to create variable amplitude surface-relief gratings for the containment and alignment of liquid crystals, specifically for the VGA-FLC device outlined in Chapter 4. The methods outlined here go beyond the standard operating procedures for SU-8 by implementing modifications to the photoresist processing guidelines to create non-digital surface-relief gratings using an otherwise digital technique.

The use of direct write lithography (DWL) was introduced in Chapter 3, Section 3.3, as a means to easily create permanent, micron-sized structures on glass substrates using the photoresist SU-8 2025 (MicroChem Corp.) [156]. ITO glass was chosen as the structures could easily be incorporated into test cells without the need for replication processes. It was important to keep the substrate type constant throughout prototyping as it has an effect on the film thickness when spin coating. It also affects the dose of UV required due to potential variations in reflectivity, in turn affecting the final height and quality of the structures. SU-8 2025 was chosen as a permanent, negative photoresist for creating structures to

align liquid crystals, due to its relatively high aspect ratio and being chemically and thermally stable once cured [156]. Dilutions of SU-8 were made to control the film thickness on spin-coating, as described in Chapter 3. At this stage it should be mentioned that an uncontrollable experimental variable during processing was the room temperature, which varied from 15 $\rightarrow$ 30 $^{\circ}C$ and directly affects the viscosity of the photoresist, and so its thickness on spin coating. This thickness can't be measured until the photoresist is cured, resulting in some small variations of predicted structure heights during processing. As such, the results in this Chapter are presented as functions of the final thickness of the SU-8, rather than its initial dilution. Controlling the temperature of the photoresist during processing is important, where possible, especially when working close to their fabrication limits as even small fluctuations can lead to large differences.

5.1.1 Creating Sinusoidal-Like Surface-Relief Gratings

The photoresist SU-8 has been introduced in Chapter 3, Section 3.3.1. SU-8 is most sensitive to i-line radiation ($\lambda = 365\ nm$), and does not cure with h-line radiation ($\lambda = 405\ nm$). Therefore using the DWL (direct write lithography machine) to create structures in SU-8 was limited to a 2 μm diameter, $\lambda = 365\ nm$ laser. Therefore a 2 μm diameter circle is the smallest feature that could be made with this method at the current facility. Alternatively, a mask aligner with its broadband UV source can be used to cure SU-8, where the smallest feature is now limited to the features of the photomask and the resolution of the photoresist. It should be noted that its the broadband UV source that is important, not the capability of aligning a mask. Photomasks can be made in-house using the DWL where features are limited by the 0.6 μm laser working with h-line radiation ($\lambda = 405\ nm$). Creating photomasks adds additional steps of complexity to the photolithography methodology, and quickly becomes unresourceful during prototyping. Therefore grating fabrication was limited to use of the DWL for creating prototypes and masters.

Fabricating a sinusoidal-surface relief grating using 2D photolithography is not trivial, but can be achieved using the following methods. As an initial example, a 5×5 μm^2 square written into a 5 μm film of SU-8 using the DWL gives a $5 \times 5 \times 5$ μm^3 cube. This assumes that the dose of UV and processes are optimum. Samples that are exposed with UV radiation more or less than the optimum dose show rounded corners and edges, and the side walls are no longer completely vertical.

Using these concepts and the methods described in Section 3.3.4 allow for curved features to be fabricated using this 2D technique. The higher solvent levels in the SU-8 film present when using an ambient temperature SB allows for more mobile SU-8 monomers and photo-acid diffusion. Coupled with higher doses of UV, this interestingly allows for control over the "roundness" of the structure. In the case of fabrication of SU-8 on ITO glass, the photo-acid diffusion seems to be concentrated closest to the substrate, likely due to reflections from the glass. This results in more rounded features towards the substrate side of the structure, creating "bell shaped" structures. This can be used to turn a digital grating design into a sinusoidal-like grating structure. An example of the design that is written with the DWL machine is given in Figure 5.1a. The pitch of the design is 4 μm (in y), chosen due to the limitations of the $2\mu m$ diameter laser (lowest line width specified by the manufacturer is 2 μm). Figures 5.1 b-d show the variable structures that can be made in a 1.6 ± 0.1 μm SU-8 film (30 % SU-8 2025 diluted in 70 % cyclopentanone), measured with a surface profilometer (see Chapter 3, Section 3.4.2). This sample had 9 different gratings (1.2×1.2 mm^2 square areas), each made with a different exposure doses (from 550 $mJcm^{-2}$ to 4000 $mJcm^{-2}$).

Figure 5.1b shows the peak-to-peak amplitude (A_{PP}) of the gratings, measured from the trough to the peak of the structures. The amount of offset under the grating is also shown, which is calculated from the substrate to the bottom of the grating trough. There is no offset of the gratings below a 800 $mJcm^{-2}$ exposure dose. This is due to the nature of writing with a digital design. As the dose is increased, the diffusivity of SU-8 monomers and photo-acid increases up to a point where the unexposed areas begin to polymerise, characterised by

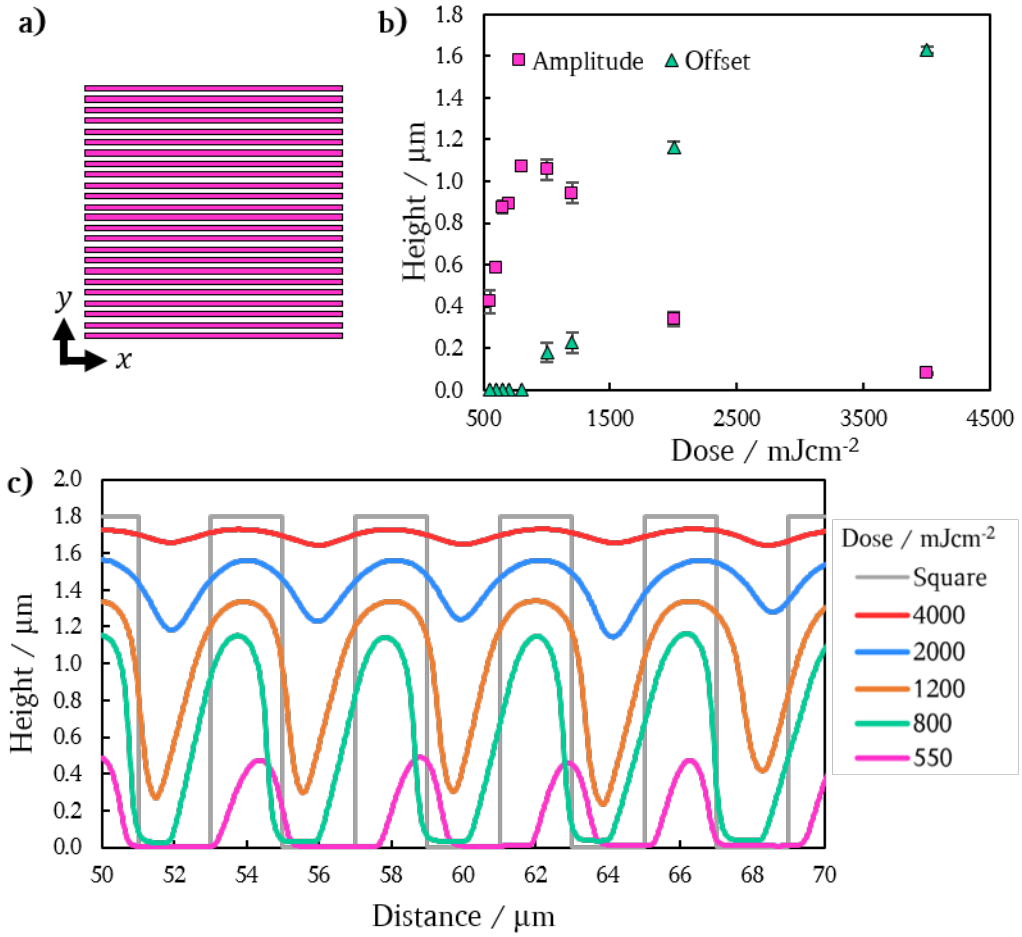
a)
y
x
b)
Amplitude
Offset
Height / µm
Dose / mJcm-2
c)
Height / µm
Distance / µm
Dose / mJcm-2
Square
4000
2000
1200
800
550

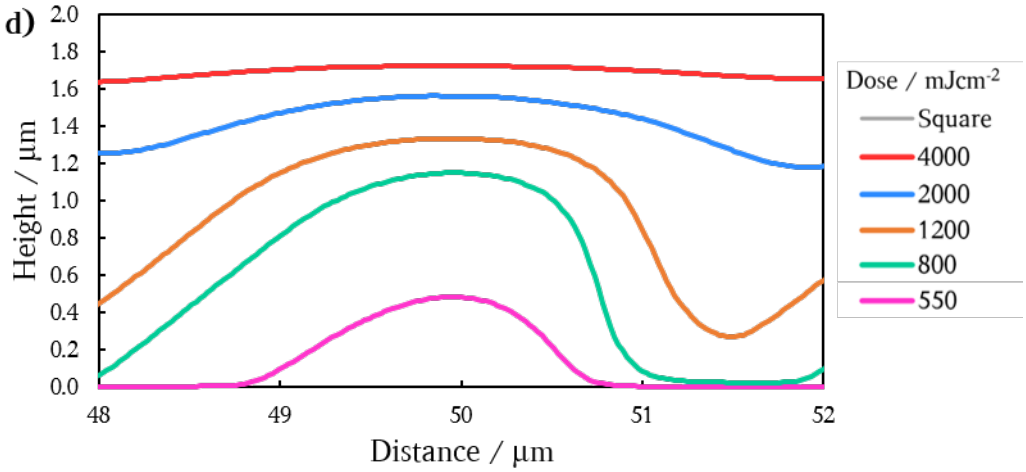

Figure 5.1: The variation of the peak-to-peak amplitude (A_{PP}) of surface-relief gratings by controlling the exposure dose during direct write lithography (DWL) of the negative-tone photoresist SU-8 2025. a): The digital grating design used to create a 4 μm pitch, sinusoidal-like surface-relief grating masters. The size of the exposed regions are $y = 2$ μm by x="length of desired grating" (limited by the size of the substrate), with gaps of the same distance, repeating in y. These structures can also be created using a photomask with the desired feature sizes. b): A plot of A_{PP} and grating offset versus exposure dose, using a $\lambda = 375$ μm, 2 μm diameter laser. The SU-8 film thickness is 1.6 ± 0.1 μm. The offset begins at 0 μm, until the exposure dose is large enough to facilitate sufficient photo-acid and SU-8 monomer diffusion into the unexposed regions. The offset then continues to increase until a flat structure is created, loosing the grating profile (tending towards infinite dose). c): The grating profile measured in the y direction, parallel to the grating vector $\mathbf{g}$ using a surface profilometer. Doses of purple= 550, teal= 800, orange= 1200, blue= 2000 and red= 4000 $mJcm^{-2}$ are shown, showing variations in grating profiles. The *grey* line shows the profile that would be obtained if using the optimum, standard processing parameters with minimised photo-acid and SU-8 monomer diffusion (a 4 μm pitch, digital square grating). d): A 4 μm snapshot of the grating profile, where the axes are scaled to the same length scale to emphasise the profile of the grating.

an increase in the grating offset. The offset increases up to the thickness of the film. At this point, the grating structures can become a square block of SU-8, as the dose tends to infinity. The A_{PP} follows a different trend. At low doses, the structures don't fully cure, and so A_{PP} is less than the film thickness. This confirms that most polymerisation occurs closest to the substrate. As the dose increases, the A_{PP} increases up to a maximum at 800 $mJcm^{-2}$. Note that this is still lower than the maximum film thickness. As the dose is further increased, the A_{PP} reduces following a decay-like curve. This is due to polymerisation occurring in the gaps in the grating design due to the high levels of diffusion of the SU-8. Eventually, A_{PP} reduces to zero as a solid block of SU-8 is created. The result is the ability to fabricate surface-relief gratings with controllable A_{PP}.

Figure 5.1c shows the surface profiles of the gratings measured using a surface profiler, where the distance is measured parallel to the grating vector $\mathbf{g}$ (in the y-direction in Figure 5.1a. It is clear that the 4 μm pitch of the grating is maintained, and that A_{PP} and the offset vary as a function of exposure dose. The grey line indicates the expected digital structure at an optimum dose, and low levels of photo-acid diffusion. Using the processing methods for "thin" films, this digital structure cannot be obtained. At low exposure doses, the grating at 550 $mJcm^{-2}$ is "wobbly" due to under-exposure, resulting in low adhesion, and so is not a uniform grating. However, it helps understand how the process of grating fabrication develops with increasing exposure dose, so is shown here as an example. Usually such structures are destroyed, or damaged, in the development process. Figure 5.1d highlights one peak of the gratings, where the axes are set to be at the same scale. This emphasises the different profiles of gratings that can be fabricated using this technique. It also emphasises the asymmetrical nature of these processing parameters due to the apparent blaze that is clear in the profile at doses of 800 and 1200 $mJcm^{-2}$. The cause of this is unknown, and is thought to be an artefact created by limitations in the maximum gradient that can be measured by the surface profilometer.

When these gratings are replicated by making stamps in a resin and embossing onto patterned electrodes as described in Chapter 3, the offset is removed

if the embossing speed and pressure are chosen carefully. Therefore high dose ($> 1200\ mJcm^{-2}$) SU-8 gratings provide the optimum masters for low-amplitude, 4 μm pitch gratings. Creating masters with an optimum grating structure proved difficult as there were variations in repeated experiments. Variations using the same dilution of SU-8 2025 (29.97 ± 0.05 %) are shown in Figure 5.2. The processing parameters are kept constant for each experiment, with the uncontrolled variables being the room temperature during spin coating, and the length of time before the PEB of the structures after exposure. Variations in temperature cause differences in the film thickness, while the length of time before developing the structures may change the amount of photo-acid diffusion before the PEB, although this is challenging to confirm and likely to have minimal effect. A solution is to choose the exposure dose based on the spin-coating temperature to obtain a particular grating profile.

The grating amplitude is theoretically limited to the maximum film thickness, controlled by varying the dilution of SU-8, although in practice tends to be less than this due to processing conditions. Figure 5.3 shows A_{PP} for three different film thicknesses of $1.4 \pm 0.1\ \mu m$, $3.0 \pm 0.2\ \mu m$ and $5.6 \pm 0.2\ \mu m$ respectively. The trends are similar to those observed in Figure 5.2, where increasing the exposure dose causes A_{PP} to reduce due to increased photo-acid and SU-8 monomer diffusion. There appears to be a limit on the maximum A_{PP} than can be obtained. For example, below doses of 700 $mJcm^{-2}$ in Figure 5.3, only the $1.4 \pm 0.1\ \mu m$ thick film shows a reduction in A_{PP}. Meanwhile, $3.0 \pm 0.2\ \mu m$ and $5.6 \pm 0.2\ \mu m$ thick films continue to increase in A_{PP}. This therefore highlights the affect of the ambient temperature SB, such that the photo-acid and SU-8 monomers can diffuse outside of the exposed regions at a rate faster than the SU-8 feature can be created. This is an ideal situation for creating sinusoidal-like surface relief gratings, although does indicate a limit of A_{PP} that can be made at this pitch and SB process. Fortunately, we are looking for low-amplitude ($< 1\ \mu m$) gratings. To make higher amplitude gratings, the SB step would need to be performed at a higher temperature to remove some of the residual solvent, but sufficiently low to prevent square features from being obtained.

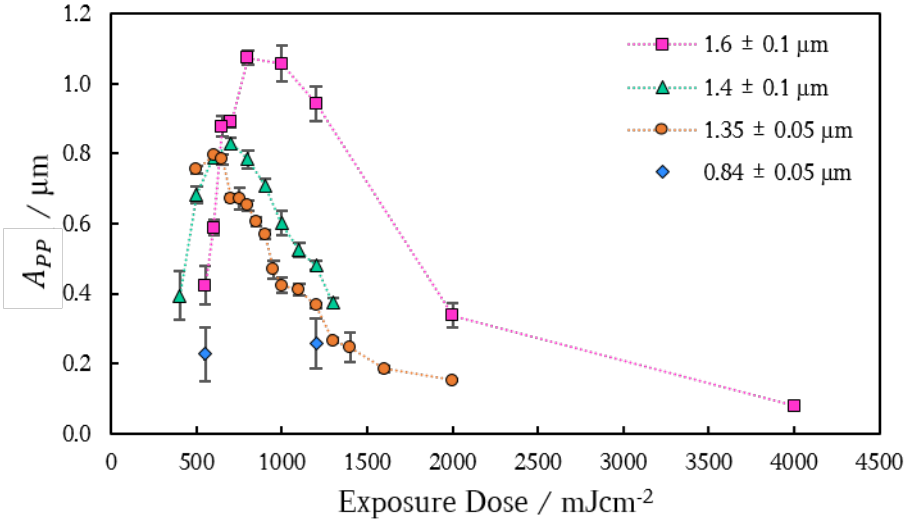

Figure 5.2: The variation in peak-to-peak amplitude (A_{PP}) versus the exposure dose using direct write lithography (DWL) for four different surface-relief grating experiments using dilutions of 29.97 ± 0.05 % SU-8 2025 in cyclopentanone. The films vary in thickness by 1.3 ± 0.3 μm due to variations in temperatures during processing. The trends in A_{PP} are comparable to those of a 1.6 μm thick sample shown in Figure 5.1. A_{PP} increases up to a maximum, at which point it decreases towards the limit and a flat SU-8 film is obtained. This is due to high levels of photo-acid and SU-8 monomer diffusion occurring caused by the relatively high exposure doses. The curves appear have shifted with increasing film thickness for a particular exposure dose.

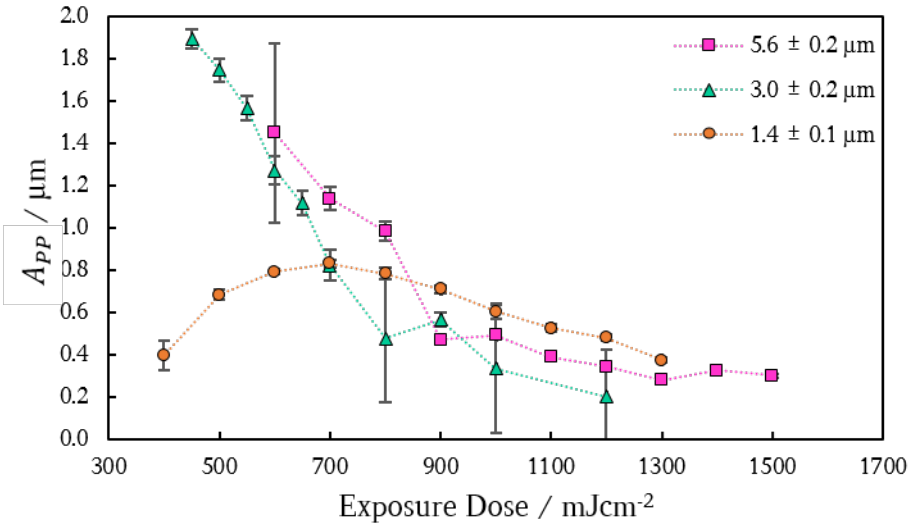

Figure 5.3: Variations in the peak-to-peak amplitudes (A_{PP}) versus exposure dose for different thicknesses of SU-8 2025 films. Purple squares: 65.5 % SU-8 in cyclopentanone, for a 5.6 ± 0.2 μm thick film. Teal triangles: 46.1 % SU-8 for a 3.0 ± 0.2 μm thick film. Orange circles: 29.9 % SU-8 for a 1.4 ± 0.1 μm thick film. The 1.4 ± 0.1 μm thick film shows the same trends as observed in Figure 5.2, whereby A_{PP} first increases with increasing dose, and then begins to decrease. The thicker films don't show this initial increasing A_{PP}, and instead start from a maximum and decease on increasing dose.

5.1.2 SEM of Surface-Relief Gratings

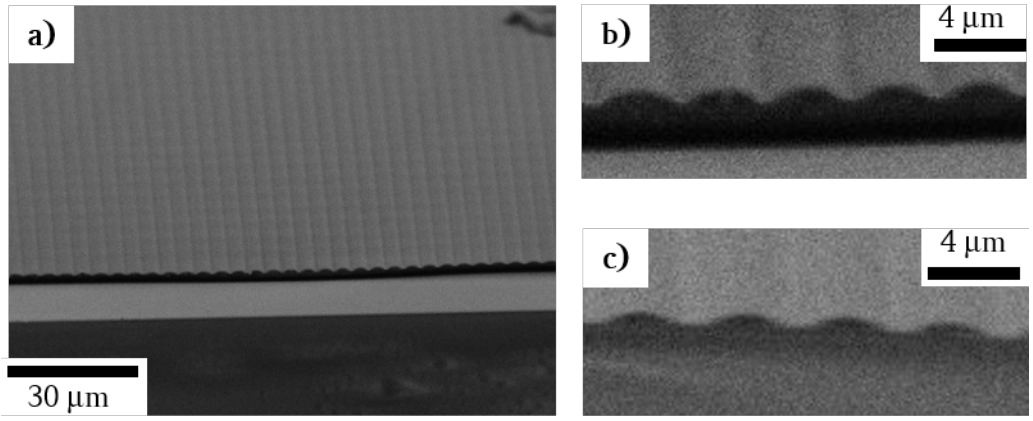

Figure 5.4: SEM images of SU-8 surface relief gratings. a,b): $h_{film} = 2.32 \pm 0.05\ \mu m$, dose of 500 $mJcm^{-2}$, resulting in a $A_{PP} = 0.77 \pm 0.02 \mu m$ with 1.6 μm offset. c): $h_{film} = 0.66 \pm 0.09\ \mu m$, dose of 1000 $mJcm^{-2}$, resulting in $A_{PP} = 0.59 \pm 0.05\ \mu m$ with no offset.

Figure 5.4 shows some preliminary results of prototype gratings obtained through SEM as described in Chapter 3 Section 3.4.1. The gratings are fabricated as described in this Chapter, and the samples are cut on the back of the ITO glass with a scorer and snapped to obtain a cross-section of the grating profile. This method confirms their sinusoidal-like nature.

Figure 5.4 a and b show the same gratings at different magnifications made with $2.32 \pm 0.05\ \mu m$ thick SU-8 with a dose of 500 $mJcm^{-2}$ resulting here in $A_{PP} = 0.77 \pm 0.02 \mu m$. The 1.6 μm offset under the grating is clear. Figure 5.4c shows a different grating made with $0.66 \pm 0.09\ \mu m$ thick SU-8 with a dose of 1000 $mJcm^{-2}$. This grating has no offset, and $A_{PP} = 0.59 \pm 0.05\ \mu m$. The limitations of this SEM technique are apparent as measurements become difficult due to the poor resolution as the features are significantly smaller. It is unclear if the features have been damaged on snapping the sample to observe the cross-section. This confirms that measurements made with the surface profiler are accurate,

and the "walls" of the gratings are indeed curved, with a rounded or flat trough depending on the dose and film thickness.

5.1.3 Optics of Surface-Relief Gratings

A film of SU-8 has a high optical transmission (> 95 %) across the visible wavelengths (measured from $350 \rightarrow 750$ nm), and so is well suited as a permanent structure for use in electro-optic devices [156]. Gratings are well known for their refractive and diffractive properties [219]. It is therefore important to ensure that the refractive and diffractive nature of these components are minimised to ensure high optical transmissions in electro-optic devices. These two optic effects are caused by:

- Diffraction: Light is diffracted due to the periodicity and spatial structure of the optic component.
- Refraction: Light is refracted due to continuous surface profiles of the optical component.

The pitch of the surface-relief gratings has been limited to 4 μm, and the A_{PP} allowed to vary. If $A_{PP} = 0$ (i.e. there are no gratings) then the maximum transmission is expected. Here, this is considered to be a transmission of 100 %. As A_{PP} increases, the transmission is expected to decrease due to the introduction of both diffractive and refractive effects. Figure 5.5 shows the variations of the transmission for the surface-relief gratings introduced in Figure 5.1 with varying A_{PP}. Figure 5.5a shows the transmission across a range of wavelengths for each grating profile, and Figure 5.5b shows the average transmission over $\lambda = 450 \rightarrow 700$ nm as a function of A_{PP}. Here, a near-linear trend is obtained, clearly demonstrating the decrease in optical transmission with increasing A_{PP}. A decrease in $T_r \approx 45$ % is obtained for $A_{PP} \approx 1$ μm.

As mentioned in Chapter 3, Section 3.5.2, the diffractive properties of the surface-relief gratings can be removed by index matching the photopolymer to the ordinary refractive index of the LC [167]. Doing so is beyond the capabilities

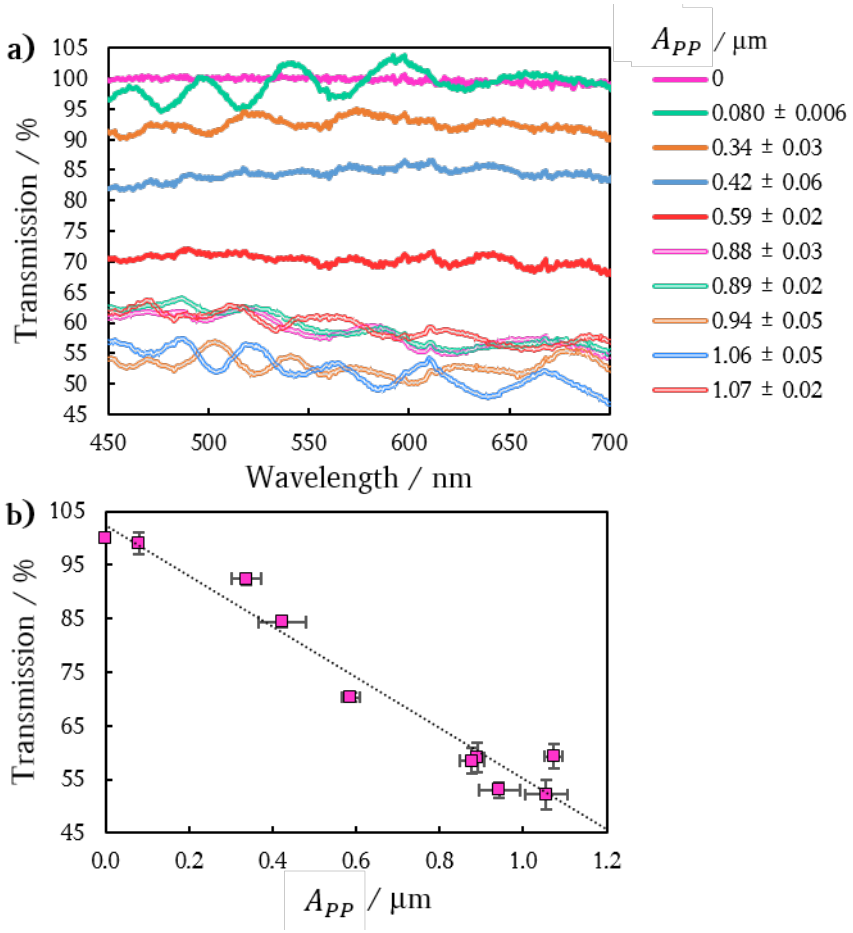

Figure 5.5: The white light transmissions of SU-8 surface-relief gratings, normalised against ITO glass. Figure 5.1 shows the profile of these gratings. a): The transmission versus wavelength of light measured for 9 different grating profiles. b): The transmission versus peak-to-peak amplitude (A_{PP}) for these gratings. A linear trend is obtained showing that the transmission decreases on increasing A_{PP}.

of this work, but is certainly feasible with the appropriate materials [168]. Gratings should therefore not be disregarded for yielding low transmissions in this work.

5.1.4 Gratings for VGA-FLC Devices

The concept of the VGA-FLC device is introduced in Chapter 4, where surface-relief gratings are used to align the **c**-director of FLCs. Chapters 7 and 8 refer to two devices: Device 1 and Device 2, which are prototype VGA-FLC devices with gratings embossed onto each substrate. Figure 5.6 shows the surface profile for these two gratings. Device 1 uses the $A_{PP} = 0.23 \pm 0.08 \mu m$ grating, while Device 2 uses the $A_{PP} = 0.26 \pm 0.07 \mu m$ grating. There is a large variation in the A_{PP} of these gratings ($\sim$ 30 %). This is due to the large scale at which the gratings were made. Each grating covers an area of 4 cm^{-2}, which is much larger than the areas of the dose tests performed earlier in this Chapter (just 1.44 mm^2). This highlights the increased variation that scale adds to this fabrication technique, likely a result of the uneven evaporation of the solvent over this increased surface area. This suggests that the use of masks rather than DWL must be considered for use in future master fabrication. This will result in reducing exposure time from 17 hrs (for this particular sample) to 30 s (sample independent), and so reducing these evaporation inconsistencies. The loss in transmission due to using this double grating alignment in the VGA-FLC devices is calculated to be lower than 10 % if the gratings are aligned perfectly parallel to one another. The final devices that are referred to throughout this work, Device 1 and Device 2, are summarised in Table 5.1.

5.2 Summary - Chapter 5

This Chapter has shown the creation of variable amplitude surface-relief gratings in the photoresist SU-8 2025 using the DWL. Gratings with variable peak-to-peak amplitudes (A_{PP}) have been demonstrated by modifying the standard processing

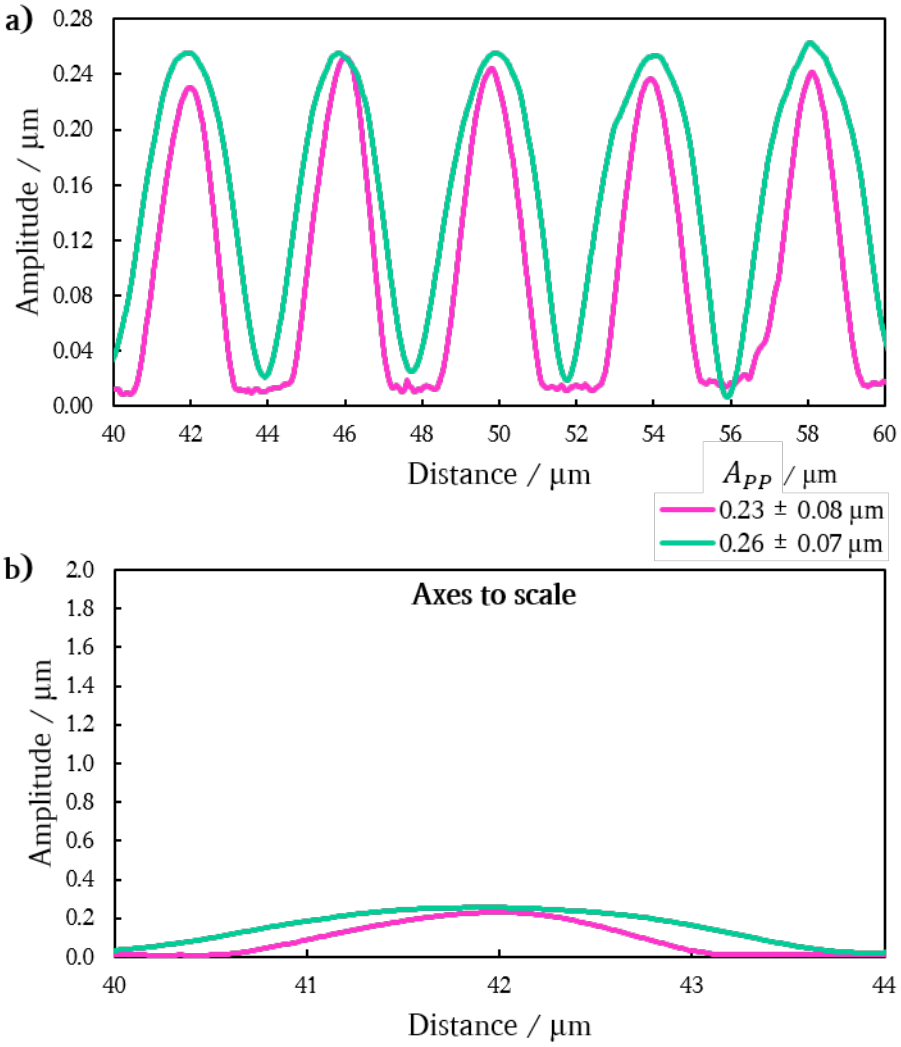

Figure 5.6: The surface profiles of the two master gratings used in Section 8 for fabricating prototype VGA-FLC devices. These masters were created using a 30 % dilution of SU-8 2025, and exposed using a 2 μm, 375 nm laser in the DWL. Final SU-8 layer thickness: 0.84 ± 0.05 μm. Grating amplitudes: Purple line: $A_{PP} = 0.23 \pm 0.08 \mu m$, using a dose of 550 $mJcm^{-2}$, and teal line: $A_{PP} = 0.26 \pm 0.07 \mu m$, using a dose of 1200 $mJcm^{-2}$. a): A 20 μm cross-section of the grating profiles measures in the y-direction, showing the differences obtained by varying the dose. b): One peak of the gratings, with the axes adjusted to be at the same scale.

Table 5.1: The two VGA-FLC devices that are used throughout Chapters 7 and 8.

Name	d	A_{PP} / μm	Ratio of SCE13* / %
Device 1	30 ± 2	0.23 ± 0.08	5 ± 1
Device 2	12 ± 2	0.26 ± 0.07	8.3 ± 0.7

procedures for SU-8. Reducing the temperatures of both the SB and PEB allowed higher levels of photo-acid and SU-8 monomer diffusion during the exposure step, and so reducing delamination and cracking of the structures. A desirable effect of this was the ability to control the surface-profile of a surface-relief grating using a digital design. The transmission of the gratings has been shown to be high using low grating amplitudes, and high amplitude gratings cause large diffractive effects. Two low-amplitude master gratings were fabricated and characterised for use in prototype VGA-FLC devices.

5. FABRICATION OF SURFACE-RELIEF GRATINGS FOR LIQUID CRYSTAL ALIGNMENT

Chapter 6

Textures of Homeotropic Smectic C Alignment

6.1 Introduction

As previously discussed, planar aligned FLCs are highly susceptible to shock induced flow, as shown in Figure 4.1. SmCs in a homeotropic alignment show greater shock resistance than in a planar alignment, as the layers can withstand induced layer compressions, and the induced flow does not significantly disrupt the layer orientation, as shown in Figure 4.2. The potential for a shock-resistant geometry for enhancing homeotropic FLC alignment in displays and devices is investigated in the following Chapters. But before introducing surface-relief gratings, the textures observed on cooling the homeotropic geometry is first investigated, along with the effects of shock induced flow. This allows a direct comparison to the textures introduced by grating alignment.

Four mixtures of SCE13* are used in this section: a chiral mixture made with one enantiomer that is referred to as SCE13*, the racemic mixture with 50% of each enantiomer resulting in a non-chiral and non-ferroelectric is referred to as SCE13-R. Two mixtures creating by combining the two are also used which are 5% and 8.3% of the $\mathbf{P}_s$ of SCE13*, shown in Table 3.1. All devices are surface treated with C_8 silane, as described in Chapter 3, Section 3.7.

The devices are heated into the isotropic phase (I) and then controllably cooled through SCE13(*)'s liquid crystalline phases to obtain the best alignment before all experimental observations. This is performed at rates no faster than 5 $°C/min$ through each phase, 1 $°C/min$ over T_{AN}, and 0.5 $°C/min$ over T_{CA}, unless otherwise stated. This results in high quality homeotropic alignment.

6.2 Textures on Cooling a Homeotropic FLC

This section is concerned with the surface-stabilised alignment of SCE13* in a homeotropic geometry. A $d = 25 \pm 1\ \mu m$ homeotropic cell (no rubbing) surface treated with C_8 silane with IDEs on one surface with no additional containments was filled with the 8.3% mixture of SCE13*. The optical textures obtained are observed and analysed.

The isotropic phase (I) appears dark at all rotations using POM. Cooling the sample into the surface-stabilised N(*) phase results in birefringent textures appearing as the **n**-director reorients to align with the homeotropic surface anchoring. In this geometry the **n**-director aligns parallel to the substrate normal, which can also be defined as a 90° pre-tilt. This state appears optically isotropic on rotation between crossed polarisers as only the ordinary refractive indices (n_o) interfere with the incident polarised light. If there is a pre-tilt in the N(*) phase due to a mechanical rubbing of the alignment or application of a non-90° alignment layer, then the N(*) phase would appear brighter on rotation between crossed polarisers, and brightest at 45°. 90° pre-tilt is therefore confirmed in the N(*) phase using the vapour phase deposition of C_8 silane for SCE13*. This also confirms that the chirality of the N(*) phase has been suppressed for this mixture, and so $R_0 \geq 100 \pm 4\ \mu m$ (from Equation 2.45).

If the N* phase had $R_0 \leq 100 \pm 4\ \mu m$ and the helix were allowed to precess about the cell then **n** would still be aligned vertically in the device and display Grandjean textures. This is observed as a "fingerprint" texture which is randomly aligned due to the lack of pre-tilt in the alignment layer. This texture can be

used to calculate the helical pitch of the N* phase. It should be noted that the direction of the helical twist in the N* is perpendicular to the substrate normal, and perpendicular to the twist direction found in the SmC*. Therefore the N* pitch can't be used to calculate the pitch of the SmC*, but is a good indication as to whether the SmC* will be surface-stabilised. Cooling the N* phase can result in loosing the fingerprint texture at a particular temperature, indicating that the surface-stabilisation limit has been reached, as the pitch is temperature dependent and increases on cooling ($R_0{}^{-1} \propto T$) [220].

The SmA phase appears optically isotropic on all rotations as the layer normal (**k**) and **n**-director are parallel to the substrate normal. These layers do not intercept the surface at any point, unlike the SmA "bookshelf" geometry. Tilted layer alignment is characterised by brighter textures on rotation between crossed polarisers, due to the tilting mesogens causing birefringence. The SmA phase does not show chirality by definition. Moreover there is little to no change in the layer spacing (d_A) over the SmA phase on cooling [221, 222]. For SCE13*, $d_A \sim 29\mathring{A}$ [102, 223]. There are no observed changes to the optical texture as the SmA phase is cooled in this simple device.

The second-order SmA to SmC(*) phase transition is where relevant changes begin to happen [200]. The SmC(*) phase is characterised by a tilt of the **n**-director within the smectic layers, characterised by the cone angle (θ_c) and the in-layer direction by the **c**-director (**c**). This geometry is shown in Figure 2.2. In the SmC(*) the **n**-director is no longer well defined as it is monoclinic with two optic axis due to its biaxiality [224]. For simplicity the SmC(*) is treated as a uniaxial material and the the monoclinic symmetry is ignored. This is acceptable for the homeotropic SmC(*) phase as **c** rotates about its cone within the layer, with little to no rotation of the molecule about ζ, and therefore no change in the observed Δn_{eff}. This does change with temperature, but again the director tilts with little to no rotation about ζ, and so the biaxiality can be deemed negligible.

All orientations of **c** within the smectic layers are equal in energy in this homeotropic geometry with no surface pre-tilt as there is no defined anchoring

direction. Therefore **c** is oriented anywhere within the smectic cone of allowed positions for the SmC(*) (Figure 2.2). With $R_0 << d$, the phase appears chiral where **c** twists through the layers, with the axis of rotation parallel to the layer normal (in the x, y-plane). This is perpendicular to the direction of chirality in the N* phase. In a narrow temperature range just below the transition from the SmA to SmC* phase (T_{CA}), the helical pitch is found to sharply increase in magnitude on cooling to a maximum value at approximately 0.5 $°C$ below T_{CA}. This then proceeds to slowly decrease with decreasing temperature following $z_d \propto (T_{CA} - T)^{-\frac{1}{3}}$ [225, 226]. If the pitch is large enough, the chirality in the SmC(*) phase will be suppressed over the operable temperature range, resulting in a SmC(*) schlieren texture with no preferred **c** orientation. A micrograph of this texture is shown in Figure 6.1a.

On further cooling the molecular tilt (θ_c) increases giving rise to a shrinkage of the smectic layer thickness as the effective molecular length has decreased ($d_C < d_A$), following the same trend as θ_c [102, 227]. In the SSFLC geometry chevrons form and the layers tilt as d_C decreases, rather than creating new smectic layers (see Chapter 2, Section 2.2.4). The magnitude of the layer tilt (δ_c) follows Equation 2.46. In the homeotropic alignment, away from the surface anchoring conditions, the bulk of the SmC(*) sample is allowed to freely align unlike in the SSFLC, and the layers do not intercept the surface, as with the SmA. This remains true on cooling where the uniform layers remain oriented parallel to the substrate normal throughout the SmC(*) phase. The layers do not tilt to form a chevron as for the SSFLC. New layers form in the bulk resulting in a bend in the layers about a disclination, as shown schematically in Figure 6.3.

Disclinations also arise in the schlieren texture of strength ± 1 due to the **c**-director orientation with no preferred alignment direction. Figure 6.1a shows SCE13* in a surface-stabilised alignment at 10 $°C$ below T_{CA}. The characteristic schlieren texture of bright and dark four-brush textures are seen emerging from ± 1 defects between crossed polarisers. There are no half strength disclinations as $\mathbf{c} \neq -\mathbf{c}$. Disclinations in this schlieren texture are characterised by a **c**-director

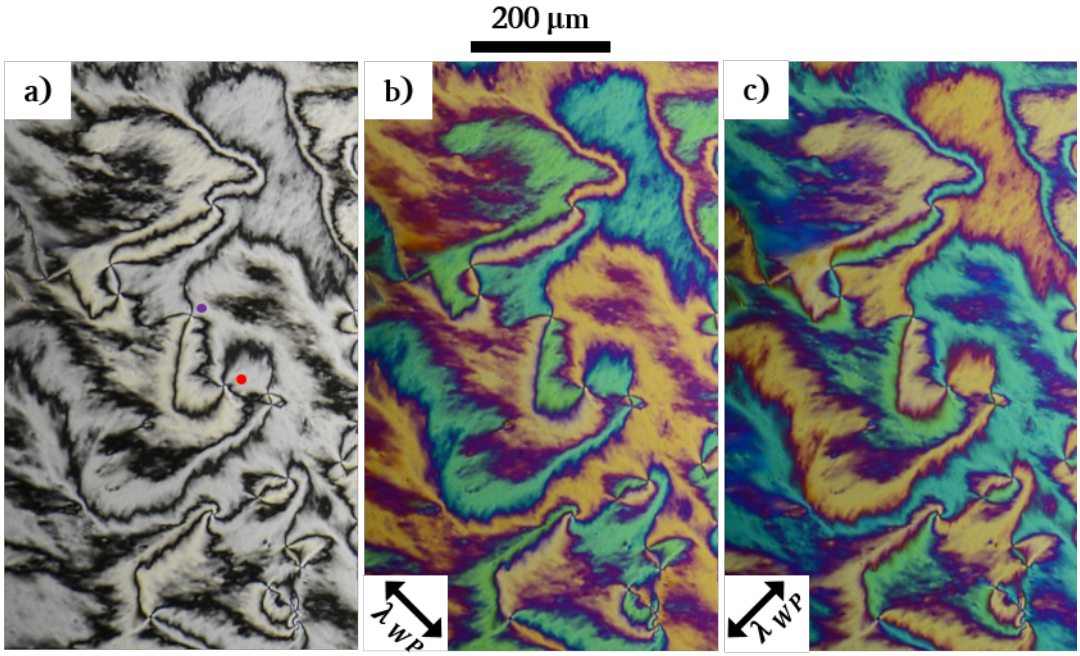

Figure 6.1: Analysis of the schlieren texture of the homeotropic, surface stabilised FLC SCE13* at 50 °C (Part 1). a): The schlieren texture found when cooling into the non-chiral Smectic C* phase, characterised by a texture of 4-brush defects. b): A full-wave plate is added at 45° to the crossed polarisers, and c): rotated 90° to its initial orientation. Areas that are blue are of a higher retardation and indicate the the **c**-director is parallel to the wave plate, and those that are orange are perpendicular.

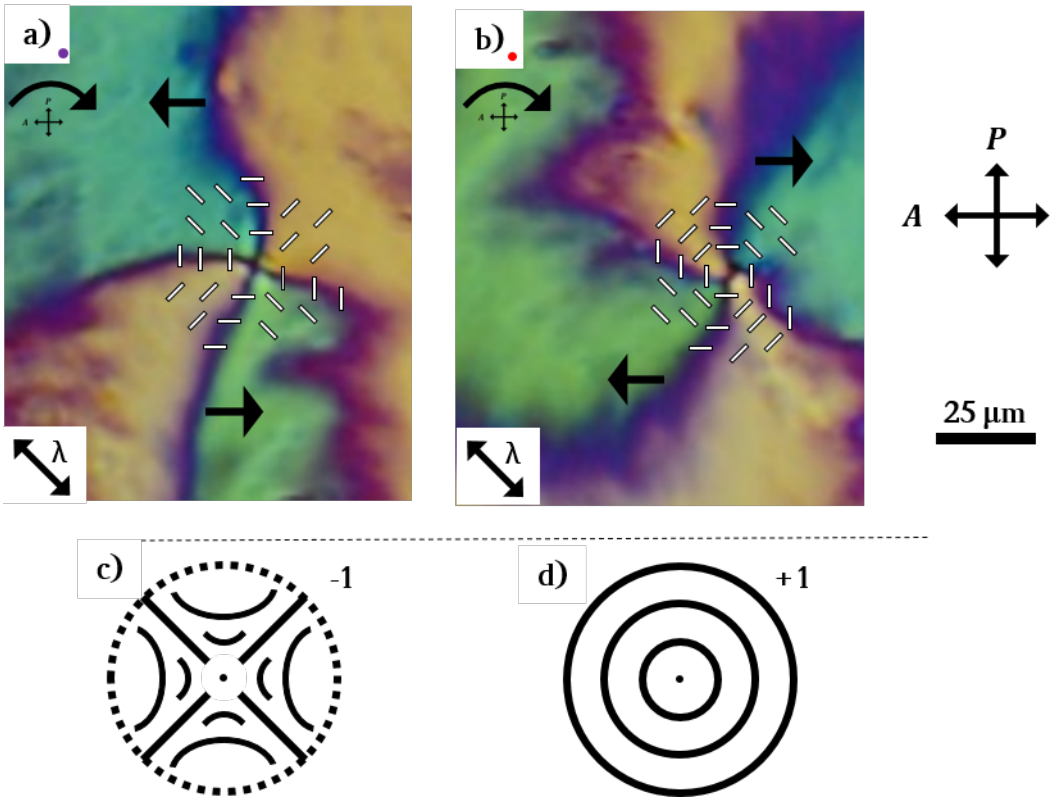

Figure 6.2: Analysis of the schlieren texture of the homeotropic, surface stabilised FLC SCE13* at 50 °C (Part 2). a): A -1 strength defect is magnified and characterised by rotation of the polarisers clockwise, and the anticlockwise brush rotation determines the defect as a saddle bend. b): Similarly a $+1$ strength defect is magnified and determined to move clockwise, with the rotation of the polarisers, indicating bend deformations in the director field. Purple and red dots indicate where the defect is located in Figure 6.1a. c,d): Sketches of the director field for ± 1 defects found in this Figure, both of which are associated with bend elastic deformations, which are expected for the SmC(*) phase.

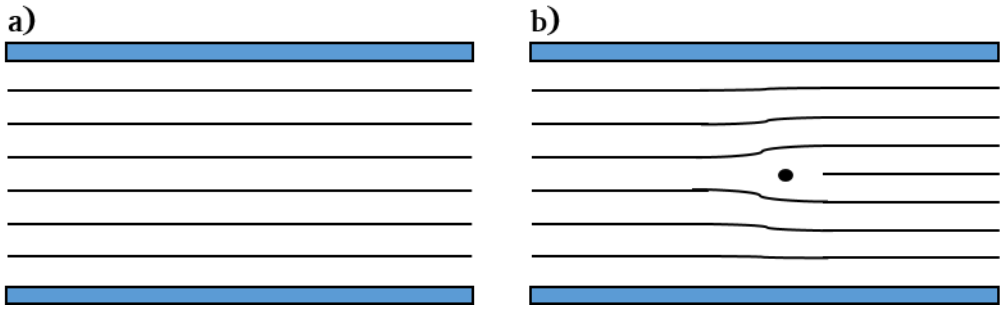

Figure 6.3: The alignment of homeotropic smectic layers. a): At a particular temperature, layers have a spacing equal to d_C. b): On cooling, new layers are formed to accommodate this layer shrinking characterised by a local tilt about a disclination formed within the smectic layers.

field that form around the disclination where the **c**-director orientation is established using a full wave-plate at $\pm 45°$ to crossed polarisers. Where the fast axis of the wave-plate aligns parallel with **c**-director, subtractive retardation occurs, and where it is perpendicular to the **c**-director, additive retardation is obtained. Figure 6.2 shows how the wave-plate shifts the retardation to the second order such that the black/dark regions become purple, the additive regions become blue, and the subtractive regions yellow. This can be checked using a Michel-Levy interference colour chart.

The **c**-director orientation in the x, y-plane was determined and found to consist of either a $+1$ tangential defect field, or the -1 saddle defect field. These are shown in Figures 6.2 d) to g). Crossed polarisers are rotated clockwise to confirm the strength of each defect. If the brushes rotate clockwise it is a $+1$ strength defect, whereas if they rotate anti-clockwise it is a -1 strength defect [228, 229]. The direction of the director can be determined, however the direction of tilt (θ_c) at either $\pm 90°$ cannot be as they look optically look identical, but importantly $\mathbf{c} \neq -\mathbf{c}$.

The **c**-director field can be used to deduce the relative magnitudes of the splay (B_2) and bend (B_1) elastic constants for SCE13*. The elastic distortions and rel-

ative **c**-director fields are shown in Chapter 2 Figure 2.8. There are two possible **c**-director fields around a +1 strength defect: radial and tangential, and only one −1 strength defect, the saddle. No radial +1 strength defects are observed in the texture with a full wave-plate, determined by the colour of the brushes relative to the fast-axis of the wave-plate (deduced by λ_{WP}). This confirms that the magnitude of B_2 must therefore be larger than B_1 in SCE13*, which is found to be true in the literature for most SmC(*) materials by up to an order of magnitude, such that $B_2 >> B_1$ [92, 100, 200].

6.2.1 Undulations in the SmC(*)

In this homeotropic geometry, the schlieren texture becomes "dressed" with a series of parallel lines following the **c**-director field on further cooling. This has been observed in homeotropic SmC(*) systems by Johnson and Saupe [200] and by Hinov and Petrov [215]. These are a result of the freedom from the surface conditions of the homeotropic layers in the bulk of the cell, unlike for the chevrons of the SSFLC. These are undulations within the smectic layers that propagate through the cell, and can occur either parallel ($\lambda_{\parallel,\,Optical}$) or perpendicular ($\lambda_{\perp,\,Optical}$) to the **c**-director field. Examples of this are shown in Figure 6.4. These undulations are stresses induced by thermal contractions due to the energy cost associated with creating new smectic layers that are required to fill the space caused by the shrinking d_C. To clarify, as the SmC(*) is cooled, d_C is reducing, and in order to compensate for this the smectic layers begin to undulate rather than tilt as is observed by chevrons in the planar geometry. Instead of spontaneously creating new layers, it appears more energetically efficient for the layers to first buckle, or undulate. As such, these undulations are not stable (at least are metastable) and eventually disappear behind a moving boundary when maintained at constant temperature. This dislocation line of layer formation is shown schematically without the undulations in Figure 6.3, and a micrograph is shown in Figure 6.4b. The undulations are here induced by cooling at a rate of $1\ ^{\circ}Cs^{-1}$, and usually appear and dissipate behind a moving boundary over several seconds. They are more metastable at lower temperatures ($\sim 30^{\circ}C$), likely

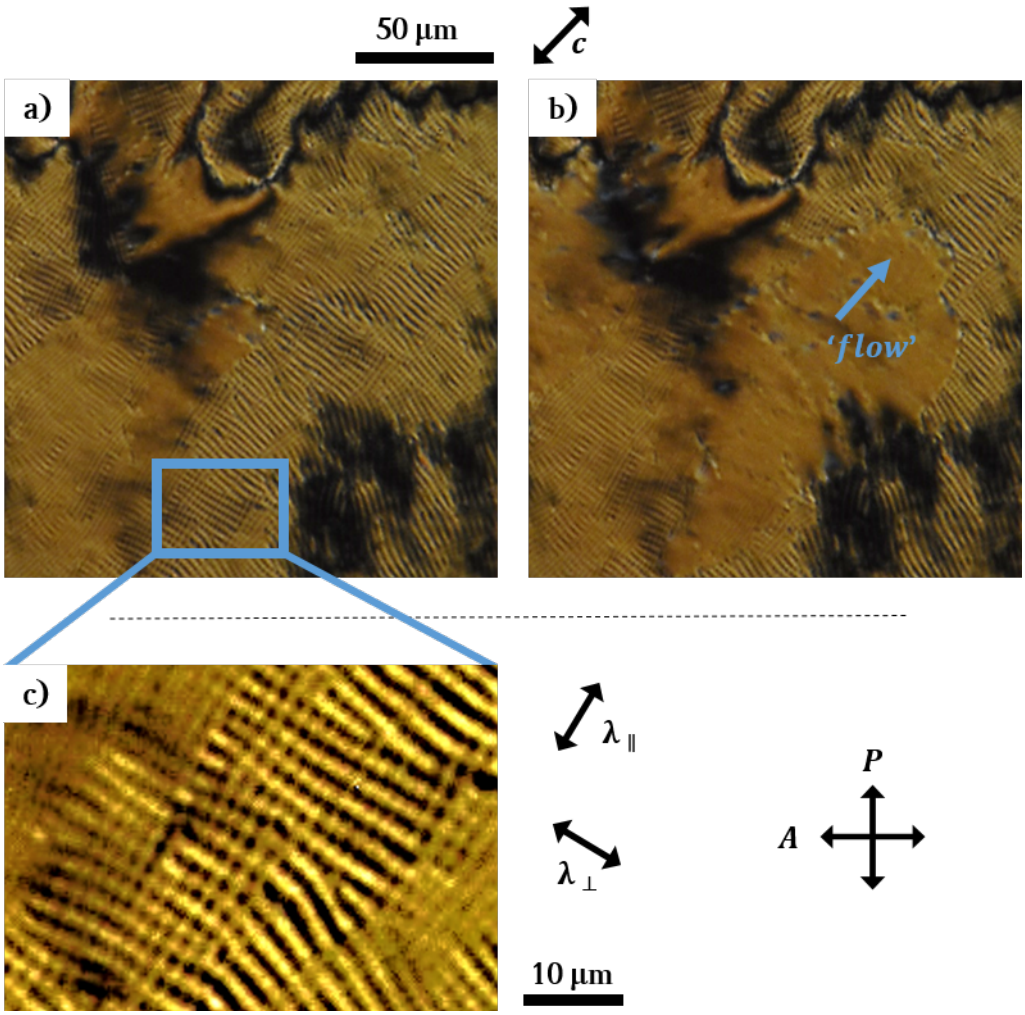

Figure 6.4: Layer undulations in the surface stabilised SmC*. Here a $d = 25 \pm 1\ \mu m$, homeotropic cell is filled with 8.3% SCE13* resulting in a schlieren texture. a): The temperature was reduced at 1 $°C/min$ through the SmC* phase to induce thermal undulations. Here, $\lambda_{\parallel,\,Optical}$ undulations are clearly observed, and some areas show double undulations where there are additional $\lambda_{\perp,\,Optical}$ undulations. b): After only a few seconds a dislocation line of layer formation sweeps across the sample, behind which the undulating textures dissapear. "Flow" indicates the direction of the thermal gradient. c): A magnification of the double undulating texture, clearly showing the two undulations of different wavelengths. The images have been enhanced to emphasise the textures.

as a direct result of the increased viscosity. This boundary is the dislocation line forming between two regions of a a different total number of smectic layers. If the sample is cooled at a slow enough rate such that the undulations are not observed, the dislocation line of layer formation can still be observed due to the small difference in Δn_{eff} arising from the reduced θ_c across said boundary. The texture of the SmC(*) continuously changes on further cooling from a state of non-undulating and undulating textures, importantly depending on the rate of cooling.

A second set of undulations form on further cooling if the initial set have not yet dissipated. These always form perpendicular to the first set of undulations, and result in a cross-hatched texture as shown in Figure 6.4c. The point at which the second set of undulation forms corresponds to the point whereby it becomes more energetically favourable to undulate in the perpendicular direction rather than increasing the amplitude of the undulation. The optics observed of bright and dark parallel lines are a product of the changing birefringence of a repeatedly undulating **c**-director in the z-direction of the device. This is shown schematically in Figure 6.5. This figure assumes that the layers undulate with the same periodicity and magnitude, which is not necessarily physical.

To explain Figure 6.5, Δn_{eff} changes due the tilting of **n**-director in a homogeneously aligned homeotropic smectic layer. The birefringence in the non-undulating layer (or at the peak or trough of an undulation) is set as "0". Between crossed polarisers, the retardation of this alignment is the same at $0°$, $90°$ $180°$,.... Now consider an A_{21} elastic deformation: the orientation of the cone must remain aligned with the now undulating layer normal (**k**), and so tilts in one of two directions. The magnitude of Δn_{eff} due to the tilt is the same in either direction, and results in an increase in Δn_{eff} which here is denoted as "+". The pitch of this optical undulating texture ($\lambda_{Optical}$) is half that of the pitch of the physical undulation (λ_{Layer}). Now consider an A_{12} elastic deformation: again there must be two directions of **c**-director tilt, however this time one increases and the other decreases in its overall Δn_{eff}. Here the pitch of the optical texture is equal to that of the pitch of the layer undulation. The

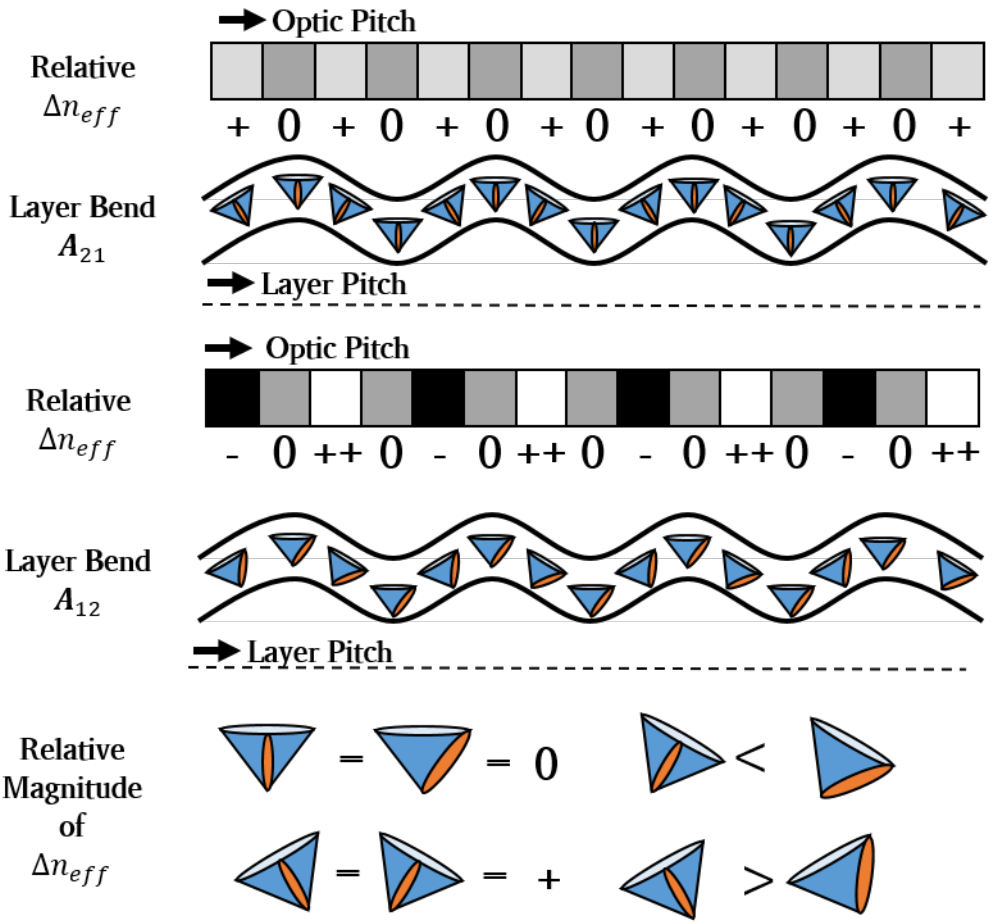

Figure 6.5: A schematic demonstrating the relative intensity and pitch obtained from undulations arising from the A_{21} and A_{12} elastic deformations in a homeotropic SmC(*).

relative magnitude of the birefringence is also greater in this A_{12} geometry, which optically results in "darker" and "brighter" undulations than those observed for the A_{21} geometry. This schematic can therefore be used to identify the elastic deformations arising from these layer undulations.

The lower energy elastic distortion is more likely to occur. The undulations are examined to establish if an A_{12} or an A_{21} is more favourable and so lower energy for SCE13(*). This is independent of the surface conditions and d, as it is a material property of SCE13(*). The relative spacing of the two layer undulations has a dependence on the cell gap, and is temperature dependent, so $\lambda_{Optical}(T) \propto \sqrt{d}$, although values are expected to very by up to 20 % of their equilibrium value due to their unstable nature [200, 215]. Where there are double undulations, the second set that form are perpendicular to the first set, and have a different undulation pitch as a direct result from Figure 6.5.

Inspection of Figure 6.4c clearly shows two optically distinct undulations. A_{12} elastic deformations have larger changes in birefringence and twice the pitch, and oscillate parallel to **c** (denoted as $\lambda_{\parallel,\,Optical}$). A_{21} elastic deformations have a lower overall change in birefringence, are half the pitch and oscillate perpendicular to **c** (denoted as $\lambda_{\perp,\,Optical}$). When both undulations are present simultaneously, there is a complex combination of A_{ii} elastic layer deformations which become more energetically favourable than further increasing the amplitude of a particular undulation. This only changes the relative birefringence and not the pitch of the undulations. It is possible that the two undulations occur at different heights in d, resulting in the same optical texture.

In Figure 6.4, measurement of the undulations results in $\lambda_{\parallel,\,Optical} = 2.7 \pm 0.2\ \mu m$ (the A_{12} elastic deformation) and $\lambda_{\perp,\,Optical} = 2.2 \pm 0.2\ \mu m$ (the A_{21} elastic deformation). This is a difference of $\lambda_{\parallel\,,Optical} \sim 1.2 \times \lambda_{\perp,\,Optical}$. This is consistent with the findings of Johnson and Saupe who report differences in the undulation pitches of around a 1.6x difference and agrees with the results of Hinov and Petrov, noting a different material, alignment conditions, cell gap and temperature [200, 215]. Note that this is not the 2 : 1 ratio that was assumed

in Figure 6.5, which indicates that the pitch of the layer undulations are not the same. The layer bend elastic constants are inversely proportional to the pitch, and so the smaller the pitch, the larger the elastic constant. Therefore the optical pitch is corrected to give the magnitude of the layer pitch of the undulations using (from Figure 6.5):

$$\lambda_{\parallel,\,Optical} = \lambda_{\parallel,\,Layers} \ , \tag{6.1}$$

$$\lambda_{\perp,\,Optical} = \frac{1}{2}\lambda_{\perp,\,Layers} \ . \tag{6.2}$$

From the experimental results, this gives $\lambda_{\parallel,\,Layer} \sim 0.6 \times \lambda_{\perp,\,Layer}$ for SCE13(*). This indicates that $\frac{1}{A_{12}} \propto 0.6 \times \frac{1}{A_{21}}$, and it is therefore concluded that:

$$A_{12} > A_{21} \ , \tag{6.3}$$

for SCE13(*). In this geometry, $\lambda_{\perp,\,Layer} = 4.4 \pm 0.4\ \mu m$.

Hinov and Petrov discuss that the origin of the undulations result from first-order or second-order effects [215]. A strong coupling between the layer curvature and the tilt direction of the **c**-director are the result of a second-order effect, resulting in an A_{21} undulation of smaller stripe period, $\lambda_{\parallel,\,Optical}$, while a first-order effect with no coupling results in an A_{12} undulation with a larger stripe period, $\lambda_{\perp,\,Optical}$.

Measurements for the magnitude of the layer bending constants are rare, and are found in combinations of A_{ii} rather than separately [92, 216]. Findon and Gleeson found that $A_{12} > A_{21}$ for a planar SmC(*) geometry [92, 216]. This is in disagreement with the experimental results of Hinov and Petrov who state that $A_{21} > A_{12}$ in a homeotropic geometry, although they did not made the distinction that the optical pitch and the layer pitch are not equal in magnitude between the A_{21} and A_{12} layer deformations [200, 215]. Correcting their result confirms $A_{12} > A_{21}$. As the homeotropic condition is induced in our devices, and the layers are free to align with little contribution from the surfaces, and considering

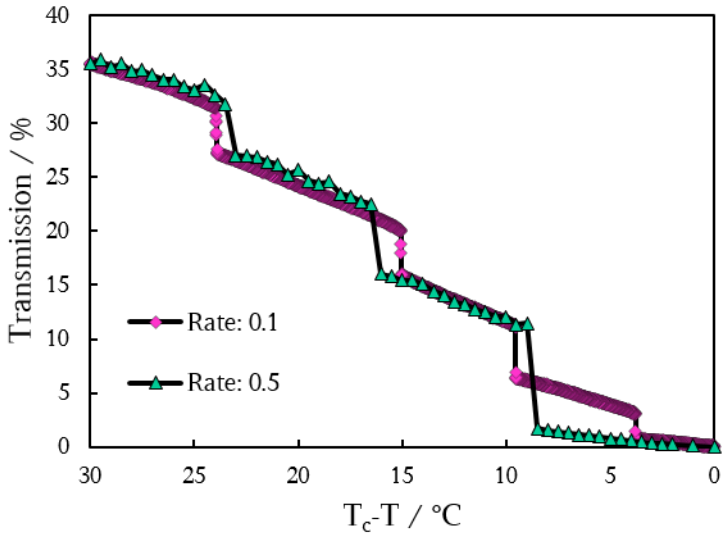

Figure 6.6: The optical transmission (I) at 550 nm through a homeotropic device versus the reduced temperature ($\Delta T = T_{CA} - T$) of a 8.3 % SCE13* mixture, $d = 9.8 \pm 0.1$ μm. Good homeotropic nematic and SmA phases were observed. There was no preferred **c**-director orientation resulting in a schlieren texture. Purple diamonds: cooling at 0.1 $°Cmin^{-1}$ from 65 $°C$. Teal triangles: cooling at 0.5 $°Cmin^{-1}$ from 65 $°C$. Black lines are added as a guide to the eye.

that $A_{12} > A_{21}$, we expect A_{21} undulations to be more energetically favourable to form. Therefore the A_{21} layer undulations should form over surface-relief gratings.

6.2.2 Transmission Measurements of Smectic C(*) Layer Undulations

The experimental set-up is described in Chapter 3, Section 3.10.2. An optically dark state can be distinguished from an undulating texture due to an increase in the transmission, allowing a simple detection method of the optical transmission to be used.

The results for a homeotropic cell are shown in in Figure 6.6. The purple

diamond points were taken at a cooling rate of 0.1 $°Cmin^{-1}$ from 65 $°C$, and the teal triangles at 0.5 $°Cmin^{-1}$. The black lines are included as a guide for the eyes. The point at which new smectic layers form is referred to as "layer jumps" here, as they are observed as a jump in the optical transmission. Layer undulations occur as θ_c increases on cooling, where the layers buckle rather than immediately form new layers (d_C remains constant despite an increasing θ_c). The jump in I indicates a point at which the smectic layer undulations reach a critical point resulting in a layer jump. These layer jumps are observed to increases in transmission, I, by ~ 5 %. Of note is the general trend of increasing I between layer jumps at a constant rate. At these slow cooling rates, undulations are not observed through the eyepieces of the microscope, however the increasing transmission indicates that there must be an increase in Δn_{eff}. This indicates that there must be a combined increase in θ_c and small magnitude undulations to result in an increased Δn_{eff} and so increasing I. Finally of note is that the layer jumps occur at the same temperature intervals. This indicates that the layer jumps occur at a particular temperature which is related to the magnitude of elastic distortion within the layers. The missed layer jump at $\Delta T =\sim 4\ °C$ for the run cooled at 0.5 $°Cmin^{-1}$ confirms that the cooling rate is an important factor determining when the layer jumps become energetically favourable.

These results suggest that no matter the cooling rate, there are always small magnitude undulations occurring within the smectic layers before new layers are created. The experiments performed in Figure 6.4 were cooled at a faster rate and the undulations were observed without the requirement for a spectrometer. The point at which new layers form is consistent on repeat measurements. This is cell gap dependent, and is explored further in Chapter 7.

6.2.3 Chiral Domains and Layer Undulations

Only undulations in the surface-stabilised SmC(*) have been discussed so far. The chirality of the FLC phases are suppressed throughout this work, but it is worth noting that the undulating domains are not observed if the **c**-director is free

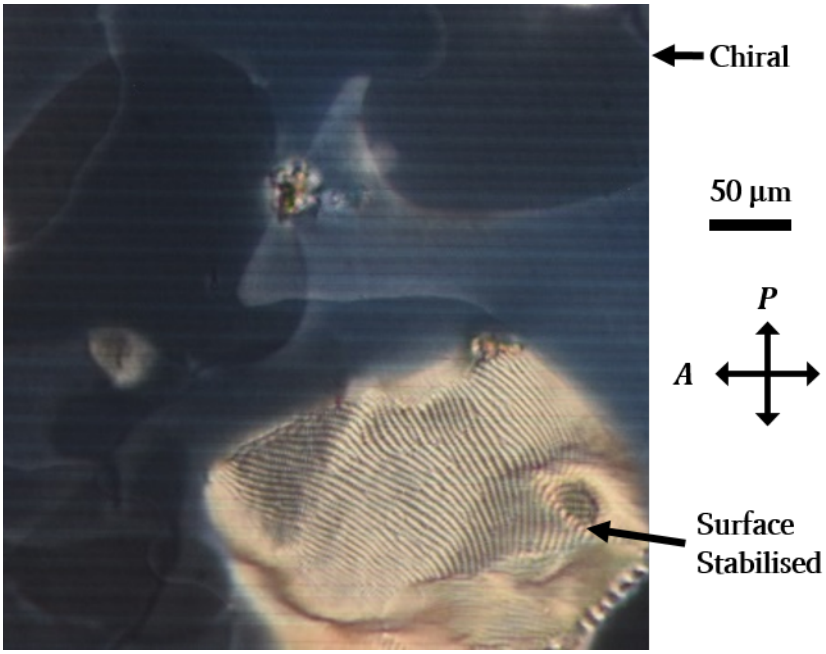

Figure 6.7: Undulations in the SmC*. A thick homeotropic cell (40 μm) filled with 100% SCE13*, close to the transition temperature (57 $°C$), showing both chiral and surface stabilised domains. The chiral domains (dark regions) show no undulating layer textures, whereas the surface stabilised domains do (brighter region).

to twist through the homeotropic geometry. This was confirmed for homeotropic geometries with cells that are close to the surface stabilisation limit of SCE13(*), and show both chiral and surface-stabilised domains. The chiral domains do not change texture where the unwound domains begin to undulate on cooling. This suggests that they do not form in the chiral SmC*, or that the chiral texture is undulating and that the undulations are precessing with the pitch of the material, resulting in no obvious optical texture. Also, no free-forming undulations of this form are observed in planar devices as the preference is for the layers to tilt rather than undulate, as described by Equation 2.46.

6.3 Shock Induced Flow in a Homeotropic FLC

The theory of shock-induced flow on a homeotropic SmC(*) has already been introduced in Chapter 4, and shown in Figure 4.2. To recap, when a SmC(*) device is shocked or compressed, flow will be induced to the **c**-director in the x, y-plane due to a decrease in available volume. There are also compressions of the smectic layers, although for simplicity these are considered small and so negligible. For a low magnitude shock the layers should remain relatively undamaged and remain in a homeotropic configuration, while showing the effects of **c**-director reorientation. At higher force shock causes the layers to become displaced from their homeotropic geometry resulting in a bright texture, and then flow back or reorient to their initial homeotropic geometry. This is provided that the layers have not created defects that pin the new configuration, which is the weakness of the planar aligned SSFLC geometry, and the strength of homeotropic smectic alignment.

Figure 6.8 shows the textures induced by a mechanical shock of the schlieren surface-stabilised SmC(*) geometry, the same device used previously in Figure 6.4. A low pressure was observed to reorient the **c**-director, with no obvious disruptions to the smectic layers. This is seen by comparing Figures 6.8a and 6.8b. There is a clear change in birefringence colours and position of the brushes arising from defects due to flow induced reorientation of the **c**-director. If there is layer disrupted and tilted by the flow, this was not observed due to being a low enough force as to not create an optical change.

A medium pressure resulted in similar **c**-director reorientations. However, on release of the mechanical pressure, the optical texture became dressed with lines similar to the thermally induced undulations observed in Figure 6.4. These soon dissipated behind a moving dislocation line in an equivalent manner, replaced by a non-undulating texture inherent of homogeneous homeotropic smectic layers. Figures 6.8 c) to e) show the texture before a pressure, immediately after the shock showing the undulating texture, and a few seconds after the initial shock when the dislocation line moves across the texture relieving the undulations. Figures 6.8 f) to h) show the same images with an increased contrast to emphasise

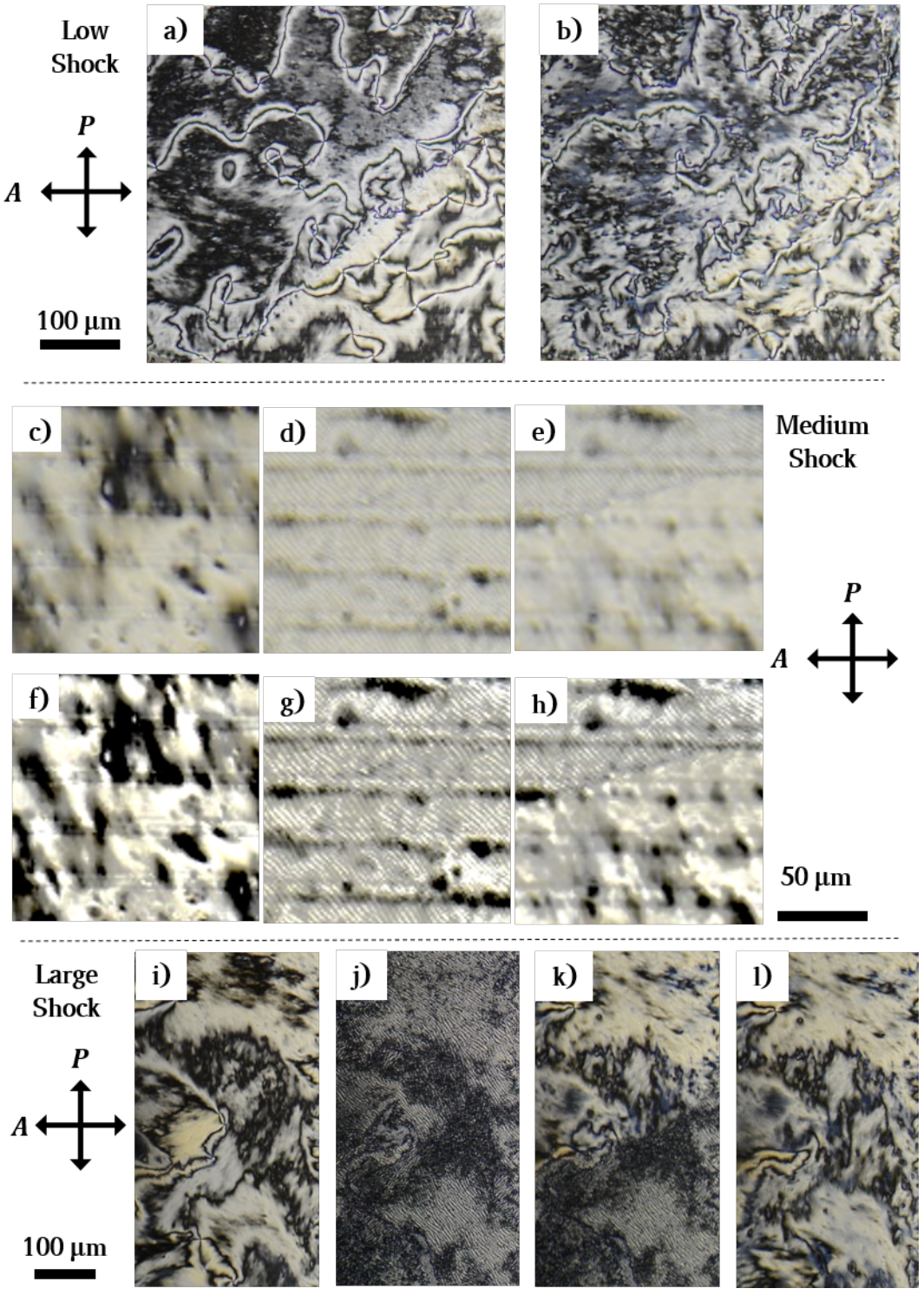
Low
Shock
P
A
100 µm
a)
b)
c)
d)
e)
Medium
Shock
P
A
f)
g)
h)
50 µm
Large
Shock
P
A
100 µm
i)
j)
k)
l)

Figure 6.8: Shock induced undulations in a surface-stabilised homeotropic SmC(*). The device is treated with C_8 silane, $d = 25 \pm 1\ \mu m$, and filled with 8.3% SCE13(*) mixture. $T = 50\ ^{\circ}C$, and observed with POM. a): Before and b): after the application of low mechanical shock, where **c**-director reorientation is observed. c): Before, d): immediately after, and e): a few seconds after a medium mechanical shock. Undulations are seen to appear in the SmC* texture once the pressure is removed, and dissipate soon after behind a moving dislocation line of layer formation. f-h): The same images as c-e with an increased contrast. i): Before, j): immediately after, k): a few seconds after, and l): one minute after the application of a high mechanical shock. Double undulating textures are observed, being darker and more pronounced than the medium shock. The undulations dissapear in the same manor as thermally induced undulations with no apparent damage to the smectic layers. m): Magnification of the induced single and double undulating textures.

the undulations.

A high pressure results in more pronounced undulations induced into the smectic texture, which are darker, and shown in Figures 6.8 i) to m). The darker textures are the result of higher amplitude undulations due to the larger displacement of the liquid crystal. The undulations are more chaotic than those observed with a medium shock, shown in Figure 6.8m. In the same way as the medium pressure undulations, the high pressure undulations dissapear behind a moving dislocation line, returning the texture to its previous schlieren state.

Based on the observations from Figure 6.8, it is concluded that the effects of shock-induced flow on a homeotropic SmC(*) are equivalent to those observed when cooling the sample at a sufficient rate to induce thermal layer undulations. Both effects occur due to an instability arising in the smectic layers. On reducing temperature, new layers form to satisfy the reducing d_C, and is observed to be energetically favourable to allow the layers to first buckle and undulate to temporarily satisfy the instability before new layers are formed. Once enough layers can simultaneously form, or the undulations become too high in amplitude and therefore become energetically unfavourable, a dislocation line of layer formation moves across the sample, restoring homogeneous smectic layers. Similarly on mechanically compressing the cell, the cell volume is reduced and so reducing the total number of allowed smectic layers. This is observed as a flow away from the compression point, where the **c**-director aligns with the flow direction, and the layers slide over one another. Once this mechanical pressure is removed and the maximum volume of the cell is restored, the LC flows back to fill this new space. As observed from thermally induced undulations, new layers don't form spontaneously, and so the layers undulate to fill the new volume first. Then, after a few seconds new layers form to satisfy the number of layers than may fill the space uniformly with no undulations. This results in a significant **c**-director reorientation, influenced by both the direction of flow and the direction of the layer formation dislocation line.

Therefore it is found that the homeotropic layer configuration remains preferred after a mechanical shock, as introduced in Chapter 4, Figure 4.3. It appears plausible that the layer undulations are the reason for this. The surface anchoring conditions ensure that the layers remain parallel to the substrate normal following shock induced flow, whereby they slide over one another in the induced direction of flow. This, combined with the layers preferably buckling rather than tilting prevents the layers locking into a new orientation. And so, the disruption in the bulk is replaced by well oriented, homeotropic smectic layers once the mechanical pressure is removed. If there is a sufficient force to lock the layers into a tilted position, this disperses as the dislocation line creates new layers, restoring the layers to form parallel to the layer normal. This geometry therefore appears to "self-heal" following a mechanical shock. As the anchoring condition has no preference to reorient the **c**-director, this remains in the orientation induced by the shock and flow once the undulations have dissipated.

6.4 Summary - Chapter 6

The homeotropic alignment of SCE13(*) has been explored. On cooling, the smectic layers must decrease in size, but first buckle and undulate rather than spontaneously form thinner layers. There is a critical point at which layer formation is observed as a dislocation line sweeping across the sample following a temperature gradient. At slow cooling rates, there evidence suggests that the layers still undulate, and only forms new layers when a certain number can be created, related to the cell gap of the containment. These undulations were used to confirm that the A_{21} layer elastic constant is smaller than the A_{12} constant for SCE13(*).

The homeotropic geometry responds to a mechanical shock in much the same way, although the undulations are more chaotic. These undulations dissipate once the shock is removed to return the number of smectic layers to the optimum for the cell gap to return to the most energetically favourable orientation. The direction of layer flow ensures little to no tilting of the smectic layers occurs, preventing

defects locking the layers in place. This is the downfall of the planar geometry. Unfortunately there is no strong preferred orientation for the **c**-director, and so despite they layers returning to a homogeneous layered alignment in a "self-healing" mechanism, a once dark state looses its optical contrast.

Chapter 7

Textures of Homeotropic Smectic C(*) Alignment in the VGA-FLC Geometry

In this Chapter the effects of using homeotropic gratings to align the SCE13(*) is explored. The VGA-FLC geometry is described in Chapter 4, and SCE13* characterised in homeotropic alignment in Chapter 6. The potential for a shock-resistant geometry for enhancing FLC alignment in displays and devices is investigated. Introducing surface-relief gratings has the chance to further disrupt the smectic layer alignment such that a dark state cannot be obtained due to induced undulations. There is also a possibility that if homogeneous layers are obtained that a mechanical shock will disrupt and reorient them such that they will not return to their initial alignment. Despite this, there is great potential for grating alignment to create a preferred alignment direction for the smectic **c**-director, which will restore the alignment following a mechanical shock. This is similar to the use of surface-relief gratings for the Zenithal Bistable Display [167]. The effects of surface-relief gratings on the homeotropic smectic layers of a FLC have not previously been studied. This Chapter explores the effect.

7.1 FLC Textures Formed on Homeotropic Surface-Relief Gratings

The goal is to induce sufficient elastic stress into the smectic layers such that the **c**-director has a preferred alignment direction and the layers are not disrupted through the bulk. Based on Chapter 6, it is expected that A_{21} undulations will be favoured at the grating surfaces as the lowest energy distortion (Equation 6.3). The grating pitch and grating amplitude must be controlled to obtain this state. From the outset it was clear that the gratings must be a low amplitude and low pitch to meet this requirement. The fabrication of surface-relief gratings is explained in Chapter 5. A pitch of 4 μm was found to be satisfactory to provide **c**-director alignment, and could be fabricated using the DWL and the SU-8 photoresist, and so was kept constant throughout this work. This pitch also approximately matches the layer undulation pitch of SCE13(*). In addition, this pitch ensures that diffractive effects from the grating are minimised. The choice of A_{PP} is explored in this Section. The homeotropic anchoring provided by the vapour phase deposition of C_8 silane was not varied as it was found to give excellent alignment to SCE13(*).

7.1.1 The Grating Amplitude and Pitch

Preliminary tests were performed with SCE13-R to avoid complications forming from chirality. This device used SU-8 surface-relief gratings written directly onto one substrate, which are $0.5 \times 0.5\ mm^2$, and spaced 0.2 μm from the next. This provides regions with no grating alignment to enable comparisons between the two. The A_{PP} varies from $0.0 \rightarrow 0.8$ μm with 4 μm pitch. The offset of the gratings was approximately 2 μm, with a cell gap of $d = 6.3 \pm 0.6$ μm.

It is predicted that the pitch of the grating is responsible for the alignment of the **c**-director on grating alignment. It was calculated from Figure 6.4 that the layer undulation pitch due to A_{21} layer bends of SCE13(*) was 4.4 μm. This is approximately the pitch chosen for the surface-relief gratings. Therefore, the

Table 7.1: The measured A_{PP} for the surface-relief gratings used in Section 7.1.1.

Colour	A_{PP} / μm
Red	0
Green	0.77 ± 0.02
Yellow	0.33 ± 0.02
White	0.3 ± 0.1

surface-relief grating pitch was matched to the lower elastic deformation undulation pitch of the smectic layers for SCE13(*). In addition, the amplitude of the gratings should be large enough to ensure a controlled A_{21} undulation and so directing the **c**-director, but small enough so as to not cause low-amplitude layer distortions through the device. This ensures the optical contrast is maximised and homogeneous layer alignment through the bulk.

The device was controllably cooled from the isotropic phase into the nematic phase, and through the SmA phase. Throughout, the texture appeared dark on rotation between crossed polarisers in all areas of the device, with no sign of disruption to the homeotropic layer alignment over the gratings. The SmC phase showed the same observations as Section 6.3 for the regions between the surface-relief gratings.

Figure 7.1 shows the induced alignment of the SmC(*) at 30 $^{\circ}C$ both over gratings and without gratings. The gratings are marked with coloured circles to identify their amplitude and their position on rotation. The amplitudes are given in Table 7.1. The grating with no amplitude (a square of SU-8) was a control to confirm that the same alignment is obtained on surface-treated ITO glass and SU-8 structures. The alignment is confirmed to be the same schlieren texture, although with lower transmission due to the offset of the SU-8, and so reduced retardation. This confirms that the surface treatment is effective on both ITO glass and SU-8, and provides no controlled **c**-director orientation. This is confirmed with rotation of these regions with the addition of a full wave-plate, shown

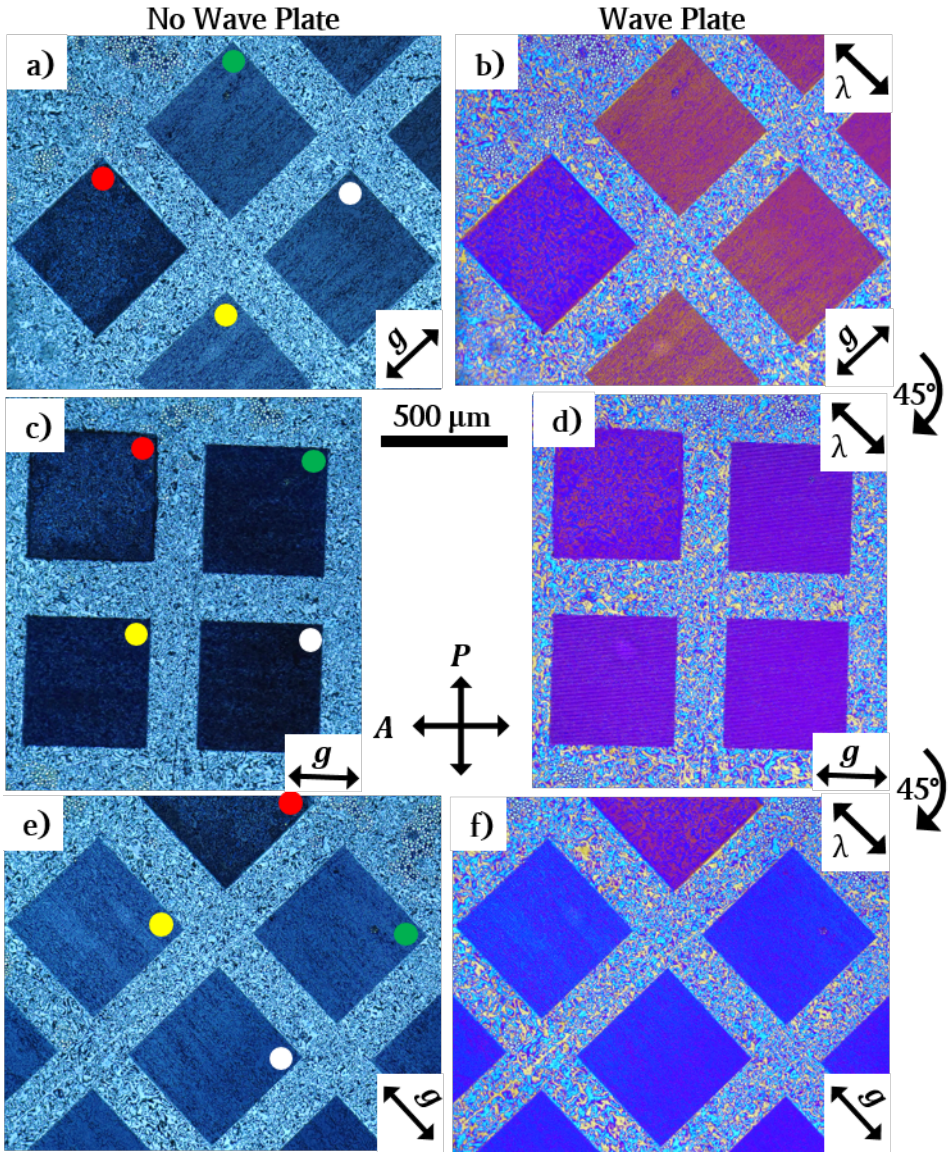

Figure 7.1: The alignment effects of homeotropic surface-relief gratings on the smectic **c**-director. A selection of $p = 4\ \mu m$, $A_{PP} = 0 \rightarrow 0.8\ \mu m$ SU-8 gratings, $d = 6.4 \pm 0.6\ \mu m$, and filled with SCE13-R. The coloured dots are a guide to the eye, and indicate the grating amplitude, with values for A_{PP} given in Table 7.1. a,c,e): Rotations of the gratings between crossed polarisers, showing regions with no gratings showing a schlieren texture, and regions with gratings induce a preferred **c**-director orientation. b,d,f): A full wave plate oriented at 45° to crossed polarisers reveals the **c**-director orientation is perpendicular relative to **g**. This reveals that the smectic layers form an A_{21} elastic deformation.

in Figures 7.1 b), d), and f).

In Figure 7.1 it is clear that the areas with surface-relief gratings do not show the same schlieren texture. The **c**-director has a preferred orientation in relation to **g**. This is evident on rotating the gratings between crossed polarisers, where the texture appears darker when parallel to the polariser, and brightest when at 45°. The three gratings indicate no obvious disruptive alignment to the homeotropic smectic layers.

The addition of a full wave plate was used to confirm a favourable orientation induced to the **c**-director, emphasised in the comparison of Figures 7.1 b), d) and f). The birefringence colours on rotation change from orange at +45°, purple at 0°, and blue at −45°. This result confirms that the **c**-director has a preference to align along the grooves of the grating, defined as perpendicular to the grating vector, **g**. This is the result of an A_{21} elastic deformation over the surface-relief grating. There are no cross-hatched textures which confirm that there is no preference for an A_{12} elastic deformation, or double undulations. This confirms the prediction made with Equation 6.3, where the A_{21} elastic deformations were observed and measured to be the smaller elastic layer deformation and would preferential form over the 4 μm pitch grating alignment. This was observed for all gratings investigated throughout this project that induced preferred **c**-director alignment to SCE13(*). A_{PP} up to 1 μm were observed to show this favourable alignment of the **c**-director, and lost controlled alignment at $A_{PP} < 0.1$ μm. No gratings $>>$ 1 μm were fabricated due to limitations of the fabrication techniques, and so the upper limit to preferentially orient the **c**-director is currently unknown.

Closer inspection of the textures on the gratings is shown in Figure 7.2. This reveals a series of defects running within the texture. There are also repetitive darker and brighter regions arising from a combination of the varying amplitude of the grating and undulations in the smectic layers. These optics are dominated by the diffractive profile of the grating rather than A_{21} undulations. This confirms that the undulations are small and do not propagate through the bulk of the cell. Looking towards the line defects, they are purple with a full wave plate

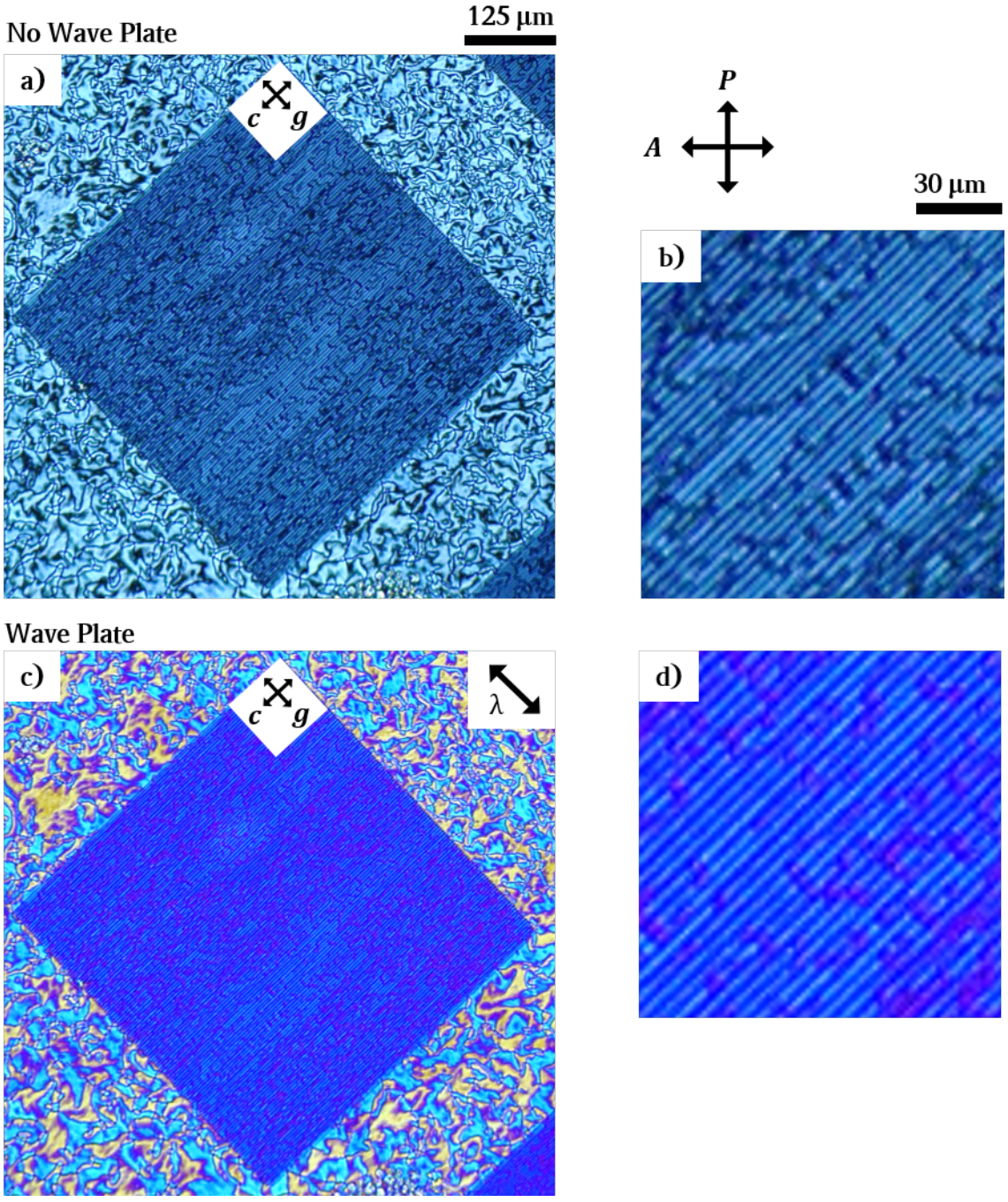

Figure 7.2: A magnification of the grating marked with a yellow dot in Figure 7.1. a): The grating at 45° rotation between crossed polarisers. b): A magnification of the texture. c,d): The same gratings with a full wave plate.

(dark/black without), and on either side the same retardation colour is observed. Chiral twisting in two opposite directions can be ruled out due to using SCE13-R. It should also be noted that the defect lines cannot be removed by reducing the cooling rate into the SmC(*) phase (as slow as 0.05 $°Cmin^{-1}$), or by applying DC electric fields (a method used for aligning bistable SSFLCs). The origin of these defects was determined with the application of electric fields, and is described in Chapter 8, Section 8.2.2.

To summarise, controlled **c**-director alignment is obtained with surface-relief gratings, controlled by the orientation of A_{21}. Optics due to A_{21} deformations are not observed indicating that they have a small amplitude and are contained to the surfaces of the grating. The bulk of the device shows non-undulating homeotropic layers.

7.1.2 Thermal Undulations and Smectic Layer Formation

This Section takes a closer look a the formation of thermal undulations in the VGA-FLC device geometry, which observed for homeotropic alignment of SCE13(*) in Section 6.2. The device examined here uses VGA-FLC Device 1, of which the key parameters are found in Table 5.1. As expected, thermal undulations still occur in the VGA-FLC geometry, and seemingly become more pronounced and stable. Figure 7.3 shows the different undulating textures obtained with grating alignment. These effects are also observed in the single grating devices shown in Section 7.1.1, but are difficult to characterise due to the large offset in the gratings. The double grating device uses low offset gratings making the textures easier to examine optically, and so is analysed here.

The sample is cooled from the I phase, through the N phase and into the SmA phase. It was cooled at a rate of 0.5 $°Cmin^{-1}$ into and through the SmC(*) phase. Importantly, the N and SmA phases were dark, showing good homeotropic aliment throughout cooling. This is shown in Figure 7.3a. The transmission remains constant on rotation between crossed polarisers, suggesting no layer tilt

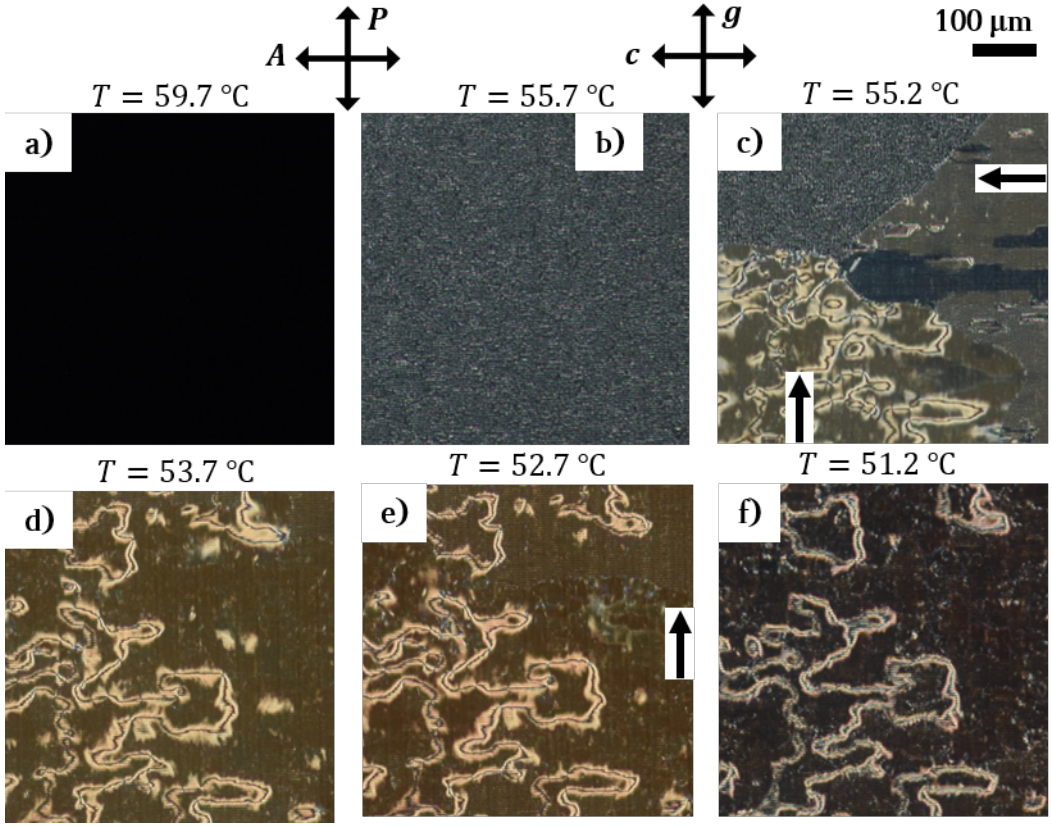

Figure 7.3: POM images on cooling VGA-FLC Device 1 at 0.5 $°Cmin^{-1}$ into the SmC(*) phase. a): $T = 59.7\ °C$ ($\Delta T = 1.1\ °C$), The dark texture at the SmA to SmC* transition before undulating textures appear, showing good homeotropic alignment. b): $T = 55.7\ °C$ ($\Delta T = 5.1\ °C$), Carpet-like textures arise below T_{CA}. c): $T = 55.2\ °C$ ($\Delta T = 5.6\ °C$), Carpet textures dissipate behind a dislocation line of layer formation. The number of defects on the grating texture depends on the direction of layer formation flow relative to **g**. d): $T = 53.7\ °C$ ($\Delta T = 7.1\ °C$), Texture free of undulations. e): $T = 53.7\ °C$ ($\Delta T = 7.1\ °C$), Undulations continuously appear and dissapear. f): $T = 51.2\ °C$ ($\Delta T = 9.6\ °C$), The texture on further cooling.

in the SmA phase. This indicates that if there are undulations induced by the gratings in the SmA they are small and contained to the boundary surfaces such that they don't propagate through the bulk.

At $\sim 59.2°C$ ($\Delta T = 1.6\ °C$) the texture becomes visibly brighter as θ_c increases. The defect lines observed in the grating alignment become visible at this point, albeit faintly (see Figure 7.2). Once the texture becomes sufficiently clear to examine optically, shown in Figure 7.3b, it becomes apparent that the texture is not the same as that of a uniformly oriented **c**-director aligned perpendicular to **g** observed in Figure 7.2. It is closer to that of the double undulating textures observed in the non-grating homeotropic geometry (see Figure 6.8).

Despite appearing random in alignment, this texture is relatively regularly ordered into a grid-like texture, with the double undulations always perpendicular to one another, much like the knit found in clothing or a carpet. At this stage the texture is termed the "carpet" texture to differentiate it from those induced by thermal undulations, as it is unique to the grating alignment. The texture becomes brighter when **g** is oriented at 45° between crossed polarisers, and is darkest at 0° when **g** is aligned with the polariser/analyser. Therefore in this texture the **c**-director is aligned by the grating. The pitch of the undulations perpendicular to **g** are difficult to measure as they don't follow the grating and "wobble", but within error are the same magnitude as those parallel to **g**.

These undulations were observed to form no matter the cooling rate from the SmA phase, ranging from 0.05 $°Cmin^{-1}$ to 5 $°Cmin^{-1}$. This is confirmed in Figure 7.4 on repeated measurements and for different rates of cooling. At faster rates of cooling, the carpet textures were observed to become more stable, whereby this disordered state can remain permanently if cooled too quickly through the SmC(*) phase. Therefore it is important to control the cooling rate through the phase transition in the grating aligned device. This frustrated carpet texture remains metastable until $\Delta T = 5\ °C$, and extends its stability proportional to the cooling rate.

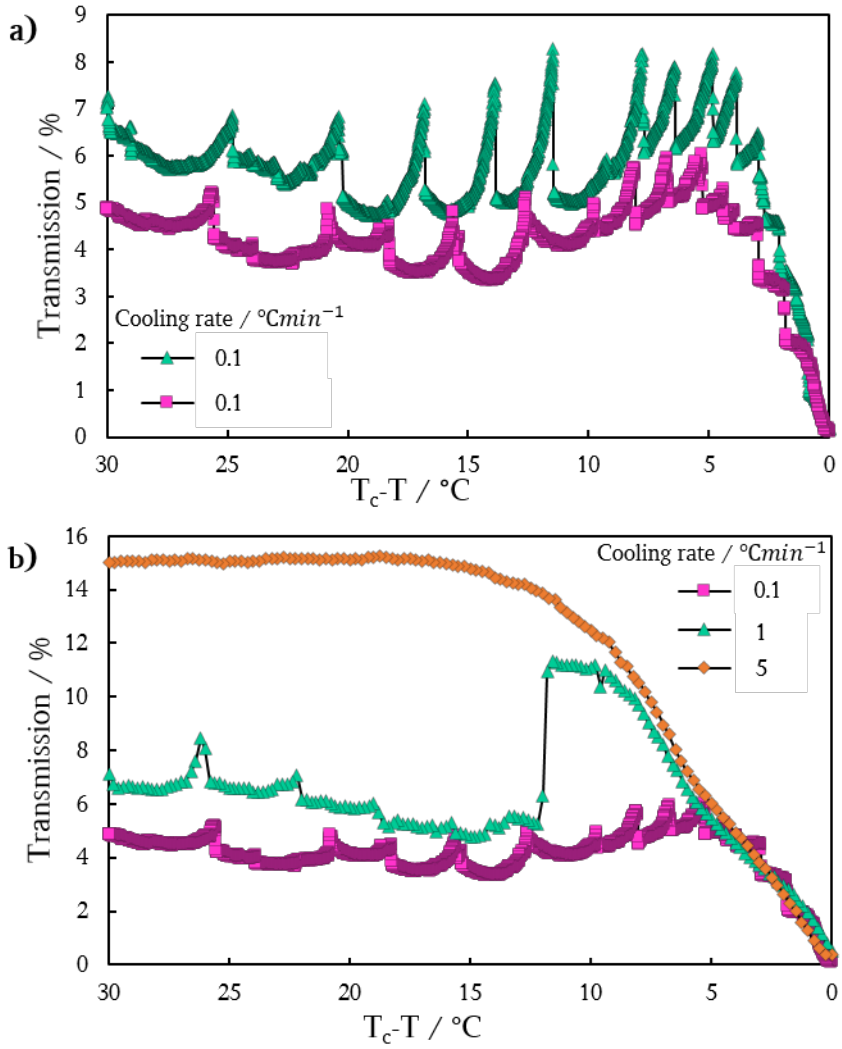

Figure 7.4: Graphs of the optical 550 nm transmission of a double grating homeotropic device versus the reduced temperature ($\Delta T = T_{CA} - T$) of Device 1: 5 % SCE13* mixture, $d = 30\ \mu m$, $A_{PP} = 0.24 \pm 0.07\ \mu m$. The black lines are a guide for the eye. a): Repeated measurements for the device cooled at 0.1 $°Cmin^{-1}$. b): Comparison of cooling the device at different rates. Purple squares: 0.1 $°Cmin^{-1}$, teal triangles: 1 $°Cmin^{-1}$, orange diamonds: 5 $°Cmin^{-1}$.

A question arises as to why the gratings induce this frustrated double undulation close to the phase transition, when not present in the SmA phase. The penetration length of the sinusoidal distortions induced into the SmA phase must be small due to no observed optical retardation. We suggest that it is the result of the combination of the penetration length of the undulations and the effect of boundary layers (z_{bl}) on the formation of the smectic C(*) layers. This is shown schematically in Figure 7.5. As the sample is cooled into the SmC(*), θ_c increases continuously, and is where the effective z_{bl} is largest. The combination of z_{bl} and the surface-relief grating forces regions of z_{bl} to overlap, specifically in the troughs or at the steepest edges of the grating. This is represented by the black arrows overlapping in Figure 7.5. This is not problematic for the SSFLC, or non-grating homeotropic smectic alignment, and so is unique for homeotropic sinusoidal-like gratings. The layers also preferentially undulate before spontaneously forming new layers on cooling. This combined effect of overlapping areas of z_{bl} and a preference to undulate rather than form new layers results in the optical carpet texture: a metastable state of frustration. This is the first time such an alignment effect has been reported.

The carpet textures dissipate on further cooling, for example at $\Delta T = 5\ ^{\circ}C$ in Figure 7.4. The carpet texture disappears behind a dislocation line of layer formation on cooling in a similar manner as observed after a mechanical shock or thermal undulations, as shown in Figure 7.3c. Of note here is that the texture that remains is influenced by the direction of flow of the dislocation line. Recall that **c** tends to align parallel to the direction of flow, either thermal or mechanical. If the flow is parallel to **g**, more defects form due to allowing two equal energy alignment states of the **c**-director to relax to. If the flow is perpendicular to the grating vector, fewer defects form as the **c**-director preferentially aligns in only one direction relative to the grating grooves. Nevertheless, the texture that remains indicates good **c**-director alignment, as seen in Figure 7.3d. Therefore it is confirmed that good surface-stabilised homeotropic SmC(*) alignment with **c**-director orientation is obtained with well aligned double gratings with small amplitudes, shown in Figure 7.3f.

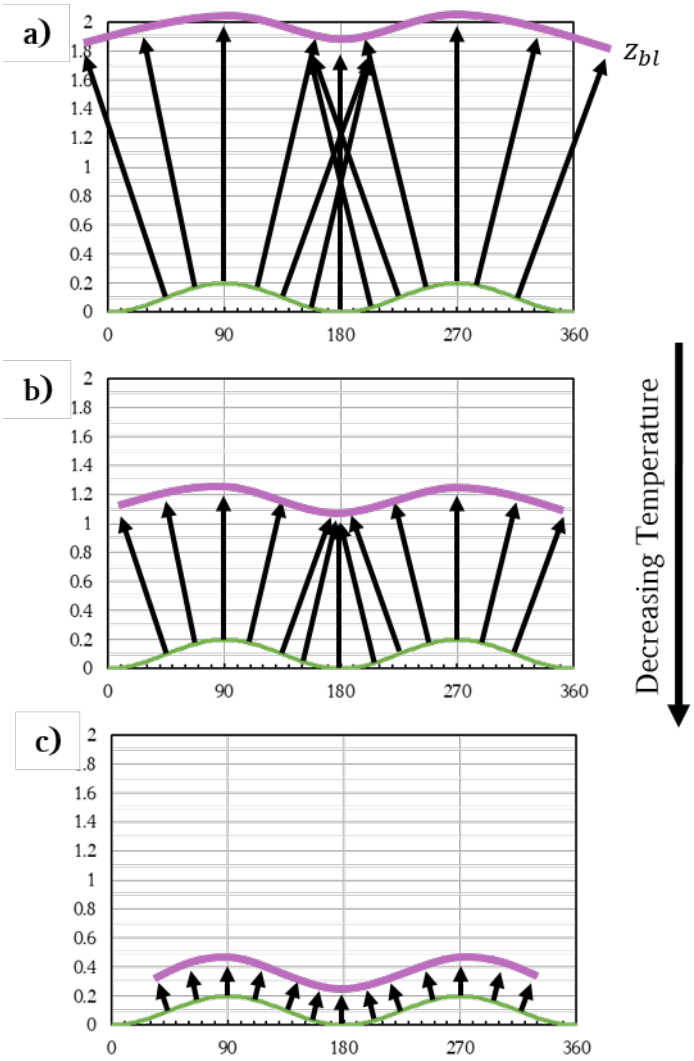

Figure 7.5: A schematic representation of the frustration in z_{bl} due to the introduction of a surface-relief grating. Black arrows are perpendicular to the grating surface normal. The grating has $A_{PP} = 0.2\ \mu m$ and $P = 4\ \mu m$. a): $z_{bl} = 1.8\ \mu m$, b): $z_{bl} = 1\ \mu m$, c): $z_{bl} = 0.2\ \mu m$

.

The bright defects running through the texture do not dissipate on further cooling. The homeotropic alignment about them is disrupted, and so the effects discussed are away from the defects. Their origin and removal are discuses in the following Chapters. Unfortunately they have not been removed during this work. They increase the transmission of the VGA-FLC geometry by approximately 3 to 5 %, and the number of defects that form is strongly correlated to the direction of the temperature gradient. This leads to the difference in lowest transmission in Figure 7.4a.

As the temperature of the grating aligned device is cooled beyond the carpet texture region, the texture continuously forms double undulations which dissipate behind the characteristic dislocation line of layer formation. These subsequent textures are less distinct than at the phase transition, as shown in Figure 7.3. These are analogous to the thermal undulations in the device with no gratings, however it appears that double undulations form more readily. The periodicity of the layer jumps is captured in Figure 7.4a. The transmission continues to increase and decrease as the thermal double undulation textures form and dissipate. The trend is to always return to a dark alignment, noting that zero transmission is not obtained due to the defects.

Figure 7.6 compares three different devices studied in this work, all cooled at a rate of 0.1 $^{\circ}Cmin^{-1}$ to obtain the best alignment of the SmC(*) phase. Device 2 shows a trend similar to the no grating cell as the gratings are misaligned by 15°, resulting in the **c**-director twisting by 15° through the device. Optically, the textures are identical to those observed for Device 1.

The important differences are that the device with no gratings tends to undulate, but this cannot be detected without a spectrometer. The single and double grating devices show ordered carpet textures undulations close to T_{CA}, that extend for $\Delta 5\ ^{\circ}C$. This is a direct effect of the grating alignment. This dissipates resulting in a uniformly oriented **c**-director and small double undulations appear and dissipate. These can be directly observed. Neither of the two grating aligned devices show 0 % transmission due to bright defects forming. The regions

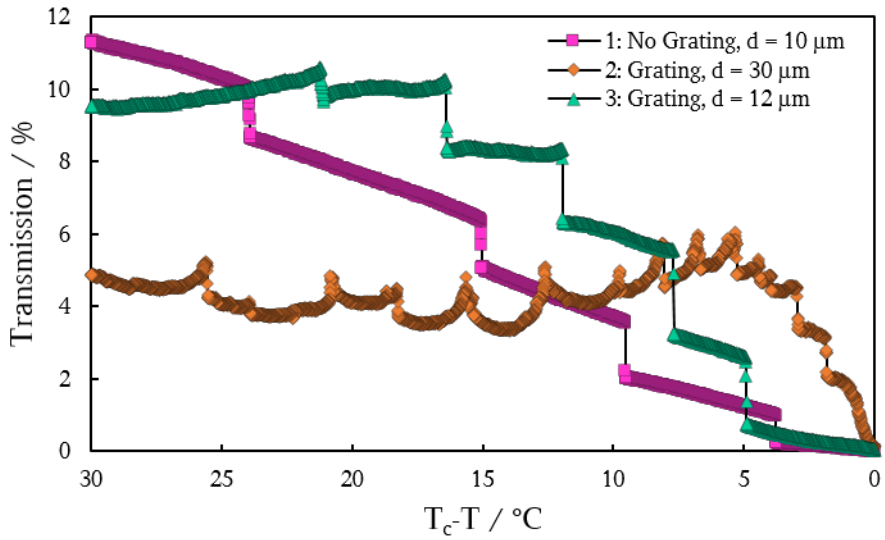

Figure 7.6: A graph comparing the three different devices examined in this Section cooled at 0.1 $°Cmin^{-1}$. Purple squares: no gratings, $d = 10\ \mu m$. Orange diamonds: VGA-FLC Device 1: $d = 30\ \mu m$. Teal triangles: VGA-FLC Device 2, $d = 12\ \mu m$.

away from these defects show good alignment that is dark, as shown in Figure 7.3.

Comparing all the devices, the larger cell gap allows more frequent layer jumps, and the smallest experiences the fewest layer jumps. There are 3 times more layer jumps in the $d = 30\ \mu m$ device than in the $d = 10\ \mu m$ device over a range of 30 $°C$. This suggests that the frequency of layer formation is determined by d, and that a layer jump occurs only when a particular number of layers can be created such that it is energetically favourable.

7.1.3 Heating VGA-FLC Devices

For practical use in a device, the VGA-FLC must not be loose its homeotropic **c**-director alignment on heating, and withhold a good dark state. Heating at a rate of 0.5 $°Cmin^{-1}$ from 30 $°C$ to 40 $°C$ is shown in Figure 7.7. Two observations

are made. Heating reveals major problems at the line defects running through the device, which grow and misalign the nearby alignment. This is particularly destructive in areas with a high density of defects, whereby they appear to merge creating larger areas of misalignment. Also, bright "speckles" appear in the dark regions away from defects. They become clearer at temperatures around $\sim 30\ ^{\circ}C$ on cooling, as can be seen in Figure 7.7a. They appear to exist at higher temperatures, but at a significantly lower transmission. It is unknown if these are induced by grating alignment, artefacts of silane deposition, or degradation of the material itself. Removal of these two negative factors by looking towards areas away from them reveals that the VGA-FLC geometry is not severely damaged on heating.

7.2 Shock Induced Flow in a Homeotropic FLC with Surface-Relief Gratings

It was found that shock-induced flow induces undulations in homeotropic smectic layers in Figure 6.8. The higher the force, the more distinct the undulations, with the possibility of forming double undulating textures. The undulations dissipated in a few seconds, resulting in shock-resistant layers, with a loss of alignment in the **c**-director. The introduction of surface-relief gratings has been shown to align the **c**-director. The shock-stability is henceforth explored.

Figure 7.8 shows a series of shocks applied to VGA-FLC Device 1. The application of these mechanical shocks is described in Chapter 3, Section 3.10.3. The optical texture of this alignment is shown in Figure 7.8a, where a well aligned dark state is shown. The image shows defect lines running through the texture, as well as an area free from defect lines. A low pressure shock is applied (approximate force shown in Table 3.2), shown in Figure 7.7b. The dark texture becomes bright due to induced flow and **c**-director reorientation. Areas with defects respond negatively to this pressure, while the areas farthest from defects show little or no disruption. Figure 7.8c shows the texture a few seconds after

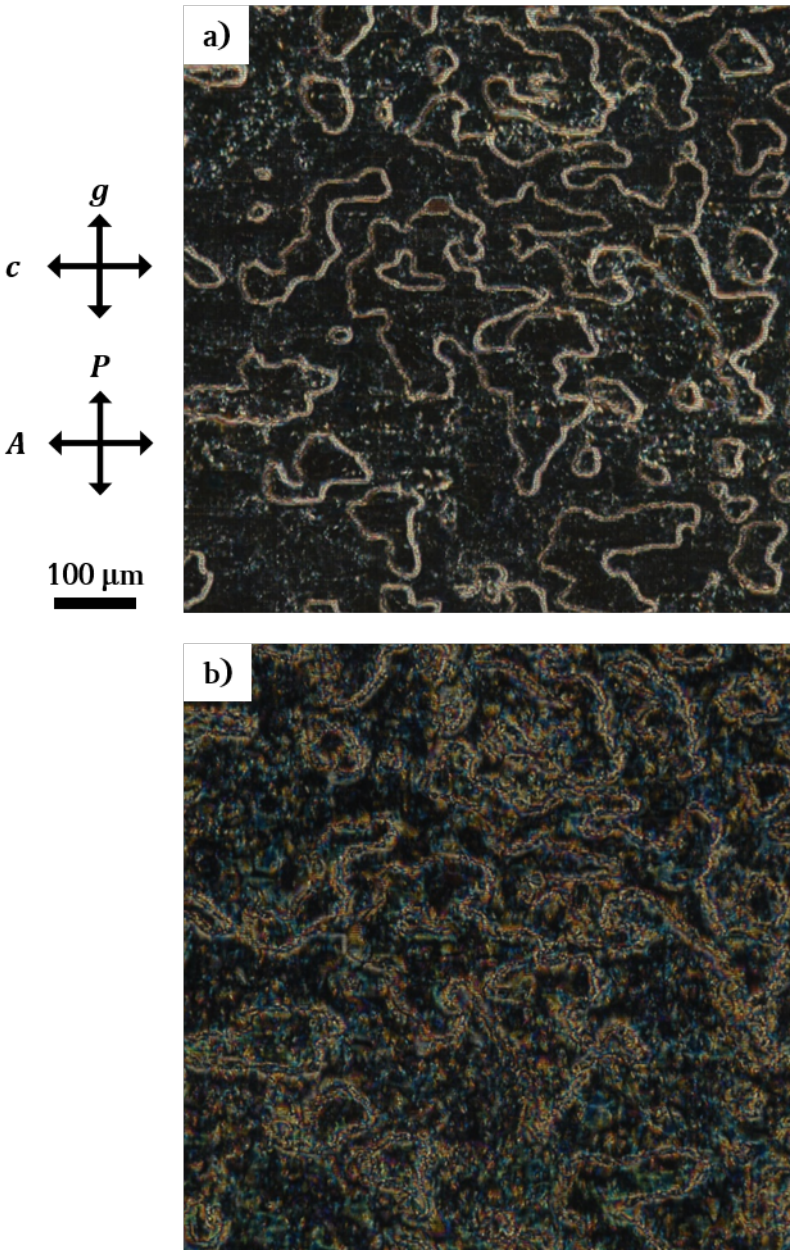

Figure 7.7: Heating of the VGA-FLC device reveals problems about the defects. Regions far from defects remain well aligned in a homeotropic layer orientation, with the introduction of "speckled" textures of unknown origin.

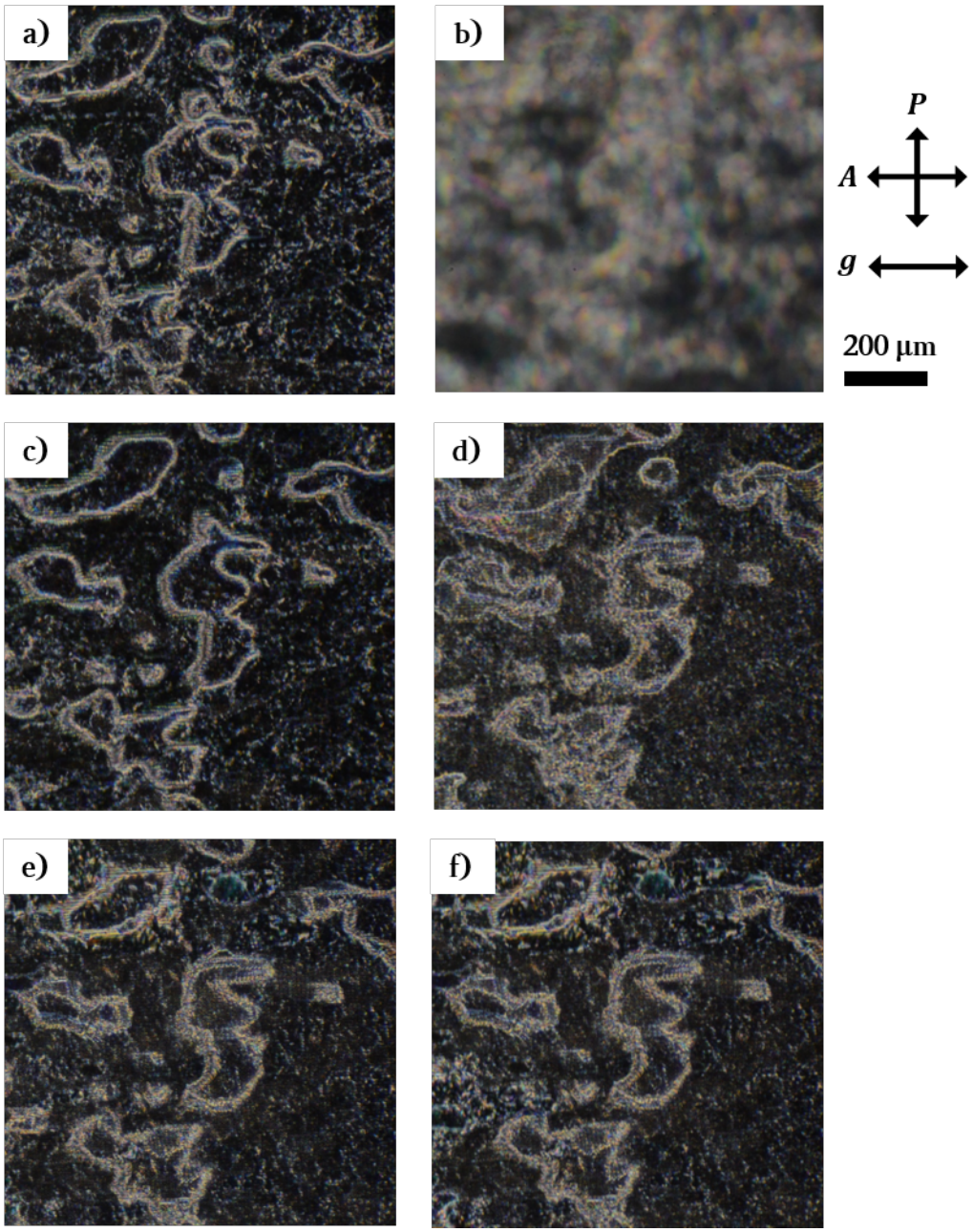
a)
b)
P
A
g
200 µm
c)
d)
e)
f)

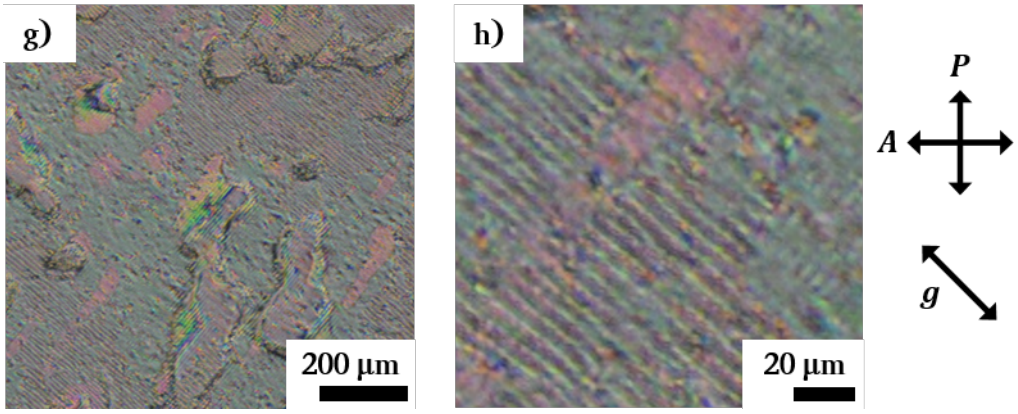

Figure 7.8: Shock induced flow of VGA-FLC Device 1 with $d = 30 \pm 2\ \mu m$ at $T = 20\ ^{\circ}C$. a): The dark texture observed with POM, with **g** is aligned with the polarisers. b): The application of a low pressure shock induces flow to the LC in the device. c): The alignment of the bulk is unaffected by the pressure. d): A large shock induces A_{12} undulations into the texture. e): The texture 10 *mins* after the initial shock. f): 30 *mins* after the initial shock, the texture remains almost unchanged. g): 45° rotation of the device. h): Magnification of g) reveals the meta-stable texture of the undulations induced by shock-induced flow, which highlight undulations induced perpendicular to **g**.

the pressure is removed. Noticeably there are reorientations around the defects, and the defect free areas have been unaffected.

A high pressure shock was then applied to the device. Figure 7.8d shows the texture immediately after the removal of this pressure. It is evident that the areas with defects have once again suffered the most distortion, where their bright texture has expanded into the previously well aligned texture. Double undulations were induced into the texture away from defects. The **c**-director is still aligned with **g**. This indicates that A_{12} elastic deformations have been introduced to the texture. These undulations do not fully dissipate within a few seconds, and appear more metastable than a shock without gratings.

Figure 7.8e shows the shocked texture after 10 *mins*. It is observed that the undulating texture is still present, and has shown signs of slowly dissipating. Figure 7.8f shows the texture 30 *mins* after the initial shock. There are no major differences in the textures, and the undulating texture is still present in some regions. Figure 7.8 g and h show this texture rotated by 45°. It can be seen that this state is bright confirming the retained **c**-director orientation. The metastable undulation texture that has been induced into the texture is apparent, as well as regions with undulations that have dissipated to the initial alignment before the mechanical shock.

Grating alignment has solved **c**-director misalignment following shock induced flow. However, on high pressures, A_{12} layer undulations are induced into the texture that are more metastable than observed without gratings. These undulations cause only minor increases to the transmission of the dark texture, and slowly dissipate back to a homogeneous homeotropic alignment. Importantly the layers are not forced and locked into a tilted geometry and so creating new defects or increasing Δn_{eff}. The A_{12} undulations are more stable due to A_{21} undulations already existing due to the gratings, and previous observations suggest that double undulations occur rather than the existing undulating amplitude increasing past a critical point.

7.3 Oily streaks: A Hypothesis for the Grating Defects

One question that arose, and remains an open question regards the form of the defects at or near the grating surface. A well aligned homeotropic sample with no gratings and aligned **c**-director has no defects, other than those that arise during layer formation as d_C decreases. Once surface-relief gratings are introduced, there are no defect free structures that can form over the grating whilst maintaining a well aligned homeotropic texture through the bulk. Such defects must be found near to, or at the surfaces of the grating. The hypothesis is that they take a

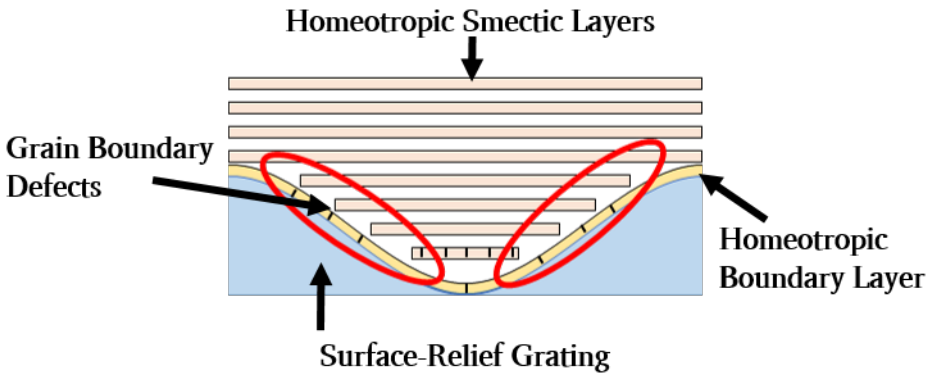

Figure 7.9: A sketch showing how the boundary layer over the surface-relief grating must lead to regions of defect formation in the VGA-FLC device. There are no observations of these defects in the textures of SmC* alignment, and so their effect must be small and ordered near to or on the grating surface.

form similar to those described by Nemitz et al. whilst exploring films of SmA and SmC materials with hybrid alignment (that is, planar and homeotropic alignment on either surface) [230, 231]. A sketch is given in Figure 7.9. This shows that there must be some discontinuity at the edges of the surface-relief grating. Nemitz et al. describe a rotating grain boundary, where two smectic layers at different orientations meet. They also describe an area where this boundary is 90° (the intersection of a planar and homeotropic layer), however based on the sketch in Figure 7.9, this does not occur in the regime of low amplitude grating alignment. Therefore the defect structure expected in the VGA-FLC device is described as a rotating grain boundary, which results in small dislocation lines which follow the grating surface and cause little disruption to the smectic layers and so minimal optical losses.

7.4 Summary - Chapter 7

The VGA-FLC geometry with SCE13(*) has been explored in this Chapter. Good homeotropic alignment was obtained. The VGA-FLC device geometry was pro-

posed to give a strong preferred alignment to the **c**-director, and displays the first time that gratings have been used for the homeotropic alignment of FLCs. Single gratings with SCE13-R were shown to favourably align the **c**-director by forming A_{21} elastic layer undulations at the grating surface, and maintaining homogeneous homeotropic alignment of the smectic layers though the bulk. Double grating devices were shown to surface-stabilise high pitch chiral mixtures of SCE13(*) and induce controlled **c**-director alignment. Thermal undulations were found to form carpet textures which dissipate to form good alignment at slow enough cooling rates. Recurring and dissipating undulations were observed in this alignment, similar to the alignment without gratings, with a preference to form aligned double undulations, while the **c**-director remained oriented with **g**. Low pressure shock induced flow was found to have no effect on the SmC(*) **c**-director, and larger forces induced metastable undulations into the texture. These undulations were small, and resulted in low transmission increases. Therefore this Chapter has introduced the VGA-FLC geometry as a promising approach to create a shock-stable FLC electro-optic device.

7. TEXTURES OF HOMEOTROPIC SMECTIC C(*) ALIGNMENT IN THE VGA-FLC GEOMETRY

Chapter 8

Addressing the VGA-FLC Device with In-Plane Electric Fields

8.1 Introduction

The homeotropic grating alignment of FLCs has shown good alignment and shock stability. In this geometry, the $\mathbf{P}_s$ is in the plane of the cell (x, y-plane), and so requires in-plane fields to switch the **c**-director to prevent disrupting the smectic layers. The success of active matrix addressing using TFTs and LCoS has enabled the use of IPS modes, and is used commercially for high viewing angle LCDs. The VGA-FLC geometry coupled with IDEs enables fast switching of the **c**-director by coupling the in-plane electric field to the FLC polar term. The result is to enable a shock-stable and ultra-fast switching optical modulator for use in displays and devices, and enabling modes that can't be achieved through NLCs. This Chapter explores the VGA-FLC device geometry and whether it can achieve fast optical response times.

Two VGA-FLC devices are explored in this Chapter, both of which have one IPS electrode on one surface, surface-relief gratings on both surfaces, and treated with C_8 silane to induce homeotropic alignment. This geometry is introduced in Figure 4.4, and the properties of the Devices given in Table 5.1. The IDEs have $l = 22.1 \pm 0.7\ \mu m$ and $w = 7.9 \pm 0.7\ \mu m$, over an area of $5 \times 5\ mm^2$, and are

fabricated as described in Chapter 3.

8.2 In-Plane Fields and the VGA-FLC Device

The aim is to obtain a 90° twist of the **c**-director through the device in the ON state, which will return to its OFF state with an applied restorative field (see Figure 4.4). The SSFLC reached microsecond switching times due to the ability to apply an OFF pulse to restore the OFF state in the same time as the ON pulse (see Equation 2.70). Therefore the VGA-FLC geometry must ensure that both the ON and OFF times are equally fast, to emphasise the strength of using FLCs over NLCs. The expected electro-optic response dynamics for the VGA-FLC geometry are given by the equations in Section 4.4.1.1.

8.2.1 ON Response

Obtaining the ON state is relatively simple. Applying a DC pulse to the VGA-FLC is the fastest way to induce a 90° twist of **c** through the device. **c** increases its total rotation through the cell as a function of applied **E**. At the furthest point between two electrodes ($z = 0$), **E** varies with cell gap (d) exponentially, as described by Equation 4.7, although this is usually considered to be approximately linear as given by Equation 4.9. This results is a description of the twist angle (ϕ) through the device (z-direction) as [207]:

$$\phi(z) = \phi_m \sin\left(\frac{\pi z}{d}\right) \ , \tag{8.1}$$

where strong anchoring is assumed such that $\phi(0) = \phi(d) = 0$ and the greatest amount of twist occurs at the centre of the cell such that $\phi(\frac{d}{2}) = \phi_m$. The rate of change of twist of **c** is not expected to be constant through the device, due to first exponentially decaying fields with d, and anchoring conditions. This also doesn't consider variations in the x, y-plane. Needless to say, the effects of in-plane fields

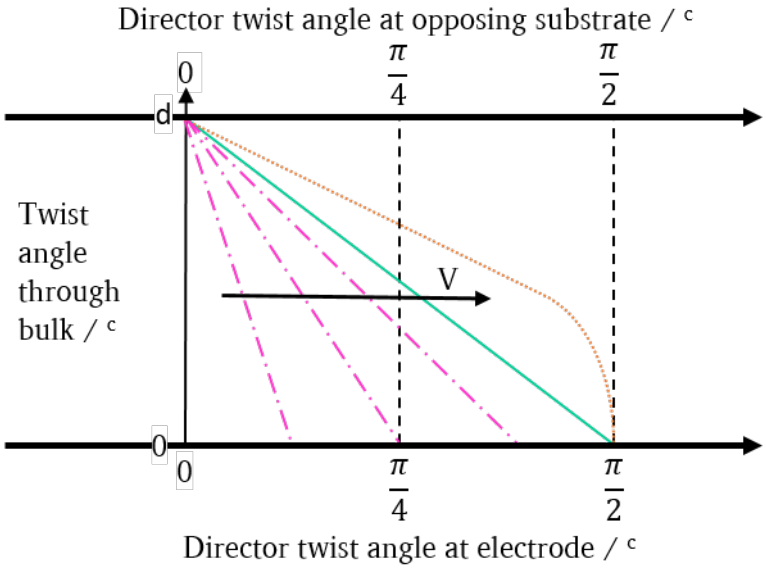

Figure 8.1: A schematic diagram showing how the total twist of the **c**-director is expected to vary through the cell (z-direction) as a function of applied voltage. The IDEs are located on the bottom axis of the diagram. The purple dotted and dashed lines show a twist less than 90°, or $\frac{\pi}{2}^c$. The teal solid line shows the an optimum 90° twist through the device. The orange dotted line shows an over-twist of the **c**-director, which results in a reduced I.

are complex, and so making some assumptions regarding their overall effect is necessary. Therefore the following statements are assumed to hold true:

- The total twist through the VGA-FLC device will increase on increasing **E**, and a twist of 90° results in the maximum transmission.
- Further increases to **E** beyond that required to obtain a 90° twist will begin to unwind the induced twist and reduce I.

Figure 8.1 shows a schematic diagram of the twist angle is approximately expected to vary with an applied voltage. Too little, and the twist will be $< 90°$ (purple dashed lines), too large and **c** will over-twist $< 90°$ (orange dotted line), and just right results in the maximum transmission (teal solid line).

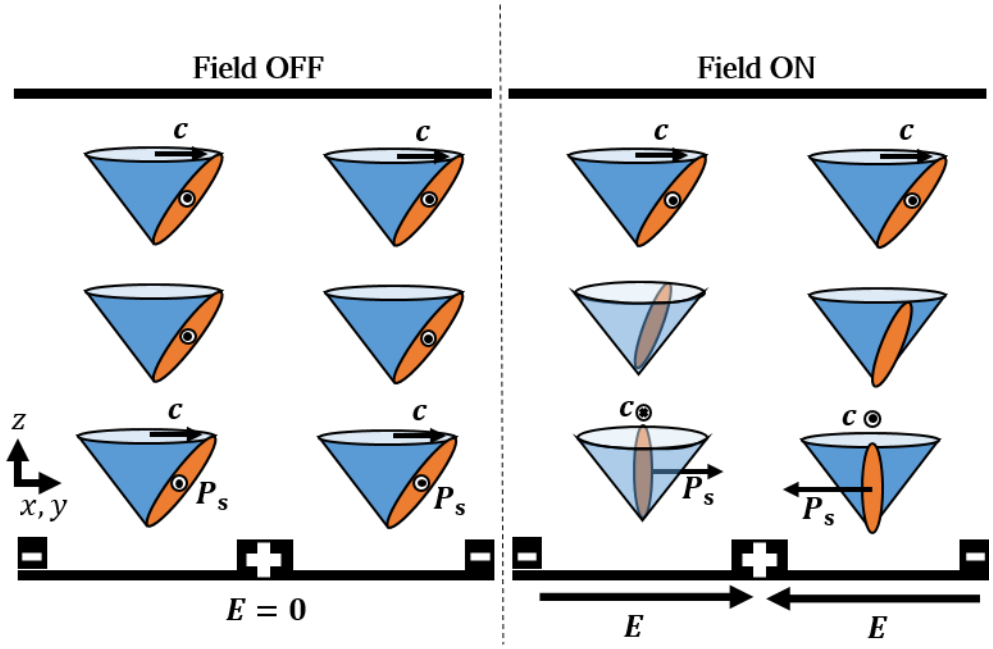

Figure 8.2: A schematic diagram showing how the **c**-director twists either ±90° depending on its orientation between IDEs.

The important consideration, and where the device becomes more complicated than NLCs dressed using TFTs is that $\mathbf{c} \neq -\mathbf{c}$. This means that the direction of the field relative to **c** will result in two possible twist directions, either left-handed or right-handed. This is shown schematically in Figure 8.2. Here, **c** is oriented in the same direction on either sides of an electrode (importantly $\mathbf{c} \perp \mathbf{E}$ through design). The field is the same magnitude on either side of the electrode, but opposite magnitude ($\pm\mathbf{E}$). The $\mathbf{P}_s$ aligns with the field, resulting in rotating the mesogen within the smectic layer. It is energetically favourable to rotate through the smallest angle, so in Figure 8.2 this is seen as the mesogens on the LHS of the positive electrode terminal twisting anti-clockwise, and the mesogens on the RHS twisting clockwise. When the field is removed, the mesogens relax to their initial alignment. This is a unique response resulting from the VGA-FLC geometry.

8.2.2 Determination of Defect Origin

This response was confirmed with the addition of a full wave-plate, and the application of a DC pulse with V less than that required to twist $\mathbf{c}$ by 90°. An example of this is shown in Figure 8.3d. Over the electrode, two different colours are observed (either orange or blue), which is the result of a twist of $\mathbf{c}$ in two opposing directions relative to the fast-axis of the wave-plate.

The origin of the defects that arise over the grating alignment when cooling into the SmC(*) phase was confirmed with this technique. A schematic diagram and POM micrograph are shown in Figure 8.3. This effect was observed over all line defects that populate the grating alignment. Over the defect line, blue or orange retardation colours are observed. This implies that $\mathbf{c}$ is twisting either clockwise or anticlockwise over the defect in the same sign electric field (between the same electrodes). The result is that $\mathbf{c}$ is aligned at ±90° over the defect line. This is allowed by the symmetry of the grating. The $\mathbf{c}$-director has two possible orientations of equal energy as $\mathbf{g} = -\mathbf{g}$. Therefore the defects arise when cooling from the SmA into the SmC(*) phase as $\mathbf{c}$ orients with $\mathbf{g}$ in one of two equal energy orientations.

8.2.3 OFF Response

Complications arise considering how the $\mathbf{c}$-director dynamically responds to the OFF pulse. Once the DC field is removed, $\mathbf{c}$ will relax back to its initial unwound orientation at some τ related to the rotational viscosity (γ_ϕ) of the FLC. This is the standard method for addressing NLCs using IPS and TFTs: no restorative pulse is applied, and the OFF time is determined solely by the viscosity and elastic constants of the material. Despite using FLCs, this OFF time is predicted to be the same magnitude as for NLCs.

Applying the opposite sign DC pulse to the VGA-FLC device will not return the device to its OFF state. In the NLC geometry, switching the magnitude of the ON pulse (from $+\mathbf{E} \rightarrow -\mathbf{E}$) is indistinguishable as $\mathbf{n} = -\mathbf{n}$. Therefore the

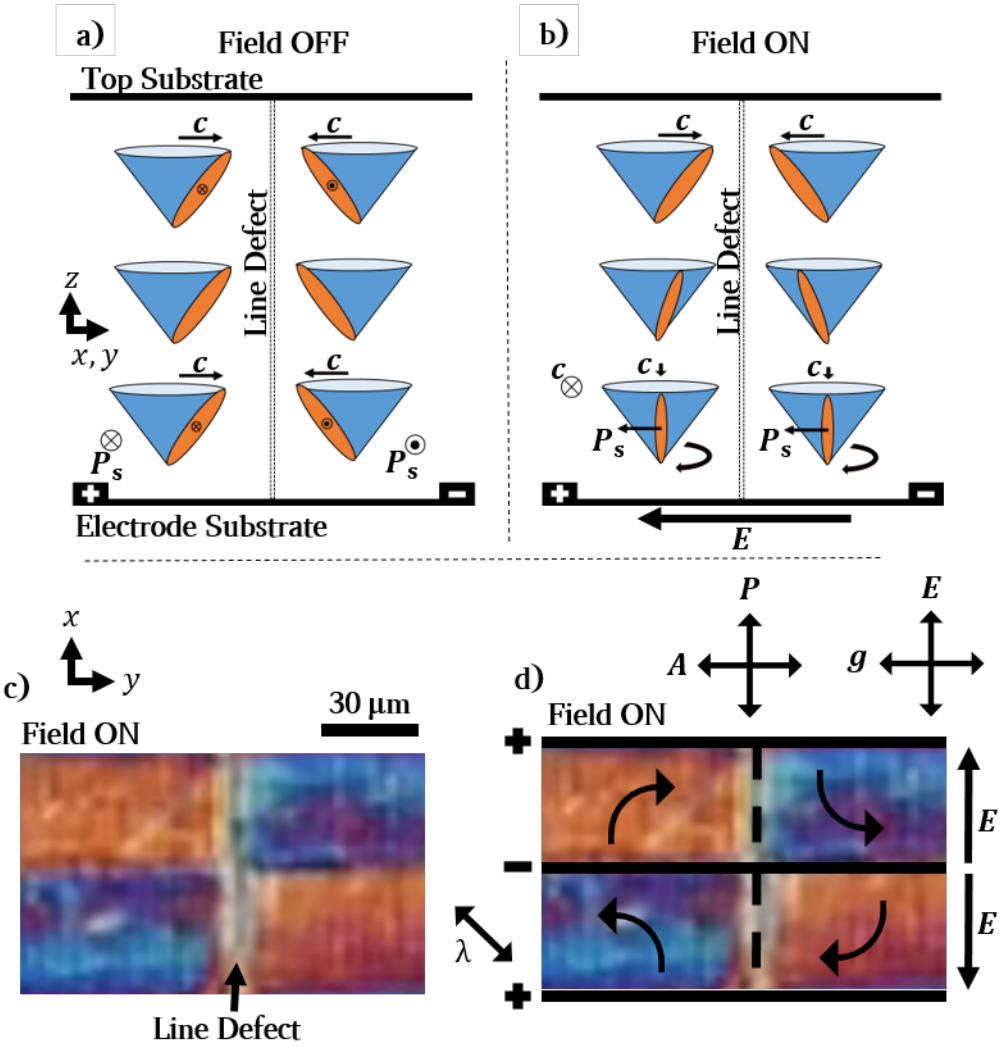

Figure 8.3: A schematic diagram showing the origin of the defects that arise on a homeotropic grating. a): Field OFF, and b): Field ON. As the **c**-director is initially at a 180° twist over the defect, an applied in-plane electric field will rotate the **c** in opposite directions. c,d): Experimental results showing how a full wave plate is used to determine the direction of **c** with a small electric field.

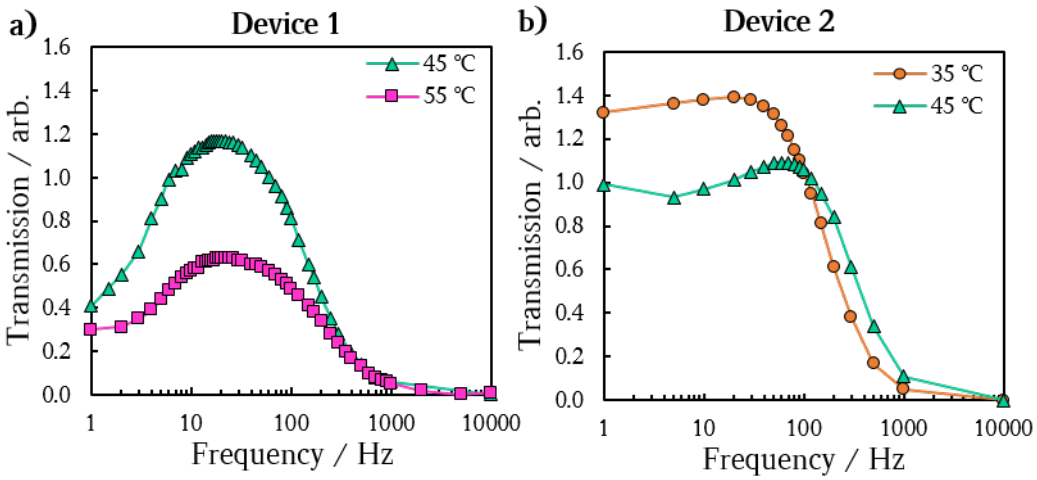

Figure 8.4: The transmission versus frequency response of the two VGA-FLC devices (see Table 5.1). a): VGA-FLC Device 1: $V_{rms} = 20\ V$. Teal triangles: $T = 45\ ^{\circ}C$. Orange circles: $T = 35\ ^{\circ}C$. b): VGA-FLC Device 2: Purple squares: $T = 55\ ^{\circ}C$, $V_{rma} = 30\ V$. Teal triangles: $T = 45\ ^{\circ}C$ $V_{rms} = 35\ V$. Transmissions (I) were measured with a photodiode and averaging the transmission over a cycle of square waves. The measured I is lower than that the theoretical maximum for these geometries due to **c** oscillating between dark and bright states. The experimental errors are approximately the size of or smaller than the data points. The lines are guides for the eye.

OFF pulse does not restore the OFF state as it is equivalent of the ON pulse. NLCs are not addressed to the OFF state, the field is just removed. The case for the SmC(*) is more complex due to the added factor that $\mathbf{c} \neq -\mathbf{c}$, as described by Figure 8.2. Therefore the sign of the field will cause a reorientation of the **c**-director, whereby it will twist in 180° in the opposite direction. To visualise this, imagine applying a low-frequency sine wave ($F = 1\ Hz$) where the field gradually oscillates resulting in I oscillating between dark and bright states as the **c** twist varies from $+90° \rightarrow 0° \rightarrow -90°$. This is equivalent for NLCs. Now imagine a high frequency input ($F = 10\ kHz$). This results in the NLC remaining bright or in the ON state, as $\mathbf{n} = -\mathbf{n}$. For the FLC, this results in no response, that is the **c**-director remains in its equilibrium OFF orientation. This is shown for two temperatures in Figure 8.4. As the frequency is increased for the VGA-FLC, the transmission decreases from a maximum value. Note that this is not an issue for addressing with TFTs where the refresh rate is 60 Hz. It does however create difficulties when measuring the electro-optic response of the VGA-FLC, as ionic build up needs to be considered. This is discussed further in Section 8.2.5.

8.2.4 Electro-Optic Response

The transmission (I) versus applied voltage (V) response was measured for the VGA-FLC device to confirm that the switching mechanism was as predicted. This is shown in Figure 8.5. Indeed, on increasing V, and therefore **E**, I was observed to increase up to a maximum value where a 90° twist is induced through the device. On increasing fields, I decreases approximately linearly as the twist through the cell becomes unevenly distributed (twist at the electrode surface). This is the same trend as seen in $-\Delta\varepsilon$ NLCs with IPS [35]. The differences in voltage required to obtain the peak transmission differ due to varying frequency between temperatures (to maximise I), coupled with increasing $\mathbf{P}_s$ and rotational viscosity. The transmission does not drop off substantially in the larger cell gap device on increasing **E** past that required for a 90° twist.

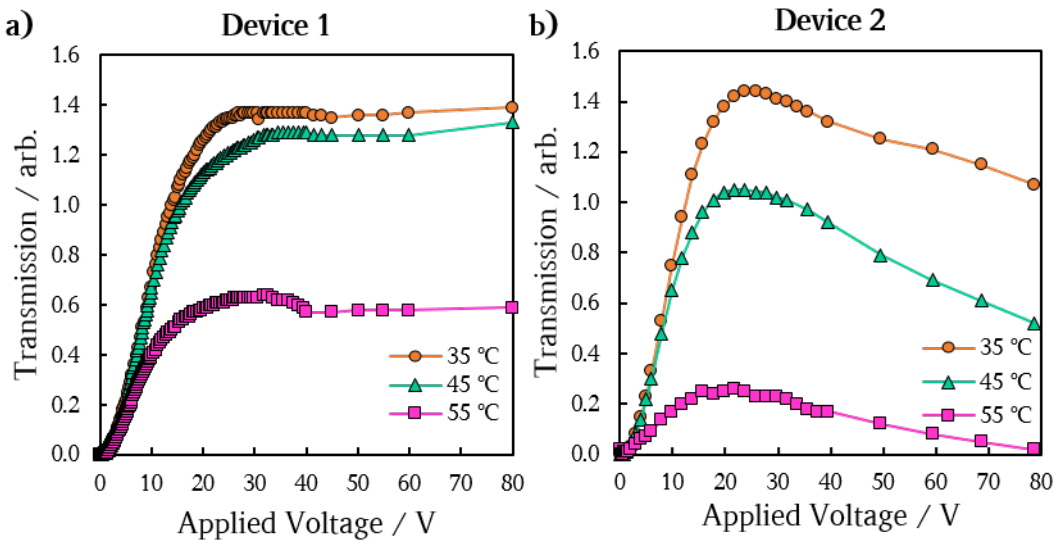

Figure 8.5: The transmission versus applied voltage of two VGA-FLC devices (see Table 5.1). a): VGA-FLC Device 1: $V_{rms} = 20\ V$, $F = 22\ Hz$. b): VGA-FLC Device 2: Purple squares: $T = 55\ ^{\circ}C$, $F = 100\ Hz$. Teal triangles: $T = 45\ ^{\circ}C$, $F = 50\ Hz$. Orange circles: $T = 35\ ^{\circ}C$, $F = 22\ Hz$. The frequency was varied for each measurement to obtain the maximum transmission (I). The transmission was measured with a photodiode and averaging the transmission over a cycle of square waves. The measured I is lower than that of the theoretical maximum for these geometries as **c** oscillates between dark and bright states. The experimental errors are approximately the size of or smaller than the data points. The lines are guides for the eye.

The effect of increasing voltage on the transmission was also explored by rotating the device between crossed polarisers. Here, 0° and 90° indicate the initial dark state obtained at 0 V, where both **g** and so **c** are aligned with crossed polarisers. At this rotation, following the curve with increasing voltage gives the results in Figure 8.5. As the device is rotated, I increases to a maximum at 45° between crossed polarisers, as expected for this device. A cell gap of 16 μm gives the maximum transmission for the quarter wave plate condition (see Equation 2.50) at $T = 45\ ^{\circ}C$, which is the reason for the relative I being larger for $d = 12\ \mu m$ when compared to $d = 30\ \mu m$. The transmission curve on rotation flattens out on increasing the applied voltage due to an increasing twist of **c** through d. The peak was expected to be at 0° and 90°, with slightly lower I at 45°. However here the average transmission is taken over a continually switching field, and so 0° and 90° switch through a dark state, while 45° switches through a bright state, and so skewing the average measured transmissions. The trend of the curves are as expected. Taking 40 V (blue diamonds) to be the optimum 90° **c** twist through the device for both devices, the cell gap at $d = 30\ \mu m$ gives a higher maximum transmission than that of $d = 12\ \mu m$ as it is closer to satisfying the Gooch-Tarry maximum given by Equation 2.64.

Figures 8.4, 8.5 and 8.6 confirm that the VGA-FLC device is responding to electric fields as expected. Importantly, the device continues to maintain its **c**-director alignment on repeated addressing. That is, on the removal of the electric fields the **c**-director returns to align perpendicular to **g**.

8.2.5 Ion Flow in FLCs

Before exploring the response times for the VGA-FLC device, the effect of ion flow in SCE13(*) and therefore considerations for the electrical addressing of the device will is discussed. Figure 8.7 shows the I response for various applied voltages over a range of temperatures and applied frequencies. The concern is that I drops during the continual application of an applied voltage, and reaches an equilibrium I, here $> 50\%$ lower than the maximum, seen in Figure 8.7a. When the voltage is

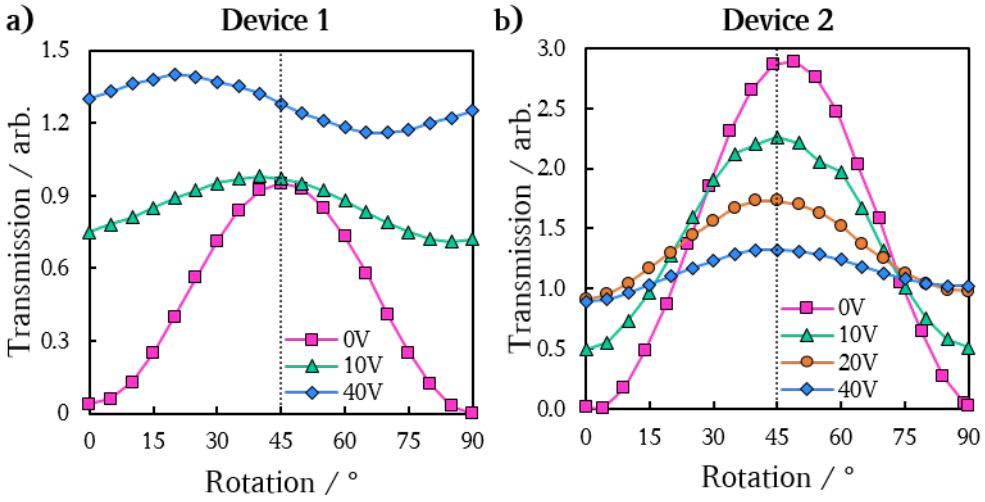

Figure 8.6: The transmission versus rotation of the device between crossed polarisers of the two VGA-FLC devices at $T = 45\ ^{\circ}C$ (see Table 5.1). a): VGA-FLC Device 1. b): VGA-FLC Device 2. The frequency was constant at 20 Hz and 50 Hz for the two devices respectively, to obtain the maximum average transmission. Purple squares: 0 V. Teal triangles: 10 V. Orange circles: 20 V. Blue diamonds: 40 V. The transmission (I) was measured with a photodiode and averaging the transmission over a cycle of square waves. Therefore the measured I is lower than that of the theoretical maximum for these geometries due to the **c**-director (**c**) oscillating between dark and bright states. The experimental errors are approximately the size of or smaller than the data points. The lines are guides for the eye.

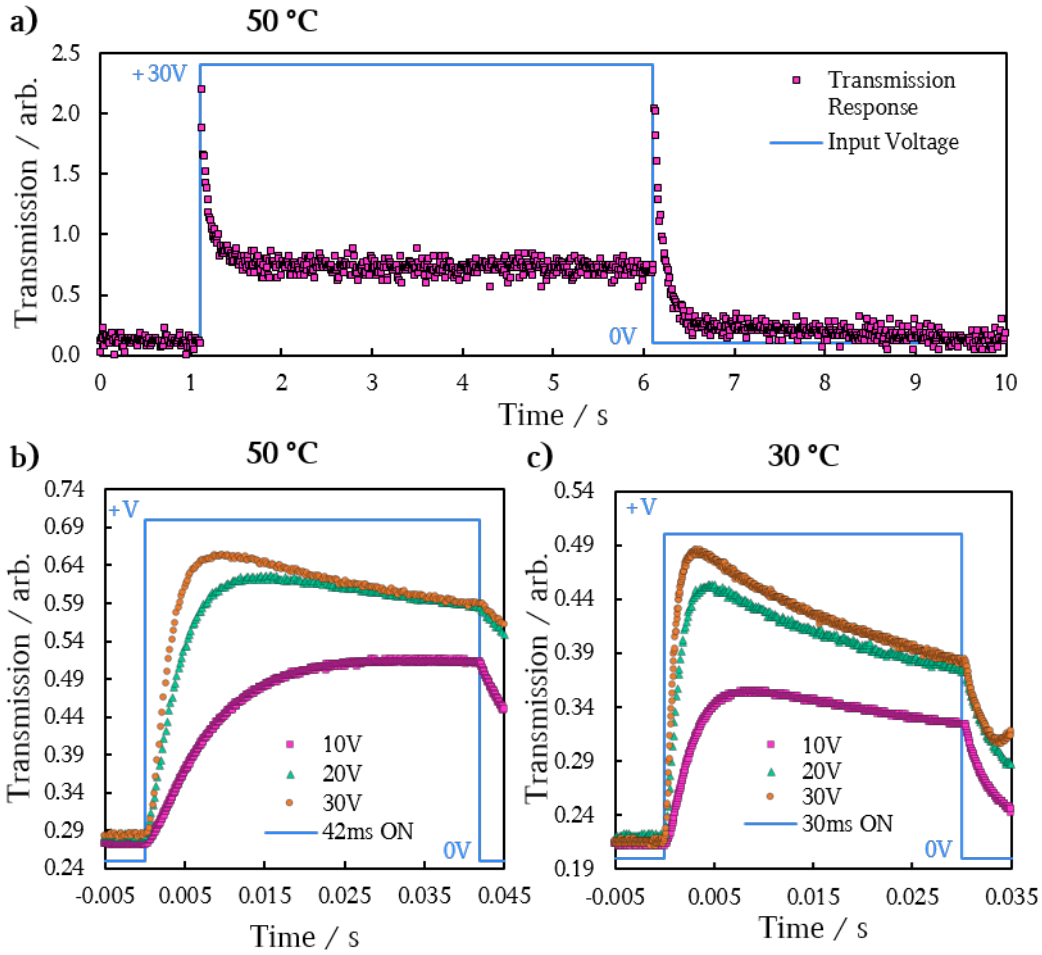

Figure 8.7: The transmission versus time of measurement for VGA-FLC Device 1: a): A $V_{rms} = 15\ V$, $F = 0.1\ Hz$ DC pulse is applied with a $V = 15\ V$ offset (such that ON is 30 V and OFF is 0 V, shown by the blue line) at $T = 50\ °C$. b): A 42 ms DC pulse applied to Device 1 at $T = 50\ °C$. c) A 30 ms DC pulse applied to Device 1 at $T = 30\ °C$. Purple squares: 30 V, teal triangles: 20 V, orange circles 10 V. The response of the **c**-director depends on the length of the applied pulse, and voltage applied at. The experimental errors are approximately the size of or smaller than the data points.

removed, I first increases back to a maximum, and then returns to the OFF state.

There are two factors responsible for this. First is that the applied V is large enough such that **c** is over-twisting past an optimum of 90° required for the maximum I. This is reasonable as on removal of V there is a peak in I suggesting that on returning to the dark state **c** must return via the optimum 90° twist. Second is that there is a shielding of the field caused by ionic charges building up at the electrodes. This is an issue frequently observed in FLC's [232]. This same of SCE13(*) is also relatively old (synthesised in 1980/1990's) and has not been purified to remove the ions as is required for TFT addressing. Ions respond to the field by moving to their oppositely charged electrode, creating an increased electrical current. Once the ions reach the opposite electrode, the current flow begins to reduce, until most the free ions have arrived. The flow of the ions is determined by the ionic mobility which is related to the viscosity of the material. Figure 8.7a suggests that **c** is over-twisting, due to the I peak on field removal.

This is not the case on examination of Figures 8.7b and 8.7c. Here, various pulses are applied for 42 ms and 30 ms respectively. The same trend is seen during an applied voltage, that is I increases up to maximum, and if V is large enough to form a 90° twist then I decreases. This is seen in Figure 8.7a. On removal of the field, I immediately decreases. This confirms that the decrease in I is due to ion shielding rather than an over-twist of **c**. At $V_{rms} = 10\ V$, I gradually decreases back to its OFF state. However, at $V_{rms} = 30\ V$, I goes through a turning point and then increases. It reaches a new maximum of lower magnitude than before, before returning to a dark state. An explanation for this is that when the field is removed, **c** begins to untwist back to its OFF position, but instead of stopping at this OFF position it continues to twist further in the opposite direction. That is, the effect is caused by the build up of ionic charge at the electrodes.

The amount of ions at the surface of the electrodes will be proportional to the applied voltage (simple plate capacitor: $C = \frac{Q}{V}$). Once the field is removed, the ions tend to diffuse towards the bulk of the cell and so creating a current in the opposite direction of the applied voltage. This is proportional in magnitude

to the initial applied V and length of time charged for. This results in **c** twisting in the opposite direction, and if of a large enough magnitude to rotate **c** beyond its OFF state.

8.2.6 Method for Addressing the VGA-FLC Device

These ionic effects are important when addressing the VGA-FLC device. In modern TFT addressing, the LC is purified such that it has few ions. It is therefore important to ensure that the results presented are not influenced by ion flow in the FLC. In the case of determining response times, the ion flow is considered to occur on a longer time-scale than the response of **c**. The peak in current back-flow occurs in 10's of milliseconds compared to the millisecond response times normal for FLC devices [232].

Ion flow has no effect on measuring the ON times (τ_{ON}) if the electric pulse is applied when the device is in its OFF state. The OFF times (τ_{OFF}) are more challenging and less repeatable because they are highly dependent on the applied V, and the length of time before removing V. Therefore to obtain the optimum results for τ_{OFF} based on purely **c**-director relaxation back to its initial orientation, the ON pulse should be terminated immediately once the peak I is obtained. This ensures no ionic effects influence the **c**-director relaxation.

The effect of electrically addressing τ_{OFF} to quickly restore the OFF state was also explored. It should be noted that for a TFT driven device, the time of the pulse is fixed, and it is the voltage that must be varied. Here τ_{OFF} was measured by applying the opposite magnitude voltage to the device at the point of maximum I. The length of the applied restorative pulse required to be varied, and was not the same as required for τ_{ON} due to over-twisting of **c** past the OFF state. This is shown in Figure 8.8a, where $V_{rms} = \pm\ 15V$, the ON pulse is applied for 5 ms, and three OFF pulses are applied for durations of 0, 1 and 5 ms. Here, with no OFF pulse applied (purple squares), **c** relaxes back

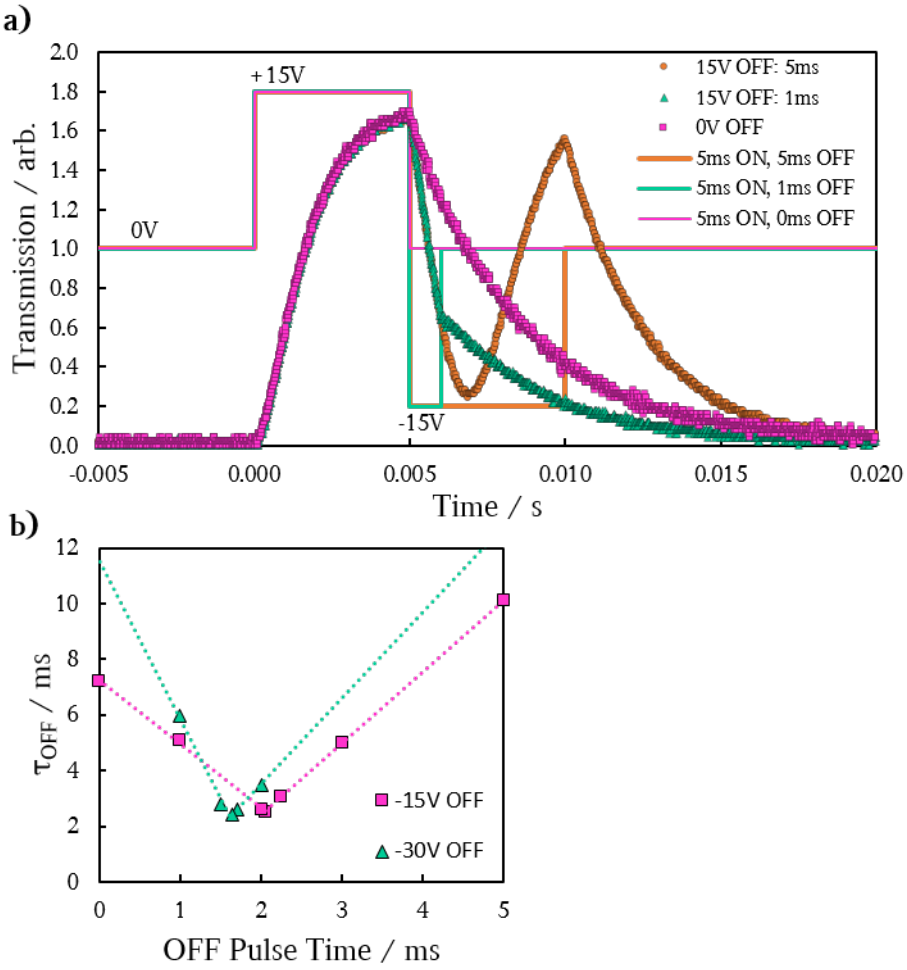

Figure 8.8: The transmission versus time of optical response for a variety of OFF pulses at $T = 50\ ^{\circ}C$ for Device 1: a): A constant $+15\ V$ on pulse is applied for $5\ ms$. Three OFF pulses are then applied. Purple squares: no OFF pulse. Teal triangles: a $-15\ V$ pulse for $1\ ms$. Orange circles: a $-15\ V$ pulse for $5\ ms$. The coloured lines indicate the time which the voltages are applied. b) A selection of OFF times obtained by applying pulses for different times and voltages. Purple squares: OFF times at $-15\ V$ measured after a $5\ ms$ ON pulse at $+15\ V$. Teal triangles: OFF times at $-30\ V$ measured after a $3\ ms$ ON pulse at $+30\ V$. The dotted lines are liner fits and act as a guide to the eye. The experimental errors are approximately the size of or smaller than the data points.

to its OFF state in the expected way. The shortest OFF pulse of 1 ms reorients **c** faster, shown by the steeper gradient, however the pulse in not applied for long enough to restore the OFF state. The remainder of the OFF response is similar to the 0 V relaxation. An OFF pulse of 5 ms (orange circles) causes a transmission minimum and then increases I as **c** twists in the opposite direction.

Figure 8.8b shows the trends obtained for the OFF times, and indicates how to obtain the fastest OFF times. Linear fits are shown to emphasise the trend, although are a more complex combination of two separate times: those assisted by a field ($\propto \frac{1}{\mathbf{P}_s}$), and those with no field (a decay curve related to γ_φ, B_{22} and the initial energy state). The gradient of the -30 V field is steeper than those of the -15 V field, and so shorter pulses are required for higher fields, as expected. τ_{OFF} doesn't reduce substantially despite requiring shorter pulses compared to τ_{ON}. Figure 8.8b emphasises the importance of electrically addressing τ_{OFF} with the correct restorative pulse. The same curves should be obtained on varying voltage and keeping the applied OFF time constant.

The example of the OFF response given in Figure 8.8 gives rise to some interesting results regarding the effect of the grating alignment. As expected τ_{ON} with an applied voltage is faster then τ_{OFF} if not addressed, such that $\tau_{(ON,\,+15V,\,5ms)} < \tau_{(OFF,\,0V)}$. τ_{ON} is approximately equal to or slower than τ_{OFF} if both are electrically addressed with the correct length pulses. This is in direct agreement with Equation 2.70, which says that in the SSFLC the ON and OFF times are approximately equal. In fact, if the OFF times for the VGA-FLC geometry are faster than the ON times, this implies that the gratings are acting to restore the alignment, and so creating a restorative torque to the ON times and assertive to the OFF times. This would be positive if considering the shock-stability of the device, and can be used in future to examine the effect of the surface-relief gratings in further detail. Alternatively it may be the effect of B_{22} acting to restore **c** to its lower energy unwound state.

8.3 Response Times of the VGA-FLCD

Response times were measured for two VGA-FLC devices at various temperatures and applied voltages, as described in Section 8.2.6. The devices and IDEs have properties as described in Section 8.1. Material properties for SCE13*, including $\mathbf{P}_s$, are given in Chapter 3, Section 3.10.1.

8.3.1 τ_{ON} Measurements

The fastest measured response times for a given voltage and temperature are summarised in Figure 8.9. The response times were measured as described in Chapter 3, Section 3.10.4, such that τ_{ON} represents the time that the measured intensity takes to go from 10% to 90% its minimum and maximum respectively. The maximum transmission was that at the peak of the curves shown by Figure 8.8. The general trend for the ON times are as follows. The higher the applied voltage, the larger the electric field, and therefore the faster τ_{ON}, as expected from Equation 2.70. As temperature decreases, τ_{ON} increases, despite an increasing $\mathbf{P}_s$ (Equation 2.26). This is due to an increasing rotational viscosity (γ_ϕ), where γ_ϕ follows the Arrhenius law [233]:

$$\gamma_\phi = \gamma_0 \exp\left(\frac{E_A}{R_g T}\right) , \tag{8.2}$$

where E_A is the activation energy, R_g is the gas constant, and γ_0 the pre-exponential constant of viscosity. Thus γ_ϕ increases at a greater rate than $\mathbf{P}_s$, and so resulting in slower τ_{ON} on reducing temperature. This is found for all FLC devices [234–236]. Of note is the decreasing gradient of τ_{ON} at varying T and constant V. The difference between these two devices is the cell gap, d, where:

$$\frac{d_{Device1}}{d_{Device2}} = \frac{30 \pm 2\ \mu m}{12 \pm 2\ \mu m} = 2.6 \pm 0.6 , \tag{8.3}$$

and it was expected that at constant V and T, $\tau_{ON} \propto d$. A ratio of 2.72 ± 0.02 is obtained at $T = 30\ ^\circ C$, but increases to 3.7 ± 0.3 at $T = 50\ ^\circ C$. These values are

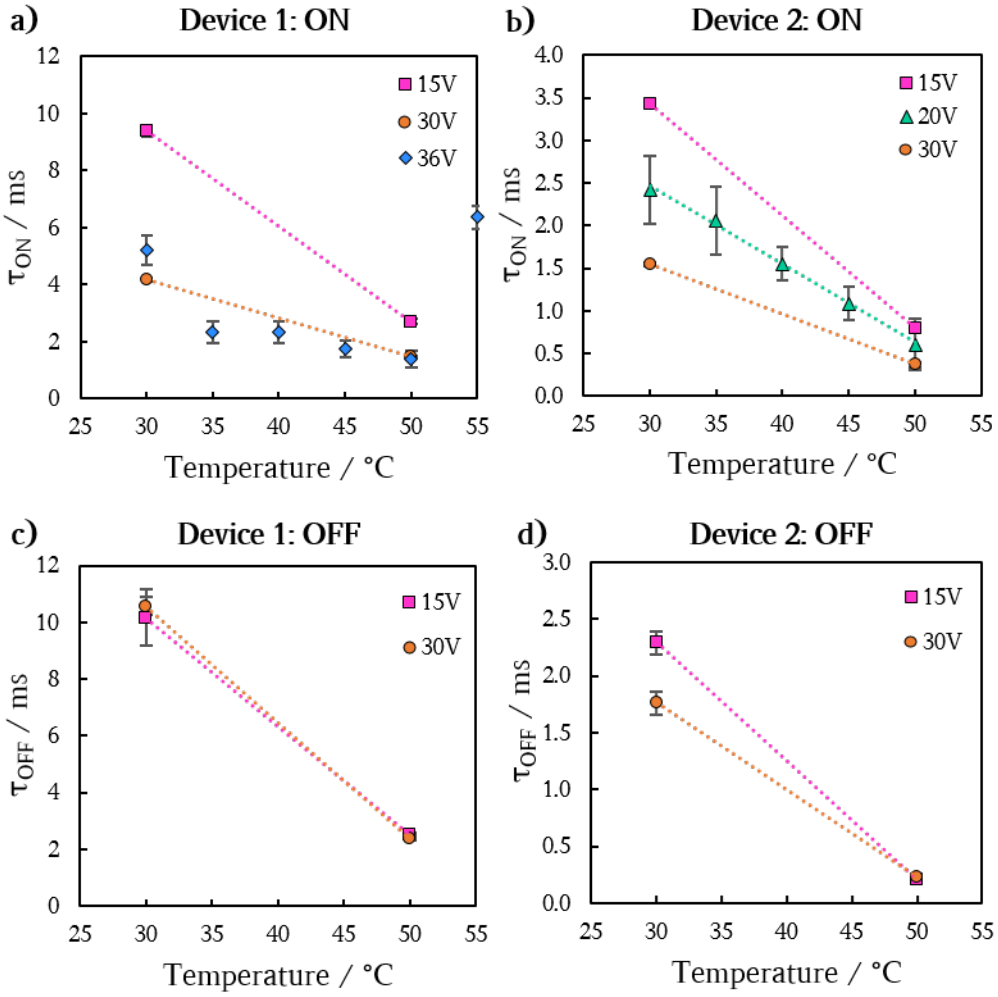

Figure 8.9: The response times for two VGA-FLC devices versus temperature for various applied voltages. Measurements were made with ON and OFF pulses of the same but opposite magnitude voltage ($\pm V$), but the times applied were varied depending on reaching a peak or minimum T_r, as described in Section 8.2.6. Measurements taken at 15 V and 30 V were taken over a number of repeats, while those at 20 V and 36 V are for just one measurement. Response times (τ) are calculated from 10 % to 90 % of the minimum and maximum T_r respectively. a): ON times for Device 1, b): ON times for Device 2, c): OFF times for Device 1, d): OFF times for Device 2. Purple squares: ± 15 V. Teal triangles: ± 20 V. Orange circles: ± 30 V. Blue diamonds: $\pm 15V$. All lines of best fit are guides for the eye, and are not necessarily expected to be linear.

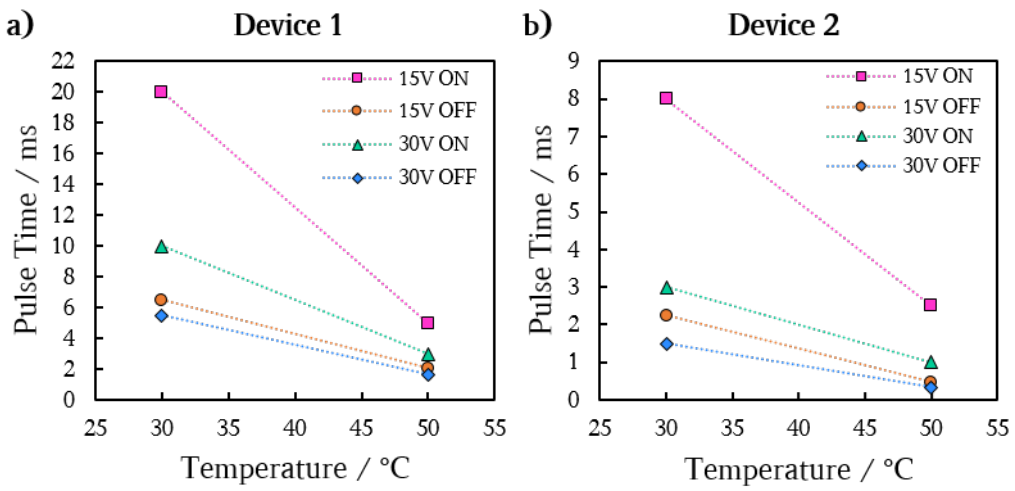

Figure 8.10: The length of electrical pulse required to obtain maximum I shown versus temperature, as a function of applied voltage. a): Device 1. b): Device 2. The lines of best fit are guides for they eye, and are not necessarily expected to be linear.

within error, but it should be noted that the values at $T = 50\ ^{\circ}C$ have a larger than expected difference.

8.3.2 τ_{OFF} Measurements

These τ_{OFF} values have been obtained by applying the same sign field as for τ_{ON} as described in Section 8.2.6 and shown in Figure 8.8 for the optimum length of time to restore the OFF state. These times are summarised in Figure 8.10.

The OFF times for the VGA-FLC devices are similar in magnitude to those of the ON times, and follow the same trends. This confirms that Equation 2.70 holds true when the VGA-FLC geometry is electrically addressed. The length of time of the OFF pulses depends on the length of time of the ON pulse. The OFF times always require a shorter pulse time than the ON times. This is a result of

ion flow on switching, and that the induced twist (B_{22}) is being unwound which is energetically favourable. Relaxation times for no field have not been presented, however an example of these times is given in Figure 8.8b. The trend is that the higher the applied voltage and the longer applied for, the longer the relaxation time back to its initial alignment.

8.3.3 Achieving Sub-millisecond Response Times

These τ_{ON} times are too slow to justify the use of this VGA-FLC device geometry for fast-switching electro-optic devices. They must be sub-millisecond, otherwise NLCs can be used instead. Indeed, this was a limitation of the choice of FLC material, and not a restriction of the device itself. Now that the geometry has been shown to function successfully as a switchable electro-optic device, optimisation of the materials and physical device properties can be explored. This was not achieved during this project. However, predictions based on the results in this Chapter can be made with a high level of confidence.

The most detrimental aspect for measuring "slow" response times was the use of mixtures of SCE13* with SCE13-R to increase the helical pitch. This was essential for characterisation of the alignment of the FLC in the VGA-FLC geometry. The two mixtures of SCE13 at 30 $^{\circ}C$ have a reduced R_0 (and therefore $\mathbf{P}_s$) to ensure a surface-stabilised device, resulting is a reduction from $\mathbf{P}_s(100\%) = 26 \pm 1\ \mu m$ to $\mathbf{P}_s(5\%) = 1.0 \pm 0.1\ \mu m$ and $\mathbf{P}_s(8.3\%) = 2.0 \pm 0.1\ \mu m$. This is shown in Figure 3.15. If using SCE13* with a cell gap of 22 μm (calculated for maximum I) and satisfying $4d > P$, the maximum $\mathbf{P}_s$ mixture of SCE13(*) is only 11%. This means that it is not possible to obtain sub-millisecond switching with SCE13* in the current design of the VGA-FLC device.

There are commercial FLC mixtures that have larger R_0 and $\mathbf{P}_s$. Consider the FLC Felix-015 which has the physical properties at 30 $^{\circ}C$ given in Table 8.1 [237]. Comparing this to SCE13*, the main differences are $R_{0,\,Felix015} = 10 \times R_{0,\,SCE13^*}$, and $\mathbf{P}_{s,\,Felix015} = 0.4 \times R_{0,\,SCE13^*}$. This results in the pure Felix-015 mixture being

Table 8.1: Material properties of the FLC Felix-015 at 30 $^{\circ}C$ [237].

θ_c	$\mathbf{P}_s$	R_0	γ_ϕ
24°	10 $nCcm^{-2}$	> 100 μm	0.05 Pas

unwound in the VGA-FLC device geometry, with a 5× larger $\mathbf{P}_s$ than possible with a mixture of SCE13*. Scaling the results in Figure 8.9, theoretical times for τ_{ON} at 30 $^{\circ}C$ of $\tau_{ON,\ 15V,\ Felix015} = 0.7\ ms$, and $\tau_{ON,\ 30V\ Felix015} = 0.3\ ms$, obtained by multiplying by a scaling factor of 0.073. These aren't the sub-millisecond responses predicted possible by Clark and Lagerwall, and are still an order of magnitude larger than can be obtained with commercial FLC devices ($\sim 10\ \mu s$) [28, 126]. It is possible to imagine further reducing these ON times with an FLC purposefully designed for use in the VGA-FLC geometry: high cone angle, large spontaneous polarisation and high pitch. If a material with a much larger θ_c or Δn can be used, a smaller cell gap can be used to satisfy the Gooch-Tarry equation. For example, if Δn_{eff} can be halved, then d can too be halved, resulting in a further reduction in τ by 50 %. This is of course predicting that these materials will align in the VGA-FLC device geometry in the same way as SCE13*, and leads towards some possible future work.

Another aspect of the VGA-FLC device that can be optimised is the spacing of the IDEs, where in this device $l = 22\ \mu m$, and commercial electrodes are usually $l_{commercial} = 6 \rightarrow 8\ \mu m$, which is $\sim 3\times$ smaller. These electrodes can therefore be considered to produce an electric field that is $\sim 3\times$ larger for a given voltage, by considering Equations 4.8 and 4.9. With this consideration, our experimental values for SCE13* are reduced below 1 ms at 30 V for Device 2 at $T = 30\ ^{\circ}C$.

8.4 Summary - Chapter 8

The response of the VGA-FLC device to in-plane electric fields has been explored over a range of temperatures, voltages and cell gaps. In-plane electric fields in-

duce a 90° twist of the **c**-director through the device, and returns to its initial alignment determined by the surface-relief gratings when removed. Due to differences in geometry to other devices, new considerations were made to optimise the VGA-FLC performance, involving an unsymmetrical OFF pulse to quickly restore the dark state of the device. Fast response times are obtained for this prototype device, although fall short of sub-millisecond times at 30 $°C$. Simple optimisation of the device is discussed, where it is shown that sub-millisecond response times are possible by considering a higher performance FLC and reduction of the electrode spacing. Obtaining response times in the order of 10's of microseconds appears unlikely, and is limited to FLCs showing higher values for θ_c and Δn in the homeotropic geometry such that the cell gap, and therefore τ, can be reduced. Nevertheless, this novel device geometry provides promising results, and can hopefully form the basis for future research into TFT addressed grating-aligned FLC devices.

Chapter 9

Conclusions and Future Work

"Don't adventures ever have an end? I suppose not. Someone else always has to carry on the story."

— J.R.R. Tolkien, The Lord of the Rings

9.1 Conclusions

Ferroelectric liquid crystals are of particular interest for use in the micro-display and spatial light modulator industries as they exhibit significantly faster electro-optic response times compared to those obtainable through nematic liquid crystals. The smectic layers of ferroelectric liquid crystals make them highly sensitive to shock-induced flows. A well aligned sample, once disrupted, can result in permanently displaced layers yielding devices inoperable. This work introduces the VGA-FLC mode: a vertical alignment geometry aided by surface-relief gratings. The vertical geometry is shown to be more shock resistant than planar aligned layers famously utilised in the SSFLC. The vertical geometry aided by surface-relief gratings control both the smectic layer normal and smectic **c**-director, and enable a "self-healing" of the smectic layers when distorted by a mechanical shock. The device is shown to be operable using interdigitated electrodes, and so suitable for active matrix addressing using thin-film transistors. Millisecond response times are obtained for both the ON and OFF times. Simple arguments are made for achieving sub-millisecond responses using optimised FLC materials and IDEs.

As such, this geometry shows outstanding potential for improving FLCs in LCoS SLMs for use in high speed adaptive optics and head mounted displays for virtual and augmented reality applications.

Chapter One outlined the history of the LCD, from the unveiling of the dynamic scattering mode in 1968, through to modern TFT addressed nematics relying on vertically aligned modes operated with IDEs. One strong competitor at this time was the SSFLC, attracting a lot of attention. Ultimately this technology lost out due to relying on passive matrix addressing, and the lack of shock-stability for use in portable devices. FLCs are still of particular interest due to their fast electro-optic response, and see commercial success in LCoS displays. Despite these displays utilising modes that are less sensitive to shock, new shock-insensitive modes remain important to explore and develop. This formed the motivation for this thesis.

Chapter Two explored the unique physical properties of calamitic liquid crystals and how they are utilised to create electro-optic displays and devices. The order parameter, biaxiality and chirality are introduced for nematic liquid crystals, followed by the higher complexity smectic phases and the origin of ferroelectricity, the key parameter that enables sub-millisecond switching. The liquid crystal cell was introduced as a means to easily explore the alignment and behaviour of liquid crystals in specific containments. Key theories relevant for FLC devices were introduced, including those regarding the refractive indices, elastic constants, free energy, electric energies and addressing. The relevant polarisation optics for LCDs were discussed, including the general birefringent retarder and the Gooch-Tarry equation for a twisted nematic. Finally, the specific considerations for FLCs were introduced, and some operating modes beyond the SSFLC for display and non-display applications.

Chapter Three introduced the main experimental methods used throughout this work. A major emphasis was placed on photolithography, which was explained in detail for its use in fabricating permanent microstructures for liquid

crystal containment, as well as creating temporary stencils for patterned electrode fabrication. Two techniques were used for patterning photoresists: direct write lithography using the DWL for maskless prototyping, and photomasks with a mask aligner for quickly replicating electrode designs. One of the main goals of this project was to set up these processes for the Soft Matter group in the University of Leeds. Once these processes were set up and could be used to reproducibly fabricate designed structures, the processing was modified to create sub-micron and micron sized features, resulting in two optimised processes depending on the desired film thickness. The structures were analysed using scanning electron microscopy and surface profilometry. The replication of microstructures was discussed, enabled by creating stamps and embossing techniques to create low-offset in alternative photopolymers. The creation of photomasks and IDEs was discussed, along with analysis of the final electrodes. The vapour-phase deposition of silane was described for controlled, homeotropic alignment. The fabrication of cells for analysing liquid crystals was described, along with analytical techniques including polarising optical microscopy, reflection and transmission spectrometry. The current-reversal technique was employed for measuring mixtures of the FLC SCE13* and SCE13-R.

Chapter Four introduced the concept of the VGA-FLCD: a vertical grating aligned ferroelectric liquid crystal device. The geometry was designed towards enabling shock-stable FLCs, whilst taking advantage of the materials' spontaneous polarisation and therefore potential for sub-millisecond optical response times. First the difference in response between planar and homeotropic FLCs was explored, concluding that the homeotropic geometry provided more resistant due to the direction of flow of the layers under an applied pressure. However there was no control of the **c**-director, which aligned with the flow direction. A proposal was made for the VGA-FLC geometry. It was proposed that surface-relief gratings could be introduced to orient the **c**-director, and so provide an energetically favourable alignment following a shock-induced flow. The device should be addressed using IDEs positioned as to introduce a 90° twist through the device for the ON state, satisfying the Gooch-Tarry equation. The relevant theories required by this design were discussed, including considering the effective

birefringence of the SmC(*), the effect of the complex electric fields introduced by IDEs, including expected response times, the effect of compressions on smectic layers and the boundary layer conditions. This established the work for the remainder of the thesis.

Chapter Five was concerned with the fabrication of variable pitch and amplitude surface-relief gratings for use in the VGA-FLC device. The negative-tone photoresist SU-8 was explored as an option to create sinusoidal-like surface-relief gratings using the DWL. This pushed the technique to its limits, by varying the solvent levels and baking times to create curved features in an otherwise digital process. Sinusoidal-like, 4 micron pitch, variable amplitude gratings were shown, and analysed using SEM and surface profilometry. The transmission of the gratings was discussed, although deemed not particularly problematic as it was low for the gratings used in the final devices, and the photopolymer's refractive index can be matched to the LC for commercial applications.

Chapter Six looked towards homeotropic FLC alignment before the introduction of surface-relief gratings. First the textures on cooling through the nematic and smectic A phases was confirmed to show homeotropic alignment using the techniques outlined in the methodology. The optical textures observed in the schlieren SmC(*) texture were explored, with particular emphasis on the formation of optical single and double undulations in the texture at cooling rates $> 1\ ^{\circ}Cmin^{-1}$. Their origin was determined to be caused by the layers favourably undulating before new layers were created, as d_C decreases on cooling as the mesogens tilt. The relative magnitudes of the A_{21} and A_{12} layer bend elastic constants were investigated through a correlation between the optical texture pitch and the actual physical undulation pitch, and it was concluded that $A_{12} > A_{21}$ for SCE13(*). This confirmed that an A_{21} undulation was more energetically favourable, and as the layer pitch was measured at $\sim 4\ \mu m$, it should be favourable to form over a $4\ \mu m$ pitch surface relief grating and allow control of the **c**-director. Transmission measurements were made for the device to establish the frequency of the "layer jumps", where new layers are made at predictable points. Shock-induced flow of this geometry was also explored, where it was

found that similar undulations were induced into the texture depending on the applied pressure. These undulations also disappeared behind a dislocation line of layer formation.

Chapter Seven introduced surface-relief gratings to the device, and the SmC(*) alignment was explored. Importantly, the nematic and smectic A phases showed no distortions due to the gratings, and were optically equivalent to the device with no gratings. The effect of the grating amplitude was explored, and no adverse effects were seen below $A_{PP} = 1\ \mu m$. It was confirmed using a full wave-plate that the **c**-director aligned perpendicular to the grating vector, and so confirming that the SmC(*) preferentially forms an A_{21} undulation over the grating alignment as predicted in Chapter Six. Thermal undulations were observed in this geometry, with particular note of a frustrated "carpet" texture immediately below the SmA to SmC(*) transition. This was shown to be a result of the boundary layer conditions and penetration length induced by the surface-relief gratings into the smectic layers. This texture dissipated revealing a well aligned **c**-director, and low contrast dark texture. Defects were observed in this alignment, and their removal is discussed in the Future Work Section. The VGA-FLC device was subject to mechanical shock tests, and was found to strongly orient the **c**-director over all applied pressures. Metastable undulations were induced into the textures at the highest force shocks due to A_{12} undulations, however these caused little increase in optical transmission, and caused no negative device performance. A model for the defect structure that must form over the surface-relief gratings was proposed, and observed to have little contribution to the optics of the device. The geometry successfully showed good shock-resistance, purely relying on surface-relief gratings inducing A_{21} undulations into the smectic layers close to the grating surfaces.

Finally, Chapter Eight explored the electro-optic response of the VGA-FLC device with in-plane electric fields, with particular consideration for its compatibility with active matrix addressing for use in commercial applications. The geometric property of $\mathbf{c} \neq -\mathbf{c}$ for the SmC(*) phase required extra considerations to be made with regards to ON and OFF pulses and IDEs. This was because the **c**-director can twist in two possible directions despite the same sign electric field.

This was particularly useful for enabling high viewing angle displays, but results in complicated OFF pulses to restore the OFF state of the device. Experimental results showed the electro-optic response with regards to applied frequency and applied voltages. Care was made to ensure the time of the applied pulses was short to ensure no ionic effects influenced the results, which were shown to be particularly problematic. In reality, this would not be a problem as the material can be purified from ions. The OFF response was found to strongly depend on the previously applied ON pulse, but with extra considerations, OFF times were obtained at the same magnitude as the ON times. This confirmed that the VGA-FLC geometry can produce sub-millisecond electro-optic responses, although not possible with the FLC SCE13(*) material used in this work. The VGA-FLC device therefore shows great potential for enabling shock-stable FLC displays and devices.

To conclude, this Thesis is concerned with ferroelectric liquid crystals. A novel geometry, the VGA-FLCD, was invented, examined and shown to enable a shock-resistant FLC retarding layer for use in ultra-fast switching electro-optic displays and devices. This geometry should allow FLCs to see further success in LCoS device applications and VR/AR systems.

9.2 Future Work

The VGA-FLC geometry has shown great potential for shock-stable alignment of smectic C(*) materials. This Section discusses some of the most important aspects that could form the basis for further research.

9.2.1 Removal of Grating-Induced Defects

The origin of the defects that form on SmC(*) grating alignment was confirmed to arise from the **c**-director having two possible orientations relative to the grating vector, **g**. This causes two problems. The defects appear bright in the dark

OFF state, raising the required 0 % transmission by up to 5 %, reducing the maximum optical contrast that can be obtained for the device. These must be removed for practical use. They are also not shock-stable: on a mechanical shock they misalign the local well aligned homeotropic layers, resulting in a further increase in the optical transmission. They must therefore be removed. This was not achieved during this work. Some potential solutions are presented.

One method is to ensure that the surface-relief grating only induces one possible orientation to the **c**-director, such that one orientation relative to **g** is energetically favourable. On cooling from the SmA, the **c**-director will tilt in just this one direction. This would require to be induced by the geometry of the grating itself, and it it hard to image how this could easily be achieved. A solution becomes plausible if the A_{12} layer undulation is instead preferred over the grating surface. The gratings can be fabricated such that they are blazed, resulting in the two alignment orientations for **c** to no longer be of equal energy. This was a technique employed in the Zenithal Bistable Device [167, 238]. This however creates further problems, such as how do the A_{12} layer undulation become energetically favourable, and optically these undulations create more distinct grating undulations due to the average increased effective birefringence of the undulation. One might predict that the grating pitch can be varied to be of the magnitude of the A_{12} undulations ($< 3\ \mu m$) to make them favoured. This would be interesting to explore. This also raises further questions, such as what effect does the pitch have on the alignment of the homeotropic smectic layers? Can it be used to cause a preferred layer undulation, or will the A_{21} always form if it is the smaller elastic constant?

Another method is to introduce a second set of IDEs on the opposite substrate, and apply an electric field using both electrodes while cooling from the SmA into the SmC(*) phase. This would create a single orientation for the **c**-director at both surfaces between each opposing electrode. The problem with this is first from an engineering standpoint, as the electrodes would have to be well aligned, and then the device would have a redundant set of electrodes. The other issue is ensuring that when the field is removed that the **c**-director will relax to

align with the grating in the correct way. This would also reorient the formation of defect to be above the electrodes, rather than between the electrodes. This option seems simpler to implement, but less effective and practical than changing the grating profile discussed earlier.

Another option would be the use of a reactive mesogens or other alignment inducing photopolymers that could be used as a replacement for PP2 and homeotropic surface treatment [168]. This could be tuned to induce an appropriate pre-tilt in the SmC(*) to potentially remove the defects. This could result in a poor alignment in the SmA phase, resulting in tilted layers through the device. Temperature gradients could also be explored. It was observed that the direction of the temperature gradient influenced the **c**-director orientation relative to **g**.

9.2.2 Pitch, Amplitude, Surface Treatment and Ferroelectric Material

A thorough study of varying the pitch, amplitude and surface treatment of the surface-relief gratings was not performed. The pitch was kept constant at 4 μm, and the surface treatment not varied as these parameters produced a good homeotropic alignment of the FLC smectic layers. In addition, low-amplitude gratings (> 0.3 μm) were chosen as they minimised transmission losses due to diffractive and refractive effects, gave preferable **c**-director orientation, and little disruption to the smectic layers. This was by no means the optimum system. It would be interesting to investigate whether varying the pitch can be used to decide the preferred layer undulation, either A_{21} or A_{12}. It would also be beneficial to explore if the response times are influenced by varying the grating amplitude, and the effect this has on the shock-stability of the device.

The smectic C(*) material was also not varied during this project. It is expected that the geometry will work regardless of the material used, provided it shows a SmA phase to achieve the correct alignment. Felix-015 was introduced as a high pitch alternative material that could be used to confirm if the device

can achieve sub-millisecond response times at room temperature. This, or another appropriate material should be tested in this geometry. This also raises the question of the effect on FLCs that don't show a SmA phase, those that transition directly from the nematic into the smectic C(*). Perhaps this grating geometry can be used to successfully align these materials, for either use in the device, or simply performing experiments on their physical properties. If it works for $N \rightarrow SmC(^*)$ materials, perhaps it can be used for biaxial nematic materials? Perhaps the VGA-FLC geometry can be adapted for creating an ultra-fast switching device or display utilising these complex phases [239]? Ultimately, the success of the VGA-FLC geometry relies on both the device, and also the availability of an appropriate FLC material.

9.3 Publications

[1] P. J. M. Wyatt, J. Bailey, M. Nagaraj, and J. C. Jones, "P-206: Late-News Poster: A Grating-Aligned Ferroelectric Liquid Crystal Electro-Optic Shutter for Fast-Switching and Shock-Resistant Applications," in SID Symposium Digest of Technical Papers, 2019, vol. 50, no. 1, pp. 1806–1809.

[2] P. J. M. Wyatt, J. Bailey, M. Nagaraj, and J. C. Jones, "A self-healing ferroelectric liquid crystal electro-optic shutter based on vertical grating alignment," in preparation.

[3] P. J. M. Wyatt, M. Nagaraj, and J. C. Jones, "The Textures Arising from Homeotropic Ferroelectric Liquid Crystal Grating Alignment," in preparation.

[4] E. I. L. Jull, M. Wahle, P. J. M. Wyatt, C. Ellis, S. J. Cowling, J. W. Goodby, K. Usami and H. F. Gleeson, "Efficiency improvements in a dichroic dye-doped liquid crystal Fresnel lens," Optical Express, 2019, vol. 27, no. 19, p. 26799.

Chapter 10

References

[1] B. J. Lechner, "History crystallized: A first person account of the development of matrix-addressed LCDs for Television at RCA in the 1960s," *Information Display*, vol. 1, pp. 26–30, 2008. 2

[2] R. Williams, "Domains in Liquid Crystals," *The Journal of Chemical Physics*, vol. 39, no. 2, pp. 384–388, 1963. 2, 3

[3] R. Williams, "Electro-optical elements utilizing an organic nematic compound," 1967.

[4] G. H. Heilmeier and L. A. Zanoni, "Electro-optical device," 1967. 3

[5] G. H. Heilmeier, L. A. Zanoni, and L. A. Barton, "Dynamic scattering: A new electrooptic effect in certain classes of nematic liquid crystals," *Proceedings of the IEEE*, vol. 56, no. 7, pp. 1162–1171, 1968. 2, 3

[6] J. C. Jones, "The fiftieth anniversary of the liquid crystal display," *Liquid Crystals Today*, vol. 27, no. 3, pp. 44–70, 2018. 2, 4

[7] F. Reinitzer, "Beitrge zur kenntniss des Cholesterins," *Monatshefte fur Chemie*, vol. 9, pp. 421–441, 1888. 2

[8] O. Lehmann, *Flussige Kristalle: sowie Plastizitat von Kristallen im allgemeinen, molekulare Umlagerungen und Aggregatzustandsänderungen*. Verlag von Wilhelm Engelmann, 1904. 2

[9] C. Mauguin, "Sur les cristaux liquides de Lehmann," *Bulletin de la Société Française de Minéralogie et de Cristallographie*, vol. 34, pp. 71–85, 1911. 2

[10] G. Friedel, "Les états mésomorphes de la matière," *Annales de Physique*, vol. 9, pp. 273–474, 1922. 2

[11] V. Fréedericksz and A. Repiewa, "Theoretisches und Experimentelles zur Frage nach der Natur der anisotropen Flussigkeiten," *Zeitschrift fur Physik*, vol. 42, no. 7, pp. 532–546, 1927. 2

[12] B. Levin and N. Levin, "Improvements in or relating to light valves," *British Patent: 441*, p. 274, 1936. 2

[13] G. H. Brown and W. G. Shaw, "The mesomorphic state-liquid crystals," *Chemical Reviews*, vol. 57, no. 6, pp. 1049–1157, 1957. 3

[14] G. W. Gray, *Molecular structure and the properties of liquid crystals*. Academic Press, 1962. 3

[15] M. Schadt and W. Helfrich, "Voltage-dependent optical activity of a twisted nematic liquid crystal," *Applied Physics Letters*, vol. 18, no. 4, pp. 127–128, 1971. 3, 20, 108

[16] H. Kawamoto, "The history of liquid-crystal displays," *Proceedings of the IEEE*, vol. 90, no. 4, pp. 460–500, 2002.

[17] C. Hilsum, "Flat-panel electronic displays: a triumph of physics, chemistry and engineering," *Philosophical Transactions of the Royal Society A*, vol. 368, pp. 1027–1082, 2010.

[18] N. Koide, *The Liquid Crystal Display Story: 50 Years of Liquid Crystal R&D that lead The Way to the Future*. Tokyo, Japan: Springer, 2014. 3

[19] G. W. Gray, K. J. Harrison, and J. A. Nash, "New family of nematic liquid crystals for displays," *Electronics Letters*, vol. 9, no. 6, pp. 130–131, 1973. 3

[20] A. Ashford, J. Constant, J. Kirton, and E. P. Raynes, "Electro-optic performance of a new room-temperature nematic liquid crystal," *Electronics Letters*, vol. 9, no. 5, p. 118, 1973. 3

[21] J. C. Jones, "Liquid crystal displays," in *Handbook of Optoelectronics, Enabling Technologies (Volume Two)* (John P. Dakin and Robert G. W. Brown, eds.), ch. 6, pp. 137–224, CRC Press, 2 ed., 2017. 3, 4, 11, 34, 35, 36, 37

[22] G. H. Heilmeier, "Liquid crystal displays: An experiment in interdisciplinary research that worked," *IEEE Transactions on Electron Devices*, vol. 23, no. 7, pp. 780–785, 1976. 3

[23] P. Weimer, "The TFT A New Thin-Film Transistor," *Proceedings of the IRE*, vol. 50, no. 6, pp. 1462–1469, 1962. 3

[24] T. P. Brody, J. A. Asars, and G. D. Dixon, "A 6 × 6 inch 20 lines-per-inch liquid-crystal display panel," *IEEE Transactions on Electron Devices*, vol. 20, no. 11, pp. 995–1001, 1973. 3

[25] P. Alt and P. Pleshko, "Scanning limitations of liquid-crystal displays," *IEEE Transactions on Electron Devices*, vol. 21, no. 2, pp. 146–155, 1974. 3, 37

[26] C. M. Waters and E. P. Raynes, "Liquid crystal devices with particular cholesteric pitch-cell thickness ratio," 1983. 4

[27] J. C. Jones, "Bistable Liquid Crystal Displays," in *Handbook of Visual Display Technology* (J. C. Janglin, W. Cranton, and M. Fihn, eds.), pp. 1507–1543, Berlin, Heidelberg: Springer Berlin Heidelberg, 2012. 4

[28] N. A. Clark and S. T. Lagerwall, "Submicrosecond bistable electro-optic switching in liquid crystals," *Applied Physics Letters*, vol. 36, no. 11, pp. 899–901, 1980. 4, 5, 30, 41, 44, 110, 201

[29] W. E. Spear and P. G. Le Comber, "Substitutional doping of amorphous silicon," *Solid State Communications*, vol. 17, no. 9, pp. 1193–1196, 1975. 4

[30] W. E. Spear, P. G. Le Comber, S. Kinmond, and M. H. Brodsky, "Amorphous silicon p-n junction," *Applied Physics Letters*, vol. 28, no. 2, pp. 105–107, 1976.

[31] P. G. Le Comber, W. E. Spear, and A. Ghaith, "Amorphous-silicon field-effect device and possible application," *Electronics Letters*, vol. 15, no. 6, pp. 179–181, 1979.

[32] A. J. Snell, K. D. Mackenzie, W. E. Spear, P. G. LeComber, and A. J. Hughes, "Application of amorphous silicon field effect transistors in addressable liquid crystal display panels," *Applied Physics*, vol. 24, no. 4, pp. 357–362, 1981. 4

[33] Y. Ishii, "The World of Liquid-Crystal Display TVs—Past, Present, and Future," *Journal of Display Technology*, vol. 3, no. 4, pp. 351–360, 2007. 4

[34] R. Kiefer, "Inplane switching of nematic liquid crystals," in *Proc. of Japan Display '92*, 1992. 4

[35] M. Oh-E and K. Kondo, "Electro-optical characteristics and switching behavior of the in-plane switching mode," *Applied Physics Letters*, vol. 67, no. 19, pp. 3895–3897, 1995. 112, 188

[36] A. Takeda, S. Kataoka, T. Sasaki, H. Chida, H. Tsuda, K. Ohmuro, T. Sasabayashi, Y. Koike, and K. Okamoto, "41.1: A Super-High Image Quality Multi-Domain Vertical Alignment LCD by New Rubbing-Less Technology," *SID Symposium Digest of Technical Papers*, vol. 29, no. 1, p. 1077, 1998. 110

[37] Y. Koike and K. Okamoto, "Super high quality MVA-TFT liquid crystal displays," *Fujitsu Scientific and Technical Journal*, vol. 35, no. 2, pp. 221–228, 1999. 4

[38] P. Semenza, "Can anything catch TFT LCDs?," *Nature Photonics*, vol. 1, no. 5, pp. 267–268, 2007. 4

[39] E. Jang, S. Jun, H. Jang, J. Lim, B. Kim, and Y. Kim, "White-Light-Emitting Diodes with Quantum Dot Color Converters for Display Backlights," *Advanced Materials*, vol. 22, no. 28, pp. 3076–3080, 2010. 5

[40] J. Kanbe, H. Inoue, A. Mizutome, Y. Hanyuu, K. Katagiri, and S. Yoshihara, "High resolution, large area flc display with high graphic performance," *Ferroelectrics*, vol. 114, no. 1, pp. 3–26, 1991. 5

[41] S. T. Lagerwall, "Ferroelectric and Antiferroelectric Liquid Crystals," *Ferroelectric and Antiferroelectric Liquid Crystals*, vol. 301, no. 1, pp. 15–45, 2004. 5

[42] M. Koden, S. Miyoshi, M. Shigeta, K. Nonomura, M. Sugino, T. Numao, H. Katsuse, A. Tagawa, Y. Kawabata, P. A. Gass, M. J. Towler, E. P. Raynes, J. C. Jones, C. V. Brown, J. R. Hughes, A. Graham, M. J. Bradshaw, and D. G. Mcdonnell, "Ferroelectric Liquid Crystal Display," *Shapu Giho/Sharp Technical Journal*, vol. 69, pp. 47–50, 1997. 5

[43] N. Itoh, H. Akiyama, Y. Kawabata, M. Koden, S. Miyoshi, T. Numao, M. Shigeta, M. Sugino, M. J. Bradshaw, C. V. Brown, A. Graham, S. D. Haslamtt, J. R. Hughes, J. C. Jones, D. G. Mcdonnell, A. J. Slaney, P. Bonnett, P. A. Gass, E. P. Rayens, D. Ulrich, S. D. Haslam, J. R. Hughes, J. C. Jones, D. G. Mcdonnell, A. J. Slaney, P. Bonnett, P. A. Gass, E. P. Rayens, and D. Ulrich, "17-in. Video-Rate Full-Color FLCD," *The Journal of The Institute of Image Information and Television Engineers*, vol. 53, no. 8, pp. 1136–1141, 1999. 5

[44] S. Kondoh, S. Kawada, R. Takahashi, and E. Tajima, "2.7inch QVGA type FLC-device for SLM," *Ferroelectrics*, vol. 246, no. 1, pp. 121–129, 2000. 6

[45] M. Hird, "Ferroelectricity in liquid crystals—materials, properties and applications," *Liquid Crystals*, vol. 38, no. 11-12, pp. 1467–1493, 2011. 6, 43

[46] N. A. Clark, C. Crandall, M. A. Handschy, M. R. Meadows, R. M. Malzbender, C. Park, and J. Z. Xue, "FLC microdisplays," *Ferroelectrics*, vol. 246, no. 1, pp. 97–110, 2000. 6, 43

[47] M. Birch, D. Kruerke, C. Yates, A. Macartney, D. Peden, and D. Coates, "31.1: SXGA Resolution FLC Microdisplays," *SID Symposium Digest of Technical Papers*, vol. 33, no. 1, p. 954, 2002.

[48] T. D. Wilkinson, W. A. Crossland, and A. B. Davey, "Applications of Ferroelectric Liquid Crystal LCOS Devices," *Ferroelectrics*, vol. 278, no. 1, pp. 227–232, 2002. 43

[49] L. Banks, M. Birch, D. Krueerke, E. Buckley, A. Cable, N. Lawrence, and P. Mash, "73.4: Real-time Diffractive Video Projector Employing Ferroelectric LCOS SLM," *SID Symposium Digest of Technical Papers*, vol. 37, no. 1, p. 2018, 2006.

[50] R. Zhang and H. Hua, "Design of a polarized head-mounted projection display using ferroelectric liquid-crystal-on-silicon microdisplays," *Applied Optics*, vol. 47, no. 15, p. 2888, 2008. 43

[51] M. J. O'Callaghan, R. Ferguson, R. Vohra, W. Thurmes, A. W. Harant, C. S. Pecinovsky, Y. Zhang, S. Yang, M. O'Neill, and M. A. Handschy, "Bistable FLCOS devices for doubled-brightness micro-projectors," *Journal of the Society for Information Display*, vol. 17, no. 4, pp. 369–375, 2009. 43

[52] V. G. Chigrinov and A. Srivastava, "Ferroelectric Liquid Crystal Cells for Advanced Applications in Displays and Photonics," *Molecular Crystals and Liquid Crystals*, vol. 595, no. 1, pp. 39–49, 2014. 6, 45

[53] P. Holmes, "Display," *Patent: US20110304595A1*, pp. 1–10, 2011. 6

[54] S. Knust, M. Wahle, and H. S. Kitzerow, "Ferroelectric Liquid Crystals in Microcapillaries: Observation of Different Electro-optic Switching Mechanisms," *Journal of Physical Chemistry B*, vol. 121, no. 19, pp. 5110–5115, 2017. 6

[55] D. Budaszewski, A. K. Srivastava, V. G. Chigrinov, and T. R. Woliński, "Electro-optical properties of photo-aligned photonic ferroelectric liquid crystal fibres," *Liquid Crystals*, vol. 46, no. 2, pp. 272–280, 2019.

[56] Y. Ma, A. M. W. Tam, X. T. Gan, L. Y. Shi, A. K. Srivastava, V. G. Chigrinov, H. S. Kwok, and J. L. Zhao, "Fast switching ferroelectric liquid crystal Pancharatnam-Berry lens," *Optics Express*, vol. 27, no. 7, pp. 10079–10086, 2019. 6, 48

[57] M. J. Freiser, "Ordered States of a Nematic Liquid," *Physical Review Letters*, vol. 24, no. 19, pp. 1041–1043, 1970. 10

[58] P. G. de Gennes, *The Physics of Liquid Crystals*. Oxford: Oxford University Press, 2nd ed., 1993. 10, 11, 13, 22, 24, 30, 114, 116, 117

[59] L. Gattermann and A. Ritschke, "Ueber Azoxyphenolather," *Berichte der deutschen chemischen Gesellschaft*, vol. 23, no. 1, pp. 1738–1750, 1890. 10

[60] H. Kelker and B. Scheurle, "A Liquid-crystalline (Nematic) Phase with a Particularly Low Solidification Point," *Angewandte Chemie International Edition in English*, vol. 8, no. 11, pp. 884–885, 1969. 10

[61] W. Maier and A. Saupe, "Eine einfache molekular-statistische Theorie der nematischen kristallinflüssigen Phase. Teil II.," *Zeitschrift fur Naturforschung A*, vol. 15, no. 4, pp. 287–292, 1960. 10

[62] I. Haller, "Thermodynamic and static properties of liquid crystals," *Progress in Solid State Chemistry*, vol. 10, no. 2, pp. 103–118, 1975. 11, 12

[63] M. L. Magnuson, B. M. Fung, and J. P. Bayle, "On the temperature dependence of the order parameter of liquid crystals over a wide nematic range," *Liquid Crystals*, vol. 19, no. 6, pp. 823–832, 1995. 11

[64] R. Alben, J. McColl, and C. Shih, "The characterization of order in nematic liquid crystals," *Solid State Communications*, vol. 11, no. 8, pp. 1081–1084, 1972. 12, 13

[65] J. W. Emsley, G. R. Luckhurst, and C. P. Stockley, "The deuterium and proton-(deuterium) N.M.R. spectra of the partially deuteriated nematic liquid crystal 4-n-pentyl-4-cyanobiphenyl," *Molecular Physics*, vol. 44, no. 3, pp. 565–580, 1981.

[66] J. D. Bunning, D. A. Crellin, and T. E. Faber, "The effect of molecular biaxiality on the bulk properties of some nematic liquid crystals," *Liquid Crystals*, vol. 1, no. 1, pp. 37–51, 1986. 13

[67] L. Fletcher, "The Optical Indicatrix and the Transmission of Light in Crystals," *Mineralogical Magazine and Journal of the Mineralogical Society*, vol. 9, no. 44, pp. 278–388, 1891. 15

[68] J. C. Jones, *Optical and Dielectric Studies of Smectic C Liquid Crystals*. Ph. d., University of Hull, 1991. 15, 23, 24, 32, 88

[69] P. E. Dunn, *Physical properties of smectic C liquid crystal cells*. Ph. d., University of Exeter, 1998. 15, 30, 31, 44

[70] F. C. Frank, "I. Liquid crystals. On the theory of liquid crystals," *Discussions of the Faraday Society*, vol. 25, pp. 19–28, 1958. 16, 17

[71] I. W. Stewart, "Static Theory of Nematics," in *The Static and Dynamic Continuum Theory of Liquid Crystals* (G. W. Gray, J. W. Goodby, and A. Fukida, eds.), ch. 2, pp. 13–56, London, New York: Taylor & Francis, 1 ed., 2004. 16

[72] D. W. Berreman, "Solid Surface Shape and the Alignment of an Adjacent Nematic Liquid Crystal," *Physical Review Letters*, vol. 28, no. 26, pp. 1683–1686, 1972. 18

[73] L. T. Creagh and A. R. Kmetz, "Mechanism of Surface Alignment in Nematic Liquid Crystals," *Molecular Crystals and Liquid Crystals*, vol. 24, no. 1-2, pp. 59–68, 1973. 18

[74] B. Jerome, "Surface effects and anchoring in liquid crystals," *Reports on Progress in Physics*, vol. 54, no. 3, pp. 391–451, 1991. 18

[75] L. M. Blinov, A. Y. Kabayenkov, and A. A. Sonin, "Invited Lecture. Experimental studies of the anchoring energy of nematic liquid crystals," *Liquid Crystals*, vol. 5, no. 2, pp. 645–661, 1989. 18

[76] H. Sackmann and D. Demus, "The Polymorphism of Liquid Crystals," *Molecular Crystals*, vol. 2, no. 1-2, pp. 81–102, 1966. 20

[77] D. Demus, S. Diele, S. Grande, and H. Sackmann, "Polymorphism in Thermotropic Liquid Crystals," *Advances in Liquid Crystals*, vol. 6, pp. 1–107, 1983. 20

[78] A. de Vries, "The Implications of the Diffuse-Cone Model for Smectic A and C Phases and A - C Phase Transitions," *Molecular Crystals and Liquid Crystals*, vol. 49, no. 6, pp. 179–185, 1979. 20

[79] T. R. Taylor, J. L. Fergason, and S. L. Arora, "Biaxial Liquid Crystals," *Physical Review Letters*, vol. 24, no. 8, pp. 359–362, 1970. 20

[80] W. Helfrich and C. S. Oh, "Optically Active Smectic Liquid Crystal," *Molecular Crystals and Liquid Crystals*, vol. 14, no. 3-4, pp. 289–292, 1971. 20

[81] J. P. F. Lagerwall, F. Giesselmann, and M. D. Radcliffe, "Optical and x-ray evidence of the "de Vries" Sm-A*-Sm-C* transition in a non-layer-shrinkage ferroelectric liquid crystal with very weak interlayer tilt correlation," *Physical Review E*, vol. 66, no. 3, p. 031703, 2002. 22, 100

[82] J. P. F. Lagerwall and F. Giesselmann, "Current Topics in Smectic Liquid Crystal Research," *ChemPhysChem*, vol. 7, no. 1, pp. 20–45, 2006.

[83] J. C. Roberts, N. Kapernaum, Q. Song, D. Nonnenmacher, K. Ayub, F. Giesselmann, and R. P. Lemieux, "Design of Liquid Crystals with "de Vries-like" Properties: Frustration between SmA- and SmC-Promoting Elements," *Journal of the American Chemical Society*, vol. 132, no. 1, pp. 364–370, 2010. 22, 100

[84] P. Rudquist, M. A. Osipov, and F. Giesselmann, "On the orientational distribution functions in de Vries-type smectic liquid crystals," *Liquid Crystals*, vol. 45, no. 13-15, pp. 2097–2108, 2018. 22

[85] J. P. Straley, "Ordered phases of a liquid of biaxial particles," *Physical Review A*, vol. 10, no. 5, pp. 1881–1887, 1974. 22

[86] S. Dumrongrattana and C. C. Huang, "Polarization and tilt-angle measurements near the smectic-A chiral smectic-C transition of p-(n-decyloxybenzylidene)-p-amino-(2-methyl-butyl) cinnamate (DOBAMBC)," *Physical Review Letters*, vol. 56, no. 5, pp. 464–467, 1986. 23

[87] R. B. Meyer, L. Liebert, L. Strzelecki, and P. Keller, "Ferroelectric liquid crystals," *Journal de Physique Lettres*, vol. 36, no. 3, pp. 69–71, 1975. 23

[88] W. Kuczyński and H. Stegemeyer, "Ferroelectric properties of smectic C liquid crystals with induced helical structure," *Chemical Physics Letters*, vol. 70, no. 1, pp. 123–126, 1980. 24, 87

[89] R. B. Meyer, "Ferroelectric Liquid Crystals; A Review," *Molecular Crystals and Liquid Crystals*, vol. 40, no. 1, pp. 33–48, 1977. 24, 88

[90] F. M. Leslie, I. W. Stewart, T. Carlsson, and M. Nakagawa, "Equivalent smectic C liquid crystal energies," *Continuum Mechanics and Thermodynamics*, vol. 3, no. 4, pp. 237–250, 1991. 24, 25, 26

[91] F. M. Leslie, I. W. Stewart, and M. Nakagawa, "A Continuum Theory for Smectic C Liquid Crystals," *Molecular Crystals and Liquid Crystals*, vol. 198, no. 1, pp. 443–454, 1991. 24

[92] I. W. Stewart, "Theory of Smectic C Liquid Crystals," in *The Static and Dynamic Continuum Theory of Liquid Crystals* (G. Gray, J. W. Goodby, and A. Fukida, eds.), ch. 6, pp. 247–320, London, New York: Taylor & Francis, 1 ed., 2004. xxii, 25, 29, 30, 115, 116, 118, 144, 149

[93] Orsay_Group, "Simplified elastic theory for smectics C," *Solid State Communications*, vol. 9, no. 10, pp. 653–65, 1971. 26

[94] T. Carlsson, I. W. Stewart, and F. M. Leslie, "Theoretical studies of smectic C liquid crystals confined in a wedge. Stability considerations and Frederiks transitions," *Liquid Crystals*, vol. 9, no. 5, pp. 661–678, 1991. 26

[95] I. Dahl and S. T. Lagerwall, "Elastic and flexoelectric properties of chiral smectic-C phase and symmetry considerations on ferroelectric liquid-crystal cells," *Ferroelectrics*, vol. 58, no. 1, pp. 215–243, 1984. 27, 29

[96] T. Carlsson, I. W. Stewart, and F. M. Leslie, "An elastic energy for the ferroelectric chiral smectic C* phase," *Journal of Physics A: Mathematical and General*, vol. 25, no. 8, pp. 2371–2374, 1992. 27

[97] S. T. Lagerwall, *Ferroelectric and antiferroelectric liquid crystals*. John Wiley & Sons, Ltd, 2008. 29

[98] J. C. Jones and E. P. Raynes, "Measurement of the biaxial permittivities for several smectic C host materials used in ferroelectric liquid crystal devices," *Liquid Crystals*, vol. 11, no. 2, pp. 199–217, 1992. 29

[99] P. Maltese, R. Piccolo, and V. Ferrara, "An addressing effective computer model for surface stabilized ferroelectric liquid crystal cells," *Liquid Crystals*, vol. 15, no. 6, pp. 819–834, 1993.

[100] C. V. Brown, P. E. Dunn, and J. C. Jones, "The effect of the elastic constants on the alignment and electro-optic behaviour of smectic C liquid crystals," *European Journal of Applied Mathematics*, vol. 8, no. 3, pp. 281–291, 1997. 29, 144

[101] J. C. Jones, "The relationship between the smectic C director and layer profiles and the surface anchoring energies," *Ferroelectrics*, vol. 178, no. 1, pp. 155–165, 1996. 30, 31

[102] J. C. Jones, "On the biaxiality of smectic C and ferroelectric liquid crystals," *Liquid Crystals*, vol. 42, no. 5-6, pp. 732–759, 2015. 31, 41, 139, 140

[103] D. C. Ulrich and S. J. Elston, "The effects of pre-tilt angle on the stability of C1 and C2 in rubbed polymer aligned FLC cells," *Ferroelectrics*, vol. 178, no. 1, pp. 177–186, 1996. 31

[104] D. C. Ulrich and S. J. Elston, "The director structure in smectic C-filled cells with strong surface anchoring," *Applied Physics Letters*, vol. 68, no. 2, pp. 185–187, 1996. 31

[105] M. A. Handschy and N. A. Clark, "Structures and responses of ferroelectric liquid crystals in the surface-stabilized geometry," *Ferroelectrics*, vol. 59, no. 1, pp. 69–116, 1984. 32

[106] T. P. Rieker, N. A. Clark, G. S. Smith, and C. R. Safinya, "Layer and director structure in surface stabilized ferroelectric liquid crystal cells with non-planar boundary conditions," *Liquid Crystals*, vol. 6, no. 5, pp. 565–576, 1989. 32

[107] R. C. Jones, "A New Calculus for the Treatment of Optical Systems. I Description and Discussion of the Calculus," *Journal of the Optical Society of America*, vol. 31, no. 7, p. 488, 1941. 32, 34

[108] S. Chandrasekhar, D. Krishnamurti, and N. V. Madhusudana, "Theory of Birefringence of Nematic Liquid Crystals," *Molecular Crystals*, vol. 8, no. 1, pp. 45–69, 1969. 32

[109] P. Yeh and C. Gu, *Optics of liquid crystal displays*. Hoboken, New Jersey, USA: Wiley, 2 ed., 2010. 32

[110] A. Roorda and D. Williams, "The arrangement of the three cone classes in the living human eye," *Nature*, vol. 397, no. 6719, pp. 520–522, 1999. 33

[111] K. R. Welford and J. R. Sambles, "Analysis of Electric Field Induced Deformations in a Nematic Liquid Crystal for any Applied Field," *Molecular Crystals and Liquid Crystals*, vol. 147, no. 1, pp. 25–42, 1987. 34

[112] C. Gooch and H. Tarry, "Optical characteristics of twisted nematic liquid-crystal films," *Electronics Letters*, vol. 10, no. 1, pp. 2–4, 1974. 34, 36

[113] C. H. Gooch and H. A. Tarry, "The optical properties of twisted nematic liquid crystal structures with twist angles less than 90 degrees," *Journal of Physics D: Applied Physics*, vol. 8, no. 13, pp. 1575–1584, 1975. 36

[114] E. P. Raynes and R. J. A. Tough, "The Guiding of Plane Polarized Light by Twisted Liquid Crystal Layers," *Molecular Crystals and Liquid Crystals Letters*, vol. 2, no. 5, pp. 139–145, 1985.

[115] E. P. Raynes, "The Optical Properties of Supertwisted Liquid Crystal Layers," *Molecular Crystals and Liquid Crystals Letters*, vol. 4, no. 3-4, pp. 69–75, 1987. 34, 35

[116] S. T. Wu and D. K. Yang, *Reflective liquid crystal displays*. Chichester, New York: Wiley, 2001. 36, 37

[117] E. Lueder, "Addressing of Liquid Crystal Displays with a-Si Thin Film Transistors (a-Si-TFTs)," in *Liquid crystal displays : addressing schemes and electro-optical effects*, ch. 14, pp. 239–338, Chichester, West Sussex, UK: Wiley, 2nd ed., 2010. 40

[118] S. Kelly and M. O'Neill, "Chapter 1 - Liquid crystals for electro-optic applications," in *Handbook of Advanced Electronic and Photonic Materials and Devices* (Hari Singh Nalwa, ed.), ch. 1, pp. 1–66, Academic Press, 2001. 40

[119] H. Orihara, K. Nakamura, and Y. Ishibashi, "Anomalous switching behavior of a ferroelectric liquid crystal due to dielectric anisotropy," *Ferroelectrics*, vol. 85, no. 1, pp. 143–151, 1988. 44

[120] J. Jones, M. Towler, and J. Hughes, "Fast, high-contrast ferroelectric liquid crystal displays and the role of dielectric biaxiality," *Displays*, vol. 14, no. 2, pp. 86–93, 1993. 44

[121] P. W. H. Surguy, P. J. Ayliffe, M. J. Birch, M. F. Bone, I. Coulson, W. A. Crossland, J. R. Hughes, P. W. Ross, F. C. Saunders, and M. J. Towler, "The "JOERS/Alvey" ferroelectric multiplexing scheme," *Ferroelectrics*, vol. 122, no. 1, pp. 63–79, 1991. 44

[122] A. K. Srivastava, V. G. Chigrinov, and H. S. Kwok, "Ferroelectric liquid crystals: Excellent tool for modern displays and photonics," *Journal of the Society for Information Display*, vol. 23, no. 6, pp. 253–272, 2015. 44, 47, 48

[123] S. Fukushima, H. Kozawaguchi, T. Kurokawa, and S. Matsuo, "Bistable spatial light modulator using a ferroelectric liquid crystal," *Optics Letters*, vol. 15, no. 5, p. 285, 1990. 44

[124] L. A. Beresnev, V. G. Chigrinov, D. I. Dergachev, E. P. Poshidaev, J. Fünfschilling, and M. Schadt, "Deformed helix ferroelectric liquid crystal display: A new electrooptic mode in ferroelectric chiral smectic C liquid crystals," *Liquid Crystals*, vol. 5, no. 4, pp. 1171–1177, 1991. 45

[125] E. P. Pozhidaev, "Electro-optical properties of deformed-helix ferroelectric liquid crystal display cells," in *Advanced Display Technologies: Basic Studies of Problems in Information Display* (V. V. Belyaev and I. N. Kompanets, eds.), vol. 4511, (Flowers), pp. 92–99, International Society for Optics and Photonics, 2001. 45

[126] V. Presnyakov, Z. Liu, and V. G. Chigrinov, "Fast optical retarder using deformed-helical ferroelectric liquid crystals," in *Photonic Applications in Devices and Communication Systems* (P. Mascher, A. P. Knights, J. C. Cartledge, and D. V. Plant, eds.), vol. 5970, (Toronto, Canada), p. 59701K, International Society for Optics and Photonics, 2005. 45, 46, 201

[127] M. D. Wand, R. T. Vohra, M. J. O'Callaghan, B. Roberts, and C. Escher, "Easily aligned deformable-helix ferroelectric liquid crystal mixture and its use in devices," in *Liquid Crystal Materials, Devices, and Applications* (P. S. Drzaic and U. Efron, eds.), vol. 1665, (San Jose, CA, USA), pp. 176–183, International Society for Optics and Photonics, 1992. 46

[128] G. Hegde, P. Xu, E. Pozhidaev, V. Chigrinov, and H. S. Kwok, "Electrically controlled birefringence colours in deformed helix ferroelectric liquid crystals," *Liquid Crystals*, vol. 35, no. 9, pp. 1137–1144, 2008. 46

[129] E. P. Pozhidaev, M. Minchenko, V. Molkin, S. Torgova, A. K. Srivastava, V. Chigrinov, H. S. Kwok, V. Vashenko, and A. Krivoshey, "High frequency low voltage shock-free ferroelectric liquid crystal: a new electro-optical mode with electrically suppressed helix," in *Proc. of 31-th International Display Research Conference EuroDisplay*, pp. 19–22, 2011. 46

[130] A. K. Srivastava, V. G. Chigrinov, and H.-S. Kwok, "Electrically suppressed helix ferroelectric liquid crystals for modern displays," *Journal of the Society for Information Display*, vol. 23, no. 4, pp. 176–181, 2015. 46

[131] E. P. Pozhidaev, A. K. Srivastava, A. D. Kiselev, V. G. Chigrinov, V. V. Vashchenko, A. I. Krivoshey, M. V. Minchenko, and H.-S. Kwok, "Enhanced orientational Kerr effect in vertically aligned deformed helix ferroelectric liquid crystals," *Optics Letters*, vol. 39, no. 10, p. 2900, 2014. 46, 47

[132] Y. Hisakado, H. Kikuchi, T. Nagamura, and T. Kajiyama, "Large Electro-optic Kerr Effect in Polymer-Stabilized Liquid-Crystalline Blue Phases," *Advanced Materials*, vol. 17, no. 1, pp. 96–98, 2005. 46, 47

[133] G. D. Love and R. Bhandari, "Optical properties of a QHQ ferroelectric liquid crystal phase modulator," *Optics Communications*, vol. 110, no. 5-6, pp. 475–478, 1994. 47

[134] H. R. Kim, Y. W. Lee, S. J. Kim, D. W. Kim, Y. U. Chang-Jae, B. Lee, and S. D. Lee, "A rotatable waveplate using a vertically aligned deformed-helix ferroelectric liquid crystal," *Ferroelectrics*, vol. 312, no. 1, pp. 57–62, 2004. 47

[135] E. P. Pozhidaev, A. D. Kiselev, A. K. Srivastava, V. G. Chigrinov, H.-S. Kwok, and M. V. Minchenko, "Orientational Kerr effect and phase modulation of light in deformed-helix ferroelectric liquid crystals with subwavelength pitch," *Physical Review E*, vol. 87, no. 5, p. 052502, 2013. 47

[136] A. D. Kiselev, V. V. Kesaev, and E. P. Pozhidaev, "Orientational Kerr effect in liquid crystal ferroelectrics and modulation of partially polarized light," *Journal of Physics: Conference Series*, vol. 1092, no. 1, p. 012056, 2018. 47

[137] S. P. Kotova, S. A. Samagin, E. P. Pozhidaev, and A. D. Kiselev, "Light modulation in planar aligned short-pitch deformed-helix ferroelectric liquid crystals," *Physical Review E*, vol. 92, no. 6, p. 062502, 2015. 47

[138] L. Rao, J. Yan, S. Wu, S. Yamamoto, and Y. Haseba, "A large Kerr constant polymer-stabilized blue phase liquid crystal," *Applied Physics Letters*, vol. 98, no. 8, p. 081109, 2011. 48

[139] F. Fan, A. K. Srivastava, V. G. Chigrinov, and H. S. Kwok, "Switchable liquid crystal grating with sub millisecond response," *Applied Physics Letters*, vol. 100, no. 11, p. 111105, 2012. 48

[140] F. V. Podgornov, A. M. Suvorova, A. V. Lapanik, and W. Haase, "Electrooptic and dielectric properties of ferroelectric liquid crystal/single walled carbon nanotubes dispersions confined in thin cells," *Chemical Physics Letters*, vol. 479, no. 4-6, pp. 206–210, 2009. 48

[141] S. J. Woltman, J. N. Eakin, G. P. Crawford, and S. Žumer, "Electro-optical investigations of holographic-polymer-dispersed ferroelectric liquid crystals," *Journal of the Optical Society of America A*, vol. 24, no. 12, p. 3789, 2007. 48

[142] A. K. Srivastava, W. Hu, V. G. Chigrinov, A. D. Kiselev, and Y. Q. Lu, "Fast switchable grating based on orthogonal photo alignments of ferroelectric liquid crystals," *Applied Physics Letters*, vol. 101, no. 3, p. 031112, 2012. 48

[143] X. Q. Wang, A. K. Srivastava, V. G. Chigrinov, and H. S. Kwok, "Switchable Fresnel lens based on micropatterned alignment," *Optics Letters*, vol. 38, no. 11, p. 1775, 2013. 48

[144] A. K. Srivastava, X. Q. Wang, S. Q. Gong, D. Shen, Y. Q. Lu, V. G. Chigrinov, and H. S. Kwok, "Micro-patterned photo-aligned ferroelectric liquid crystal Fresnel zone lens," *Optics Letters*, vol. 40, no. 8, p. 1643, 2015. 48

[145] M. J. Madou, "Photolithography," in *Fundamentals of microfabrication and nanotechnology*, ch. 1, pp. 1–86, CRC Press, 3 ed., 2012. 52, 55, 56, 62

[146] D. Meyerhofer, "Characteristics of resist films produced by spinning," *Journal of Applied Physics*, vol. 49, no. 7, pp. 3993–3997, 1978. 55

[147] L. E. Scriven, "Physics and Applications of DIP Coating and Spin Coating," *MRS Proceedings*, vol. 121, no. 1, p. 717, 1988. 55

[148] C. Arnone, "The laser-plotter: A versatile lithographic tool for integrated optics and microelectronics," *Microelectronic Engineering*, vol. 17, no. 1-4, pp. 483–486, 1992. 56

[149] R. Menon, A. Patel, D. Gil, and H. I. Smith, "Maskless lithography," *Materials Today*, vol. 8, no. 2, pp. 26–33, 2005. 56

[150] Durham Magneto Optics Ltd., "Scientific instrumentation for nanotechnology research and development," 2019. 58

[151] P. Le Barny, "Chemistry of polymer molecules for ultrathin films," *Thin Solid Films*, vol. 152, no. 1-2, pp. 99–150, 1987. 60

[152] H. Ito, "Chemical amplification resists: History and development within IBM," *IBM Journal of Research and Development*, vol. 41, no. 1.2, pp. 119–130, 1997. 61, 62

[153] J. M. Shaw, J. D. Gelorme, N. C. LaBianca, W. E. Conley, and S. J. Holmes, "Negative photoresists for optical lithography," *IBM Journal of Research and Development*, vol. 41, no. 1.2, pp. 81–94, 1997. 61

[154] A. Del Campo and C. Greiner, "SU-8: A photoresist for high-aspect-ratio and 3D submicron lithography," *Journal of Micromechanics and Microengineering*, vol. 17, no. 6, pp. 81–95, 2007. 61, 62

[155] O. P. Parida and N. Bhat, "Characterization of optical properties of SU-8 and fabrication of optical components," in *International Conference on Optics and Photonics*, (Chandigarh, India), pp. 4–7, CSIO, 2009.

[156] MicroChem, "Processing Guidelines For: SU-8 2025, SU-8 2035, SU-8 2050 and SU-8 2075," tech. rep., MicroChem Corp., Westborough, MA, 2019. xviii, 61, 62, 71, 121, 122, 131

[157] S. Keller, G. Blagoi, M. Lillemose, D. Haefliger, and A. Boisen, "Processing of thin SU-8 films," *Journal of Micromechanics and Microengineering*, vol. 18, no. 1, pp. 125020–125030, 2008. 62, 65, 66, 68, 70

[158] A. Olziersky, P. Barquinha, A. Vilà, L. Pereira, G. Gonçalves, E. Fortunato, R. Martins, and J. R. Morante, "Insight on the SU-8 resist as passivation layer for transparent Ga2O3–In2O3–ZnO thin-film transistors," *Journal of Applied Physics*, vol. 108, no. 6, p. 064505, 2010. 62

[159] MicroChem, "OmniCoat: Processing Guidelines," tech. rep., MicroChem Corp., Westborough, MA, 2019. 62, 64

[160] D. Pesántez, E. Amponsah, and A. Gadre, "Wet release of multipolymeric structures with a nanoscale release layer," *Sensors and Actuators B: Chemical*, vol. 132, no. 2, pp. 426–430, 2008. 64

[161] H. K. Chang and Y. K. Kim, "UV-LIGA process for high aspect ratio structure using stress barrier and C-shaped etch hole," *Sensors and Actuators A: Physical*, vol. 84, no. 3, pp. 342–350, 2000. 65

[162] J. D. Williams and W. Wang, "Study on the postbaking process and the effects on UV lithography of high aspect ratio SU-8 microstructures," *Journal of Microlithography, Microfabrication and Microsystems*, vol. 3, no. 4, pp. 563–568, 2004.

[163] B. Li, Miao Liu, and Quanfang Chen, "Low-stress ultra-thick SU-8 UV photolithography process for MEMS," *Journal of Micro/Nanolithography, MEMS, and MOEMS*, vol. 4, no. 4, p. 043008, 2005. 65

[164] T. A. Anhoj, A. M. Jorgensen, D. A. Zauner, and J. Hübner, "The effect of soft bake temperature on the polymerization of SU-8 photoresist," *Journal of Micromechanics and Microengineering*, vol. 16, no. 9, pp. 1819–1824, 2006. 66

[165] Bruker, "DektakXT Stylus Profiler: 10th Generation Stylus Profiling System," tech. rep., Bruker Corporation, Tucson, AZ, USA, 2019. 68

[166] R. M. Amos, G. P. Bryan-Brown, E. L. Wood, J. C. Jones, and P. T. Worthing, "Embossing method and apparatus," 2003. 70

[167] J. C. Jones, "The Zenithal Bistable Display: From concept to consumer," *Journal of the Society for Information Display*, vol. 16, no. 1, pp. 143–154, 2008. 74, 131, 159, 209

[168] M. Wahle, B. Snow, J. Sargent, and J. C. Jones, "Embossing Reactive Mesogens: A Facile Approach to Polarization-Independent Liquid Crystal Devices," *Advanced Optical Materials*, vol. 7, no. 2, p. 1801261, 2019. 70, 133, 210

[169] DuPont, "DuPont Teflon AF 1601S and 2400S: Amorphous Fluoroplastic Solutions," tech. rep., DuPont, 2013. 73

[170] S. A. Jones, J. Bailey, D. R. E. Walker, G. P. Bryan-Brown, and J. C. Jones, "Method for Tuneable Homeotropic Anchoring at Microstructures in Liquid Crystal Devices," *Langmuir*, vol. 34, no. 37, pp. 10865–10873, 2018. 74, 83, 84

[171] S. Y. Chou, P. R. Krauss, and P. J. Renstrom, "Imprint of sub-25 nm vias and trenches in polymers," *Applied Physics Letters*, vol. 67, no. 21, pp. 3114–3116, 1995. 75

[172] Shipley, "Microposit MF-319 Developer," tech. rep., Shipley Company, Marlborough, MA, 1997. 77, 78

[173] Shipley, "Microposit S1800 Series Photo Resists," tech. rep., Union Carbide Corporation, 2019. 78

[174] G. Y. Jung, Z. Li, W. Wu, Y. Chen, D. L. Olynick, S. Y. Wang, W. M. Tong, and R. S. Williams, "Vapor-Phase Self-Assembled Monolayer for Improved Mold Release in Nanoimprint Lithography," *Langmuir*, vol. 21, no. 4, pp. 1158–1161, 2005. 83

[175] BDH, "Ferroelectric Smectic C Liquid Crystal SCE13 and SCE13R," tech. rep., BDH Limited, Poole, England, UK, 1988. 87, 89

[176] M. J. Bradshaw, V. Brimmell, and E. P. Raynes, "A novel alignment technique for ferroelectric smectics," *Liquid Crystals*, vol. 2, no. 1, pp. 107–110, 1987. 87

[177] C. H. Bahr, G. Heppke, and B. Sabaschus, "Chiral-racemic phase diagram of a ferroelectric liquid crystal with high spontaneous polarization," *Ferroelectrics*, vol. 84, no. 1, pp. 103–118, 1988. 88

[178] K. Miyasato, S. Abe, H. Takezoe, A. Fukuda, and E. Kuze, "Direct Method with Triangular Waves for Measuring Spontaneous Polarization in Ferroelectric Liquid Crystals," *Japanese Journal of Applied Physics*, vol. 22, no. 10, pp. 661–663, 1983. 89

[179] K. Skarp, I. Dahl, S. T. Lagerwal, and B. Stebler, "Polarization and Viscosity Measurements in a Ferroelectric Liquid Crystal by the Field Reversal Method," *Molecular Crystals and Liquid Crystals*, vol. 114, no. 1-3, pp. 283–297, 1984. 89

[180] M. Stanley, S. E. Day, D. A. Dunmur, and &. M. Grayson, "Comparison of modelling and experimental values of non-linear optical coefficients of SCE13(*)," *Ferroelectrics*, vol. 179, no. 1, pp. 249–256, 1996. 89

[181] D. E. Shoosmith, *Properties of Organosiloxane Liquid Crystals for Dye Guest Host Ferroelectric Display Devices*. Ph. d., University of Southampton, 2001. 89

[182] Instron, "Instron Series 5500 Load Frames Reference Maual," tech. rep., Instron Corporation, Norwood, Massachusetts, United States, 2005. 92

[183] N. Wakita, T. Uemura, H. Ohnishi, H. Mizuno, and H. Yamazoe, "Shock-problem free flcds and mechanism of alignment destruction by mechanical shock," *Ferroelectrics*, vol. 149, no. 1, pp. 229–238, 1993. 96, 103

[184] S. A. Jenkins, J. C. Jones, P. E. Dunn, and R. M. Richardson, "X-ray studies of layer structure and needle defects in anti-parallel aligned SSFLC devices with medium pre-tilt," *Ferroelectrics*, vol. 244, no. 1, pp. 83–93, 2000. 99

[185] H. Furue, T. Miyama, Y. Iimura, H. Hasebe, H. Takatsu, and Shunsuke Kobayashi, "Mesogenic Polymer Stabilized Ferroelectric Liquid Crystal Display Exhibiting Monostability with High Contrast Ratio and Grayscale Capability," *Japanese Journal of Applied Physics*, vol. 36, no. 2, 11B, pp. L1517–L1519, 1997. 99

[186] H. Sato, H. Fujikake, Y. Iino, M. Kawakita, and H. Kikuchi, "Flexible Grayscale Ferroelectric Liquid Crystal Device Containing Polymer Walls and Networks," *Japanese Journal of Applied Physics*, vol. 41, no. Part 1, No. 8, pp. 5302–5306, 2002. 99

[187] J. Brill, E. Lueder, M. Randler, S. Voegele, and V. Frey, "A flexible ferroelectric liquid-crystal display with improved mechanical stability for smart-card applications," *Journal of the Society for Information Display*, vol. 10, no. 3, pp. 189–194, 2002. 99

[188] D. W. Kim, C. J. Yu, Y. W. Lim, J. H. Na, and S. D. Lee, "Mechanical stability of a flexible ferroelectric liquid crystal display with a periodic array of columnar spacers," *Applied Physics Letters*, vol. 87, no. 5, p. 051917, 2005. 99, 100, 114

[189] M. Ozaki, A. Tagawa, Y. Sadohara, S. Oda, and K. Yoshino, "Electrooptic Effect in Homeotropically Aligned Ferroelectric Liquid Crystal," *Japanese Journal of Applied Physics*, vol. 30, no. 9B, pp. 2366–2368, 1991. 100

[190] J. S. Jo, M. Ozaki, and K. Yoshino, "Electrooptical Switching in Homeotropically Aligned Cell Geometry of Ferroelectric Liquid Crystal," *Molecular Crystals and Liquid Crystals*, vol. 410, no. 1, pp. 191–200, 2004. 100, 114

[191] R. A. Soref, "Field effects in nematic liquid crystals obtained with interdigital electrodes," *Journal of Applied Physics*, vol. 45, no. 12, pp. 5466–5468, 1974. 100

[192] D. M. Walba, C. A. Liberko, R. Shao, and N. A. Clark, "Smectic liquid crystal alignment using mechanically rubbed n-octadecylsiloxane self-assembled monolayers," *Liquid Crystals*, vol. 29, no. 8, pp. 1015–1024, 2002. 100

[193] C. R. Safinya, E. B. Sirota, and R. J. Piano, "Nematic to Smectic-A Phase Transition under Shear Flow: A Nonequilibrium Synchrotron X-Ray Study," *Physical Review Letters*, vol. 66, no. 15, pp. 1986–1989, 1991. 103

[194] P. Panizza, P. Archambault, D. Roux, and R. Effects, "Effects of Shear on the Smectic A Phase of Thermotropic Liquid Crystals," *Journal de Physique II*, vol. 5, no. 2, pp. 303–311, 1995.

[195] H. G. Walton, I. W. Stewart, and M. J. Towler, "Flow past finite obstacles in smectic liquid crystals: permeative flow induced SA to SC phase transition," *Liquid Crystals*, vol. 20, no. 5, pp. 665–668, 1996.

[196] P. A. Gass, M. J. Towler, M. Shigeta, K. Tamai, H. Uchida, P. E. Dunn, S. D. Haslam, and J. Jones, "FLCD Mechanical Stability, Setting and Achieving Realistic Targets," in *Proceedings of the 17th International Display Research Conference*, (Toronto, Canada), pp. L28–L29, 1997. 103

[197] G. K. Auernhammer and R. H. Brand, "Shear-induced instabilities in layered liquids," *Physical Review E*, vol. 66, no. 061707, pp. 1–14, 2002. 105

[198] S. M. Jeong, J. K. Kim, Y. Shimbo, F. Araoka, S. Dhara, N. Y. Ha, K. Ishikawa, and H. Takezoe, "Perfluoropolymer Surface for Shock-free Homeotropic Alignment of Smectic Liquid Crystals," *Advanced Materials*, vol. 22, no. 1, pp. 34–38, 2010. 105

[199] N. A. Clark and R. B. Meyer, "Strain-induced instability of monodomain smectic A and cholesteric liquid crystals," *Applied Physics Letters*, vol. 22, no. 10, pp. 493–494, 1973. 105

[200] D. Johnson and A. Saupe, "Undulation instabilities in smectic C phases," *Physical Review A*, vol. 15, no. 5, pp. 2079–2085, 1977. 105, 115, 139, 144, 148, 149

[201] E. J. Davis and J. W. Goodby, "Symmetry and Chirality in Liquid Crystals," in *Handbook of Liquid Crystals. Volume 1: Fundamentals of Liquid*

Crystals (J. W. Goodby, P. J. Collings, T. Kato, C. Tschierske, H. F. Gleeson, and P. Raynes, eds.), ch. 7, pp. 197–230, Wiley-VCH Verlag GmbH & Co. KGaA, 2nd ed., 2014. 109

[202] F. Yang, J. R. Sambles, and G. W. Bradberry, "Measurement of the refractive indices of a ferroelectric liquid crystal," *Journal of Applied Physics*, vol. 78, no. 4, pp. 2187–2192, 1995. 109

[203] F. Yang, G. W. Bradberry, J. R. Sambles, and L. Crystal, "Optical confirmation of the extended mean-field theory for a smectic-C* - smectic- A transition," *Physical Review E*, vol. 50, no. 4, pp. 2834–2838, 1994. 109

[204] R. Lu, X. Zhu, S. T. Wu, Q. Hong, and T. X. Wu, "Ultrawide-View Liquid Crystal Displays," *Journal of Display Technology*, vol. 1, no. 1, pp. 3–14, 2005. 110

[205] V. Y. Reshetnyak, O. V. Shevchuk, and M. Osyptchuk, "Director profile in the in-plane switching of nematic liquid crystal cell with strong director anchoring," in *SPIE 5507, XVI International Conference on Spectroscopy of Molecules and Crystals* (G. O. Puchkovska, T. A. Gavrilko, and O. I. Lizengevich, eds.), (Bellingham, WA), pp. 283–292, 2004. 111, 112

[206] M. Oh-E and K. Kondo, "Response mechanism of nematic liquid crystals using the in-plane switching mode," *Applied Physics Letters*, vol. 69, no. 5, pp. 623–625, 1996. 112

[207] M. Oh-E and K. Kondo, "The in-plane switching of homogeneously aligned nematic liquid crystals," *Liquid Crystals*, vol. 22, no. 4, p. 390, 1997. 112, 182

[208] P. Martinot-Lagarde, "Unwinding of the Helical Texture of a Smectic C* Liquid Crystal, Through Ferroelectric and Dielectric Anisotropic Coupling With an Applied Field," *Molecular Crystals and Liquid Crystals*, vol. 66, no. 1, pp. 61–66, 1981. 113

[209] J. S. Jo, M. Ozaki, and K. Yoshino, "Electrooptic Effect Based on Helix Deformation in Homeotropically Aligned Ferroelectric Liquid Crystal," *Japanese Journal of Applied Physics*, vol. 42, no. 1, 2A, pp. 526–530, 2003. 113, 114

[210] L. M. Blinov and S. P. Palto, "A New Insight on the Bistability and Relevant Phenomena in Ferroelectric Smectic C* Liquid Crystals," *Molecular Crystals and Liquid Crystals*, vol. 429, no. 1, pp. 31–53, 2005. 113

[211] V. G. Chigrinov, A. K. Srivastava, and E. P. Pozhidaev, "Ferroelectric Liquid Crystals: Physics and Applications," *Liquid Crystals and their Application*, vol. 16, no. 1, pp. 9–21, 2016. 114

[212] R. Ribotta and G. Durand, "Mechanical instabilities of smectic-A liquid crystals under dilative or compressive stresses," *Journal de Physique*, vol. 38, no. 2, pp. 179–204, 1977. 115, 117

[213] S. Stallinga and G. Vertogen, "Elasticity theory of smectic and canonic mesophases," *Physical Review E*, vol. 51, no. 1, pp. 536–543, 1995. 115

[214] I. W. Stewart, "Layer distortions induced by a magnetic field in planar samples of smectic C liquid crystals," *Liquid Crystals*, vol. 30, no. 8, pp. 909–920, 2003. 115

[215] H. P. Hinov and M. Petrov, "Observations of Sm C Layer Undulations and Sm C Edge-Dislocations in NOBA Films," *Molecular Crystals and Liquid Crystals*, vol. 100, no. 3-4, pp. 223–251, 1983. 117, 144, 148, 149

[216] A. Findon and H. F. Gleeson, "Elastic Constants of an Achiral Smectic-C Material," *Ferroelectrics*, vol. 277, no. 1, pp. 35–45, 2002. 117, 149

[217] N. Ul Islam and S. J. Elston, "The structure of homeotropic smectic C (SmC) alignment within liquid crystal cells," *Liquid Crystals*, vol. 26, no. 5, p. 716, 1999. 118, 119

[218] L. Ruan, J. R. Sambles, and M. J. Towler, "The effect of an electric field on a homeotropically aligned smectic C liquid crystal," *Liquid Crystals*, vol. 18, no. 1, pp. 81–86, 1995. 119

[219] S. Sinzinger and J. Jahns, *Microoptics*. Wiley-VCH, 2 ed., 2003. 131

[220] B. W. Van Der Meer, G. Vertogen, A. J. Dekker, and J. G. J. Ypma, "A molecular-statistical theory of the temperature-dependent pitch in cholesteric liquid crystals," *The Journal of Chemical Physics*, vol. 65, no. 10, pp. 3935–3943, 1976. 139

[221] T. P. Rieker, N. A. Clark, G. S. Smith, D. S. Parmar, E. B. Sirota, and C. R. Safinya, ""Chevron" Local Layer Structure in Surface-Stabilized Ferroelectric Smectic-C Cells," *Physical Review Letters*, vol. 59, no. 23, pp. 2658–2661, 1987. 139

[222] F. Giesselmann, P. Zugenmaier, I. Dierking, S. T. Lagerwall, B. Stebler, M. Kaš, V. Hamplová, and M. Glogarová, "Smectic-A*-smectic-C* transition in a ferroelectric liquid crystal without smectic layer shrinkage," *Physical Review E*, vol. 60, no. 1, pp. 598–602, 1999. 139

[223] C. Brown, P. E. Dunn, J. C. Jones, S. A. Jenkins, and R. M. Richardson, "X-ray structural studies of ferroelectric liquid crystal devices," *Molecular Crystals and Liquid Crystals*, vol. 402, no. 1, pp. 55–75, 2003. 139

[224] N. V. Solodkov, M. Hird, and J. C. Jones, "Alignment and electro-optical properties of SmC* with direct transition to N* phases," *Molecular Crystals and Liquid Crystals*, vol. 647, no. 1, pp. 162–168, 2017. 139

[225] B. Zeks, "Landau Free Energy Expansion for Chiral Ferroelectric Smectic Liquid Crystals," *Molecular Crystals and Liquid Crystals*, vol. 114, no. 1-3, pp. 259–270, 1984. 140

[226] M. Brunet and N. Isaert, "Periodic structures in smectic C*-pitch and unwinding lines," *Ferroelecfrics*, vol. 84, no. 1, pp. 25–52, 1988. 140

[227] J. P. F. Lagerwall and F. Giesselmann, "Current Topics in Smectic Liquid Crystal Research," *ChemPhysChem*, vol. 7, no. 1, pp. 20–45, 2006. 140

[228] S. Chandrasekhar and G. Ranganath, "The structure and energetics of defects in liquid crystals," *Advances in Physics*, vol. 35, no. 6, pp. 507–596, 1986. 143

[229] J. E. Lydon, H. Gleeson, and E. I. L. Jull, "The identification of the sign and strength of disclinations in the schlieren (nucleated domain) texture of the nematic phase, by optical microscopy," *Liquid Crystals*, vol. 44, no. 12-13, pp. 1775–1786, 2017. 143

[230] I. R. Nemitz, A. J. Ferris, E. Lacaze, and C. Rosenblatt, "Chiral oily streaks in a smectic-A liquid crystal," *Soft Matter*, vol. 12, no. 31, pp. 6662–6668, 2016. 178

[231] I. R. Nemitz, R. G. Petschek, B. Zappone, C. Rosenblatt, I. Gryn, M. Goldmann, N. Boudet, R. P. Lemieux, and E. Lacaze, "Observations of a streak texture in the hybrid-aligned smectic-C phase," *Soft Matter*, vol. 14, no. 3, pp. 460–469, 2017. 178

[232] B. Maximus, E. De Ley, A. De Meyere, and H. Pauwels, "Ion transport in SSFLCD's," *Ferroelectrics*, vol. 121, no. 1, pp. 103–112, 1991. 193, 194

[233] C. Escher, T. Geelhaar, and E. Bohm, "Measurement of the rotational viscosity of ferroelectric liquid crystals based on a simple dynamical model," *Liquid Crystals*, vol. 3, pp. 469–484, apr 1988. 197

[234] K. Kondo, S. Era, M. Isogai, and A. Mukoh, "New Room-Temperature Ferroelectric Liquid Crystals –Material Constants and Electro-Optic Properties–," *Japanese Journal of Applied Physics*, vol. 24, no. 11, pp. 1389–1393, 1985. 197

[235] L. Beresnev and W. Haase, "Ferroelectric liquid crystals: development of materials and fast electrooptical elements for non-display applications," *Optical Materials*, vol. 9, no. 1, pp. 201–211, 1998.

[236] J. Prakash, A. Choudhary, D. S. Mehta, and A. M. Biradar, "Effect of carbon nanotubes on response time of ferroelectric liquid crystals," *Physical Review E*, vol. 80, no. 1, p. 012701, 2009. 197

[237] L. M. Blinov, S. P. Palto, F. V. Podgornov, H. Moritake, and W. Haase, "Hysteresis-free electro-optical switching in conductive ferroelectric liquid

crystals: experiments and modelling," *Liquid Crystals*, vol. 31, no. 1, pp. 61–70, 2004. 200, 201

[238] G. P. Bryan-Brown, C. V. Brown, and J. C. Jones, "Bistable Nematic Liquid Crystal Device," 2001. 209

[239] M. Nagaraj, Y. P. Panarin, J. K. Vij, C. Keith, and C. Tschierske, "Liquid crystal display modes in a nontilted bent-core biaxial smectic liquid crystal," *Applied Physics Letters*, vol. 97, no. 21, p. 213505, 2010. 211